Engineering of Electrically Conductive Cardiac Microtissues to Study the Influence of Gold Nanomaterials on Maturation and Electrophysiology of Cardiomyocytes

By

Ali Navaei

A Dissertation Presented in Partial Fulfillment
of the Requirements for the Degree
Doctor of Philosophy

Approved June 2018 by the
Graduate Supervisory Committee:

Mehdi Nikkhah, Chair
David Brafman
Raymond Q. Migrino
Sarah Stabenfeldt
Brent Vernon

ARIZONA STATE UNIVERSITY

August 2018

ABSTRACT

Myocardial infarction (MI) remains the leading cause of mortality and morbidity in the U.S., accounting for nearly 140,000 deaths per year. Heart transplantation and implantation of mechanical assist devices are the options of last resort for intractable heart failure, but these are limited by lack of organ donors and potential surgical complications. In this regard, there is an urgent need for developing new effective therapeutic strategies to induce regeneration and restore the loss contractility of infarcted myocardium. Over the past decades, regenerative medicine has emerged as a promising strategy to develop scaffold-free cell therapies and scaffold-based cardiac patches as potential approaches for MI treatment. Despite the progress, there are still critical shortcomings associated with these approaches regarding low cell retention, lack of global cardiomyocytes (CMs) synchronicity, as well as poor maturation and engraftment of the transplanted cells within the native myocardium. The overarching objective of this dissertation was to develop two classes of nanoengineered cardiac patches and scaffold-free microtissues with superior electrical, structural, and biological characteristics to address the limitations of previously developed tissue models. An integrated strategy, based on micro- and nanoscale technologies, was utilized to fabricate the proposed tissue models using functionalized gold nanomaterials (GNMs). Furthermore, comprehensive mechanistic studies were carried out to assess the influence of conductive GNMs on the electrophysiology and maturity of the engineered cardiac tissues. Specifically, the role of mechanical stiffness and nano-scale topographies of the scaffold, due to the incorporation of GNMs, on cardiac cells phenotype, contractility, and excitability were dissected from the scaffold's electrical conductivity. In addition, the influence of GNMs on conduction velocity of CMs was investigated in both coupled and uncoupled gap junctions using microelectrode array technology. Overall, the key contributions of this work were to generate new classes of electrically conductive cardiac patches and scaffold-free microtissues and to mechanistically investigate the influence of conductive GNMs on maturation and electrophysiology of the engineered tissues.

DEDICATION

To my wonderful, lovely, and caring wife, Shima. I cannot imagine undertaking this challenge without her help. She has been always my rock! I wish I can be there for her as she has been always there for me.

To my parents, Ferdows & Aliakbar, my brother, Mohsen, and my sisters, Kobra, Mina, and Samira, for their unconditional love and support.

To my parents-in-law, Mohammadali & Hamideh, for their help and support.

ACKNOWLEDGMENTS

I would like to acknowledge my advisor, Dr. Mehdi Nikkhah, for his guidance and support during my PhD. Under his mentorship, I have been able to enrich my scientific knowledge and experimental experience, which tremendously helped me to become more mature researcher. Also, his mentorship on effective communication skills has educated me to perform productive and pleasant collaborative works.

I would also like to acknowledge my advisory committee members, Dr. David Brafman, Dr. Raymond Q. Migrino, Dr. Sarah Stabenfeldt, and Dr. Brent Vernon, for their invaluable instructive and constructive guidance and support.

I would like to thank all current members, Danh, Harpinder, Nitish, Eric, Alex, Yuka and alumni, Ryan, Nathan, and Mariam of Nikkhah Lab for their help and contributions.

I would like to acknowledge Dr. Robert Ros, Dr. Wayne Christenson and Kirash Rahmani for their help on AFM testing; Dr. Oliver Graudejus and Dr. Ruben Ponce Wong for their help and contribution on MEA electrophysiology; Dr. Raymond Q. Migrino and Nina Karamanova for their help on western blot; Dr. John Heffernan and Dr. Amrita Pal from Dr. Vernon's lab for their help on rheology experiments; Ninad Chamele from Dr. Michael Kozicki's lab and Shiyi Liu from Dr. Junseok Chae's lab for their help on impedance measurement; Crystal Willingham from Dr. Stabenfeldt's lab for her help on immunocytochemistry; Dr. Shubhangi Agarwal from Dr. Vikram Kodibagkar's lab for her help on DLS measurements; Russell Urie from Dr. Kaushal Rege's lab for his help on GNMs synthesis; and Dr. Barbara Smith for her significant support and advice on surviving PhD life. I would also like to acknowledge the use of facilities with the LeRoy Eyring Center for Solid State Science and Bioimaging Facility/Keck Lab at Arizona State University.

Lastly, I would like to acknowledge all funding agencies including the Arizona State University Start-up funding, School of Biological and Health Systems Engineering, Ira A. Fulton Schools of Engineering, Phoenix Children's Hospital and National Science Foundation, for their generous support towards my PhD.

TABLE OF CONTENTS

Page

CHAPTER Page

LIST OF TABLES

Table Page

LIST OF FIGURES

Figure Page

Figure Page

PREFACE

The chapters 2, 3, and 6, presented in this PhD dissertation document, have been previously published as described below:

Chapter 2: Navaei et al, Gold nanorod-incorporated gelatin-based conductive hydrogels for engineering cardiac tissue constructs. Acta Biomaterialia, 2016, 41, 133-146.

Chapter 3: Navaei et al, Electrically conductive hydrogel-based micro-topographies for the development of organized cardiac tissues. RSC Advances, 2017, 7(6), 3302-3312.

Chapter 6: Navaei et al, PNIPAAm-based biohybrid injectable hydrogel for cardiac tissue engineering. Acta Biomaterialia, 2016, 32, 10-23.

CHAPTER 1

INTRODUCTION

1.1. Myocardial Infarction Statistics and Burden

Myocardial infarction (MI), commonly referred to as “heart attack”, is one of the major leading causes of death in the United States (Benjamin, 2017). The deteriorating impact of MI on the heart often involves decreased contractility and cardiac output, abnormal remodeling and stress distribution throughout the heart muscle, and ultimately catastrophic heart failure (Aaronson, 2013). Based on the “Heart Diseases and Stroke Statistics-2017” published by the American Heart Association (AHA), approximately 790,000 Americans annually will experience MI, with 580,000 new cases and 210,000 recurring attacks (Benjamin, 2017). The death toll of MI was reported to be 150,000 in 2014, and it is estimated that nearly 14% of cases will lead to patient death. Individuals who experienced MI are up to 15 times more vulnerable to disease and death than the general population (Benjamin, 2017). The life expectancy for male and female patients over, 45 years old after their first MI, is about 8.2 and 5.5 years, respectively (Benjamin, 2017). In addition to the substantial morbidity and mortality, enormous amounts of hospitalization and medical costs are among the major healthcare and society burdens of MI. Specifically, the estimated healthcare cost of patient care with MI in 2011 was reported to be $11.5 billion, placing it among the top 10 most expensive illnesses within the U.S. (Benjamin, 2017; Pfuntner, 2006). Due to these facts, substantial concern has been granted for developing new effective therapies to reduce the incidence of MI and prevent heart failure and patient death.

1.2. Myocardial Infarction Pathophysiology

1.2.1. From onset to chronic stage

MI is defined as the ischemic necrosis of the myocardium due to the lack of blood supply caused by the occlusion of coronary arteries (Frangogiannis, 2015). Thrombotic occlusion, which leads to MI, is the most prevalent cause of obstruction in coronary arteries (Ridolfi, 1977). The thrombotic occlusion of coronary arteries is initiated with the rupture of a vulnerable

atherosclerotic plaque, which contains a lipid-rich core covered by a thin fibrous crust, due to the shear stress applied by circulating blood and/or the self-bursting of the accumulated lipid inside the plaque (Stefanadis, 2017). The rupture of this atherosclerotic plaque exposes the subendothelium and the lipid core to the blood, which triggers the aggregation of platelets, activation of the clotting cascades, and formation of the occlusive thrombus (Maseri, 1986). Immediately after the onset of ischemia, cardiomyocytes (CMs), within the affected area, lose their contractility (hypokinesis or stunned myocardium) (Frangogiannis, 2015). After 15 to 30 minutes, myocardial necrosis and the formation of infarcted tissue begin and progress from the subendocardium outward towards the epicardium (Kumar, 2017). The duration and level of ischemia within the area at risk determine the amount of generated infarct, ranging from only partial (subendothelial) to a full (transmural) infarction of the ventricular wall (Chan, 2006).

From onset to the chronic stage of MI, a series of micro- and macroscopic pathophysiological alterations occurs that substantially changes the appearance and function of the myocardium. At early time points (0-4 hours), aerobic glycolysis within the ischemic myocardium is stopped due to the lack of oxygen supply through the coronary arteries. This oxygen shortage results in a significant depletion of adenosine triphosphate (ATP), and a drop in intracellular pH caused by lactic acidosis (Neely, 1986; Vogt, 2002). ATP depletion induces the dysfunction of ATP-dependent calcium ion (Ca^{2+}) pumps, which leads to high cytoplasmic concentration of Ca^{2+} and mitochondrial swelling (Linkermann, 2015). The swelling of the mitochondrial membrane has significant adverse effects on a wide range of cellular activities, most importantly ATP production, which ultimately induces apoptosis and necrosis in CMs (Webster, 2012). The substantial drop in intracellular pH of CMs, due to the accumulation of lactic acid, also increases the cytoplasmic Ca^{2+} concentration (Kubasiak, 2002; Sharma, 2015), and accordingly leads to mitochondrial swelling and cell death (Linkermann, 2015). These early stage microscopic alterations are considered to be potentially reversible if the ischemia duration is less than approximately 40 minutes, otherwise, irreversible myocardial necrosis will take place as a function of the induced ischemia duration (Frangogiannis, 2015; Kumar, 2017).

The earliest macroscopic pathophysiological event, known as dark mottling, develops within 3 days post-MI. Dark mottling appears because of coagulative necrosis of the ischemic myocardium along with tissue edema and hemorrhage (Frangogiannis, 2015). This process consists of CMs swelling as well as deterioration of intracellular organelles and proteins (Frangogiannis, 2015; Kumar, 2017). Additionally, the contractile force of the heart causes the excessive death of healthy CMs at the infarct border (Kumar, 2017). With the progression and accumulation of coagulative necrosis, excessive numbers of immune cells, mainly neutrophils, infiltrate within the infarct zone, initiating the inflammation phase of MI (Carbone, 2013; Prabhu, 2016). The proteolytic enzymes secreted by neutrophils, during the inflammation phase, degrades the dead cells and damaged extracellular matrix (ECM) proteins. Afterwards, the infarct undergoes dissociation and softening, which subsequently initiates the removal process (i.e. phagocytosis) of dead tissue by macrophages (Horckmans, 2017; Lambert, 2008). The phagocytosis process continues progressively up to 10 days post-MI and is followed by the formation of granulation tissue at the infarct boundary, a process known as the proliferative phase of MI (Frangogiannis, 2015; Kumar, 2017; Prabhu, 2016). During the proliferative phase, the granulation tissue, mainly composed of neovascularized connective tissue develops and ultimately turns into a gray-white non-contractile fibrous scar tissue. Within 2-8 weeks, the generated scar tissue becomes a highly crosslinked thin matrix featuring dense collagen fibers and low cellular content, which replaces the infarct (i.e. the maturation phase of MI) (Prabhu, 2016; Weber, 1996). The primary role of scar tissue is to maintain the structural integrity of the myocardium after infarction and prevent ventricular wall rupture (Talman, 2016). The production and architectural organization of scar tissue is mostly performed by a unique fibroblast-like cell type, known as myofibroblasts, with abundant smooth muscle actin microfilaments (Van Den Borne, 2009). Myofibroblasts are largely originated from resident interstitial fibroblasts, which have been activated by locally secreted factors including TGF-β (Sousa, 2007). Myofibroblasts secrete massive amounts of ECM proteins, especially collagen, which transform the infarct into a dense fibrous scar tissue.

After 2-3 months, the scar tissue further thins and expands to the remote non-infarcted myocardium, deteriorating the residual myocardium contractile capacity (Aikawa, 2001; Christia, 2013; Prabhu, 2016). The thinning of scar tissue and additional negative morphological and functional changes is a phenomenon called ventricular remodeling which most often leads to heart failure (Konstam, 2011). Ventricular remodeling is a pathophysiological process in which the volume, shape and contractility of the left ventricle (LV) undergo massive adverse alterations (Sutton, 2000). Specifically, the LV volume increases due to the expansion and thinning of scar tissue, resulting in ventricular dilation (Cleutjens, 1995). In addition, the viable CMs undergo hypertrophy to compensate for the decreased contractile capacity of the LV, because of the CMs death following MI (Pfeffer, 1990). The CMs hypertrophy transforms the native elliptical shape of LV into a spherical one, which results in chamber enlargement (Mitchell, 1992). These alterations in shape and volume cause uneven stress distribution within the LV wall, resulting in further ventricular dilation and the deterioration of cardiac function (Sutton, 2000). Although LV remolding starts to compensate for the MI-induced loss of contractile capacity of the heart, its adverse pathophysiological effects, such as LV dilation, hypertrophy and uneven stress distribution, can lead to ventricular aneurysm and eventually heart failure.

1.2.2. Standard therapeutic options for treatment of MI

Emergency treatments for MI are mainly focused on reducing the heart's workload, preventing further coronary occlusions, and delivering oxygen to the ischemic myocardium (Mercado, 2013). Next, restoring the occluded coronary blood flow and reperfusion of the ischemic myocardium is the most important action to undertake. The main purpose of these emergency treatments is to prevent or minimize further damage and necrosis to the ischemic myocardium (Mercado, 2013). To restore the blocked coronary blood flow and induce reperfusion, two major procedures are extensively practiced: the use of thrombolytic drugs and primary percutaneous coronary intervention (P-PCI). Thrombolytic drugs (e.g. Anistreplase and Tenecteplase) promote plasminogen activation, which consequently increases the degradation of thrombotic occlusions (Marder, 2013). P-PCI, also known as coronary angioplasty, is a catheter-

based intervention to open the occluded coronary artery using either a stent or balloon, commonly inserted through the femoral artery to restore blood perfusion within the myocardium (Khera, 2016). In addition, there are other surgical procedures, including coronary bypass surgery to induce reperfusion of the infarcted myocardium, as well as ventricular assist devices and cardiomyoplasty to augment the heart pumping ability (Mercado, 2013). Heart transplantation is the final viable solution to prevent patient death due to MI-induced total heart failure (Tonsho, 2014).

1.3. Regenerative Medicine as a Potential Strategy for MI Treatment

The endogenous reparative capacity of human myocardium reduces significantly after the neonatal stage (Kikuchi, 2012). The low proliferation rate of adult CMs has been associated with their inability to enter the cell division cycle (Bergmann, 2009). Moreover, the massive loss of functioning CMs, due to the necrosis and apoptosis induced by MI (Frangogiannis, 2015; Kumar, 2017), prevents the proper healing of the injured myocardium. Therefore, there have been extensive efforts to develop new effective therapies for treatment for MI. Despite the significant therapeutic outcomes of heart transplantation as the ultimate remedy for MI, it still encounters several critical limitations. In particular, organ donor shortage and risk of transplant rejection are two of the major issues that can negatively influence the efficacy of transplantation (JA Robertson, 1987; Tonsho, 2014). Furthermore, heart transplantation is extremely complicated and expensive, putting a financial burden and prolonged post-surgery recovery on patients (JA Robertson, 1987).

Regenerative medicine has been introduced as one of the innovative strategies to induce efficient repair and restoration of the lost functionalities of infarcted myocardium obviating the need for heart transplantation (Hansson, 2013). In the next section, regenerative medicine as a potential strategy for treatment of MI will be discussed. This strategy is commonly categorized into two main branches: scaffold-based tissue engineering (Eschenhagen, 2012) and scaffold-free cell-based therapy (Sanganalmath, 2013).

1.3.1. Cell-based therapies and scaffold-free cardiac tissue engineering

Scaffold-free cell-based therapy (i.e. cell therapy) has been tremendously studied as a potential treatment to prevent or limit heart failure induced by MI over the past two decades (Sanganalmath, 2013). This approach aims to deliver cells within injured myocardium with minimal invasiveness in order to induce tissue regeneration and reestablish the loss of contractility upon MI (Sanganalmath, 2013). In addition, cell transplantation within the infarct can inhibit scar expansion and further deterioration of unaffected myocardial tissue (Farahmand, 2008; Shintani, 2009). It is speculated that the growth factors released by the transplanted cells may trigger an endogenous regeneration within the infarcted myocardium. To date, several cell sources, including skeletal myoblasts, cardiac stem cells (CSCs), mesenchymal stem cells (MSCs), embryonic stem cells (ESCs), and induced pluripotent stem cells (iPSCs), have been used for cardiac cell therapy (Masoudpour, 2017; P. K. Nguyen, 2016). The original cardiac cell therapy studies started with the use of skeletal myoblasts (Lavine, 1937; Taylor, 1998). Skeletal myoblasts can be acquired from autologous origin (Ince, 2004) and are proliferative and hypoxia-resistant (Scaringi, 2013). The injection of skeletal myoblasts within myocardium resulted in reduced scar size, attenuated ventricular remodeling, and improved cardiac function (Farahmand, 2008). However, the poor trans-differentiation of skeletal myoblasts into CMs and failure to create mature intercalated disks, composed of N-cadherins and connexins, lead to poor electro-mechanical integration with the host myocardium and caused fatal arrhythmia (Reinecke, 2000; Reinecke, 2002b).

Adult stem cells (e.g. MSCs and CSCs), ESCs and iPSCs are other cell sources that have been utilized in cardiac cell therapy (Jing, 2008). The capabilities of self-renewing and differentiation to multi-lineages are the two most important characteristics of stem cells which make them attractive for cardiac regeneration (Jing, 2008). MSCs are multipotent stem cells residing in various autologous tissues (Hass, 2011), which are to some extent capable of differentiating into CMs (Toma, 2002). Also, MSCs have shown significant potential to promote vascularization within myocardial scar tissue by secreting various paracrine signaling cues (e.g.

VEGF) (Singh, 2016). The vascularization of infarct reduces scar expansion as well as ventricular remodeling and enhances cardiac function (Silva, 2005). CSCs or cardiac progenitors are another type of adult stem cell capable of differentiating to CMs (Le, 2016). CSCs encompass a heterogeneous population of cardiac progenitor cells including c-kit^{+}, islet-1^{+}, Sca-1^{+}, and cardiospheres, distributed throughout the heart (Le, 2016). Pre-clinical reported studies demonstrated that the injection of CSCs in a MI-induced rat model significantly decreased ventricular chamber dilation and wall stress, resulting in an improved ejection fraction and myocardium regeneration (Beltrami, 2003; Hong, 2014; Nadal-Ginard, 2014). In recent clinical trials using CSCs (Chugh, 2012; Malliaras, 2014) also similar therapeutic outcomes, including high level of biosafety, significant reduction of scar size, induced cardiac regeneration and improved regional ventricular function, were observed. Pluripotent stem cells, including ESCs and iPSCs, are other available candidates which have shown substantial promises for cell-based cardiac therapies (Masoudpour, 2017). These cells offer differentiation to a wide range of cell types specifically CMs. CMs derived from ESCs and iPSCs express cardiac transcription factors (e.g. GATA-4 and Nkx2.5) and have spontaneous beating and heterogeneity in cardiac population (e.g. nodal, atrial, and ventricular) (Eng, 2016; He, 2003). The *in vivo* studies of implanting ESC- and iPSC-derived CMs in rodent and primate MI-models have demonstrated the formation of intact cardiac muscles within infarct, attenuated adverse ventricular remodeling and improved cardiac function (Chong, 2014; Shiba, 2016; Ye, 2014). Despite the promising outcomes, the existing risk of teratoma formation and potential arrhythmogenesis are the major roadblocks that limit their clinical translation (Patricia K. Nguyen, 2015; Shiba, 2016; Y Zhang, 2011).

In general, the efficacy of cardiac cell therapy for regeneration of injured myocardium has been shown to be significantly reduced *in vivo*, primarily due to low viability, retention (less than 2% (Hou, 2005)), and lack of long-term engraftment of injected cells (Jadczyk, 2013; L Li, 2016a). This failure has been attributed to the harsh microenvironment of the infarct, cell transplant leakage due to the vigorously contracting myocardium, and the imperfect routes of cell delivery (Bonios, 2011; Robey, 2008). The harsh microenvironment of the infarcted myocardium which

includes hypoxia, inflammation, and a high concentration of reactive oxygen species (ROS), does not provide a suitable substrate for adhesion and retaining of transplanted cells (Angelos, 2006; Song, 2010). For example, the presence of hypoxia and ROS within the infarct deteriorates expression and assembly of integrins, which induces cell apoptosis through anoikis (i.e. lack of cell-ECM interactions) (Song, 2010). In addition, cells delivered using intracoronary and intravenous infusions have shown lower retention in the site of injury compared to direct injection within the tissue (intramyocardial), clearly demonstrating the impact of delivery method (Kanelidis, 2017). One of the advancements that have been introduced to improve viability and retention of cells after transplantation, is developing 3D scaffold-free multicellular cardiac microtissues instead of single cell delivery method. 3D structure of scaffold-free microtissues offers a physiologically relevant microenvironment with enhanced cell-cell (e.g. cadherins and connexins (Chang, 2009; EJ Lee, 2012)) and cell-ECM (e.g. production of endogenous ECM (W-Y Lee, 2011)) interactions. Additionally, the endogenous secreted ECM within microtissue promotes expression of integrins and prevents anoikis of transplanted cells. Furthermore, the cell-cell mechanical and electrical interactions, through N-cadherins and connexins respectively, are virtually completely absent when single cells are injected. However, injection of cells in the format of microtissues with enhanced cell-cell interactions can induce their electro-mechanical integration with the host myocardium, leading to higher therapeutic outcomes (EJ Lee, 2012; S Zhang, 2015b). At last, the hypoxic core of tightly packed microtissues can passively act as proangiogenic factors, and induce vascularization within the damaged myocardium (Bhang, 2011).

1.3.2. Scaffold-based cardiac tissue engineering

Tissue engineering is an approach, involving scaffold, cells and bioactive cues, to create and develop biomimetic tissue constructs for regeneration applications. Particularly, cardiac tissue engineering includes designing and fabricating artificial tissue surrogates in order to heal injured myocardium after MI, and to re-establish heart contractility (Eschenhagen, 2012). The implantation of tissue surrogates can also prevent or limit the adverse effects of post-MI

ventricular remodeling (Xiong, 2011). Engineered cardiac tissues (ECTs) are typically composed of a scaffolding biomaterial embedded with cells and bioactive signaling cues, such as growth factors (Eschenhagen, 2012). Scaffolds generally provide structural support and/or a suitable delivery vehicle for cells and signaling cues, until complete integration of the ECT with the host tissue occurs. Among a wide range of available scaffolds for cardiac tissue engineering (Locke Davenport, 2015), hydrogels have been at the center of attention as promising candidates for developing ECTs (Z Li, 2011). The aqueous macroporous structure (swollen) of hydrogels is similar to the native ECM (Fan, 2017). This unique and beneficiary characteristic allows adhesion, infiltration and growth of cells within hydrogel-based scaffolds (Fan, 2017). A wide range of different hydrogels with both natural and synthetic origins have been utilized for cardiac tissue engineering. For example, collagen (Zimmermann, 2006), fibrin (Xiong, 2011), gelatin (Saini, 2015), alginate (Shachar, 2011) and chitosan (Pok, 2013) are the mostly used naturally-derived hydrogels. In addition, poly(N-isopropylacrylamide) or PNIPAAm (Navaei, 2016b), poly-2-hydroxyethyl methacrylate or PHEMA (Zuwei Ma, 2010) and poly(ethylene glycol) or PEG (Habib, 2011) are the frequently employed synthetic hydrogels. In addition, a combinatorial class of hybrid hydrogels has been developed to exploit advantages of both natural and synthetic biomaterials. For example, a hybrid of PNIPAAm-gelatin can be synthesized to incorporate the bioactivity and high cellular adhesion affinity of gelatin within a PNIPAAm hydrogel with well-tuned mechanical and gelation properties (Navaei, 2016b).

Hydrogel-based ECTs are usually administered to the injured myocardium as cardiac patches (J Zhang, 2015a) or injectable cell-laden biomaterials (Hasan, 2015). Cardiac patches are made by seeding on or encapsulating cells within a hydrogel construct, and subsequently are implanted onto the injured myocardium. Based on published studies, cardiac patches have been able to provide structural support for thinned myocardium, reduce ventricular dilation and wall stress, augment cell-host integration, and increase contractile capacity of the heart (Xiong, 2011; Zimmermann, 2006). For example, fibrin hydrogel patches encapsulated with human induced pluripotent stem cell (hiPSC)-derived CMs and hiPSC-endothelial cells (ECs) were implanted in MI-induced animal models (Bellamy, 2015; Weinberger, 2016). The fibrin patch significantly

enhanced cell engraftment, neovascularization, and ventricular contractility and attenuated the adverse ventricular remodeling in the MI-induced animals. In one step further to advance cardiac patches, hydrogel-based ECTs with micro- and nano-scale topographies have been introduced to mimic the native myocardium anisotropic cytoarchitecture (Annabi, 2013; D-H Kim, 2010; Navaei, 2017; Weining, 2014). It has been widely accepted that the electrical and contractile functionalities of myocardium are strongly correlated with the anisotropic cytoarchitecture within the cardiac myofibers (Buckberg, 2008). Therefore, cardiac patches with anisotropic cellular alignments can exert electrical and mechanical functionalities in the same direction as the host myocardium to maximize their therapeutic contribution (Fleischer, 2017; Weining, 2014). For instance, tropoelastin methacrylate (MeTro) hydrogels with micron size groove-like topographies were fabricated using UV photolithography (Annabi, 2013). Cardiac cells seeded on the grooved MeTro hydrogels demonstrated highly aligned cardiac myofiber assemblies similar to the native myocardium with significant anisotropic contractions.

Cell-laden hydrogel ECTs also can be injected within injured myocardium preferably through minimally invasive procedures, such as transendocardial catheterization (Hasan, 2015). The use of injectable ECTs offers clear advantages in comparison to the cardiac patches. First, the injection of cell-laden hydrogels inside the infarcted area increases the retention and engraftment of ECTs by providing maximized contact area thorough a 3D ECT-host interface (Traverse, 2012). Second, injectable ECTs can be delivered within the injured myocardium using minimally invasive procedures, including intracoronary, intramyocardial, transendocardial, and intravenous catheterizations (Johnson, 2013), which may be less complicated and intense compared to the open-chest operations for cardiac patch implantation (Montgomery, 2017; Seif-Naraghi, 2013). The major considerations for developing injectable ECTs are the rheology properties (e.g. stiffness and gelation) and bioactivity (e.g. cell adhesion affinity) of hydrogels (Fitzpatrick, 2010; Ifkovits, 2010). For example, shear thinning hydrogels provide minimized shear stress on cells during their delivery through needles or catheters, which leads to high cellular viability post-injection (Rodell, 2016). In addition, incorporation of a bioactive natural polymer within an injectable synthetic hydrogel improves spreading, growth, and maturation of

encapsulated cells, leading to enhanced functionalities of ECT (Kraehenbuehl, 2008). Injectable cell-laden ECTs are in situ gelling scaffolds. Thus, specific biological conditions, such as pH or temperature, can be used to trigger gelation of injectable hydrogels. As an excellent example, temperature-responsive PNIPAAm-based hydrogels have been extensively utilized to synthesize injectable hydrogels for cardiac tissue engineering applications (Cai, 2015; Peña, 2016; Tang, 2017). For instance, in a comprehensive *in vivo* study by (Tang, 2017), human cardiac stem cells were embedded within a PNIPAAm-based injectable hydrogels and transplanted in rat and pig MI-models. The injection of cell-laden hydrogels resulted in the reduction of scar size, promoted vasculature formation, and improvement of the cardiac function (e.g. ejection fraction) in both animal models. In another work by Li (XY Li, 2010) bone marrow stem cells were encapsulated within PNIPAAm-based hydrogels and injected in MI-induced animal models. The outcomes clearly demonstrated improved ejection fraction, ventricular fractional shortening, decreased infarct size, and promoted vascularization within the injured myocardium.

1.4. The Use of Functional Nanomaterials in Cardiac Tissue Engineering

In the previous section, a brief introduction about the conventional scaffold-based ECTs and scaffold-free cell-based therapies for heart regeneration was covered. The noteworthy outcomes of these approaches were discussed in terms of limiting scar expansion, reducing adverse effects of ventricular remodeling, and enhancing cardiac function (Hansson, 2013). However, despite the promising results, there are critical shortcomings associated with both scaffold-based and scaffold-free approaches that need to be further addressed (Kharaziha, 2016). In this section, the recent advances in the use of conductive nanomaterials and their applications to address the limitations of scaffold-based and scaffold-free cardiac tissue engineering will be discussed (Figure 1.1.).

1.4.1. Nanocomposite ECTs with enhanced material properties.

The key characteristic of hydrogels for developing ECTs is their macroporous structure with similar architecture to the native ECM (Section 3.1.). Such macroporous structure enables cellular growth as well as the diffusion of nutrients and oxygen within hydrogel matrices (Fan,

2017). On the other hand, the native cytoarchitecture of myocardium consists of tightly connected CMs, forming uniaxially-aligned anisotropic myofibers (Coghlan, 2001). CMs within myofibers are electrically coupled by means of specific electrical gap junctions known as connexins (Oyamada, 1994). This tight electrical connectivity through connexins allows the rapid conduction of ions between CMs, which results in synchronized contractions (Oyamada, 1994). Therefore, such specific cellular structure-function relationship should be considered for developing ECTs as potential therapeutics for MI (Engelmayr Jr, 2008; Liau, 2012).

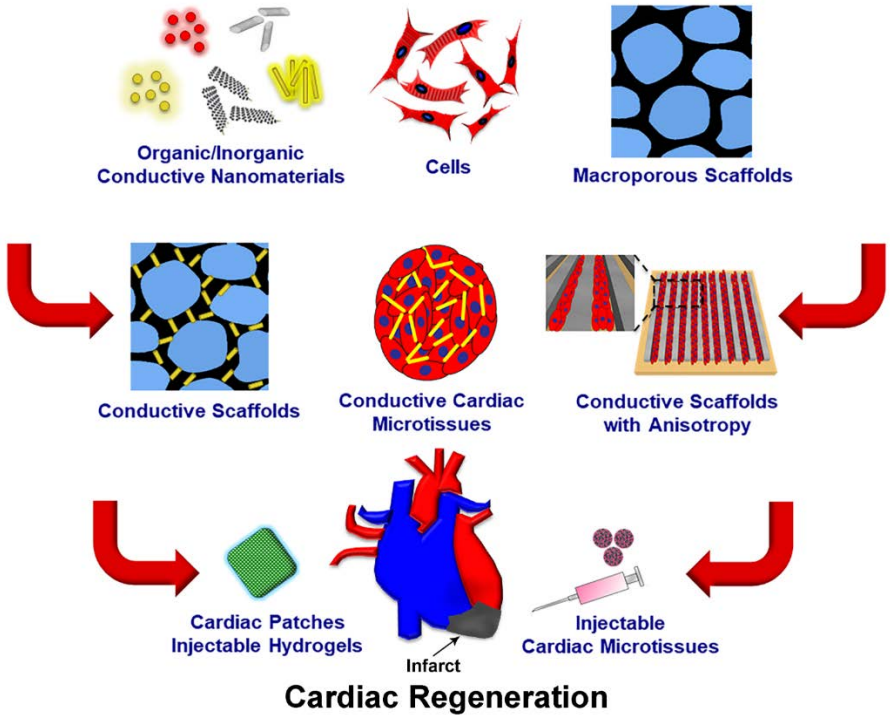

Figure 1.1. The utilization of conductive nanomaterials to develop engineered cardiac tissues (e.g. cardiac patches, injectable hydrogels and scaffold-free microtissues) with enhanced electrical, mechanical, topographical, and biological properties as potential treatments for MI.

Hydrogel matrices typically do not offer electrically conductive microenvironments (Nenad Bursac, 2007; Dvir, 2011). CMs adhered within the pores of hydrogel matrix are electrically isolated by non-conductive polymeric scaffold, which can delay the conduction of action potential throughout the ECT (Dvir, 2011; Tian, 2012). Furthermore, low conduction velocity and subsequent unsynchronized contractions can lead to poor electro-mechanical integration of the

ECT with the native myocardium (Liau, 2012). These heterogeneous electrical and contractile patterns in the ECT-myocardium interface may result in arrhythmogenesis (Miura, 2010; Ter Keurs, 2011), leading to low efficacy or failure of the therapy (Liau, 2012). To develop electrically conductive ECTs, different organic and inorganic nanomaterials have been incorporated within the matrix of hydrogel scaffolds (Figure 1.1.) (Monteiro, 2017). The core rational behind this idea is to primarily facilitate the propagation of electrical signals, either action potential or external stimulation, among CMs throughout the ECT (Y Wu, 2018). The basic understanding of the interactions between conductive nanomaterials and cells was first explained in the context of ultra-sensitive nanosensors and nanoelectronics (Timko, 2010). Unlike macro-scale conductive materials, which only accumulate induced charges on their surfaces, one-dimensional (1D) nanomaterials (e.g. nanowires or nanorods) can transfer the surface charges into their bulk, leading the flow of electrical current (Timko, 2010). Therefore, the charges induced by CMs action potential can be conducted through the nanomaterials (Timko, 2010; Y Wu, 2018). This technology has been used to increase the electrical activity of neurons including excitability and signal transfer (Cellot, 2008; Lovat, 2005; Mazzatenta, 2007; Tian, 2012), therefore, could be used to improve the electrophysiology of CMs.

The incorporation of conductive nanomaterials also increases the mechanical and surface topography of the hydrogels (Gaharwar, 2014). Nanomaterials act as reinforcing nanofillers, which reduce the motility of the polymeric backbone of the hydrogel matrix and enhance the stiffness (Tjong, 2006). Additionally, nanomaterials' surface charge and functionalization can create physiochemical bonds (e.g. electrostatic, π-π stacking, and hydrophobic interactions) with the hydrogel backbone, which further improves matrix stiffness (Q Li, 2016b). Mechanical stiffness and surface topographies of the scaffolding hydrogels critically influence the cardiac maturation of ECTs (Bhana, 2010; Boothe, 2016; Carson, 2016; Deok-Ho, 2005). Cardiac maturation of ECTs can be simplistically defined as the ability of CMs to induce excitation-contraction cycles *via* generating action potential resulting in mechanical contractions of the tissue (Kolanowski, 2017). In addition, conduction velocity of action potential as well as the

magnitude of contractile force in CMs are other important elements of cardiac maturation (C Robertson, 2013).

One of the factors that has a significant impact on the maturation of CMs is their affinity for adhesion and expressing integrins within the surrounding matrix (Israeli-Rosenberg, 2014). CM-matrix interactions are primarily modulated by the expression of integrins (Israeli-Rosenberg, 2014). Accordingly, the expression level of integrins influences the maturation of CMs, regarding expressions of connexin43 (Cx43) gap junctions (Czyz, 2005), Ca^{2+} ion channels (YG Wang, 2000b), and contractile proteins, such as sarcomeric α-actinin (SAC) and cardiac troponin I (cTnI) (X Wu, 2010). Specifically, the expression of integrins leads to the assembly of Costameres and thereafter activation (i.e. phosphorylation) of a wide range of signaling molecules including ILK, FAK, paxillin, vinculin, talin, and PINCH (Israeli-Rosenberg, 2014). The phosphorylation of these molecules results in the activation of AKT, ERK, MAPK, RhoA and WNT signaling pathways (Samarel, 2005), leading to the enhanced expression and maturation of intercalated disks (e.g. Cx43), contractile machinery (e.g. SAC and cTnI) and Ca^{2+} handling within CMs. Many studies have shown that stiff hydrogel scaffolds increase the adhesion and spreading of CMs (Bhana, 2010). The same scenario has been reported about hydrogels incorporated with nano-scale topographies. Such topographies can act as anchoring points for CMs and improve their adhesion and spreading (Deok-Ho, 2005), ultimately leading to the intact formation of cell-cell junctions and tissue maturation. In the following sections, the frequently used conductive nanomaterials for engineering functional ECTs will be discussed (Table 1.1.).

1.4.1.1. Gold nanomaterials

Gold nanomaterials (GNMs), such as gold nanorods (GNRs) and gold nanowires (GNWs), with high electrical conductivity, biocompatibility (Connor, 2005; Khlebtsov, 2011), and facile synthesis and functionalization (Dykman, 2012; Lloret, 2013), have been employed for various biomedical applications including cardiac and neural tissue engineering (Baranes, 2016; Dvir, 2011). In a pioneering study, Dvir (Dvir, 2011) incorporated GNWs within alginate hydrogels (Figure 1.2A.) and seeded with neonatal rat ventricular CMs (NRVCMs) to fabricate electrically

conductive ECTs. The length of GNWs was selected to be approximately 1 μm to increase the probability of electrically bridging cell clusters within the alginate pores with wall thickness of about 500 nm. The conductive atomic force microscopy (Figure 1.2A.) results confirmed the existence of many electrical connections within a 500 nm thick alginate-GNW hydrogel film. In addition, alginate-GNW hydrogels showed significantly higher bulk electrical conductivity compared to pristine alginate. Alginate-GNW ECTs were electrically stimulated to evaluate the ability of GNWs to electrically bridge the alginate porous scaffold. Their finding demonstrated that only CMs on alginate-GNW hydrogels received the propagated electrical stimuli resulting in the contractions of remote CMs (Figure 1.2B.). The maturation of cardiac specific markers including SAC, cTnI and Cx43 were also assessed using immunostaining and western blotting. The results revealed that CMs on alginate-GNW hydrogels produced higher amounts of cardiac proteins with mature phenotypic morphology (i.e. striated sarcomeres). In addition to induced electrical conductivity, incorporation of GNWs improved the mechanical properties (compressive modulus) of pristine alginate by acting as nanoscale reinforcements within the hydrogel backbone. However, the impacts of enhanced stiffness on CMs functionalities were not investigated. Overall, these findings demonstrated for the first time that conductive nanomaterials could electrically connect CMs within the porous scaffold of a hydrogel and induce maturation of contractile proteins and electrical gap junctions. In another study (Baei, 2016), gold nanoparticles (GNPs) were mixed with thermo-responsive chitosan hydrogels encapsulated with MSCs. Apart from extensive material characterizations, this study demonstrated that electrically conductive chitosan-GNP hydrogels enhanced cardiogenic differentiation of MSCs. However, no specific experiments were performed to evaluate the influence of electrical conductivity and enhanced mechanical stiffness on MSC-derived CMs electrophysiology and contractility.

1.4.1.2. Carbon-based nanostructures

Carbon-based nanostructures, such as carbon nanotubes (CNTs) (SR Shin, 2013; Zhou, 2014) and reduced graphene oxide (rGO) (SR Shin, 2016), are among the other popular nanomaterials which have been widely utilized for developing conductive hydrogel-based ECTs

(Martinelli, 2013a). These nanostructures offer high electrical conductivity, and unique mechanical and topographical properties (Eatemadi, 2014). In a pioneering study (SR Shin, 2013), CNTs were embedded within photocrosslinkable gelatin methacrylate (GelMA), to fabricate thin films (~50 μm) of GelMA-CNT hydrogels.

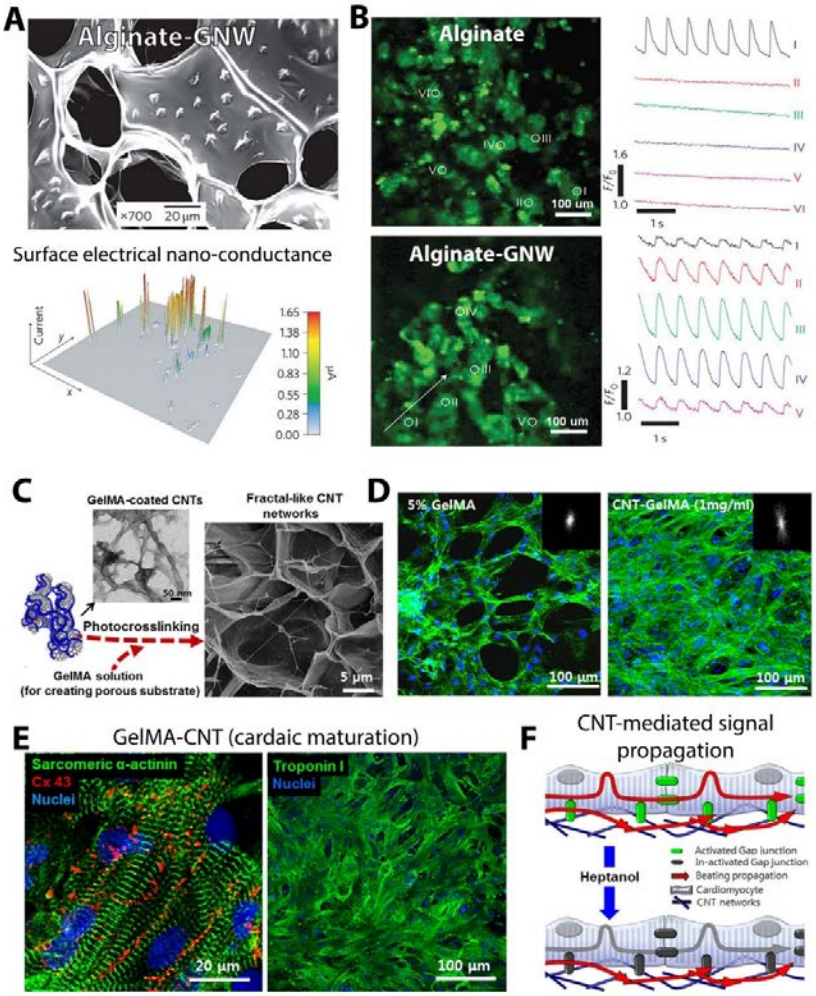

Figure 1.2. A) The SEM micrograph of alginate-GNW hydrogel matrix showing the generated surface conductive nano-topographies by GNWs. B) Ca^{2+} spikes within CMs upon electrical point stimulation displaying synchronous propagation of the signal (Dvir, 2011). C) Electron microscopy images of GelMA-CNT hydrogel matrix. D) F-actin staining (green) images demonstrating the improved CMs retention and spreading on GelMA-CNT. E) The enhanced maturation of CMs mediated by the CNTs within the GelMA hydrogel matrix. F) The schematic illustrating the conductance of electrical signal via CNTs within CMs when the Cx43 gap junctions are blocked (SR Shin, 2013).

The embedded CNTs significantly increased electrical conductivity and mechanical stiffness of GelMA matrix. In addition, scanning electron microscopy (SEM) images depicted the localization of CNTs within macroporous matrix of GelMA as nano-scale topographies (Figure 1.2C.). The enhanced stiffness and induced surface nano-topographies resulted in the significant increase in adhesion, retention, and viability of CMs on GelMA-CNT hydrogels (Figure 1.2D.). Their results also demonstrated that CMs cytoskeleton on GelMA-CNT hydrogels were more spread and aligned compared to pristine GelMA. This change can be associated with nano-topographies created by the incorporation of CNTs within the GelMA matrix. Furthermore, CMs maturation in terms of the expressions of SAC, cTnI, and Cx43 was substantially enhanced on GelMA-CNT hydrogels, based on immunostaining and western blotting results (Figure 1.2E.). Two tests were performed to analyze the impact of scaffold conductivity on electrophysiology of CMs. First, ECTs were electrically paced by field stimulation; GelMA-CNT tissues showed 3- to 4-fold lower excitation voltage thresholds. Second, cell-cell electrical coupling was disrupted using gap junction blocker (heptanol); where GelMA-CNT tissues maintained their synchronized spontaneous contractions upon heptanol treatment (Figure 1.2F.). These data showed that scaffold's conductivity can enhance excitability and sustain signal propagation within the ECT. In another study (Pok, 2014), CNTs were chemically coated with chitosan to achieve more biocompatible nanomaterials with higher aqueous dispersity. Coated CNTs were then mixed with chitosan hydrogel to develop conductive and stiff scaffolds. Chitosan-CNT hydrogels increased SAC protein expression and electrical conduction velocity among CMs, which was consistent with other studies that developed conductive CNT-embedded ECTs for cardiac tissue engineering applications (Ahadian, 2016; SR Shin, 2013; H Sun, 2017).

The promising *in vitro* studies (Martinelli, 2013a) led to implantation of CNT-embedded hydrogel ECTs in MI-induced rat models (X Li, 2014; Zhou, 2014). In a study by Zhou (Zhou, 2014), gelatin-CNT hydrogels were fabricated and seeded with CMs. Then, ECTs were implanted onto the infarct region of MI-induced rats. The *in vivo* findings indicated that the exogenous CMs and CNTs were migrated from the ECT into the infarct. This was an indicative sign of ECT-myocardium integration. In addition, vascularization was observed within the gelatin-CNT ECT as

well as in the interface of ECT-infarct. In terms of limiting adverse ventricular remodeling post-MI, both end-diastolic and end-systolic diameters of the left ventricle were maintained in animals implanted with gelatin-CNT ECTs, confirming minimized chamber dilation. Furthermore, implantation of gelatin-CNT ECTs in rats with infarcted myocardium resulted in significantly enhanced cardiac functions, in terms of ejection fraction and fractional shortening. In contrast no change or diminished myocardial functionalities were observed in implanted pristine gelatin group. These cellular- and organ-level functional improvements were associated with the enhanced cardiac maturation and adhesion of CMs on gelatin-CNT hydrogels. Specifically, expressions of Cx43, N-cadherin, and voltage-gated Na^+ channels were upregulated. Furthermore, adhesion related proteins, including integrin-β1, integrin linked kinase (ILK), and β-catenin, were highly expressed. Despite the comprehensive investigation on cardiac maturation of gelatin-CNT ECTs, the impact of induced electrical conductivity by CNTs on electrophysiology of CMs and infarcted myocardium were not assessed.

Other scaffolding biomaterial s were also mixed with GNMs and carbon-based nanomaterials to enhance their electrical, mechanical and topographical properties. For instance, GNPs were sputter coated on poly(caprolactone)-based electrospun nanofibers to increase electrical conductivity and mechanical stiffness of the fibrous scaffolds (Fleischer, 2014; Michal Shevach, 2013). In another study (You, 2011), GNPs were chemically bonded to the HEMA-based porous scaffolds for developing electrically conductive ECTs. CNTs similar to GNMs have been also incorporated within nanofibrous porous scaffolds, such as poly(glycerol sebacate) (Kharaziha, 2014), chitosan (Pok, 2014), and poly(lactic-co-glycolic acid) (Stout, 2014), to create electrically conductive and mechanically robust ECTs. In all these studies similar findings compared to the hydrogel-based nanocomposite ECTs were reported, including increased adhesion and retention of CMs as well as enhanced expressions of Cx43 gap junctions, SAC, and cTnI. In addition, lower excitation voltage threshold required to induce electrical stimulations within the ECTs, was reported.

Table 1.1.

The scaffold-based tissue engineering approach for developing electrically conductive cardiac patches (ECTs).

Conductive nanomaterial	Scaffolding biomaterial	Cell type	Biological outcomes
Gold nanomaterials			
GNWs (Dvir, 2011)	Alginate hydrogel	NRVCMs	• Increased expressions of SAC, cTnI, and Cx43 • Synchronized Ca^{2+} transients • Enhanced electrical signal propagation
GNPs (Baei, 2016)	Chitosan hydrogel	MSCs	• Enhanced cardiogenic differentiation
GNPs (Fleischer, 2014)	PCL nanofibers	NRVCMs	• Uniaxially-aligned myofibers • High contraction amplitude and frequency • Low excitation voltage threshold
GNPs (You, 2011)	HEMA scaffold	NRVCMs	• Increased expression of Cx43
Carbon-based nanostructures			
CNTs (SR Shin, 2013)	GelMA hydrogel	NRVCMs	• Increased cell retention and spreading • Increased expressions of SAC, cTnI, and Cx43 • Low excitation voltage threshold • Synchronized beating in presence of heptanol
CNTs (Pok, 2014)	Chitosan hydrogel	NRVCMs	• Increased expressions of SAC • Enhanced formation of sarcomere structures • Faster conduction velocity
CNTs (Zhou, 2014)	Gelatin hydrogel	NRVCMs	• Integration with the native myocardium • Increased expressions of Cx43, N-cadherin, and Na^{+} channels • Enhanced cardiac output and reduced adverse ventricular remodeling in MI-model rats *in vivo*
CNTs (Kharaziha, 2014)	PGS-Gelatin nanofibers	NRVCMs	• Improved cell retention and metabolic activity • Enhanced cellular anisotropic alignment • Low excitation voltage threshold

1.4.1.3. Gaps and challenges

Incorporation of conductive nanomaterials within macroporous scaffolds leads to three major material modifications: 1) enhanced mechanical stiffness, 2) generation of nano-scale surface topographies, and 3) enhanced electrical conductivity. As discussed in previous sections, several studies have shown that each of these modifications alone or in combination exerts significant impacts on CMs functionalities and maturation (Bhana, 2010; Boothe, 2016; Carson, 2016; Deok-Ho, 2005; Pok, 2014; Y Wu, 2018; You, 2011).

Overall, there are two mechanisms which lead to enhanced functionalities of scaffold-based ECT through incorporation of conductive nanomaterials. Enhancing mechanical stiffness of scaffolds increases integrin expression and CMs adhesion (Young, 2014). Upregulation of integrin expression in CMs results in an improvement in handling of cytoplasmic Ca^{2+} concentrations through the maturation of Ca^{2+} ion voltage-gated channels, SERCA pumps and ryanodine receptors (Boothe, 2016; X Wu, 2010). This improvement leads to complete excitation-contraction cycles (Rodriguez, 2011). Expression of Cx43 gap junctions can be also upregulated by increasing CMs adhesion affinity (Czyz, 2005; Israeli-Rosenberg, 2014). Similar to the improved stiffness, nano-scale topographies and surface roughness of the scaffolds induce CMs adhesion and integrin expression as well (Carson, 2016; Deok-Ho, 2005). Therefore, the mechanical and topographical enhancements from addition of conductive nanomaterials within the scaffolds, regardless of nanomaterials' electrical conductivity, lead to amplified signal propagation and synchronized contractility among CMs.

Electrical conductivity of scaffolds also intensifies signal propagation within both skeletal and cardiac muscle cells, without altering their adhesion-dependent properties (Hsiao, 2013; Mawad, 2016; Mihic, 2015; You, 2011). For instance, in a study by Mihic (Mihic, 2015), two strips of rat leg skeletal muscle were separated (25 mm apart) using conductive poly(pyrrole)-chitosan hydrogels. When one of the strips was electrically stimulated, action potential signals were transmitted to the other strip through the conductive hydrogel substrate, an event that only occurred at significantly higher voltages for non-conductive chitosan hydrogel. Furthermore,

conductive poly(pyrrole)-chitosan hydrogel increased the calcium transient velocity among CMs *in vitro* and electrical excitability of healthy and infarcted myocardial tissue *in vivo*. In addition to existing experimental data, the enhancement of intercellular electrical coupling using conductive nanomaterials has been confirmed using theoretical models (Lovat, 2005; Y Wu, 2018). The simulations illustrated that CMs bridged by conductive nanomaterials can communicate electrically if the action potential amplitude is high enough, and cells are in tight contact with the nanomaterials (Y Wu, 2018).

Overall, incorporation of conductive nanomaterials within scaffolds leads to a combinatorial enhancement of all electrical, mechanical, and topographical characteristics. However, to date, none of the studies focusing on the development of conductive nanomaterial-embedded ECTs have aimed to elucidate the individual impacts of these enhancements (stiffness, nano-topography, conductivity) on CMs functionalities, such as CMs electro-mechanical coupling. In other words, could non-conductive nanomaterials, with similar morphology as the conductive ones, induce synchronized electrical and contractile functionalities among CMs by only enhancing the cardiac maturation rather than inducing the exogenous electrical conductivity?

1.4.2. Nanomaterials-embedded scaffold-free cardiac microtissues

In recent years, conductive nanomaterials have been at the center of attention to promote electrical and contractile maturation of CMs in scaffold-free tissues for cell-based therapies (Table 1.2.). Early studies on cell-nanomaterial interactions revealed that CMs cultured on CNT-coated substrates were notably more metabolically active compared to those cultured on gelatin-coated substrates (Martinelli, 2012, 2013b). The CNTs also induced electrophysiological maturation by reducing resting membrane potential, enhancing their ability to fire action potential, and increasing the expression of Cx43 gap junctions. Genetically, CMs cultured on CNTs demonstrated upregulation of physiological (e.g. α-MHC and SERCA2a), and downregulation of pathophysiological (e.g. β-MHC, ANP and Sk-Actin) genes (Richards, 2016). Following these promising outcomes, other conductive nanomaterials, including rGO nanoflakes (rGONFs) (Park, 2015) and silicon nanowires (SiNWs) (Richards, 2016; Y Tan, 2015), were used for developing

scaffold-free cardiac microtissues for minimally invasive cell-based therapies. Conductive cardiac microtissues are created by culturing cells and nanomaterials on ultra-low attachment substrates (Desroches, 2012). Cells are self-assembled as spherical microtissues usually known as cardiac spheroids.

rGONFs are carbon-based nanostructures with high physiochemical surface reactivity and electrical conductivity (Dreyer, 2010; Gómez-Navarro, 2007). Due to the abundance of reactive functional groups (e.g. hydroxyl and carboxyl) on rGONFs, they can be used as surfaces for protein adsorption. Due to the fact that the ischemic myocardium is not suitable for cellular adhesion and retention (Gailit, 1993; Song, 2010), many of the transplanted cells undergo anoikis because of the lack of cell-ECM interactions and low integrin expression (Song, 2010). In this regard, Park (Park, 2015) demonstrated that incorporated rGO within scaffold-free MSC microtissues prevented anoikis of stem cells (Figure 1.3A.) by increasing interactions between cells and ECM proteins (e.g. fibronectin). The enhanced cell-ECM interactions also promoted secretion of angiogenic growth factors (e.g. VEGF), and subsequently higher expression of Cx43 gap junctions (Figure 1.3B.). In addition, rGONFs offer electrical conductivity along with high physicochemical reactivity. The induced electrical conductivity within MSC microtissues by rGONFs elevated expression of Cx43 gap junctions, consistent to the results reported for scaffold-based conductive ECTs (You, 2011). The benefits of increased MSCs survivability, and upregulation of angiogenic factors and Cx43 were significantly translated to high vascularization and cardiac function upon implantation of MSC-rGO microtissues in MI-induced rat models (You, 2011). In another sets of studies, cardiac microtissues have also been combined with electrically conductive SiNWs to promote maturation of iPSC-derived CMs (Richards, 2016; Y Tan, 2015). SiNWs are electrically conductive inorganic nanomaterials, which can be degraded *in vivo* (Anderson, 2003). The cardiac microtissues created using iPSC-derived CMs and SiNWs (Richards, 2016; Y Tan, 2017) demonstrated higher expressions of cell-cell junctions (e.g. N-cadherins and Cx43) and contractile proteins (e.g. SAC and cTnI) compared to the pure CMs spheroids using western blotting (Figure 1.3C.). Faster release of cytoplasmic Ca^{2+} upon action potential was another indication of maturation of iPSC-derived CMs induced by SiNWs. When

utilized synergistically with chronic external electrical stimulations (Radisic, 2004), SiNWs significantly promoted iPSC-derived CMs ventricular specific maturation (i.e. less nodal-like CMs).

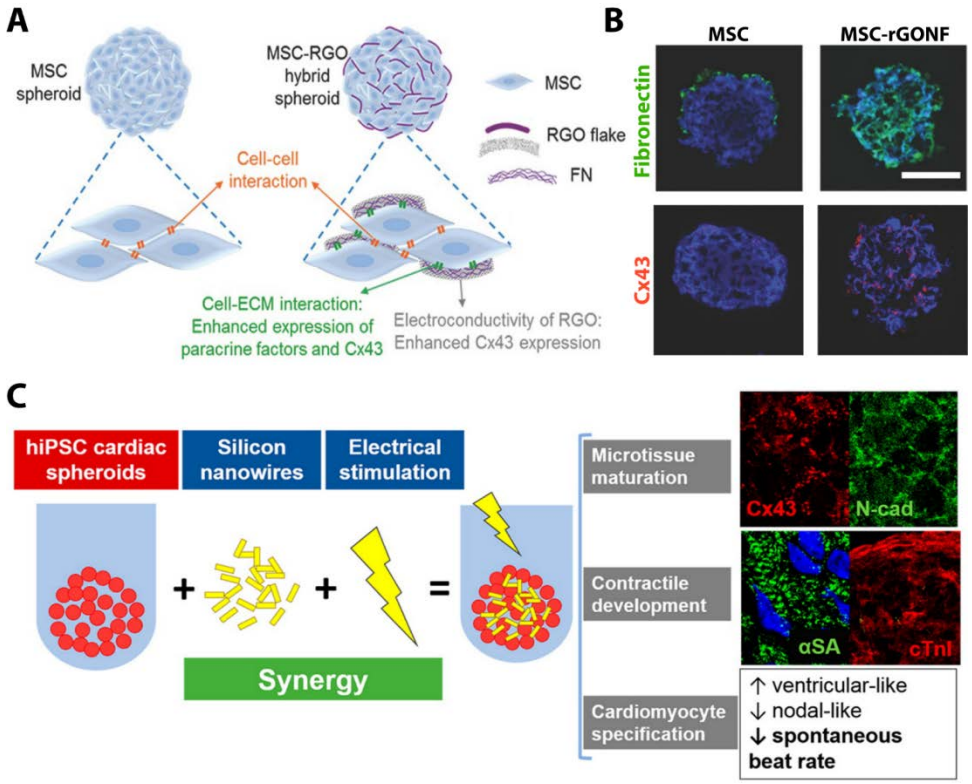

Figure 1.3. A) The schematic drawing depicting the interaction of MSC with the embedded with rGONFs. B) Immunostained images showing the enhanced expressions of fibronectin (green) and Cx43 (red) within MSC-rGONF microtissues (Park, 2015). C) The schematic and immunostained images demonstrating the fabrication and the influence of SiNWs on the cardiac maturation of hiPSC-CMs (Richards, 2016).

Iron oxide nanoparticles (IONPs), with magnetic and semi-conductive electrical properties, also have been used for engineering scaffold-free cell therapies for treatment of MI. In a study by Han (Han, 2015), IONPs were employed to indirectly enhance the expression of Cx43 in MSCs. Specifically, IONPs first were transferred inside rat myoblasts to induce Cx43 expression. The underlying mechanism was explained to be based on the release of Fe^{2+} from IONPs inside the cytoplasm of myoblasts (K Li, 2013). Then, over-expressed rat myoblasts were co-cultured with MSCs to enhance Cx43 expression within MSCs. The *in vivo* results of implanted engineered

tissue comprising co-culture of myoblast-MSC in MI-induced rat models demonstrated increased cardiac function along with reduced scar size. Despite the introduction of sophisticated techniques for engineering MSCs, no characterizations were performed to evaluate the impact of electrical conductivity of IONPs on electrophysiology of MSCs either *in vivo* or *in vitro*.

Table 1.2.

The scaffold-free tissue engineering approach for developing electrically conductive cardiac microtissues for cell therapies.

Conductive nanomaterial	Cell type	Biological outcomes
rGONFs (Park, 2015)	MSCs	• Enhanced cellular viability and reduced anoikis • Increased expressions of VEGF and Cx43 • Improved vascularization and cardiac output in MI-induced animal models *in vivo*
SiNWs	iPSC-CMs	• Increased expressions of SAC, cTnI, Cx43, and N-cadherin • Enhanced dynamic and handling of cytoplasmic Ca^{2+} • Increased ventricular-like population of CMs • Reduced spontaneous beating
IONPs	MSCs	• Induced upregulation of Cx43 expression • Increased cardiac function and reduced scar size in MI-induced animal models *in vivo*

1.4.2.1. Gaps and challenges

Despite the promising outcomes demonstrating the potential of conductive nanomaterials to enhance the maturation of scaffold-free cardiac microtissues, the impact of nanomaterials' electrical conductivity on signal propagation and electrophysiology of the cells/tissues have not been investigated. There is still a knowledge gap on whether the incorporated conductive nanomaterials (without the presence of any scaffolding biomaterial) could facilitate the action potential propagation (i.e. conduction velocity) among CMs. Furthermore, the localization and fate of these nanomaterials within the cells has not been fully identified. Transmission electron

microscopy images have spotted the nanomaterials in the extracellular microenvironment within the microtissues (Park, 2015; Y Tan, 2015). However, most of reported studies regarding cell-nanomaterial interactions only have focused on the acute period (e.g. ~72 hours) (Huff, 2007; Linares, 2014). Therefore, comprehensive studies evaluating the localization of nanomaterials over long-term time periods are needed.

1.5. Objectives and Specific Aims

Over the past few decades, regenerative medicine has emerged as a new strategy to develop scaffold-based cardiac patches and scaffold-free cell therapies as potential approaches for MI treatment. Despite the progress, there are still critical shortcomings associated with these approaches regarding low cell adhesion-retention and lack of global CMs electrical coupling within the cardiac patch, as well as poor engraftment of transplanted cell therapies within the native myocardium. These issues have resulted in diminished functionalities of the therapies, such as unsynchronized contractility and lack of electromechanical integration with the native myocardium, leading to low efficacy or failure of the therapies. The overarching objective in this proposal is to develop two classes of ECTs with superior electrical, mechanical, topographical, and biological functionalities to address the limitations associated with previously developed tissue models as potential treatments for MI. The research design is founded upon a two-fold strategy; scaffold-based and scaffold-free tissue engineering, which are described below.

Scaffold-based tissue engineering: Electrically conductive nanomaterials, including CNT and rGO, have been utilized to enhance electrical signal propagation as well as adhesion-retention of CMs on the cardiac patches. Despite these advances, controversial debate on the cytotoxicity of CNT and rGO limits their clinical translation. Alternatively, GNMs, featuring high electrical conductivity, biocompatibility, and various nanostructures have shown promising results for fabricating cardiac patches with improved CMs electrical coupling and cellular adhesion-retention. Thus, the first objective is to develop conductive gelatin-GNM hybrid cardiac patches with synchronized electrical and contractile functionalities as a potential treatment for MI. In

addition, grooved microtopographies are introduced on gelatin-GNM hydrogels to develop cardiac patches with native-like anisotropic cellular architecture.

In addition, an injectable biohybrid cell-laden hydrogel was developed as a minimally invasive approach for treatment of MI. CMs alone and in co-culture with CFs were encapsulated within a PNIPAAm-gelatin hydrogel, and extensive *in vitro* characterizations were performed. This work was a collaborative effort with Dr. Vernon's lab at Arizona State University.

Scaffold-free tissue engineering: Multicellular cardiac microtissues embedded with conductive nanomaterials, such as rGO, have been developed to improve electrical and contractile functionalities as well as engraftment of cells within the native myocardium. However, these nanomaterials are dispersed randomly within cardiac microtissues with unspecific adhesion affinity to the cells, and minimal electrophysiological studies have been performed. Thus, our second objective is to develop electrically conductive scaffold-free injectable cardiac microtissues embedded with GNMs to address the limitations of cell-based therapeutics.

We propose to complete this study through the following specific aims:

1.5.1. Specific Aim1

Development of gelatin-GNM cardiac patches (with and without grooved micropatterns) with enhanced contractile and electrical functionalities.

1.5.2. Specific Aim2

Engineering and characterization of electrically conductive scaffold-free injectable cardiac microtissues.

1.5.3. Specific Aim3

Fabrication and extensive material and *in vitro* biological characterizations of biohybrid injectable PNIPAAm-gelatin hydrogel tissues for cardiac regeneration.

CHAPTER 2

GOLD NANOROD-INCORPORATED GELATIN-BASED CONDUCTIVE HYDROGELS FOR ENGINEERING CARDIAC TISSUE CONSTRUCTS

2.1. Introduction

MI is a major cause of mortality amongst cardiovascular diseases in the United States accounting for approximately one death per minute (Mozaffarian, 2015). Due to limited availability of donors and high complications associated with the heart transplantation, cell-based therapies (Orlic, 2001; Williams, 2013) and tissue engineering (Engelmayr Jr, 2008; Leor, 2000; Zimmermann, 2006) have been considered as promising strategies for treatment of MI. Particularly, tissue engineering approaches have enabled the development of biomimetic cardiac patches (Annabi, 2013; Dvir, 2009; Kharaziha, 2013), meshes (M Shin, 2004; Teplenin, 2015) and cell sheets (Masuda, 2008; Masumoto, 2014; Matsuura, 2011). In this regard, hydrogel-based biomaterials have been proven to be suitable matrices for cardiac regeneration and repair (Camci-Unal, 2014; Kharaziha, 2016; Paul, 2014). To date, several synthetic and natural hydrogels, such as collagen (Pedron, 2011), gelatin (R-K Li, 1999; McCain, 2014; Saini, 2015), alginate (Khalil, 2009), Matrigel® (Radisic, 2004), and PNIPAAM (Navaei, 2016b) have been utilized to develop tissue substitutes to replace dysfunctional heart muscle. Although, these hydrogels have offered ECM-like microenvironment to support cardiac cell functions, the nano-scale architectural and electrical properties of the previously developed hydrogels are inferior to the characteristics of the native myocardium (Dvir, 2011; Kharaziha, 2016; SR Shin, 2013; Tian, 2012). Inadequate cell adhesion affinity along with electrically insulated structure of conventional hydrogels ultimately lead to poor cell-cell coupling between CMs and thereby diminished functionalities of the engineered tissue (Liau, 2012; Zhou, 2014).

Many recent studies have demonstrated that employing electrically conductive nanomaterials enables addressing the current shortcomings of conventional hydrogel-based scaffolds for cardiac tissue engineering (Pok, 2014; SR Shin, 2012; SR Shin, 2013). In particular, CNTs have been amongst the prevalent conductive nanomaterials for engineering advanced

biomaterials to support cardiac cell functions (Martinelli, 2012). CNTs-embedded scaffolds (Kharaziha, 2014; SR Shin, 2013) have demonstrated enhanced electrical properties facilitating the signal propagation and consequently improved cell-cell coupling. While incorporation of CNTs results in superior tissue level properties, controversial cytotoxicity issues have raised numerous concerns for their use in clinical practice (H-F Cui, 2010; Dumortier, 2013; Firme, 2010; Jain, 2012). In this regard, several strategies such as surface coating and/or functionalization (Vardharajula, 2012) have been considered to reduce the cytotoxicity of CNTs. However, these alterations are expected to compromise the electrical properties of the nanoengineered scaffolds (YY Huang, 2012b; Liu, 2010). Additionally, the low solubility of carbon nanotubes may require complex fabrication procedures (Vardharajula, 2012). Therefore, utilizing electrically conductive nanomaterials with minimized cytotoxicity and less intensive fabrication procedures provides an ideal solution to develop cardiac tissue constructs with enhanced functionalities.

Gold nanostructures such as nanoparticles, nanorods, nanowires, etc. are amongst the most promising nanomaterial candidates for biomedical applications (Cobley, 2011; X Huang, 2009; X-M Jiang, 2012). High electrical conductivity, facile fabrication and modification processes (Frens, 1973), diverse nano-scale architecture (Dykman, 2012) and minimized cytotoxicity (Connor, 2005; Kharaziha, 2016; Khlebtsov, 2011; Shukla, 2005) are the key advantages of gold nanomaterials. Several studies, exploiting gold nanostructures incorporated scaffolds, including alginate (Dvir, 2011), poly(ε-caprolactone) (Fleischer, 2014; Michal Shevach, 2013), thiol-HEMA (You, 2011), and decellularized omentum matrix (Michal Shevach, 2014) have illustrated high potency of these nanomaterials for cardiac tissue engineering. Despite outstanding findings, several aspects of the previously developed scaffolds, including cell adhesion, spreading and the formation of a uniform tissue layer still need to be improved to enhance the functionalities of the engineered cardiac tissues. In the pioneer work of Dvir (Dvir, 2011), alginate hydrogel incorporated with GNWs, was used to form cardiac tissue constructs. Despite the significant outcome and outstanding findings, alginate may not provide a suitable microenvironment for cell binding and attachment. Therefore, it is required to explore hydrogel-based matrices with superior

cell adhesion characteristics along with enhanced electrical conductivity to support the functionalities of cardiac cells.

In this chapter, we developed GNR-embedded GelMA hybrid hydrogels with enhanced material and biological characteristics, for cardiac tissue engineering applications. GelMA is a photocrosslinkable hydrogel, composed of dehydrated gelatin functionalized with methacrylate groups (Van Den Bulcke, 2000), suitable for a wide range of tissue engineering applications (Bertassoni, 2014; Nichol, 2010; Nikkhah, 2012). In particular, we fabricated GelMA-GNR hybrid hydrogels with variable GNR concentrations and performed extensive analyses to assess the material properties of the proposed hydrogel matrix. Furthermore, we conducted substantial biological studies to investigate cardiac cell retention, survival, cytoskeletal organization, expression of specific markers, as well as tissue-level beating and Ca^{2+} transient. The enhanced electrical properties of GelMA-GNR hybrid hydrogels and the nanoengineered architecture of the matrix resulted in improved cell-matrix interaction and cell-cell coupling, ultimately promoting the structural and functional properties of the engineered tissue.

2.2. Experimental Methods

2.2.1. Materials

Gold (III) chloride trihydrate ($HAuCl_4$) (>99.9%), sodium borohydride ($NaBH_4$) (>99%), hexadecyltrimethylammonium bromide (CTAB) (>99%), silver nitrate ($AgNO_3$) (>99%), and L-ascorbic acid (>98%) were purchased from Sigma Aldrich and used without further purification. Gelatin (Type A, 300 bloom from porcine skin), methacrylic anhydride (MA), 3-(trimethoxysilyl) propyl methacrylate (TMSPMA), and 2-hydroxy-1-(4-(hydroxyethoxy) phenyl)-2-methyl-1-propanone (the photoinitiator) all were obtained from Sigma Aldrich. Deionized water (DIW) (18 MΩ) was used for GNR fabrication processes.

2.2.2. GNR synthesis

GNRs were synthesized using a previously established seed mediated growth method (Appendix Figure A.1.) (Nikoobakht, 2003). Briefly, first $HAuCl_4$ (0.5 mM) was dissolved in DIW

and mixed with a 2 mL aqueous solution of CTAB (0.2 M), which turned the color of the solution to deep yellow. Next, 240 µL of ice-cold $NaBH_4$ was added all at once to the solution under stirring and was kept agitated for 2 min. The color of the solution turned from deep yellow to brown-yellow immediately, indicating the formation of GNPs (seed solution). The seed solution contained GNPs with a mean diameter of less than 4 nm (Nikoobakht, 2003). Afterwards, the growth solution was prepared by adding 1.12 mL $AgNO_3$ (4 mM in DIW) to 20 mL CTAB (0.2 M in DIW) followed by the addition of a 20 mL aqueous solution of $HAuCl_4$ (1 mM), which created a deep yellow solution. Subsequently, 280 µL ascorbic acid (13.88 mg in 1 mL DIW) was added gently to this solution, immediately making the solution colorless. The temperature was kept at 25 °C during all the processes. Finally, a 48 µL aliquot of seed solution was poured into the growth solution at 30 °C and the color of solution turned to brown-red over a period of half an hour, confirming the formation of GNRs. To obtain longer GNRs, the solution was kept overnight at 30 °C. The solution contained GNRs with an average aspect ratio (length/width) of 3.15 (Table A.1.). Before further experimentation, the GNRs colloid was centrifuged at 12,000 rpm for 10 min and washed 2 times with DIW to remove the excess CTAB.

2.2.3. Preparation of GelMA-GNR hybrid hydrogels

First, photoinitiator (0.5% wt/v) was completely dissolved in Dulbecco's phosphate-buffered saline (DPBS), and then to this solution, lyophilized GelMA (5% wt/v), with high degree of methacrylation (96.41 ± 1.54%) (data not shown), was added and kept at 80 °C until a clear solution was achieved. Second, certain amounts of centrifuged GNRs (0.5, 1 & 1.5 mg/mL) were mixed with GelMA prepolymer solution followed by water bath sonication for 1 h to obtain a homogeneous mixture. To prepare hybrid constructs (Figure 2.1.), 15 µL of the GelMA-GNR mixture was located between two 150 µm tall spacers and covered by glass slides coated with TMSPMA. The constructs were formed via photopolymerization by UV light (800 mW, 360-480 nm) for 6, 8, 25, and 35 s exposure time for 0, 0.5, 1, and 1.5 mg/mL GNR concentrations, respectively.

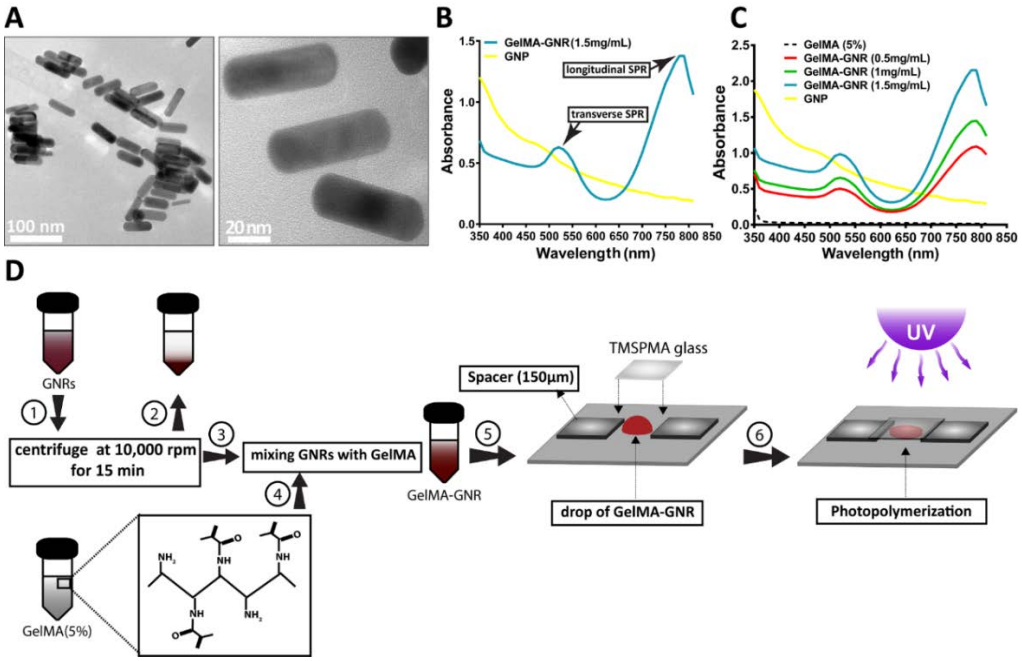

Figure 2.1. A) TEM micrographs of synthesized GNRs. B) UV-Vis absorption spectra of GNPs and GNRs, showing longitudinal and SPR peaks. C) UV-Vis absorption spectra of pure GelMA and GelMA-GNR hybrid prepolymer solutions with 0.5, 1, and 1.5 mg/mL GNRs concentrations. D) Schematic illustration of the fabrication procedure of GelMA-GNR hybrid hydrogel construct.

2.2.4. Characterization of GNRs and GelMA-GNR hybrid hydrogels

GNRs micrographs were obtained by using TEM (Philips CM200-FEG, USA) operating at an accelerating voltage of 200 kV. In addition, the energy dispersive X-ray spectroscopy (TEM-EDX, Philips CM200-FEG, USA) was utilized to further confirm the presence of GNRs within GelMA hydrogel. The porous micro-structure of hydrogel constructs was evaluated by means of SEM (XL30 ESEM-FEG, USA). To prepare samples for SEM, fabricated hydrogels located in DPBS inside an incubator (37 °C) for 24 h. The swollen hydrogels were then submerged in liquid nitrogen followed by freeze-drying, and coating with Au/Pd (4 nm). However, the hydrogel constructs, which were used for localizing GNRs within GelMA hydrogel matrix, were coated with carbon followed by utilizing backscattered electron microscopy (SEM-BSE). Five SEM images were acquired to analyze the porosity and average pore size of the hydrogel constructs using NIH ImageJ software. To measure the mechanical stiffness (Young's modulus) of the hydrogel

constructs, 150 μm thick swollen hydrogels in DPBS were tested by an AFM (MFP-3D AFM, Asylum Research) with silicon nitride tips (MSNL, Bruker). Three samples were used for each GNR concentration and the contact model for a cone indenter was used (Peela, 2016; Sneddon, 1965). For impedance analysis, hydrogel constructs were located between two indium tin oxide (ITO) coated glass slides (Sigma Aldrich) with an AC bias sweeping (Agilent 4284A LCR meter) from 20 Hz to 1 MHz. Four samples were analyzed per each GNR concentration. To evaluate swelling behavior of pure and hybrid hydrogel constructs, 10 mm radius disc-shape (150 μm height) hydrogel constructs were prepared and immediately soaked in the DPBS and stored inside 37 °C for 24 h. Constructs were blotted gently with Kim Wipe to remove the residual DPBS, and the weight values were subsequently recorded. The swollen hydrogels were immersed in liquid nitrogen, followed by lyophilization. The swelling ratio defined as below (Equation 2.1.):

$$Swelling\ ratio = \frac{M_{wet} - M_{dry}}{M_{wet}} \quad (1)$$

where M_{wet} is the mass of swollen and M_{dry} is the mass of lyophilized hydrogels. Three identical samples were selected for each hybrid and pure hydrogels.

2.2.5. CMs isolation and culture

NRVCMs were harvested from the ventricular region of 2-day old neonatal rats based on previously developed protocol (Saini, 2015) accepted by the Institution of Animal Care (IACUC) at Arizona State University. After isolation, the CMs were separated from cardiac fibroblasts by pre-plating the isolated cell suspension for 1 h. Before seeding CMs, the hydrogel constructs were washed 2 times, 10 min intervals, in 1% (v/v) penicillin-streptomycin (Gibco, USA) in DPBS and then washed 2 times in 10 min periods in the cardiac culture medium containing Dulbecco's modified eagle medium (DMEM) (Gibco, USA), fetal bovine serum (FBS) (10%) (Gibco, USA), L-Glutamine (1%) (Gibco, USA), and penicillin-streptomycin (100 units/mL). Harvested CMs were seeded on top of disk-shape constructs (diameter × height, 10 mm × 150 μm; 7.5×10^5 cells/well) and were cultured in the cardiac specific culture media for 7 days under static condition.

2.2.6. Characterization of survival, retention, metabolic activity, and cytoskeleton organization

CMs viability was determined using standard Live/Dead assay kit (Life technologies, USA) based on manufacturer's instruction. Triplicate samples were used for each hydrogel construct and three individual areas were selected within each replicate (n = 9). Fluorescent images were acquired using a fluorescent microscope (Zeiss Observer Z1) and the subsequent quantifications were performed utilizing NIH ImageJ software. The viability was quantified as number of live cells divided by total number of cells. Cell retention was measured by quantifying area fraction, using ImageJ software, one day upon seeding the cells. Five phase contrast images were taken within each sample (three samples for each hydrogel construct, (n = 15)). To examine metabolic activity of cells on the constructs, Alamar Blue assay kit (Invitrogen, USA) was used according to manufacturer's protocol at day 3, 5, and 7 of the culture. Three samples were specified for each hydrogel construct and results were normalized with respect to day 1.

To assess the cytoskeleton organization, hydrogel constructs were stained for F-actin fibers. Cells were fixed in paraformaldehyde (PF) and soaked in Triton X-100 for 45 min at room temperature to permeabilize the plasma membrane, and then blocked in 1% (v/v) bovine serum albumin (BSA) for 1 h. Finally, CMs were stained (1:40 dilution in 1% BSA) with Alexa Fluor-488 phalloidin (Life technologies, USA) for 40 min, and counter-stained with 40,6-diamidino-2-phenyl indole dihydrochloride (DAPI, 1:1000 dilution) for ≈18 min. Z-stack fluorescent images were taken by a fluorescent microscope equipped with ApoTome2 (Zeiss, Germany) and analyzed by ImageJ (FFT built-in plugin). Cells' nuclei alignment was quantified similar to previously established procedures (Bertassoni, 2014; Saini, 2015). Briefly, an ellipse (built-in plugin, ImageJ) was fitted to the nuclei (DAPI) and deviation angle from the main axis of ellipse with respect to the x-axis was determined. All alignment angles were normalized by subtracting from average angle of each image and presented in 10° increment spans.

2.2.7. Immunostaining for CMs specific markers and cell-matrix interaction

Immunocytochemistry technique was used to visualize cardiac specific markers including SAC, Cx43 and cTnI. CMs were fixed in 4% PF for 40 min, followed by treatment with 0.1% Triton X-100 for 45 min at room temperature to permeabilize the plasma membrane. Then, cells were blocked in 10% goat serum for 2 h at 4 °C. Afterwards, CMs were stained with primary antibodies (1:100 dilution in 10% goat serum for SAC and Cx43, and 2 µg/mL in DPBS for cTnI) and placed in cold room (4 °C) for 24 h. After primary staining (Abcam, USA), samples were washed three time in DPBS and stained with secondary antibodies (Life Technologies, USA) comprised of Alexa Fluor-594 (pseudo-colored with green) for SAC, Alexa Fluor-488 for cTnI, and Cx43 (pseudo-colored with red) at 1:200 dilution in 10% goat serum for 6 h. Eventually, cells were stained with DAPI (1:1000 dilution in DPBS) for ≈18 min to label the nucleus. For adhesion specific marker, integrin-β1, all staining steps were similar to cardiac specific markers except that the cells' membranes were not permeabilized and Alexa Fluor-594 secondary antibody was used to stain integrin-β1. High magnification (100x) images of SAC and Cx43 were obtained using confocal microscopy (Leica TCS SP5 AOBS Spectral Confocal System). cTnI images were obtained using a fluorescent microscope equipped with ApoTome2.

2.2.8. Analysis of beating behavior of the cells

The spontaneous beating of CMs was measured and monitored from day 1 to day 7 of the culture. For each data point, 3 videos (30 s long) were captured per sample (12 replicates for each group of hydrogel constructs). Representative beating signals were acquired using a custom written MATLAB code (SR Shin, 2013).

2.2.9. Intracellular Ca^{2+} transient assay

To assess intracellular Ca^{2+} transient within cultured CMs on pure and hybrid hydrogels, calcium indicator assay kit (Life Technologies, USA) including Fluo-4 AM and Pluronic F127 (20% in DMSO) was utilized. All samples (pure and hybrids) on day 7 of the culture were washed one time with pre-warmed DPBS, followed by loading (10 µL/mL in DPBS) the calcium indicator

solution (a mixture of 50 µg of Fluo-4 Am in 50 µL of Pluronic F127) for 45 min. Next, the indicator was discarded, and the hydrogel constructs were soaked in pre-warmed Tyrode solution (Sigma-Aldrich, pH ~7.4) to allow de-esterification for 40 min. Afterwards, spontaneous increase in intracellular Ca^{2+} concentration were imaged using a fluorescent microscope (at 50 frame/s) at 488 nm wavelength. To analyze the change in Ca^{2+} concentration, the fluorescent dye intensity (F) during cells' contractions was normalized by dividing to the background intensity (F_0) and plotted over the time.

2.2.10. External electrical stimulation

The response of the cultured CMs on top of pure and hybrid hydrogels to the external electrical stimulation was investigated according to previously established protocol (Tandon, 2009). Primarily, a chamber was assembled using 2 carbon electrodes (5 mm) with 1 cm spacing attached to a plastic petri dish (6 mm diameter) by silicone adhesive (Figure 2.10A.). Platinum wires were connected to the carbon electrodes (at the opposite ends of each electrode) and all connections were sealed using silicone adhesive. The assembled chamber was sterilized before use by placing under UV light for 1 h. Pulsatile electrical signals produced by a pulse generator (BK PRECISION 4052) were applied on the pure GelMA and hybrid GelMA-GNR hydrogels. Electrical pulses with 2 ms durations at three different frequencies (1, 2, and 3 Hz) were considered for the experiment. The minimum required voltage to observe contraction of CMs was defined as the excitation threshold.

2.2.11. Statistical analysis

All the data collected in this chapter were analyzed using one-way and two-way ANOVA analyses and reported as mean ± standard deviation (SD). To determine a statistically significant difference between groups, we used a Tukey's multiple comparison test with a p-value <0.05 considered to be significant. All the statistical analyses were performed by GraphPad Prism (v.6, GraphPad San Diego).

2.3. Results and Discussion

2.3.1. Fabrication and characterization of GelMA-GNR hybrid hydrogels

The GNRs were synthesized *via* a seed-mediated growth technique (Nikoobakht, 2003) (Appendix Figure A.1.). TEM micrographs (Figure 2.1A.) confirmed the rod-like shape of the GNRs. Figure 2.1B. shows the UV-Vis absorption spectrum with the longitudinal (~810 nm) and transverse (~530 nm) surface plasmon resonance (SPR) (X Huang, 2009) wavelength peaks of the GNRs, demonstrating the successful fabrication of GNRs consistent with the previously published studies (Gole, 2004; Nikoobakht, 2003). The average aspect ratio of the synthesized GNRs was calculated using TEM micrographs, approximately 3.15. The GelMA-GNR prepolymer solution was sonicated to prepare a homogeneous hydrogel solution. All prepared prepolymer solutions (0.5, 1, and 1.5 mg/mL of GNRs) exhibited similar transverse and longitudinal wavelength peaks (Figure 2.1C.), confirming that the GNRs did not break into smaller sizes during the sonication process. The final GelMA-GNR hybrid hydrogel constructs (150 μm thick) were formed through UV photopolymerization, as shown schematically in Figure 2.1D.

The TEM images (Figure 2.2A. and Appendix Figure A.2A) of a thin layer (1-5 μm) of the GelMA-GNR constructs showed that GNRs were successfully embedded within the hydrogel matrix (white dashed area). The EDX microscopy (Appendix Figure A.2B.) of the selected area (dashed line) further confirmed the presence of gold (Au) within the hydrogel layer. Additionally, SEM-BSE images (Figure 2.2B.) of GelMA-GNR hydrogel (1.5 mg/mL) demonstrated that GNRs located within the hydrogel matrix, specifically on the walls of pores. Furthermore, Figure 2.2C. shows similar micro-architecture within GelMA and GelMA-GNR hydrogel constructs. The SEM images demonstrated analogous micro-architecture of pure and hybrid hydrogels as well as no micro-agglomerations of GNRs within the hybrid hydrogel with 1.5 mg/mL GNR concentration. The SEM results clearly demonstrated that the incorporation of GNRs did not cause any considerable alteration within the GelMA micro-structure.

Next, impedance analysis was performed to evaluate the electrical conductivity of the hybrid and pure hydrogel constructs. Figure 2.3A. indicates that GelMA-GNR hybrid hydrogels,

with high concentrations of GNRs (1 and 1.5 mg/mL), exhibited relatively lower electrical impedance as compared to pure GelMA hydrogel at physiologically relevant frequencies (You, 2011). The low electrical impedance of the hybrid hydrogels can be attributed to the resistive current passing through the bridging GNRs, suggesting that high concentration of GNRs improved the overall electrical conductivity of the hydrogel matrix. Such properties have been shown to facilitate signal propagation and coupling between cardiomyocytes (Dvir, 2011; Martinelli, 2012).

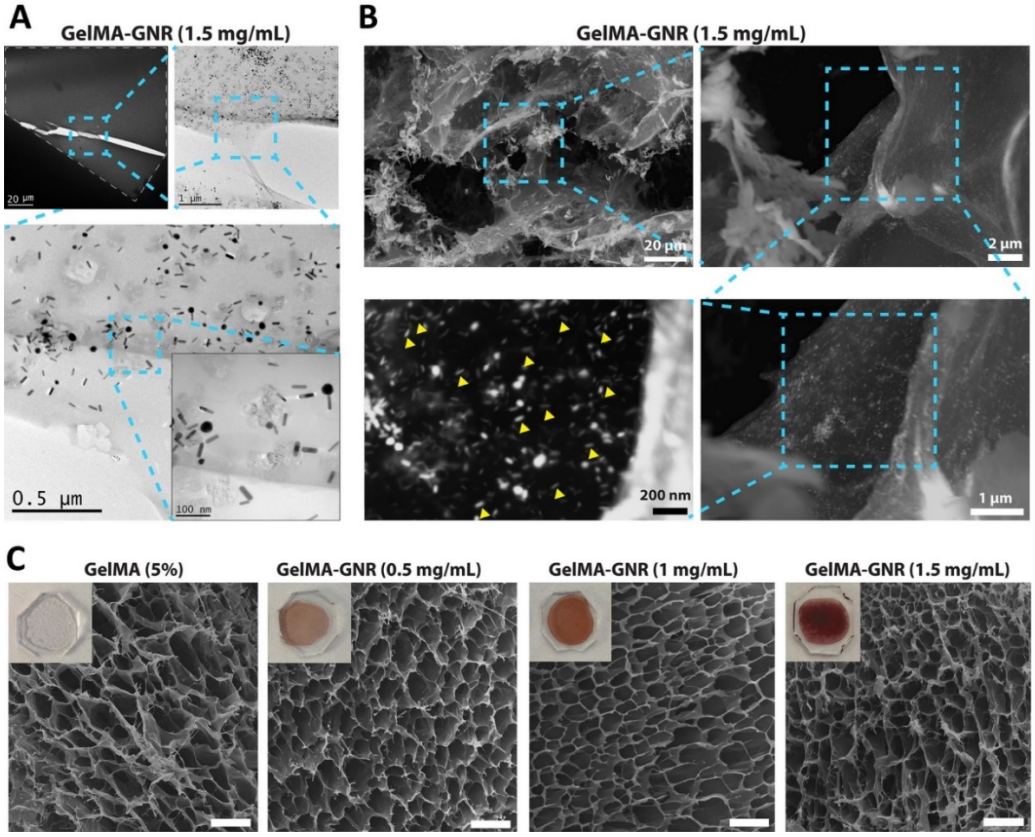

Figure 2.2. A) TEM micrographs showing GNRs embedded within a thin layer (white dashed line) of GelMA-GNR hybrid hydrogel (1.5 mg/mL) (black region is the TEM sample holder). B) SEM-BSE of GelMA-GNR (1.5 mg/mL) hybrid hydrogels displaying the presence of GNRs (yellow arrow heads) within the GelMA matrix located on the pores. C) SE-SEM images illustrating cross-section of GelMA-GNR and pure GelMA hydrogels (insets are photographs of the related hydrogels). Scale bars represent 20 µm.

Swelling and porosity are amongst other important properties of hydrogel-based scaffolds which directly influence nutrients and gas exchanges, specifically in case of cell encapsulation (Dolatshahi-Pirouz, 2014; Nikkhah, 2012) and cell ingrowth within the constructs (Annabi, 2010). As illustrated in Figure 2.3B., incorporation of high concentrations of GNRs (1 and 1.5 mg/mL) within the hydrogel matrices led to a statistically significant decrease in the swelling ratio, from 51 ± 4% for pure GelMA to 23 ± 2% for 1.5 mg/mL GelMA-GNR hybrid hydrogel. This decrease can be associated to the smaller average pore size (Figure 2.3C.) of the hybrid hydrogels (8 ± 2 μm for 1 and 1.5 mg/mL GNRs) as compared to the pure GelMA (12 ± 2 μm), ultimately leading to a decrease in the overall water content. Although incorporation of GNRs resulted in a decrease in pore size, nano-scale porous structures were still available for nutrient and gas exchanges within the hydrogel constructs (Annabi, 2010; YH Lee, 2005). In addition, incorporation of GNRs did not notably influence the porosity percentage of the hydrogel constructs (Figure 2.3D.).

The Young's modulus, as a representative of mechanical stiffness of hydrogels, was measured using AFM, based on nano-indentation, to investigate the constructs' capability for enduring generated compressive forces by CMs. The samples were indented in 4 × 4 grids up to a maximum depth of 4 μm and analyzed in 1 μm sections similar to previous studies (Fuhrmann, 2011). Figure 2.3Ea. and 2.3Eb. show the distribution of local Young's moduli of the hydrogels. The heterogeneity of stiffness increased as a function of GNR concentration. The average Young's moduli for indentation depths of 3-4 μm (Figure 2.3F. and Appendix Figure A.3.) confirmed a significant increase in elastic moduli of GelMA-GNR hybrid constructs up to ≈1.3 kPa with 1 mg/mL GNRs in comparison to ≈450 Pa for pure GelMA. The Young's modulus for pure GelMA construct (150 μm thickness, 6 s UV exposure), quantified herein, relatively correlated to similar studies for a 1 mm thick hydrogel with 60 s UV exposure (Nichol, 2010; Xavier, 2015). The improved mechanical stiffness of hybrid hydrogels can be attributed to the increased structural integrity of the matrix caused by electrostatic interaction between positively charged GNRs (Gole, 2004; X Huang, 2009) and the negatively charged carboxyl groups (Nichol, 2010) of GelMA backbone. Also, GNRs are envisioned to act as reinforcing fillers and thus inducing enhanced mechanical properties (Tjong, 2006). Despite the fact that incorporation of GNRs improved

mechanical stiffness of pure GelMA hydrogel up to 1.3 kPa, this value was still considerably lower than the stiffness of the native human myocardium during contraction cycle (Hassaballah, 2013). However, cardiac patches (Dvir, 2009; Dvir, 2011; SR Shin, 2013) with similar Young's moduli have demonstrated the suitability of these scaffolds, in terms of mechanical robustness, to accommodate cultured CMs contractile forces.

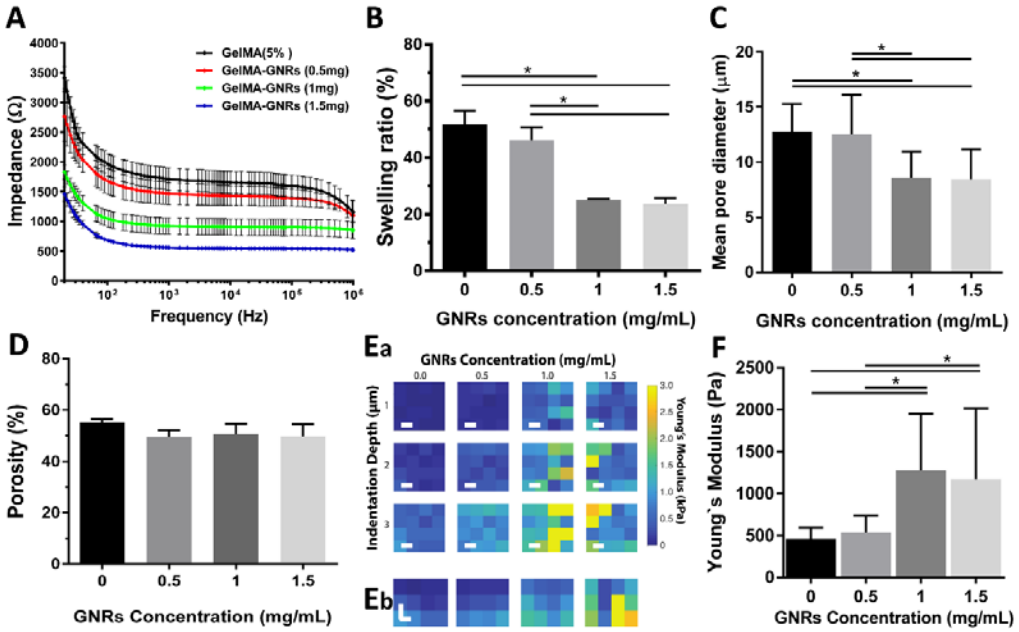

Figure 2.3. A) Impedance of whole hydrogel construct (150 μm thick). B) Swelling ratio percentage as a function of GNRs concentration (*p < 0.05); C) Mean pore diameter and D) porosity percentage of GelMA and GelMA-GNR hydrogel constructs (n = 5; *p < 0.05). Ea) Maps of Young's moduli for different indentation depths. The force indentation curves were fitted in 1 μm segments (0-1 μm, 1-2 μm, and 3-4 μm indentation depths). Eb) Cross section of depth dependent fit for different GNR concentrations. F) Average Young's moduli for all hydrogels (*p < 0.05). (Scale bars: vertical 1 μm; horizontal 20 μm).

Previous studies have shown that due to the presence of MMP-sensitive moieties, GelMA hydrogel degrades in biological environment mainly because of the action of collagenase enzyme (Nichol, 2010). Consistently, many studies in the literature have investigated the fate of other conductive nanomaterials (e.g. CNTs) embedded within hydrogel constructs *in vivo* (Zhou, 2014). The findings of these works have clearly confirmed that the CNTs remained within the proximity

of the cells and further facilitated cell-cell coupling (Martinelli, 2012; Zhou, 2014). Therefore, GelMA-GNR hybrid hydrogels are envisioned to degrade upon implantation. However, extended *in vivo* study is required to assess the fate of GNRs upon degradation of the matrix. *In vivo* studies will be the subject of our future work.

2.3.2. CMs retention, survival, and metabolic activity

To evaluate the capability of the nanoengineered hydrogel constructs to support cell adhesion and spreading, the fraction area of the construct covered by seeded CMs (day 1), was quantified as an indicator for cell retention. The phase-contrast images on day 1 (Figure 2.4A.) demonstrated higher number, more packed and homogeneous distribution of adhered CMs on GelMA-GNR hybrid hydrogels contrary to the discrete and agglomerated cell adhesion patterns on pure GelMA hydrogel. Furthermore, a significant increase in cell retention (Figure 2.4B.) was observed as a function of GNR concentration; from 11 ± 3% for pure GelMA to 26 ± 11%, 49 ± 11%, and 58 ± 6% for 0.5, 1, and 1.5 mg/mL GelMA-GNR hybrid hydrogels, respectively. This major dissimilarity between cell adhesion affinity of GelMA and GelMA-GNR hydrogels can be attributed to the increased stiffness and the presence of GNRs providing cell anchoring points within the hydrogel constructs. To further confirm that the presence of GNRs was the main driver for higher cellular adhesion and retention, we prepared control hydrogel substrates using 20% GelMA with comparable stiffness to GelMA-GNR (1 and 1.5 mg/ml) hybrid constructs (Appendix Figure A.4A. and A.4B.). As expected, cellular retention was significantly lower on 20% GelMA hydrogel as compared to GelMA-GNR hybrid constructs with 1 and 1.5 mg/ml concentrations of GNRs (Appendix Figure A.4C. and A.4D.). These findings clearly demonstrate that GNRs embedded within GelMA hydrogel not only improved the stiffness of the constructs, but also presented higher cell adhesion moieties thereby promoting overall cellular retention, specifically at the initial points of culture.

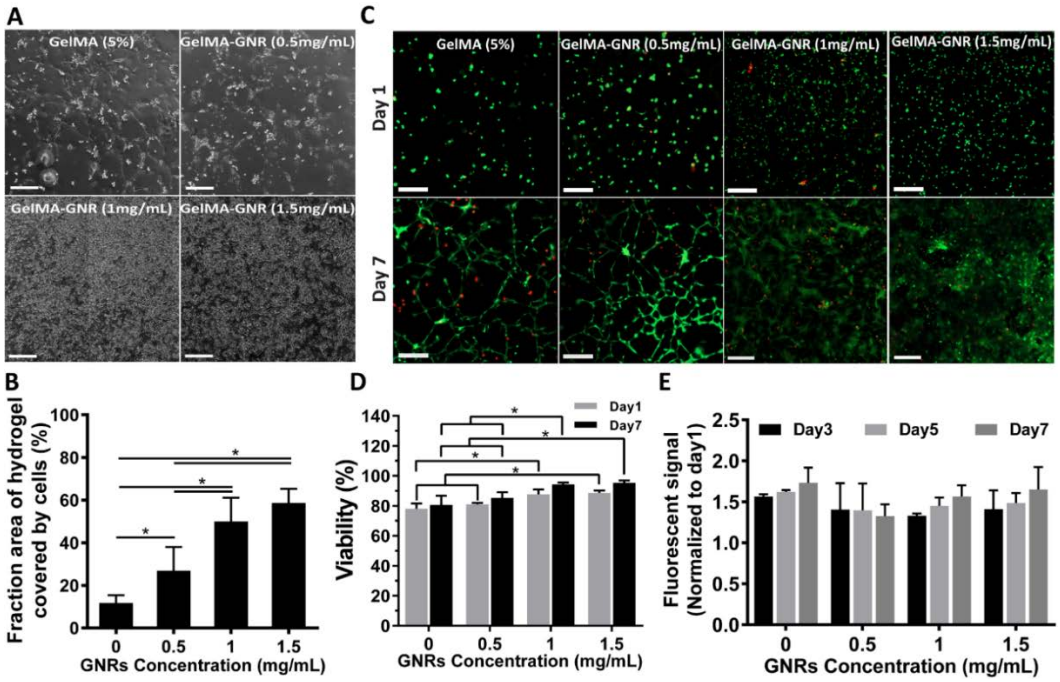

Figure 2.4. A) Phase-contrast images and B) fraction area of hydrogels covered by CMs on day 1 (cell retention). (*p < 0.05). C) Representative fluorescent images of live (green) and dead (red) cells and D) quantified cellular viability at day 1 and 7 of culture (*p < 0.05). E) Normalized Alamar Blue fluorescent signal at day 3, 5, and 7 of culture. All scale bars represent 250 μm.

Such properties make GelMA-GNR hybrid hydrogels as superior matrices due to suitable cellular adhesion sites (Aubin, 2010; H-B Wang, 2000a), stiffness as well as electrical conductivity in comparison to previously reported gold-impregnated scaffolds for cardiac tissue engineering. For instance, Dvir (Dvir, 2011) incorporated gold nanowires within alginate hydrogel, which may not provide sufficient adhesion points to promote cell retention. In the study by You et al. (You, 2011), gold nanoparticles were embedded within thiol-HEMA/HEMA scaffolds. However, due to the cell-repellant nature of HEMA (Nikkhah, 2012), the developed constructs had to be treated with fibronectin (Mosher, 1981) to increase cell adhesion prior to cell seeding. Next, cell viability studies were performed at day 1 and 7 of the culture to provide a comprehensive (from seeding to the end culture period) investigation on survival of CMs seeded on the fabricated hybrid hydrogels (Figure 2.4C. and 2.4D.). Figure 2.4D. illustrates that cardiomyocytes viability increased significantly from 78 ± 3% in pure GelMA hydrogel to 87 ± 3% in 1 mg/mL and 88 ± 1%

in 1.5 mg/mL GelMA-GNR hybrid hydrogels at day 1. Similarly, viability values at day 7 within pure GelMA and hybrid hydrogels confirmed that the seeded cardiomyocytes maintained a considerably high level of survival. In addition, the statistically significant lower cellular viability within 20% GelMA control hydrogel (Appendix Figure A.4E. and A.4F.) as compared to hybrid GelMA-GNR constructs, further strengthens the argument that the presence of GNRs along with enhanced stiffness, enhanced cell retention and eventually led to higher viability of seeded cells. We further determined the metabolic activity of the cultured cells using Alamar Blue assay at day 3, 5, and 7 of the culture (Figure 2.4E.) (normalized to day 1). Across all pure and GelMA-GNR hybrid hydrogels, no statistically significant cellular metabolic activity was observed. However, cultured cells exhibited a gradual increase in metabolic activity within each construct at day 5 and 7 as compared to day 3 of culture which can be due to presence of small population of cardiac fibroblasts during isolation of cardiomyocytes (SR Shin, 2013).

Overall, GelMA-GNR hybrid hydrogels supported CMs culture and exhibited no major risk of cytotoxicity. Our findings are consistent with previous studies by Connor et al. [46] which demonstrated that CTAB-capped gold nanoparticle, washed 2 times with DIW before use, did not result in acute toxicity on the leukemia cells. Consistently, Shukla et al. [48] reported similar findings for exposing gold nanoparticles to the macrophages. In future studies, our group will further perform experiments to investigate the fate of GNRs using *in vivo* MI model.

2.3.3. Actin cytoskeleton organization and formation of cardiac tissue layer

To investigate the F-actin cytoskeleton organization of the CMs and the formation of interconnected cell network (tissue layer), the cells were stained for F-actin fibers at day 7 of the culture. The expression of F-actin fibers enhanced on GelMA-GNR hydrogels with 1 and 1.5 mg/mL of GNR concentrations, in contrast to pure GelMA and hybrid hydrogel with 0.5 mg/mL of GNR concentration (Figure 2.5A.). The improved expression of F-actin fibers can be directly correlated to the enhanced cell retention (Figure 2.4B.) on hybrid hydrogels as also shown by phase contrast images (Figure 2.4A.). Furthermore, at high concentration of GNRs, specifically at 1.0 mg/mL and 1.5 mg/mL, improved local alignment of F-actin fibers (Figure 2.5A., white arrows)

was observed. This can also be observed from Fast Fourier Transform (FFT) analysis of F-actin images which depicted enhanced local alignment of fibers within GelMA-GNR hybrid at high concentrations of GNRs as compared to pure GelMA hydrogel (Figure 2.5A. insets).

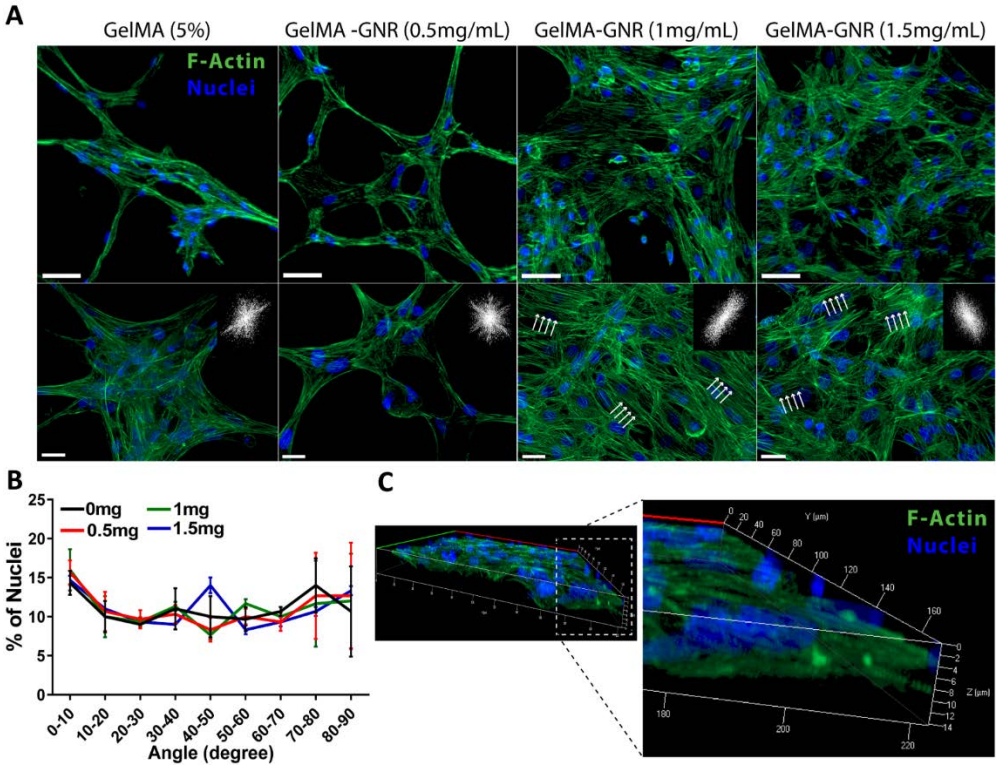

Figure 2.5. A) Z-stack (top-view) fluorescent images of F-actin stained (green) at day 7 of the culture for pure GelMA and hybrid GelMA-GNR hydrogels. Local fiber alignment is shown with white arrows. DAPI (blue) represents stained nuclei. FFT images (top right insets) demonstrating local alignment of F-actin fibers. (top-row scale bars represent 50 μm; bottom-row scale bars represent 20 μm). B) CMs' nuclei alignment distribution from 0 to 90 degrees. C) A 3D Z-stack fluorescent image of the GelMA-GNR (1.5 mg/mL) tissue construct.

Such induced local alignment at high concentration of GNRs is significant, since no global alignment (Figure 2.5B.) was observed due to absence of any micropatterned feature on the hydrogel constructs (Saini, 2015). The elongated and highly packed cells within the hybrid GelMA-GNR hydrogels led to the formation of a uniform and interconnected tissue layer. Particularly, the Z-stack fluorescent (Figure 2.5C.) and phase contrast images (Figure A.5.)

confirmed the formation of an intact tissue layer on top of hybrid hydrogel constructs over 7 days of the culture. Overall, the improved cellular spreading, induced by the bioactivity of gelatin structure and mediated cell adhesion by incorporation of GNRs, led to the formation of an integrated cardiac tissue layer.

2.3.4. Cardiac-specific markers and cell-matrix interaction

Cardiac-specific markers including SAC, Cx43, and cTnI were immunostained to assess the phenotype of the cultured CMs over the culture period. While SAC and cTnI are the two specific proteins, involved in the actin-myosin contraction complex, Cx43 is a well-known gap junction protein responsible for synchronous contraction of the cells (Guerrero, 1997; Oyamada, 1994; Saini, 2015; You, 2011). As shown in Figure 2.6. and Appendix Figure A.6., at day 1 of culture, the cells mainly adopted a round morphology without intact formation of sarcomeres and cTnI within all the hydrogel constructs. However, the immunostained images on day 3 displayed the formation of a few sarcomere structures specifically in case of GelMA-GNR hydrogels with 1 and 1.5 mg/mL GNRs (white arrows). Eventually on day 7, uniform and highly organized SAC structures were evident across hybrid hydrogels (e.g. 1.0 and 1.5 mg/mL) in contrast to pure GelMA constructs. Similar observations were made in cTnI immunostained images, demonstrating extended architecture as a marker of contractile machinery within hybrid hydrogels with high concentrations of GNRs. Thus, the assembled tissue on GelMA-GNR hybrids, with high concentration of impregnated GNRs, exhibited more organized myofilament assembly, consistent to previously reported studies (Dvir, 2011; Kharaziha, 2014; SR Shin, 2013; Zhou, 2014). Our immunostaining results for Cx43 gap junction proteins also demonstrated a similar trend. While on day 1, Cx43 expression was agglomerated and undispersed across all the groups, by day 7, a more homogenous distribution of Cx43 was observed, specifically on GelMA-GNR hybrid hydrogels (1 and 1.5 mg/mL). Therefore, GelMA-GNR hybrid hydrogels with high concentrations of GNRs demonstrated improved cell-cell coupling with mature contractile machinery as compared to pure GelMA hydrogel.

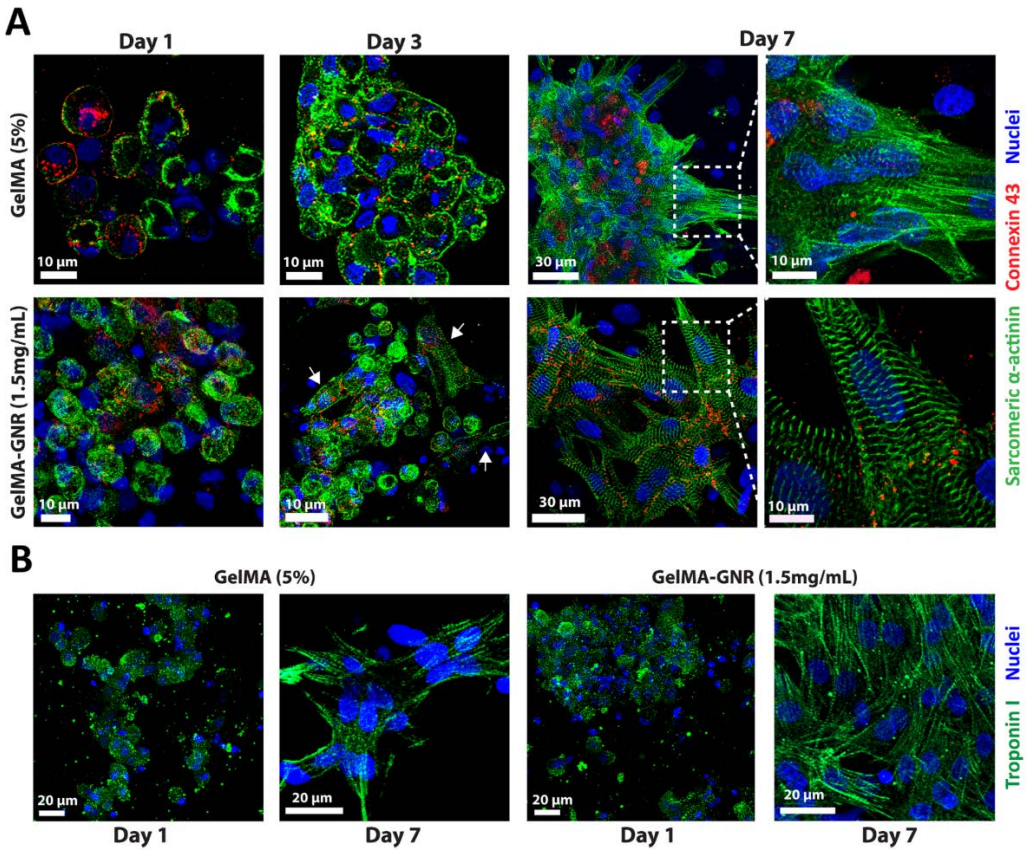

Figure 2.6. A) Representative immunostained images showing the expression of SAC (green) and Cx43 (red) on day 1, 3 (arrows showing sarcomeres formation), and 7 of the culture. B) Immunostained images of cTnI (green) on day 1 and 7 of culture for GelMA and 1.5 mg/mL GelMA-GNR hybrid hydrogels.

Further, to analyze the cell-matrix interaction on the synthesized hydrogel, samples were stained with Integrin-β1 which is a transmembrane protein and plays a significant role in mechano-transduction (Zhou, 2014). Figure 2.7. shows immunostained images of the cells at different magnifications (20x and 40x) on day 7 of the culture, confirming the abundance of integrin-β1 and consequently cell adhesion sites with higher concentrations of GNRs. The expression of integrin-β1 further confirmed our observations on improved cellular retention (Figure 2.4B.) and the abundance and organization of F-actin fibers (Figure 2.5A.) on hybrid constructs with higher concentrations of GNRs (1 and 1.5 mg/mL).

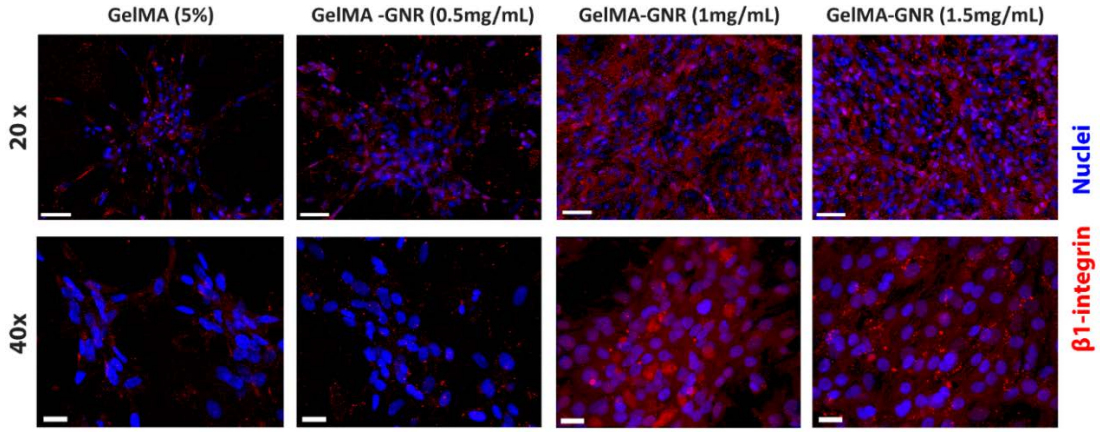

Figure 2.7. Immunostained Z-tack images (20× and 40×) of integrin-β1 for pure GelMA and GelMA-GNR hybrid hydrogels (0.5, 1, and 1.5 mg/mL) on day 7, showing the presence and distribution of cell adhesion affinities. Scale bars represent 50 μm for 20× and 20 μm for 40× figure panel.

Overall, seeded CMs on GelMA-GNR hybrids, specifically with 1 and 1.5 mg/mL concentrations of GNRs, demonstrated improved tissue structure as compared to pure GelMA hydrogel. To further investigate the influence of conductive GelMA-GNR hydrogels on tissue-level functionalities, we analyzed the spontaneous beating and intracellular Ca^{2+} transient of the CMs as a function of time.

2.3.5. Beating behavior of CMs

To assess tissue-level functionalities, beating behavior (represented as an average number of synchronous beats per minute (BPM)) of CMs seeded on hydrogel constructs was further analyzed through real-time video microcopy from day 1 to day 7 of the culture. CMs started beating in a spontaneous and synchronous manner, as they created interconnected cell networks as a function of GNRs concentration on day 3. Figure 2.8A. displays average number of BPM for pure and hybrid hydrogel constructs. As can be observed, hybrid tissue constructs with 1 and 1.5 mg/mL of GNRs exhibited a significantly higher beating frequency (BPM) as compared to pure GelMA hydrogel at day 3. By day 7, CMs within 1.5 mg/mL GelMA-GNR hybrid hydrogels demonstrated notably increased beating frequency (102 ± 72 BPM), as compared to 1 mg/mL (56

± 24 BPM), 0.5 mg/mL (38 ± 11 BPM) GelMA-GNR hybrids, and pure GelMA (33 ± 9 BPM) hydrogel.

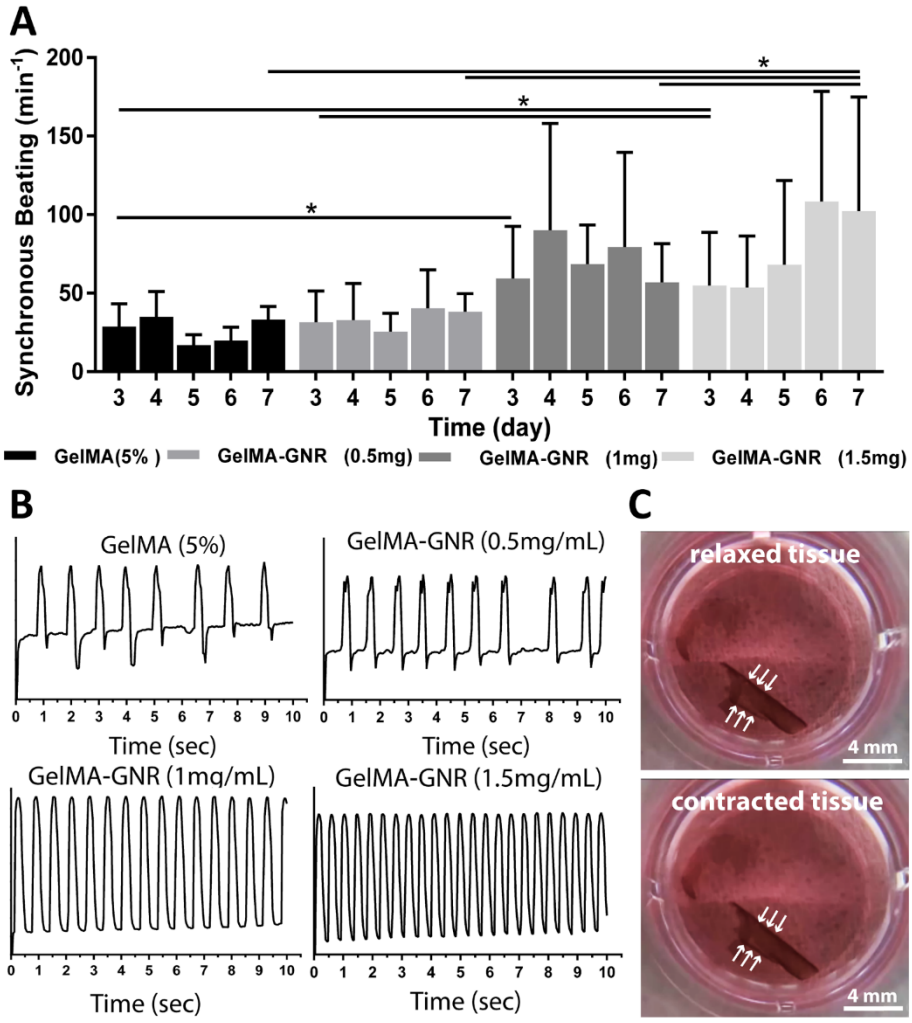

Figure 2.8. A) Synchronous beating frequency (BPM) of CMs from day 3 to day 7 of culture. (*p < 0.05). B) Representative beating signal graphs. C) Photographs of a detached centimeter scale hybrid hydrogel tissue constructs (1.5 mg/mL GelMA-GNR) displaying contraction (white arrows) of the whole hydrogel construct by seeded CM.

Furthermore, representative beating signals (Figure 2.8B.) and real time movies (Appendix C.1., C.2., C.3. and C.4.) illustrated more synchronous, stable, and robust beating behavior within GelMA-GNR hybrids (1 and 1.5 mg/mL) in comparison to pure GelMA and hybrid hydrogel with 0.5 mg/mL GNR concentration. Such beating behavior can be attributed to the enhanced

electrophysiological characteristics and improved cell-cell coupling of the formed tissues on nanoengineered hydrogels. Additionally, to examine the capability of the formed cardiac tissue layer to contract the hydrogel construct, we detached 2 samples of hybrid hydrogels (1 and 1.5 mg/mL GelMA-GNR) at day 5 of culture from the TMSPMA glass slide and suspended the tissue in the culture media (Figure 2.8C.). We were able to successfully create a suspended beating tissue sheet (centimeter scale) (Appendix C.5. and C.6.). These observations further confirmed that the formed cardiac tissue layers, on top of GelMA-GNR hydrogels, were highly functional to bend the 150 μm thick construct.

Although similar observations for highly stiff CNT-embedded GelMA hydrogels were reported by Shin et al. (SR Shin, 2013), cytotoxicity (H-F Cui, 2010; Dumortier, 2013; Firme, 2010) and high UV absorption of CNTs (SR Shin, 2012) remain as major concerns for cardiac tissue engineering applications. Specifically, high UV absorbance of CNTs interferes with photoinitiator excitation, and consequently influences hydrogel crosslinking process (SR Shin, 2012; SR Shin, 2013) and the subsequent formation of 3D tissue constructs (beyond 150 μm thickness). This is particularly crucial in case of 3D cellular encapsulation within hydrogel constructs, where the cells have to be exposed to extended duration of UV. On the other hand, GNRs with low UV absorption (Figure 2.1B. and 2.1C.) and minimized cytotoxicity (Connor, 2005; Khlebtsov, 2011) enabled us to fabricate relatively thicker cardiac patches (e.g. 150 μm).

2.3.6. Intracellular Ca^{2+} transient

To investigate calcium signaling (puffs) within seeded CMs, calcium ions transient (Ca^{2+}) analysis was performed. First, tissue constructs were loaded with the dye, followed by capturing videos from different region of 1 mm^2 of GelMA and GelMA-GNR hybrid hydrogels. Five different sites within each region were selected and the increase in concentration of Ca^{2+} ions was represented as fluorescent intensity of dye (F) divided by the background intensity (F_0). As represented in the Figure 2.9. and Appendix C.7., intracellular Ca^{2+} puffs occurred at different frequencies across 5 considered spots on pure GelMA and GelMA-GNR (0.5 mg/mL) hydrogels. However, cardiomyocytes cultured on GelMA-GNR hydrogels with 1 and 1.5 mg/mL of GNRs

exhibited synchronized calcium spikes within all considered spots. Such calcium transient profile further confirmed enhanced cell-cell communication between CMs cultured on electrically conductive hydrogels. Specifically, GNRs embedded in GelMA hydrogel at high concentration bridged the electrically insulated structure of the matrix and further played a role to facilitated signal propagation between the cells.

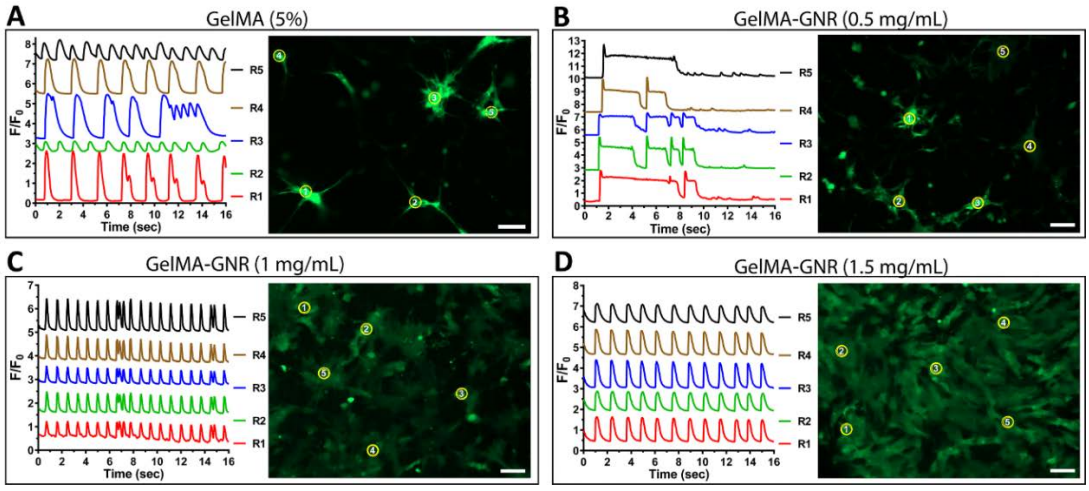

Figure 2.9. Calcium transient and extracted related frequency signals of intracellular change in concentration of Ca^{2+} within cultured CMs for A) pure GelMA (5%), B) GelMA-GNR (0.5 mg/mL), C) GelMA-GNR (1 mg/mL), and D) GelMA-GNR (1.5 mg/mL). R1 to R5 represent regions 1-5 and scale bars depict 100 µm.

2.3.7. Impact of external electrical stimulation

A custom-made electrical stimulation set up, according to the previous protocol (Tandon, 2009) (Figure 2.10A.), was utilized to evaluate the capability of the hydrogel constructs for accommodation of external electrical stimuli. Excitation threshold, which is defined as the minimum required voltage to induce synchronous contractions of CMs, was measured for three different frequencies (1, 2, and 3 Hz). Notably a lower excitation threshold (Figure 2.10B.) for 1 and 1.5 mg/mL GelMA-GNR hydrogels was observed as compared to 0 and 0.5 mg/mL GelMA-GNR hydrogel constructs at 1 and 2 Hz. In addition, at high frequency (3 Hz), only hybrid hydrogels with the highest amount of GNR concentration (1.5 mg/mL) exhibited significant difference in terms of excitation threshold. This decrease in excitation threshold can be attributed

to the relatively lower impedance of GelMA-GNR hydrogels in comparison to pure GelMA hydrogel. Despite significant decrease in excitation threshold, all pure and hybrid hydrogels were enabled to generate similar beating pattern related to the applied frequencies (Figure 2.10C. and Appendix C.8.–C.11.). Thus, it can be envisioned that GNRs incorporated within the tissue constructs could promote integration (electrically) with native myocardium as compared to pure GelMA hydrogel. Investigation of the integration of the nanoengineered constructs with the host myocardium *in vivo*, is the subject of our future studies.

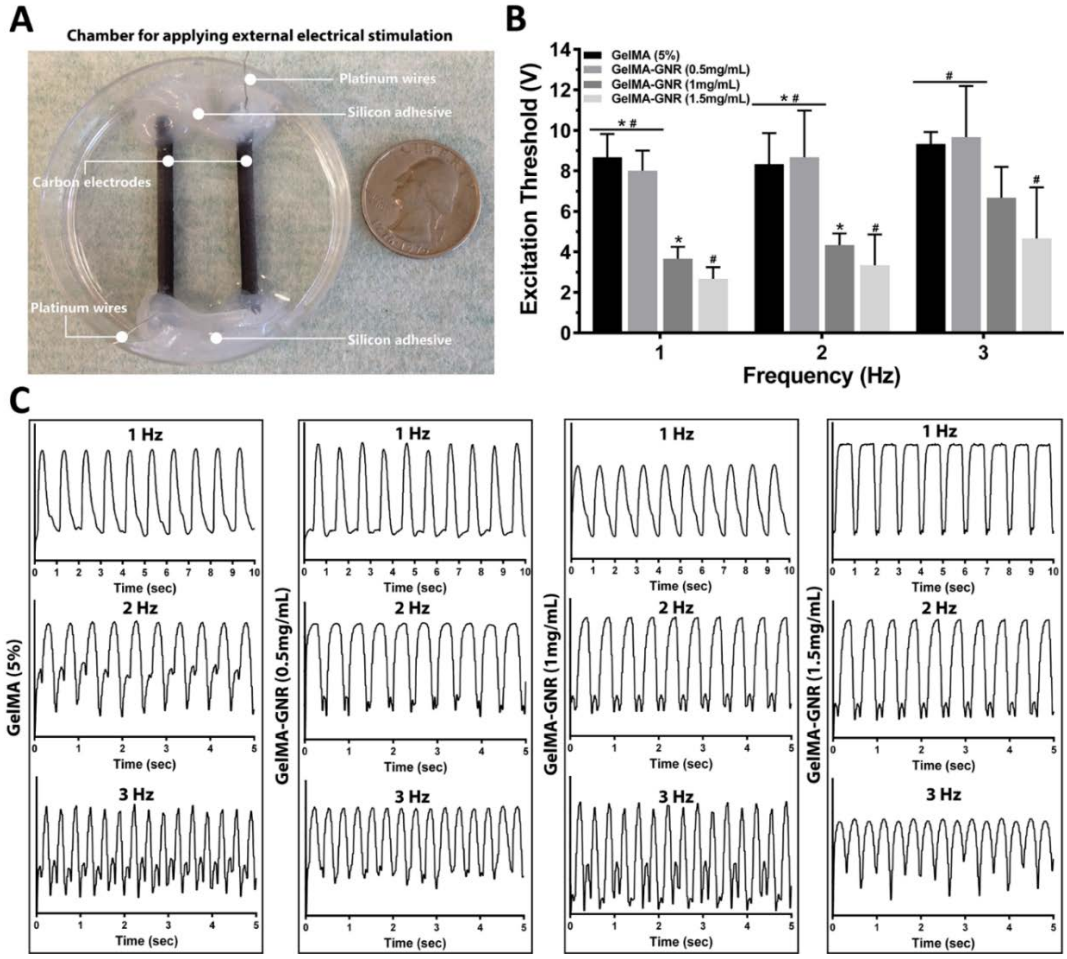

Figure 2.10. A) Fabricated chamber for external electrical stimulation photograph. B) Excitation thresholds at different frequencies (1, 2, and 3 Hz) for pure and GNR-embedded hydrogels. (*, #$p < 0.05$). C) Beating frequency signals for all types of hydrogels at different applied frequencies.

2.4. Conclusion

In this study, we developed GNR-embedded GelMA hybrid hydrogels as an advanced biomaterial to develop functional cardiac tissue constructs for myocardial regeneration and repair. GNRs with the average aspect ratio of 3.15 (16 ± 2 nm width and 53 ± 4 nm length) were synthesized and homogeneously incorporated with GelMA prepolymer solution, followed by UV crosslinking to fabricate hybrid GelMA-GNR hydrogel constructs (150 μm thick). The GelMA-GNR hybrids exhibited electrically and mechanically enhanced material characteristics as compared to pure GelMA hydrogel. Primarily, the GelMA-GNR hybrid hydrogels induced high cell retention and improved cytoskeleton organization. The highly mediated cell-matrix interactions, through integrin-β1, along with enhanced expression of cardiac specific markers (cTnI, SAC) resulted in the formation of interconnected cardiac tissue layers. Further studies confirmed that the stiffness of the matrix is not the only factor, and in fact GNRs are the major driver for higher cell adhesion and retention on the matrix. Due to the high affinity of the cells on the hybrid hydrogels, the formed tissues represented an organized, packed, and uniform architecture while maintained a high level of cellular viability and metabolic activity. Secondly, the conductive constructs facilitated cell-cell signaling and electrical signal propagation, as confirmed through the expression of Cx43 gap junctions and synchronized calcium signaling amongst CMs exposed to high concentration of GNRs (1.5 mg/mL). These enhancements eventually gave rise to higher functionalities of cardiac tissue constructs and specifically improved tissue contractility with lower excitation threshold. Notably, GelMA-GNR hybrids (1 and 1.5 mg/mL) illustrated more robust and synchronous beating behavior as compared to the pure GelMA hydrogel. In conclusion, these findings confirmed that the nanoengineered GelMA-GNR hybrid hydrogels, with excellent characteristics, provide a suitable matrix for specific applications in cardiac tissue engineering.

CHAPTER 3

ELECTRICALLY CONDUCTIVE HYDROGEL-BASED MICRO-TOPOGRAPHIES FOR THE DEVELOPMENT OF ORGANIZED CARDIAC TISSUES

3.1. Introduction

The native myocardium is a structurally orchestrated and adaptive tissue consisting of tightly packed uniaxial cytoarchitecture and electrically conductive Purkinje fibers, which provides electrical conduction through the heart (Dvir, 2011; Engelmayr Jr, 2008; Ling, 2011; Zhou, 2014). Such a unique cellular microenvironment contributes critical cues involved with initiation and development of the structure-function relationship. In particular, electrical and geometrical cues are two of the most impactful stimuli, influencing proper functionalities of the heart (D-H Kim, 2010) and efficient pumping of blood throughout the body (Pijnappels, 2010). *In vitro* investigation of these signaling cues and their subsequent effects on cytoarchitecture can lead to better understanding of the tissue function and optimization of regenerative-based therapies for treatment of heart diseases (e.g. MI).

In the past two decades, tissue engineering has emerged as a powerful strategy to develop cardiac constructs with geometrical and electrical cues that mimic the native cardiac microenvironment. Numerous hydrogel-based scaffolds along with microscale techniques (i.e. micropatterning) have been integrated (Annabi, 2013; N. Bursac, 2002; Radisic, 2004) to develop biomimetic cardiac tissue substitutes that can be used in disease modeling and regeneration studies following injury. Micropatterned constructs fabricated by GelMA (Cha, 2014; Kharaziha, 2013; Saini, 2015), MeTro (Annabi, 2013), PEG (Zhen Ma, 2015; Yeo, 2007), collagen (Camelliti, 2006; Chiu, 2012), PGS (Engelmayr Jr, 2008), and chitosan (Chiu, 2012) are among the biomaterials that have been widely used for cardiac tissue engineering due to their excellent material and biological characteristics. For instance, in a pioneering study by Engelmayr (Engelmayr Jr, 2008) PGS accordion-like honeycombs with native-like anisotropic architecture were micro-fabricated to develop organized cardiac tissue constructs. Their findings indicated enhanced formation of aligned cardiac tissue constructs with anisotropic mechanical properties

similar to native heart muscle. Photocrosslinkable hydrogels such as GelMA and MeTro have also shown promising results for cell-based studies and cardiac tissue engineering applications mainly due to their bioactivity and ease of precise fabrication (Annabi, 2013; Klotz, 2016; Nichol, 2010). The integrin-based cell adhesion moieties in GelMA hydrogel provided a desirable microenvironment for cell growth and spreading, while methacrylated polymer chains enabled formation of micro-topographies (Klotz, 2016; Nichol, 2010). For example, Saini et al. (Saini, 2015) fabricated cell-laden GelMA hydrogel constructs to develop 3D rectangular cardiac microtissues with variable geometrical features encapsulated with CMs alone and with a co-culture with cardiac fibroblasts (CFs). Their results showed the necessity and critical impacts of CFs and construct geometry on cell spreading, cytoskeleton alignment, tissue formation, and overall functionalities of the cardiac microtissues.

Despite these significant progresses, there remains critical shortcoming related to the electrical properties of the previously developed micropatterned hydrogel constructs that can be further improved for cardiac tissue engineering applications (Kharaziha, 2013; Navaei, 2016a; Paul, 2014; SR Shin, 2013; SR Shin, 2016). Specifically, the electrically insulated macroporous matrix of hydrogel can interfere with cell-cell electrical coupling and signal propagation within the tissue (Dvir, 2011; Navaei, 2016a). This phenomenon can impede full electrical integration of the tissue constructs with the native myocardium, which could potentially lead to undesired arrhythmias (Furuta, 2006; Rubart, 2003; Zhou, 2014; Zimmermann, 2006). To address this, incorporation of biocompatible nanomaterials with high electrical conductivity was demonstrated to significantly reduce the hydrogel matrix's resistivity and facilitate electrical signal propagation among the cardiac cells (Dvir, 2011; Ling, 2011; SR Shin, 2013; SR Shin, 2016; Zhou, 2014). For instance, in a recent work, Ramon-Azcon and Ahadian (Ahadian, 2014) fabricated micropatterned GelMA hydrogel constructs incorporated with aligned carbon nanotubes *via* dielectrophoresis for skeletal muscle tissue engineering. The microgrooved hydrogel constructs demonstrated robust anisotropic electrical conductivity, leading to pronounced expression of skeletal muscle specific genes and proteins. However, there are numerous concerns regarding the utilization of carbon nanotubes for biomedical applications (Annabi, 2013) specifically with respect to biological toxicity

(Firme, 2010; Simon, 2014; Zhu, 2008), low solubility (YY Huang, 2012b; Vardharajula, 2012) as well as high UV light absorption which limits development of 3D thick (i.e. millimeter scale) tissue constructs using photolithography (SR Shin, 2012). Alternatively, previous work of ours (Navaei, 2016a) and others (Baei, 2016; Dvir, 2011; Fleischer, 2014; Jung, 2012; T-J Lee, 2014; Ravichandran, 2014; Michal Shevach, 2014) have exhibited the tremendous potential of GNMs for myocardial tissue engineering. Particularly, cardiac tissue constructs incorporated with GNMs showed excellent viability and metabolic activity (Baei, 2016; Navaei, 2016a) enhanced cardiogenic differentiation (T-J Lee, 2014; Ravichandran, 2014; Sridhar, 2015) upregulated expressions of cardiac proteins and genes (Dvir, 2011; You, 2011) and facilitated cell-cell electrical coupling (Dvir, 2011; Navaei, 2016a; Michal Shevach, 2014; Michal Shevach, 2013). In addition, high biocompatibility (Connor, 2005; Shukla, 2005) wide range of nanostructures (Cobley, 2011; Hu, 2006) as well as ease of fabrication and biofunctionalization (X Huang, 2009; Lloret, 2013) are among the other reported characteristics of GNMs.

We previously developed gold nanorod-incorporated GelMA hybrid hydrogels (GelMA-GNR) to assess the applicability of the conductive material in prompting cardiac cell functions (Navaei, 2016a). Specifically, 5% (wt/v) GelMA hydrogels with different concentrations of GNRs (0, 0.5, 1, and 1.5 mg mL^{-1}) were formed using photolithography technique. NRVCMs were seeded on the GelMA-GNR hydrogel constructs and subsequently cardiac cell phenotype (i.e. sarcomere organization, Cx43) as well as tissue-level functionalities were assessed. Specifically, our results confirmed the formation of highly contractile tissues on the synthesized conductive hydrogels with 1 and 1.5 mg mL^{-1} GNRs, demonstrating synchronous cell-cell coupling and Ca^{2+} transients compared to pure GelMA hydrogel. However, the developed GelMA-GNR constructs did not exhibit biomimetic geometrical (i.e. topographical) cues to induce native-like anisotropic cellular organization. Therefore, in this chapter, we utilized an integrated micro- and nano-scale strategy by simultaneous incorporation of biomimetic geometrical (i.e. anisotropic microgrooved architecture) and electrical cues (i.e. GNRs) to develop highly oriented and contractile cardiac tissue constructs. We additionally optimized the concentration of GelMA hydrogel to 10% (wt/v) incorporated with GNRs (1 mg mL^{-1}) to maintain robust pattern fidelity. We performed material

characterization to assess the electrical and mechanical properties of the new matrix. NRVCMs were seeded on pristine GelMA and GelMA hydrogel incorporated with GNRs for 7 days, and cellular organization, cardiac specific markers expression as well as tissue contractility were further assessed. The findings confirmed the formation of dense and highly organized cellular networks within GelMA-GNR microgrooved constructs. The electrically conductive and highly organized cardiac tissues exhibited continuous and synchronized contractions induced by external electrical stimuli, mimicking physiologic synchronous cardiac cell beatings. The proposed strategy demonstrates a unique approach, which can be used to develop biomimetic cardiac patches that could better integrate with native myocardium (Zhou, 2014; Zimmermann, 2006).

3.2. Experimental Methods

3.2.1. Materials

Gelatin (type A), TMSPMA, the photoinitiator, $HAuCl_4$, $NaBH_4$, $AgNO_3$, CTAB, and L-ascorbic acid were purchased from Sigma Aldrich and utilized with no further purifications. DIW (18 MΩ) was used for the all syntheses.

3.2.2. Fabrication of PDMS micromolds

The micromolds were fabricated using standardized photo- and soft-lithography methods (Betancourt, 2006; Qin, 2010; Truong, 2016). First, the groove design (50 μm width and spacing) was created using a CAD (computer aided design) software. Next, a transparent mask was created and utilized in the SU-8 photolithography. SU8-2075 (Micro Chem) was spun onto a silicon wafer until it reached a final height of 50 to 70 μm. The wafer was placed underneath the transparent mask with the microgrooved patterns and exposed to UV light. Subsequently, the wafer was transferred to a conventional oven for final crosslinking at 50 °C for 24 h. Finally, the wafers, containing of microgrooves, were developed at room temperature using SU-8 developer (Micro Chem) and hard baked at 150 °C for 30 min. Wafers were salinized using trichloro(methyl)silane (TCMS, Sigma Aldrich) for 20 min in a vacuum chamber. Next, polydimethylsiloxane (PDMS, Sylgard 184 Silicon Elastomer kit, Dow Corning) was casted over

the SU-8 wafer and baked for 1 h at 80 °C. Afterwards, the PDMS micromolds (Figure 3.1A.) was peeled off and individual micromolds were cut and sterilized using 70% ethanol and UV.

3.2.3. Fabrication of cell-seeded GelMA and GelMA-GNR microgrooved hydrogels

GNRs and GelMA prepolymer were synthesized based on previously reported protocols (Navaei, 2016a; Saini, 2015). TEM (Philips CM200-FEG, USA) operating at 200 kV accelerating voltage was used to view and confirm the formation of synthesized GNRs (Figure 3.1B.). Mean length, width, and aspect ratio of GNRs were calculated based on the TEM images (n = 10) using NIH ImageJ software. GelMA-GNR microgrooved hydrogels were fabricated using the soft lithography technique (Figure 3.1C.). A clear prepolymer solution of GelMA (10% wt/v) in photoinitiator (0.5% wt/v in DPBS) was prepared, and subsequently mixed with purified GNRs (1 mg mL^{-1} of GelMA prepolymer solution). GelMA-GNR solution was sonicated in water bath for 1 h to obtain a homogenous mixture. In the next step, PDMS micromolds (50 µm width, spacing, and depth) were treated by oxygen plasma (Harrick Plasma, USA) for 30 s to render the surface of the micromold more hydrophilic resulting in uniform penetration of hydrogel prepolymer solution within the microgrooves. The mold was placed on a droplet (15 µL) of GelMA-GNR hydrogel and the whole assembly was exposed to UV light (800 mW, 360-480 nm) for 25 seconds. To avoid any disruption in the structure, microgrooved hydrogels were soaked in the sterile DPBS for 10-15 min and then the PDMS mold was peeled off. GelMA microgrooved hydrogels (the control group) were fabricated also using the same procedure with 10 s UV light exposure. All microgrooved hydrogels were washed in an antibiotic solution (1% v/v penicillin/streptomycin in DPBS) twice with 10 min intervals, followed by a washing using cardiac culture media (containing DMEM, L-glutamine (1%), FBS (10%), and penicillin-streptomycin (100 units per mL)) in the same fashion. Afterwards, isolated 2-day old NRVCMs were seeded (1×10^6 cells/constructs) on GelMA-GNR microgrooved hydrogels (1 × 1 cm2 construct size) for 24 h, which were placed in 24 multiwell plates and incubated at 37 °C with 5% CO2. Unattached cells were washed off on the next day and 500 µL of fresh cardiac culture media were added to the samples. The media were exchanged every other day.

3.2.4. Electrical, rheology, and morphological characterizations of GelMA and GelMA-GNR hydrogels

To evaluate the electrical conductivity of the GelMA and GelMA-GNR hydrogels, the constructs were placed between two conductive glass slides (ITO coated, 30-60 Ω sq^{-1}, Sigma Aldrich) and AC bias (Agilent 4284A LCR meter) was swept from 10 Hz to 1 MHz. Real portions of the impedance complex values were averaged (n = 4) and plotted versus the frequency. A rheometer (parallel plate rheometer, Anton Paar MCR-101) was utilized to measure the storage moduli (elasticity) of crosslinked GelMA and GelMA-GNR hydrogels. In this regard, hydrogels were placed between the parallel plates of the rheometer and storage moduli were measured as a function of strain sweep (0-100%). The values at 5% strain (n = 3) were considered the ultimate storage moduli of the hydrogels. Macroporous structure of GelMA and GelMA-GNR hydrogels were investigated using SEM. Hydrogels were fabricated and mounted onto the SEM sample holders, and sputter coated by Au/Pd. Matrix porosity of both hydrogels were calculated based on SEM images (n = 6) using ImageJ software.

3.2.5. Viability, cellular alignment, and cardiac cells phenotype

Viability of cultured cardiac cells on GelMA and GelMA-GNR hydrogels were investigated using a standard Live/Dead assay kit (Thermo Fisher, USA). The samples were treated by the assay on day 1 and 7 of culture and fluorescent images were taken using an inverted microscope (Zeiss Observer Z1, USA). Cytoskeleton organization of microgrooved cardiac tissues was assessed based on F-actin fibers staining images. The hydrogel constructs were stained on day 1 and 7 of culture using Alexa Fluor® 488 Phalloidin (Thermos Fisher, USA) according to previously published protocols (Navaei, 2016b). Sequentially, samples were fixed in PF (4% v/v) for 30 min, permeabilized in Triton X-100 (0.1% v/v) for 45 min and blocked in BSA (1% v/v) for 1 h. Next, a mixture of Alexa Fluor® 488 Phalloidin (1 to 40 dilution) and DAPI (1 to 1000 dilution) in BSA was added to the samples for 1 h, and Z-stacked images were captured by a fluorescent microscope equipped with Apotome.2 (Zeiss, USA). The averaged area coverage and index of F-actin fibers were calculated (n > 15). The area coverage index specifically was defined as the

area covered by cardiac cells delineated by the F-actin fibers inside the microgrooves. In addition, fiber alignment index (n > 10) was defined as the ratio of long axis to short axis of FFT (built-in tool in ImageJ software) analysis images (Nichol, 2010; Saini, 2015). To evaluate the maturation of the created cardiac tissues on the hydrogel microgrooves, cardiac-specific markers, SAC and Cx43 gap junctions were immunostained using primary antibodies (Abcam, USA) (Navaei, 2016a). In brief, samples were fixed in PF (4% v/v) for 30 min, permeabilized in Triton X-100 (0.1% v/v) for 45 min and blocked in goat serum (10% v/v) for 1 h. Afterwards, primary antibodies (1 to 100 dilution in 10% goat serum) were loaded on the samples for 24 h at 4 °C, followed by staining using secondary antibodies (1 to 200 dilution in goat serum) (Thermo Fisher, USA) for 6 h. Finally, DAPI was added to stain the cells' nuclei. The area coverage of stained cardiac markers was averaged (n > 5) on day 7 of culture.

3.2.6. Spontaneous and stimulated beating behavior of microgrooved cardiac tissues

The spontaneous contractile behavior of GelMA and GelMA-GNR microgrooved cardiac constructs was monitored using an inverted microscope (Zeiss, USA) over 7 days, and presented as averaged BPM (n > 11). Also, a custom-made stimulation chamber was fabricated (Tandon, 2009) and utilized to induce electrical stimuli on the cardiac tissues on day 7. The cardiac microgrooved tissues were stimulated at 0.5, 1, 2 Hz and excitation thresholds (the minimum required voltage to induce synchronous cells' contraction) were recorded. To extract the beating signal from the videos, a custom-written Matlab (MathWorks, USA) code was used (SB Kim, 2011; Navaei, 2016a).

3.2.7. Statistical analysis

All results were statistically analyzed with a Student's t-test (two-tailed) method using GraphPad Prism software. A p-value less than 0.05 (two-sided) was considered statistically significant difference within the samples.

3.3. Results and Discussion

3.3.1. Development and characterization of the electrically conductive hydrogel microgrooves

Fabricated PDMS micromolds (Figure 3.1A.) with microgrooved topographies were casted and used for creating GelMA and GelMA-GNR hydrogel constructs. Similar to our previously published work (Navaei, 2016a) the synthesized GNRs (Figure 3.1B.) exhibited nanorod-like structure with average length and width of ~53 and ~16 nm respectively (aspect ratio of ~3.15). Purified GNRs were mixed and sonicated with GelMA prepolymer solution (10% wt/v). A drop of GelMA-GNR mixture was then located on TMSPMA-coated glass slides, and PDMS mold was placed on top. Finally, the microgrooved hydrogel constructs were fabricated through UV photo-crosslinking and submerged in sterile DPBS prior to biological studies (Figure 3.1C.). The microarchitecture of fabricated GelMA-GNR microgrooved hydrogels is demonstrated in Figure 3.1D. As can be seen, the microgrooves with 60 μm depth (Figure 3.1D., middle image) and 50 μm width were formed on the surface of hydrogel slab with 65 μm thickness. This result showed successful formation of surface microgrooves on GelMA-GNR hydrogel constructs.

In our recent work (Navaei, 2016a) we performed extensive studies on the synthesis and characterization of GelMA (5% wt/v) hydrogel embedded with variable concentrations of GNRs (0-1.5 mg mL^{-1}) for the development of cardiac tissue constructs. However, the aim was to assess the role of matrix properties on behavior and function of cardiac cells. Our previously developed GelMA-GNR hydrogels did not exhibit biomimetic oriented topographical features to induce cardiac cells uniaxial alignment. In these studies, we optimized hydrogel concentration using 10% wt/v GelMA incorporated with 1 mg mL^{-1} GNRs for fabrication of microgrooved features due to its superior material and biological properties to conduct biological studies (Navaei, 2016a). In other words, the control condition in this chapter was the microgrooved GelMA hydrogel constructs without the presence of GNRs (GelMA vs. GelMA-GNR).

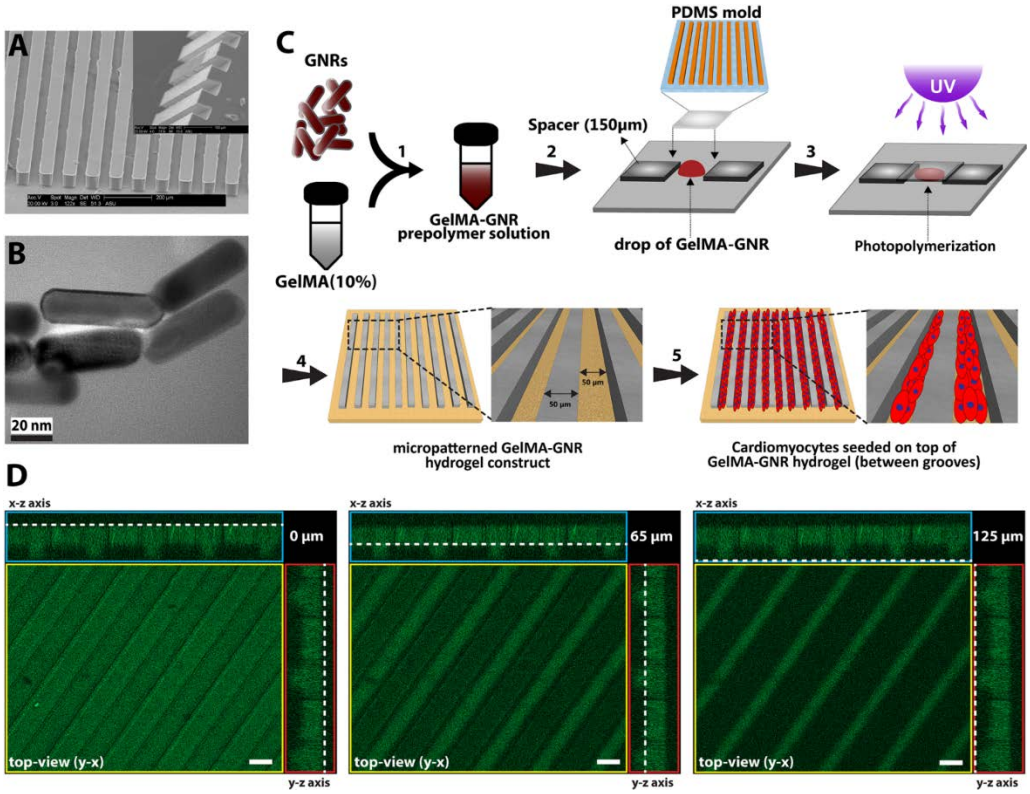

Figure 3.1. A) SEM images of casted PDMS micromolds. Inset image demonstrates higher magnification. B) TEM micrograph of synthesized GNRS. C) A schematic illustrating the fabrication procedure of GelMA-GNR microgrooved tissues. D) Z-Stack images of fluorescently fabricated GelMA-GNR hydrogel showing the 3D structure of the microgrooved patterns. Dash white lines at x-z and y-z axes indicate the relative z position of the top-view (y-x) image. Numbers at the top-right box represent the distance of dotted white line from the bottom of the construct (0 μm is the bottom, 65 μm is the height of the hydrogel slab, and 125 μm shows the whole thickness of the construct). Scale bars are 50 μm.

SEM micrographs (Figure 3.2A.) displayed the porous structure of GelMA and GelMA-GNR hydrogel matrices after 24 h hydration. As evident, both hydrogels showed similar porous architectures with no obvious aggregations of GNRs within the hydrogels' matrices. In addition, the architecture of GelMA and GelMA-GNR matrix were compared based on the measured porosity percentage (Figure 3.2B.) using SEM images. Both hydrogels demonstrated similar porosity with no statistically significant differences (GelMA 69 ± 6% and GelMA-GNR 67 ± 6%).

The results showed that incorporation of GNRs within GelMA hydrogel did not disturb the macroporous architecture of the GelMA hydrogel matrix, consistent with our previously published work (Navaei, 2016a). Matrix porosity plays a critical role in cellular viability, spreading, and function especially in the case of cell encapsulation (cell-laden constructs) within hydrogel-based tissue constructs (Annabi, 2010; Loh, 2013).

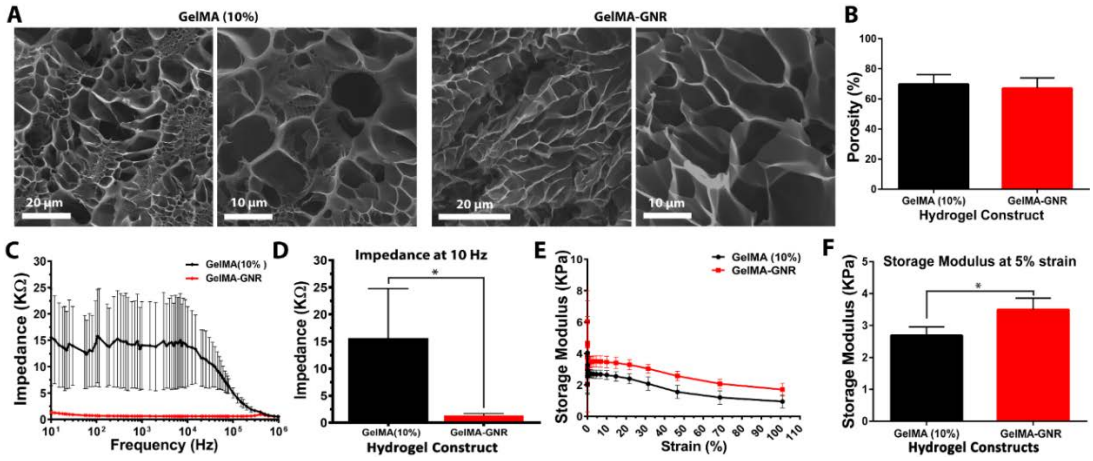

Figure 3.2. A) SEM micrographs of GelMA and GelMA-GNR hydrogels matrices at different magnifications. B) Porosity percentage of both hydrogels calculated based on the SEM images. C) The electrical impedance measurements of GelMA and GelMA-GNR at different swept frequencies. D) Comparison of matrix impedance at 10 Hz frequency. (E) Rheology analysis of GelMA and GelMA-GNR hydrogels showing the storage modulus variations as a function of the strain, and (F) ultimate storage moduli at 5% strain (*p-value < 0.05).

Electrical conductivity of GelMA and GelMA-GNR hydrogels measured as the impedance of hydrogel matrix are shown in Figure 3.2C. The results showed lower electrical impedance of GelMA-GNR hydrogel compared to pure GelMA within the frequency variations. Specifically, GNR-embedded hydrogels exhibited significantly less impedance (1.35 ± 0.36 kΩ) at the lowest tested frequency (10 Hz), which is relatively closer to the physiological range (You, 2011) compared to pure GelMA hydrogel (15.58 ± 9.18 kΩ) (Figure 3.2D.). Such characteristic can be correlated to the presence of GNRs within the GelMA matrix due to bridging of the electrically insulated hydrogel's pores. It has been shown that the electrically conductive hydrogel matrices

provide an excellent microenvironment for the growth and functioning of cardiac cells (Martinelli, 2012; You, 2011).

Mechanical properties of the hydrogels in terms of rheology (storage moduli) are shown in Figure 3.2E. The storage moduli of GelMA and GelMA-GNRs hydrogels decreased as a function of strain. At 5% strain, both hydrogels exhibited their ultimate storage moduli, where it was statistically higher for GelMA-GNR hydrogel as shown in Figure 3.2F. Improved mechanical characteristics have been consistently reported elsewhere for similar nanomaterial-incorporated hydrogels (Navaei, 2016a; SR Shin, 2013; Xavier, 2015). Specifically, electrostatic interactions between GNRs (positively charged) (Nikoobakht, 2003) and GelMA chemical structure (negatively charged carboxyl groups) (Nichol, 2010) along with the filler effect (Tjong, 2006) of incorporated GNRs are speculated to lead to higher mechanical stiffness (storage modulus) of GelMA-GNR hydrogel. However, such mechanical enhancements did not result in a several folds increase in GelMA-GNR (10% wt/v) hydrogel storage modulus. It is speculated that as hydrogel prepolymer solution (GelMA) concentration increases (e.g. 10%), the influences in the mechanical properties caused by embedding of nanomaterials (GNRs) may be compromised. For example, it was shown in chapter 2 that the incorporation of 1 or 1.5 mg mL^{-1} GNRs within GelMA hydrogels with 5% wt/v prepolymer concentration significantly increased the mechanical stiffness (Young's modulus) of the material (~2 folds) (Navaei, 2016a), measured by AFM. However, it is important to note that although increasing GelMA prepolymer concentration enhances the mechanical properties of the hydrogel, it can have adverse influence by decreasing the electrical conductivity of the hydrogel (Tarus, 2016; Veleirinho, 2008). Nevertheless, nanoengineered hydrogels with enhanced mechanical properties have exhibited superior cell adhesion, spreading and tissue formation (Grover, 2012; H-B Wang, 2000a; Zhou, 2014).

3.3.2. Cellular viability and formation of organized cardiac tissues

Figure 3.3A. illustrates phase contrast images of CMs on the GelMA and GelMA-GNR hydrogel microgrooves on day 1 and day 7 of culture. Seeded CMs formed discrete aggregated clusters inside the microgrooves on both substrates (GelMA vs. GelMA-GNR), on day 1.

However, the cell adhesion pattern inside GelMA-GNR microgrooves was more homogenous. Over 7 days of culture, CMs were spread and formed cellular networks within the microgrooves (Figure 3.3B.). Specifically, GelMA-GNR microgrooved cardiac tissues exhibited mostly concrete uniaxial cellular networks.

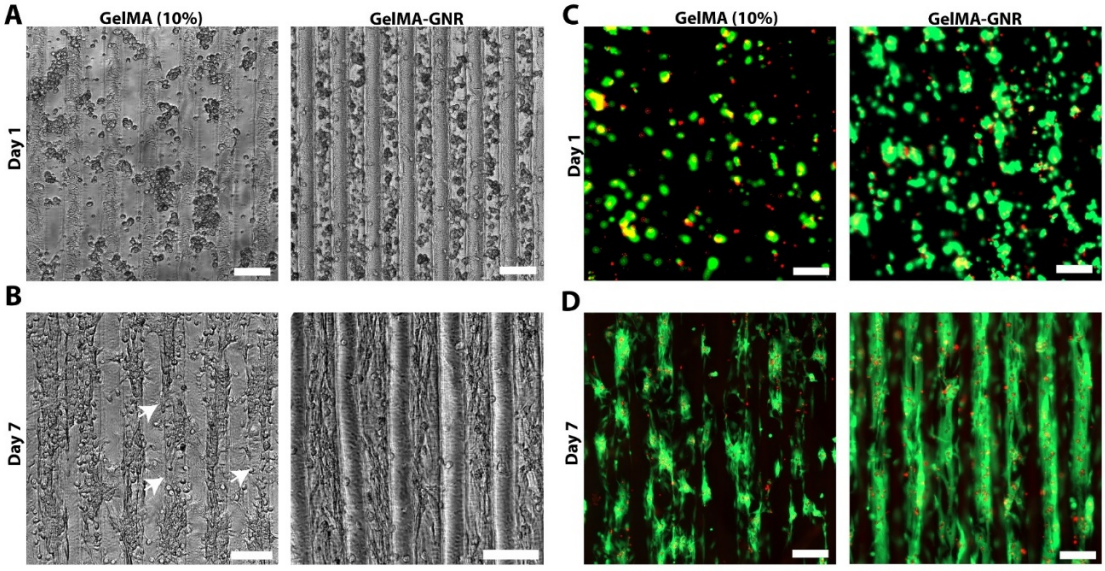

Figure 3.3. Phase-contrast images of cardiac cells seeded on GelMA and GelMA-GNR microgrooved hydrogel on A) day 1 B) and day 7 of culture. White arrows represent the disconnect between cellular clusters. Fluorescent viability images of GelMA and GelMA-GNR microgrooved cardiac tissues on C) day 1 and D) day 7. Live cells are stained in green and dead cells are stained in red. All scale bars represent 100 μm.

In contrast, cell clusters exhibited discrete spreading within microgrooves on GelMA constructs. In some locations complete disconnections (Figure 3.3B., white arrows) between the cellular clusters were evident. Cell retention comparing GelMA and GelMA-GNR on day 1 was not significantly different (data not shown). However, CMs spreading, and formation of organized tissues were profoundly improved on GelMA-GNR as compared to GelMA constructs (Figure 3.3B., day 7). The dissimilarity in the cell adhesion and spreading patterns can be associated with the difference in elasticity (storage modulus) and surface characteristics between GelMA and GelMA-GNR hydrogels. As it has been demonstrated, the hydrogels with higher stiffness

improved cell adhesion and spreading compared to the softer hydrogels, specifically in the case of 2D cell seeding on the constructs (Navaei, 2016a; SR Shin, 2013). Consistently, in our previous work, we confirmed the localization of GNRs within the micro-pores of the hydrogel constructs, which may subsequently lead to the formation of nano-scale local topographies, providing more anchoring points for cell adhesion and spreading. Higher surface roughness and nano-scale topographies were also observed in previous studies on the incorporation of CNTs within PNIPAAm hydrogels (H Sun, 2017). Regardless of hydrogel type (GelMA and GelMA-GNR), fluorescent Live/Dead images showed only few dead cells (red) on day 1 (Figure 3.3C.) and day 7 (Figure 3.3D.) of culture. In other words, purified GNRs (twice washed) (Connor, 2005) incorporated within GelMA-GNR hydrogel did not induce major cytotoxicity over 7 days. Due to formation of dense cell clusters (day 1) and 3D topographical features of microgrooves (day 7), we were not able to quantify the percentage of viability.

3.3.3. Cytoskeleton organization and cardiac cells phenotype

Cytoskeleton architecture of organized cardiac tissues on microgrooved GelMA and GelMA-GNR hydrogels were investigated through staining of F-actin fibers on day 1 (upon seeding) and day 7 of culture. As shown in Figure 3.4A., CMs were confined mostly within the microgrooves, and acquired round morphology on day 1 of culture within both hydrogel constructs. Quantified F-actin area coverage and index (Figure 3.4B. and 3.4C., day 1) also confirmed the same scenario as illustrated by immunostained images of round cells. After 7 days of culture, cardiac cells created compact and extended tissues (Figure 3.4A., day 7) with significantly higher area coverage (Figure 3.4B., day 7) on GelMA-GNR hydrogels as compared to disconnected cellular clusters on pure GelMA. Area coverage index (Figure 3.4C.) also confirmed considerable formation of organized tissues inside the GelMA-GNR microgrooves. Therefore, the major differences between GelMA and GelMA-GNR constructs were in terms of cellular connectivity, area coverage as well as formation of highly organized and compact tissues. Cytoskeleton alignment was further assessed using FFT analysis (inset images in Figure 3.4A.) on day 1 and 7.

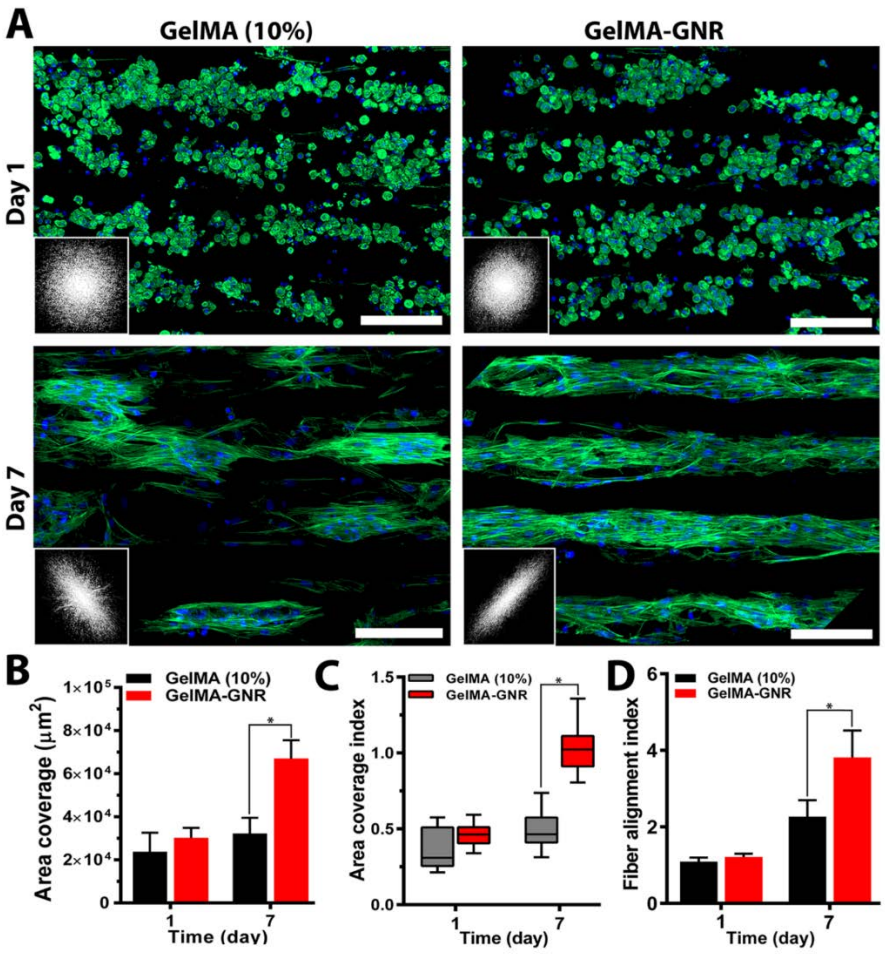

Figure 3.4. A) Staining images of F-actin fibers of cardiac tissues on day 1 and 7 of culture. Insets demonstrate FFT analyses. All scale bars represent 100 μm. B) Area coverage and C) area coverage index of F-actin fibers within GelMA and GelMA-GNR microgrooved tissues on day 1 and 7. D) F-Actin fiber alignment index on day 1 and 7 of culture (*p-value < 0.05).

The outcomes indicated notably higher F-actin fiber alignment for cardiac tissues formed on GelMA-GNR microgrooves in comparison to GelMA constructs on day 7 (Figure 3.4D.). Despite the fact that GelMA-GNR hydrogels (~3.5 kPa) provided stiffer matrices compared to GelMA (~2.5 kPa), on day 1, cell adhesion coverage data (Figure 3.4A. and 3.4B.) did not show a meaningful difference between both constructs. We speculate that GelMA hydrogel with 10% (wt/v) prepolymer concentration provided a microenvironment with sufficient stiffness for early cell adhesion but was not able to maintain cell spreading over time in comparison with GelMA-GNR

hydrogel. Such behavior may be attributed to the excess cell anchoring points provided by embedded GNRs on the hydrogel matrix, as also demonstrated in our previous work (Navaei, 2016a) improving cellular spreading and tissue formation. Overall, the data in Figure 3.4. were in agreement with our phase contrast images, confirming substantial formation of uniaxially aligned cardiac tissues directed within the microgrooves on GNR-incorporated GelMA hydrogels.

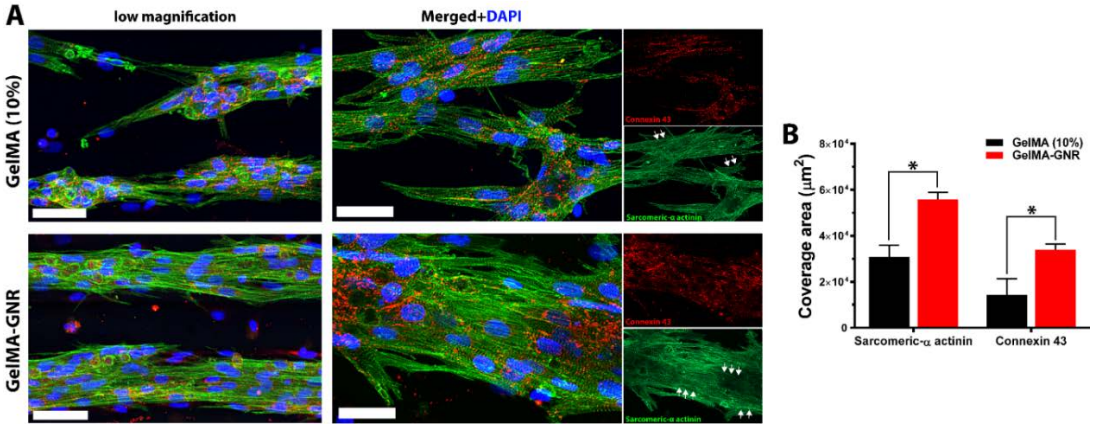

Figure 3.5. A) Immunostained images of SAC (green) and Cx43 gap junctions (red) within GelMA and GelMA-GNR microgrooved cardiac tissues on day 7 of culture. White arrows demonstrate uniaxially aligned sarcomeric structures. Scale bars represent 50 μm for low magnification images and 20 μm for merged images. B) Quantified area coverage of cardiac specific markers on day 7 (*p-value < 0.05).

The phenotype of cardiac cells on GelMA and GelMA-GNR microgrooved constructs was assessed using SAC and Cx43 gap junctions on day 7 of culture. As represented by immunostained images in Figure 3.5A. (separated channels), aligned SAC structures (white arrows) and well distributed Cx43 gap junctions are evident on both GelMA and GelMA-GNR hydrogels. However, similar to the cytoskeleton organization data (Figure 3.4A.) cellular disconnectivity and lack of tissue compactness were present on pure GelMA microgrooved constructs as compared to concrete and highly organized tissues on GelMA-GNR hydrogels. Fluorescent area coverage of SAC and Cx43 (Figure 3.5B.) further demonstrated significant differences in the formation of intact cardiac tissues comparing GelMA-GNR to GelMA (control) microgrooved constructs. These findings emphasize the critical role of hydrogel properties (e.g.

stiffness) and the nano-scale cues provided by GNRs for the development of dense cardiac patches with native like organization and architecture. In addition, the electrically conductive matrix provided by GelMA-GNR hydrogel was involved in promoting cell-cell coupling (Dvir, 2011; Fleischer, 2014; Navaei, 2016a; You, 2011).

3.3.4. Spontaneous and stimulated contractile behavior of cardiac tissue microgrooves

The functionality of aligned cardiac tissues in static culture condition and under external electrical stimulation on day 7 was further investigated using real time cellular contraction analysis (Figure 3.6.). As can be seen, cardiac tissues formed on GelMA and GelMA-GNR microgrooved constructs started beating at day 4 and continued until day 7 (Appendix C.12. and C.13.). The results (Figure 3.6A.) exhibited no statistically significant differences in terms of spontaneous synchronous BPM between GelMA and GelMA-GNR tissues. However, our previously published work (Navaei, 2016a) on 1.5 mg mL−1 GNRs-incorporated 5% (wt/v) GelMA hydrogel, without surface topographies (i.e. microgrooves), demonstrated significantly enhanced contractility (higher BPM) as compared to pure GelMA hydrogel. Despite the statistically higher mechanical stiffness of GelMA-GNR hydrogel (~3.5 kPa) as compared to GelMA (~2.5 kPa), we speculate that 10% (wt/v) GelMA with high degree of methacrylation provided sufficient mechanical cues to initiate and maintain spontaneous contractility. Therefore, it is conjectured that incorporation of GNRs within GelMA hydrogel (10% wt/v) and enhanced “electrical conductivity” (Figure 3.2A. and 3.2B.) of the matrix would provide added benefits in terms of induced (controlled) electrical stimulation and contractility. Therefore, cardiac tissues were stimulated externally at 0.5, 1, and 2 Hz frequencies using an external pulse generator and custom-made bioreactor setup (Navaei, 2016a; Navaei, 2016b). As the data shows (Figure 3.6B.), interestingly, it was not possible to induce stimulated contractions on tissues formed on pure GelMA constructs by electrical pulses up to 10 V amplitude. Conversely, highly organized tissues formed on GelMA-GNR hydrogel were successfully stimulated at all tested frequencies with relatively low excitation voltage thresholds (Figure 3.6B.). In addition, extracted beating

signals (Fig3. 6C. and Appendix C.14.) demonstrated that CMs were constantly contracted (no major peak-to-peak variation of amplitudes, dash black lines) with the same frequency provided by external stimulator.

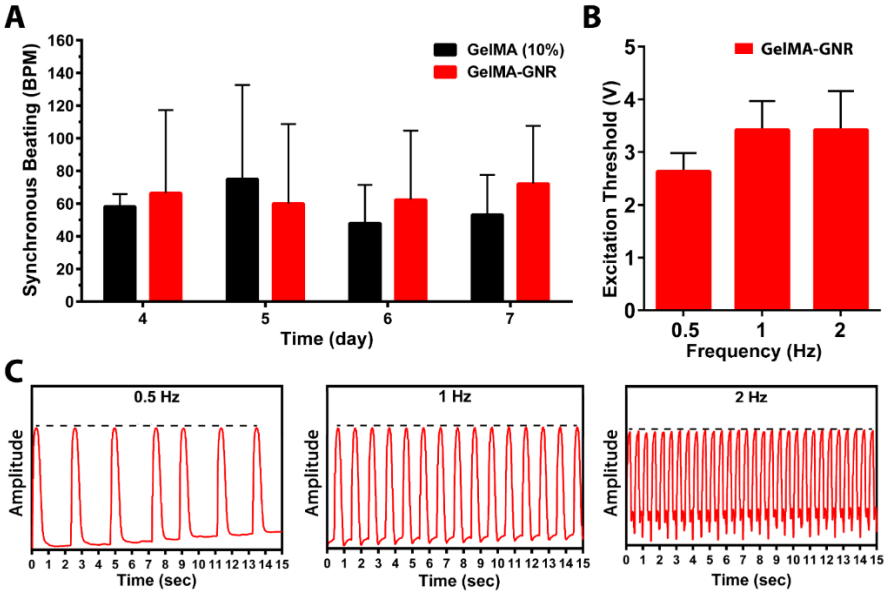

Figure 3.6. A) Synchronous spontaneous beating behavior (beats per minute; BPM) of cardiac tissues on GelMA and GelMA-GNR constructs. B) Voltage excitation thresholds and (C) extracted beating signals of GelMA-GNR cardiac tissue at different frequencies. Dash lines indicate similar peak amplitudes with no variations (*p-value < 0.05).

Therefore, addition of GNRs within the microgrooved GelMA hydrogel constructs not only induced higher cellular alignment, better connectivity and sarcomere organization but also provided a conductive matrix where the formed tissues could precisely follow external pulsed electrical stimulation regime. Therefore, it is envisioned that highly organized cardiac tissue formed on electrically conductive matrix would better integrate with the native myocardium following implantation (Zhou, 2014). This is a critically important component of a viable cardiac patch for implantation as electrical signals in native cardiac tissue are often initiated and propagated by specialized cardiac cells (e.g. sinoatrial node and His-Purkinje cells) and then rapidly propagated throughout contractile cardiomyocyte tissue to effect synchronous contraction for optimum cardiac output. A highly organized tissue construct formed on microgrooved GelMA-

GNR hydrogel that can be stimulated with low excitation threshold voltage would advance the ability to fully integrate with the synchronous contraction of native myocardium. Investigation of the functionalities of the proposed microengineered tissues *in vivo*, is the subject of our future work.

3.4. Conclusion

In this study we developed and tested novel GNR-incorporated GelMA hydrogel microgrooved constructs (GelMA-GNR) for development of uniaxially aligned cardiac tissues. As a continuation of our previous work (Navaei, 2016a) we incorporated anisotropic topographical cues on electrically conductive GelMA-GNR hybrid hydrogels to provide simultaneous topographical and electrical signals to support cardiac cells functionalities in a biomimetic fashion. Our results showed improved mechanical elasticity (storage modulus) and electrical conductivity of GelMA-GNR hydrogels (lower impedance) compared to pure GelMA constructs. Phase-contrast images exhibited more uniform cell seeding fashion (day 1) on GelMA-GNR microgrooves compared to pure GelMA. Despite the resemblance in the cell coverage on day 1 for both constructs (with and without GNRs), cardiac tissues formed on GelMA-GNR hydrogels demonstrated highly dense and uniaxially aligned architectures, mainly inside the microgrooves. A similar scenario was observed for cardiac-markers demonstrating aligned cytoarchitecture. Specifically, cardiac cells on GelMA-GNR microgrooves revealed compact sarcomeric structures, while discrete pattern with considerably lower area coverage were detected on GelMA constructs without the presence of GNRs. Although both GelMA and GelMA-GNR microgrooved tissues demonstrated spontaneous contractility from day 4 to 7 of culture, only cardiac tissues formed on the electrically conductive GelMA-GNR microgrooves were able to be externally stimulated at different frequencies (0.5, 1, and 1 Hz) at low voltages. Overall, the data presented here demonstrate that the utility of integration of micro- and nano-scale strategy to developed highly organized and native-like cardiac tissues with superior functionalities for potential applications in regenerative medicine, disease modeling and drug screening. Finally, the use of hiPSCs in regenerative medicine has dramatically increased in the past few years, due to their unique

potential to model human myocardial pathophysiology and understand the mechanism of disease progression. In this regard, our future work will be focused on the use of hiPSC-derived CMs to develop functional human cardiac patches for treatment of myocardial infarction.

CHAPTER 4

INFLUENCE OF ELECTRICALLY CONDUCTIVE AND NON-CONDUCTIVE NANOMATERIALS ON MATURATION AND EXCITABILITY OF ENGINEERED CARDIAC TISSUES

4.1. Introduction

Over the past decade, electrically conductive nanocomposite scaffolds have been at the center of attention for developing engineered cardiac tissues with enhanced contractility and biological function for regeneration of injured myocardium upon MI (Zhi Cui, 2016; Kharaziha, 2016; Monteiro, 2017). As we discussed in chapter 2 and 3, conductive tissue constructs exhibited significantly improved cell adhesion and cardiac maturation along with the enhanced electrical excitability and signal propagation (Dvir, 2011; Navaei, 2017; Navaei, 2016a; Pok, 2014; SR Shin, 2013). Conductive nanocomposite scaffolds are typically fabricated by incorporating electrically conductive nanomaterials within the matrix of scaffolding biomaterials (e.g. hydrogels). In previous studies, it has been argued that the embedded conductive nanomaterials facilitate the propagation of electrical signals within the macroporous matrix of scaffold by bridging the isolating pore walls (Dvir, 2011; Pok, 2014; SR Shin, 2013). To that end, GNMs and carbon-based nanostructures are among the mostly utilized nanomaterials for fabricating electrically conductive cardiac tissues (Martinelli, 2013a; Shapira, 2016). In an original study by Dvir (Dvir, 2011), electrically conductive cardiac tissues were formed by seeding CMs on GNW-embedded alginate hydrogels. The conductive alginate-GNW hydrogels enhanced the maturation of cardiac cells thorough upregulation of contractile proteins such as SAC and cTnI as well as Cx43 gap junctions. In addition, the external electrical stimuli were propagated globally only within the conductive alginate-GNW hydrogels, while pure alginate did not facilitate similar signal transmittance. In another pioneering study by Shin (SR Shin, 2013), gelatin-CNT nanocomposite hydrogels were synthesized for engineering conductive cardiac tissues. Engineering of conductive gelatin-CNT tissues led to mature cardiac phenotype (i.e. striated sarcomeres) and enhanced protein expression as compared to pure gelatin hydrogel. Furthermore, the electrical excitability (i.e. voltage threshold) and synchronized spontaneous contractility of CMs were

significantly promoted within the conductive gelatin-CNT hydrogels. Similar outcomes including improved cardiac maturation and electrical excitability have been reported for other conductive cardiac tissue constructs (Kharaziha, 2014; Navaei, 2017; Pok, 2014; Michal Shevach, 2014; SR Shin, 2016).

Although the primary motive for developing conductive cardiac tissues has been on enhancing the electrical signal propagation within the insulating matrix of scaffold (i.e. synchronicity) (Dvir, 2011; SR Shin, 2013), however, inclusion of conductive nanomaterials also results in enhanced mechanical and surface topographical features within the scaffold's matrix. Specifically, the incorporated nanomaterials increase matrix rigidity and stiffness by acting as reinforcing nanofillers (Q Li, 2016b; Tjong, 2006) and lead to the formation of nano-scale surface topographies (Gaharwar, 2014; H Sun, 2015). Each of these matrix characteristics, regardless of electrical conductivity, has been shown to significantly promote maturation as well as contractility of primary and stem cell-derived CMs (Bhana, 2010; Boothe, 2016; Carson, 2016; Deok-Ho, 2005; Jacot, 2008; AJS Ribeiro, 2015a). For example, in a study by Bhana (Bhana, 2010), CMs phenotypic maturation (e.g. cTnI expression) and contractile force generation were significantly enhanced by increasing the matrix stiffness. Therefore, it is speculated that the mechanical properties and surface topography play more prominent roles in maturation and synchronicity of engineered cardiac tissues compared to the matrix electrical conductivity (Dvir, 2011; Navaei, 2016a; SR Shin, 2013).

In this chapter, our aim is to dissect the role of mechanical stiffness and nano-scale surface topography from electrical conductivity of the scaffold on maturation and excitability of cardiac tissues. In chapter 2, we reported the development of characterization of electrically conductive GelMA-GNR hydrogels for engineering of functional cardiac tissues (Navaei, 2017; Navaei, 2016a). Incorporation of GNRs within GelMA significantly increased the electrical conductivity and mechanical stiffness of the hydrogel matrix (Chapter 2, Figure 2.3.). Notably, the BSE-SEM micrographs of GelMA-GNR hydrogel demonstrated localization of GNRs on the surface of macroporous GelMA matrix (Chapter 2, Figure 2.2B.), which led to generation of nano-

scale topographies. The obtained in vitro results demonstrated that GelMA-GNR hydrogels, specifically with 1 or 1.5 mg/mL GNRs concentrations, significantly increased cellular retention and spreading, cardiac maturation (e.g. protein expression and sarcomere formation), synchronized contractility and electrical excitability (Chapter 2, Figures 2.4-10.) of the cardiac tissues. In this chapter, for the first time, we developed conductive and non-conductive engineered cardiac tissues to investigate side-by-side the impact of matrix electrical, mechanical and topographical characteristics on the cellular retention, cardiac maturation and excitation threshold of CMs. The excitability of the engineered cardiac tissues was also evaluated in the presence of a gap junction uncoupler (heptanol) to further examine the potential compensatory influence of matrix conductivity on the excitation voltage threshold. Overall, our goal was to shed light upon the impact of scaffold's matrix conductivity on the maturation and excitability of the engineered cardiac tissue constructs.

4.2. Experimental Methods

4.2.1. Materials

$HAuCl_4$, $NaBH_4$, CTAB, $AgNO_3$, L-ascorbic acid, gelatin, methacrylic anhydride, TMSPMA, and the photoinitiator were purchased from Sigma Aldrich and used without any modifications. The 80 nm silica nanoparticles (SNPs) with the specific surface area of 30-40 m^2/g and skeletal density of 2.1-2.2 g/cm^3 were purchased form General Engineering and Research (San Diego, USA). DIW (18 MΩ) was used for all the synthesis and fabrication processes.

4.2.2. Fabrication and characterization of pure, SNP- and GNR-embedded gelatin hydrogel constructs

GelMA hydrogel and GNRs were synthesized based on the protocols explained in chapter 2, section 2.2. (Navaei, 2016a; Saini, 2015). To fabricate the hydrogel constructs, first, a clear solution of GelMA (5% and 20% wt/v) in 0.5% (wt/v) photoinitiator in DPBS was prepared. Next, GNRs (1.5 mg/mL) and SNPs (9.69 mg/mL) were mixed with GelMA prepolymer solution (5% wt/v) and sonicated (bath) for 1 hr to create homogenous colloid solutions. The selected concentration of SNPs provided approximately similar number of nanoparticles (1.36×10^{13}

particles/mL) as 1.5 mg/mL GNRs concentration. SNPs were ultrasonicated (on ice) in DIW for 2 hr prior to mixing with GelMA prepolymer solution to obtain a homogenously dispersed colloid. Afterwards, 150 μm thick GelMA (5%), GelMA-SNP and GelMA-GNR hydrogel constructs were fabricated by UV photo-crosslinking for approximately 6, 10, and 30 sec exposure time, respectively. GelMA (20%) samples were prepared using similar method with 10 sec UV exposure time. Electrical conductivity and mechanical stiffness of the fabricated hydrogel constructs were measured using AFM and LCR meter based on the established protocols described in chapter 2, section 2.2. (Navaei, 2016a).

4.2.3. CMs isolation and culture of the cardiac tissue constructs

All the hydrogel constructs were sterilized by washing two times (10 min intervals) in antibiotic solution (1% penicillin/streptomycin in DPBS). Samples were then washed twice using culture media prior to cell seeding. CMs were isolated from ventricular region of 2-day old neonatal rats based on the previously established protocols (Saini, 2015). Briefly, hearts were extracted from neonatal rats and cut in small (1-2 mm^3) pieces. The cut tissues were then treated by Trypsin overnight and followed by serial collagen digestions. The isolated cardiac cells were incubated for 1 hr at 37 ^oC to allow the separation of CMs and CFs. Cardiac tissue constructs were fabricated by seeding CMs (7.5×10^5/construct) for 1 day and cultured for 7 days in an incubator at 37 ^oC and 5% CO_2. The culture media, containing DMEM supplemented with 10% FBS, 1% glutamine, and 1% penicillin/streptomycin, were exchanged every other day.

4.2.4. Characterization of CMs retention and expression of cardiac markers

The retention (n=6) of seeded CMs was evaluated thorough measuring the area percentage of hydrogel constructs covered by cells on day 1. Samples were washed two times with pre-warmed culture media to eliminate the loosely adhered cells prior to the phase-contrast imaging. To evaluate cardiac maturation, hydrogel tissue constructs were immunostained on day 7 of culture for Cx43 electrical gap junctions as well as contractile proteins including SAC and cTnI. Specifically, tissue constructs were first fixed using 4% PFA (20 min), then permeabilized with 0.1% Triton X-100 (10 min) and finally blocked by 10% goat serum (1 hr) at room

temperature. Afterwards, tissue constructs were incubated with primary antibodies for SAC (Sigma Aldrich, USA), cTnI and Cx43 (Abcam, USA) overnight followed by fluorescence staining using secondary antibodies for 1-2 hr at room temperature (Life Technologies, USA). The captured immunostained images (Zeiss ObzerverZ1, USA) were analyzed using NIH ImageJ for measuring the level of protein expression (n>3). Specifically, the area of fluorescence signal (μm^2) were calculated for each protein of interest and normalized by dividing to the total number of nuclei.

4.2.5. External electrical simulation and excitability testing

A custom-made field stimulation chamber was used to apply external electrical stimuli to the hydrogel tissue constructs as previously described (Navaei, 2016a; Tandon, 2009). Tissue constructs on day 7 of culture were characterized for the excitation voltage threshold, defined as the minimum voltage potential to induce synchronous contractions, at different frequencies (0.5, 1, 2, 3, 4 and 5 Hz). Specifically, samples were placed in the stimulation chamber and the voltage potential was increased step-wise by 0.2 V until synchronous contractions of CMs were evident. For the heptanol treatment experiment, tissue constructs were incubated (37 ^oC) with 2 and 3 mM heptanol, as a gap junction uncoupler, for 20 min and the excitation voltage threshold was measured at 0.5, 1, 2 and 3 Hz. In addition, the beating stopping time, defined as the total time of spontaneous contractions (sporadic and synchronous) of CMs after addition of heptanol (2 and 3 mM), was determined by constant monitoring of tissue constructs. All the measurements were performed at 37 ^oC and pH was maintained at approximately 7 by adding 10 mM HEPES buffer to the cell culture medium. A custom-written Matlab code (SB Kim, 2011) was used for extracting the beating signals form the recorded videos.

4.2.6. Statistical Analysis

All the collected data were graphed using GraphPad Prism software. The statistical analysis was performed based on student t-test, one-way and two-way ANOVA methods. The p value less than 0.05 was considered as the statistical significance.

4.3. Results and Discussions

4.3.1. Development of hydrogels with specific matrix characteristics

As it was shown in chapter 2 (Section 2.3.1.), incorporation of GNRs within GelMA hydrogel resulted in the enhancement of mechanical stiffness (higher Young's modulus, Figure 2.3F.), electrical conductivity (lower impedance, Figure 2.3A.) and generation of nano-scale surface topographies (Figure 2.2B.).

In this study, pure GelMA (5%) hydrogel was selected as the control group with relatively low mechanical stiffness (i.e. soft matrix), low electrical conductivity and without nano-scale surface topographies. GelMA (5%) hydrogel embedded with 1.5 mg/mL GNRs was used as the hydrogel candidate (GelMA-GNR) featuring high mechanical stiffness, enhanced electrical conductivity and with nano-scale surface topographies. In addition, SNPs (Figure 4.1A.) embedded within GelMA (5%) matrix provided non-conductive (Figure 4.1C.) and relatively soft (Figure 4.1D.) hydrogels, however with presence of nano-scale surface topographies (Chen, 2003; Gaharwar Akhilesh, 2012; Khelifa, 2013). The 80 nm (diameter) SNPs were used to nearly recapitulate the morphology and size of the synthesized GNRs (Figure 4.1B.) with ~60 nm length and ~20 nm width. Furthermore, the concentration of SNPs was selected as 9.69 mg/mL to provide approximately similar number of nanoparticles (1.36×10^{13} particles per mL) within the hydrogel matrix in comparison with GelMA-GNR (1.5 mg/mL). Lastly, pure GelMA with 20% (v/v) prepolymer concentration was prepared as the hydrogel group with similar mechanical stiffness (Figure 4.1D.) to GelMA-GNR matrix, while non-conductive (Figure 4.1C.) and without the presence of nano-scale surface features.

Therefore, with the selection of proposed hydrogel candidates, we were able to modulate three different matrix properties, namely stiffness, electrical conductivity and nano-scale topography. All the hydrogel groups including GelMA (5%), GelMA (20%), GelMA-SNP and GelMA-GNR were fabricated through UV photocrosslinking on TMSPMA-coated glass slides and were further used for developing cardiac tissue constructs.

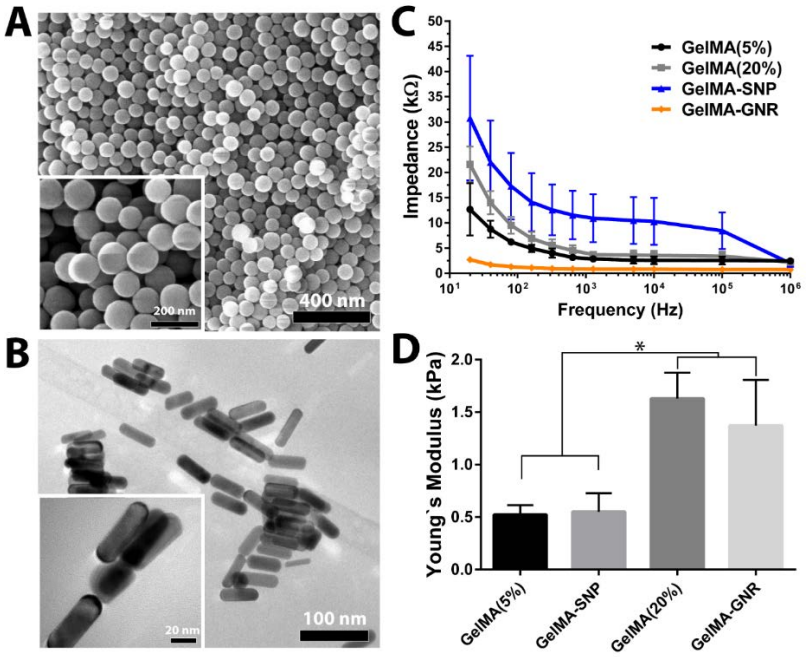

Figure 4.1. A) SEM images of SNPs (GEANDR-Co., 2018) and B) TEM images of GNRs. C) Impedance and D) Young's moduli values of all fabricated hydrogel constructs. (*p-value < 0.05).

4.3.2. Impact of matrix characteristics on CMs retention and cardiac maturation

Figure 4.2. displays the phase-contrast images and measured retention of CMs on the hydrogel constructs on day 1. The seeded CMs demonstrated a sparse and agglomerated adhesion patterns on GelMA (5%), while, more compact and uniform adhesion patterns were observed for CMs on GelMA (20%), GelMA-SNP and GelMA-GNR hydrogels. Quantification of cell retention (Figure 4.2B.) demonstrated that CMs covered approximately 30.9% of GelMA (20%), 68.8% of GelMA-SNP and 73.6% of GelMA-GNR hydrogels, which all were significantly higher than 14.2% cell retention on GelMA (5%). Overall, an increasing trend of cell retention was seen by enhancing the stiffness and nano-scale surface topographies within the GelMA matrix. However, GelMA-SNP and GelMA-GNR hydrogels promoted significantly higher cell adhesion affinity as compared to GelMA (20%). These findings indicated that stiffness and nano-scale surface topographies, via the incorporation of nanomaterials (SNPs or GNRs), has synergistic influence on higher cell adhesion affinity. Consistent with previous studies, hydrogels matrices with high stiffness and/or incorporated with nanomaterials, such as SNPs (Gaharwar, 2013;

Gaharwar Akhilesh, 2012), have also shown to promote cellular adhesion and retention (Bhana, 2010; Deok-Ho, 2005; Ren, 2017). The induced cell adhesion affinity is attributed to the enhanced integrin expression and mechanosensitive kinases including FAK, MAPK, ERK, and AKT (Young, 2014). Furthermore, nano-scale topographies formed by incorporation of nanomaterials within the macroporous matrix of hydrogel, increase surface area and protein adsorption and induce focal adhesion points, leading to overall improved cell adhesion affinity (Dalby, 2007; Gaharwar Akhilesh, 2012). In this regard, CMs retention on electrically conductive GelMA-GNR hydrogel was similar to non-conductive GelMA-SNP, demonstrating the negligible impact of matrix electrical conductivity on the cell adhesion affinity within cell-seeded nano-engineered matrices.

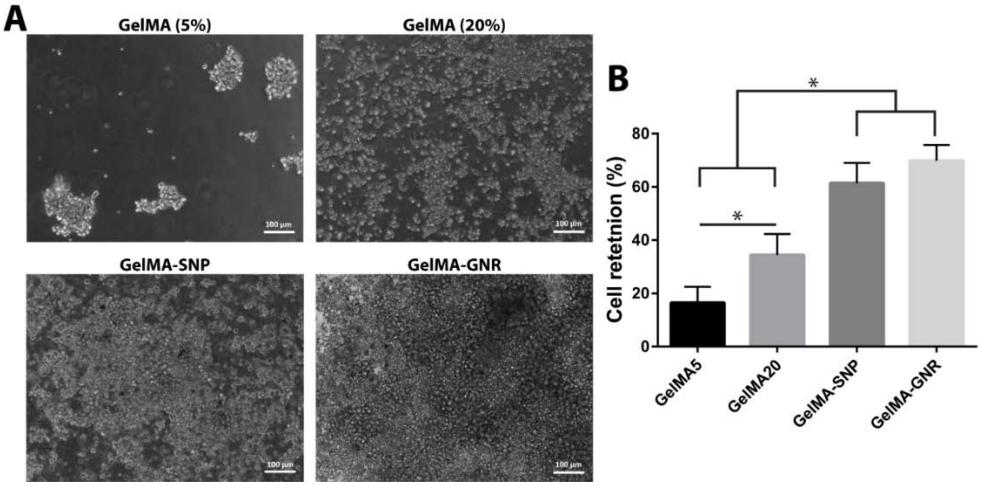

Figure 4.2. A) Phase-contrast images of CMs on the hydrogel constructs on day 1 showing the influence of the incorporated SNPs and GNRs on B) the CMs retention. (*p-value < 0.05).

Figure 4.3A. demonstrates the immunostained images of cardiac-specific proteins including SAC, cTnI as well as Cx43 gap junctions. A clear formation of striated sarcomere structures (SAC staining) were evident on GelMA (20%), GelMA-SNP and GelMA-GNR tissue constructs compared to the disoriented SAC expression on pure GelMA (5%) hydrogel. In addition, SAC stained images exhibited more elongated and uniaxially aligned striated sarcomeres on GelMA (20%), SNP- and GNR-embedded tissue constructs in contrast with the random and round morphology (white arrows) on GelMA (5%). The expression of cTnI also

followed similar pattern as SAC. GelMA (20%), GelMA-SNP and GelMA-GNR cardiac tissues illustrated extended and abundant expression of cTnI, while, scattered patterns were observed within GelMA (5%) matrix. Cx43 gap junctions (red punctuated stains) were present among CMs on all hydrogel constructs. However, less homogeneous distribution was observed on GelMA (5%) as compared to the other hydrogel groups.

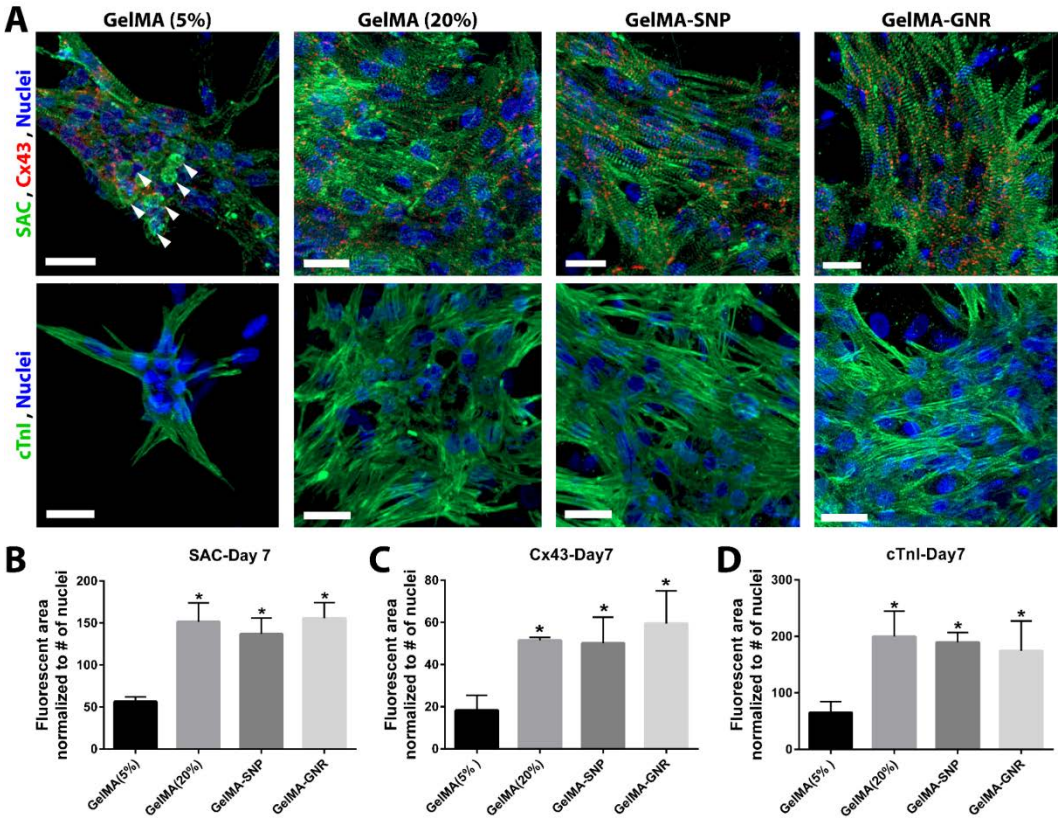

Figure 4.3. A) The immunostained images and B) measured fluorescence area of SAC, Cx43 and cTnI expressions on day 7 illustrating the enhanced cardiac maturation by the improving the hydrogel matrix mechanical, topographical and electrical characteristics. White arrow heads are pointing to the round CMs. (*p-value < 0.05).

In addition to representative immunostained images, the quantified fluorescent area (Figure 4.3B-D.) also confirmed significantly higher expressions of cardiac specific markers (SAC, cTnI and Cx43) on GelMA (20%), GelMA-SNP and GelMA-GNR hydrogels in comparison to GelMA (5%). In addition, we did not find significant differences, in terms of protein expression, between electrically conductivity GelMA-GNR and non-conductive GelMA-SNP hydrogels. These

findings demonstrate that enhanced cardiac maturation of the electrically conductive GelMA-GNR tissue constructs (Figure 4.3.) is mainly associated with improved mechanical and topographical characteristics of hydrogel matrix (Boothe, 2016; Forte, 2012; Jacot, 2008; Rodriguez, 2011), while electrical conductivity of the matrix may not solely play a role in maturity of the engineered cardiac tissues.

4.3.3. Influence of matrix characteristics on contractility and electrical excitability of cardiac tissue constructs

Figure 4.4. shows the excitation voltage thresholds and representative extracted beating signals for GelMA (5%), GelMA (20%), GelMA-SNP and GelMA-GNR tissue constructs under external electrical field stimulation, respectively. As can be seen, all the hydrogel groups were able to fully accommodate electrical stimulation frequencies up to 2 Hz. In this range, 5% GelMA cardiac tissues exhibited highest excitation voltage threshold (~8.4 V) as compared to 20% GelMA (~4.3 V), GelMA-SNP (~3.8 V) and GelMA-GNR (~3.7 V). In addition, our results did not show any significant differences for excitation thresholds across GelMA (20%), GelMA-SNP and GelMA-GNR groups. By increasing the frequency to 3 and 4 Hz, 5% GelMA and 20% GelMA cardiac tissues were no longer able to follow the stimulation regime and the tissue contractions became chaotic (Figure 4.4A-B.). On the other hand, GelMA-SNP and GelMA-GNR hydrogel tissue constructs still demonstrated contractile behavior consistent with the induced stimulation frequencies at 3 and 4 Hz (Figure 4.4C-D.). Lastly, none of the hydrogel groups could fully accommodate electrical stimulations with frequencies larger than 4 Hz (data not shown).

Figure 4.5. illustrates the excitation thresholds at 0.5, 1 and 2 Hz frequencies in presence of heptanol (gap junction uncoupler). Heptanol has been widely used to impair electrical gap junctions, such as Cx43, leading to reduced conduction velocity and unsynchronized (sporadic) contractions in CMs (Gizurarson, 2012; Takens-Kwak, 1992; G. Tse, 2016). We utilized heptanol to diminish the intrinsic electrical coupling within CMs through Cx43 gap junctions, to further elucidate the potential compensatory impact of matrix conductivity on excitability of engineered cardiac tissue constructs.

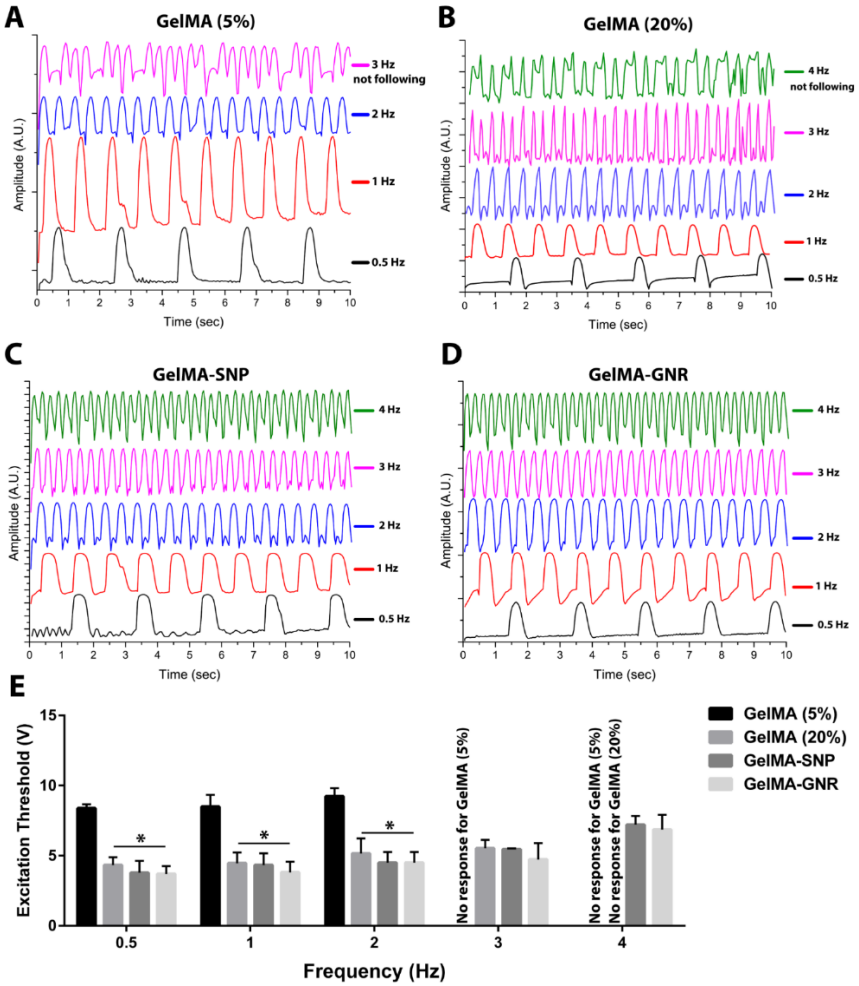

Figure 4.4. A-D) The extracted CMs beating signals in response to electrical stimulation at 0.5-4 Hz frequencies on day 7. E) The excitation voltage thresholds of pure GelMA and nanomaterial-embedded tissue constructs following the applied electrical stimuli. (*p-value < 0.05).

After 20 min exposure to 2 mM heptanol, GelMA (5%) tissue constructs did not follow the electrical stimulation at any of the applied frequencies (Figure 4.5A. and 4.5E.). Cardiac tissues cultured on GelMA (20%) hydrogels only responded to stimuli with 0.5 and 1 Hz upon heptanol treatment and were not able to follow 2 Hz stimuli. On the other hand, both GelMA-SNP and GelMA-GNR tissue constructs fully accommodated up to 2 Hz electrical stimuli even in the presence of heptanol. None of the engineered cardiac tissues were able to generate contractions upon electrical stimulation with frequencies higher than 2 Hz (data not shown). When higher

concentration of heptanol (3 mM) was tested, we were not able to induce contractions on any of the tissue contracts at any frequencies with voltage up to 10 V.

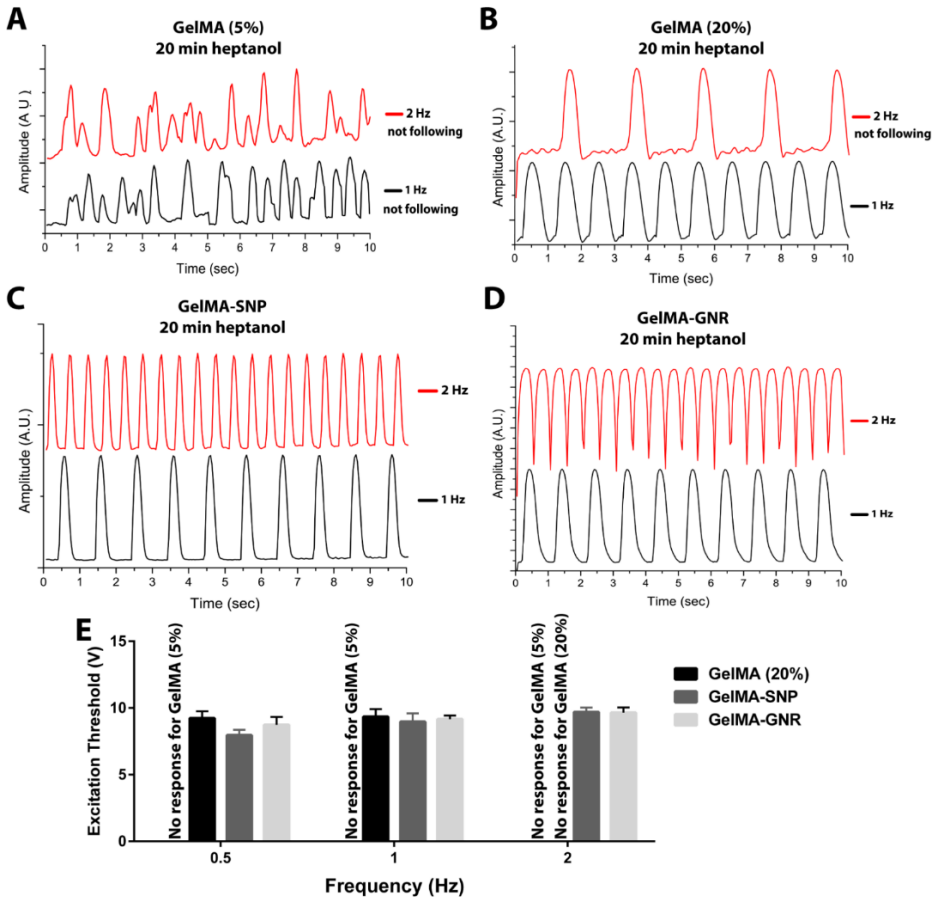

Figure 4.5. A-D) The extracted beating signals and E) excitation voltage thresholds of the electrically stimulated cardiac tissues upon 20 min treatment with heptanol (2 mM) on day 7, showing the impact of embedded SNPs and GNRs on the enhanced excitability of engineered cardiac tissue constructs.

Our findings (Figure 4.4. and 4.5.) indicated that nanomaterials (SNPs and GNRs)-embedded GelMA hydrogels induced enhanced tissue maturity, electrical excitability (lower excitation threshold) and contractility (higher stimulation frequency) of engineered cardiac tissues. Enhanced tissue maturation can be attributed to the impact of increased matrix stiffness and nano-scale topographies due to the presence of SNPs or GNRs. Finally, both conductive (GelMA-GNR) and non-conductive (GelMA-SNP) nanocomposite tissue constructs exhibited similar

excitation thresholds at all applied frequencies in both coupled and uncoupled gap junctions (Figure 4.4E. and 4.5E.). Our findings demonstrate that the stiffness and nano-scale topography of GelMA hydrogel matrix significantly improved excitability and contractility of the engineered cardiac tissues, and impact of matrix electrical conductivity was negligible.

In our study, we developed conductive (GelMA-GNR) and non-conductive (GelMA-SNP) hydrogels to investigate the impact of enhanced matrix conductivity, stiffness and nano-scale topography, due to the incorporation of GNRs and SNPs, on excitation threshold of cardiac tissues. We also evaluated excitation threshold, while Cx43 gap junctions were uncoupled using heptanol, to further investigate the compensatory influence of scaffold conductivity for maintaining the electrical excitability of cardiac tissues. Despite the significance and promising outcomes, our study was focused only on the tissue-level electrical excitability of engineered cardiac constructs via utilizing an electric field stimulation chamber to measure excitation threshold. However, there are other important factors which may induce substantial impact on excitability and electrical coupling of CMs, including membrane depolarization threshold and action potential propagation velocity, which can be the subjects of further studies. In addition, utilization of other electrophysiology techniques, such as voltage sensitive fluorescent dyes and point electrical stimulation using bipolar microelectrodes, can further provide more insight on the influence of scaffold conductivity on the electrophysiological properties (e.g. conduction velocity) of engineered cardiac tissues. In addition, we have utilized NRVCMs isolated form 2-day old rats for our studies, which are able to transit from neonatal stage to mature adult phenotype (Belostotskaya, 2014). Therefore, it is speculated that the use of other cell types, such as iPSC- and ESC-derived CMs, with typically insufficient cardiac maturation capability (Veerman, 2015) could give rise to different outcomes regarding the electrical excitability and electrophysiological properties of the engineered tissues.

4.4. Conclusion

In this study, our goal was to dissect the role of mechanical stiffness and nano-scale topography of scaffolding hydrogels on the maturation and electrical excitability of engineered

cardiac tissues, regardless of electrical conductivity. We designed and fabricated four different hydrogel groups including 5% GelMA, 20% GelMA (mechanically stiffness), GelMA-SNP (non-conductive with nano-topographies) and GelMA-GNR (conductive with nano-topographies). Our results demonstrated that GelMA-SNP and GelMA-GNR hydrogels significantly improved CMs adhesion affinity as compared to pure GelMA (5% and 20%), highlighting the influence of nano-scale topography on cellular adhesion and retention. Furthermore, cardiac specific protein expressions revealed that the increased stiffness alone promote maturation of engineered cardiac tissues, however, such increase was significantly higher in the presence of nano-scale topographies within the hydrogel matrix. In terms of electrical excitability with and without heptanol (gap junction uncoupler), the impact of increased stiffness and nano-scale topography, induced by incorporation of SNPs and GNRs, significantly lowered the required excitation voltage threshold (i.e. higher excitability). GelMA-SNP and GelMA-GNR cardiac tissues were able to accommodate external electrical stimuli at higher frequencies in both coupled and uncoupled gap junction conditions. Most importantly, no significant differences regarding cell retention, cardiac maturation and electrical excitability were observed between conductive GelMA-GNR and non-conductive GelMA-SNP tissue constructs. These findings indicate the prominent impact of hydrogel matrix mechanical stiffness and nano-scale surface topography on the overall tissue function, regardless of electrical conductivity. Further electrophysiology studies using patch clamping is required to shed more light on the influence of scaffold conductivity on CMs electrical coupling and conduction velocity.

CHAPTER 5

ENGINEERING OF SCAFFOLD-FREE CARDIAC MICROTISSUES EMBEDDED WITH FUNCTIONALIZED GOLD NANOWIRES

5.1. Introduction

Transplantation of autologous cells (e.g. MSC and skeletal myoblasts) within the infarcted myocardium has offered promising outcomes to diminish the adverse pathophysiological events post-MI and to prevent heart failure (Fisher, 2015; Passier, 2008; Sanganalmath, 2013). Cell-based therapies (i.e. cellular cardiomyoplasty), traditionally consisting of a single cell suspension, are delivered within the ischemic myocardium often based on using a minimally invasive procedures, such as intracoronary catheterization (Campbell, 2012; Suzuki, 2014). To date, numerous studies have demonstrated that cardiac cell-based therapies result in activating endogenous reparative mechanisms (Avolio, 2015; Loffredo, 2011), neovascularization (S-W Kim, 2014), reduced scar size (Amado, 2005), limited ventricular remodeling (Chung, 2015), and enhanced cardiac output (Amado, 2005). Despite promising outcomes, the regenerative efficacy of cell-based therapies has shown to be significantly limited (Gyöngyösi, 2015), primarily due to the poor survival, retention and engraftment with the host as well as cardiogenic differentiation and maturation of injected cells within the injured myocardium (Bartolucci, 2017; L Li, 2016a; Yang, 2014). These drawbacks are mainly associated with low cell adhesion affinity of ischemic myocardium due to innate hypoxia and inflammation, as well as high concentrations of ROS (Angelos, 2006; Song, 2010). To address these limitations, numerous attempts have utilized 3D scaffold-free cardiac microtissues or cellular aggregates instead of single cells injection strategy (Doan C Nguyen, 2014). The 3D structure of scaffold-free microtissues induces a physiologically relevant microenvironment (Atmanli, 2016; Kofron Celinda, 2017) and leads to enhanced cell-cell electrical (e.g. Cx43) and mechanical (e.g. N-cadherin) coupling (Chang, 2009; EJ Lee, 2012). In addition, cells in the 3D scaffold-free microtissue secrete endogenous ECM proteins, promoting the expression of integrins and minimizing anoikis (W-Y Lee, 2011).

In recent years, the use of electrically conductive nanomaterials, including CNTs, rGONFs and SiNWs, in conjunction with scaffold-free microtissues has led to substantial improvements in viability, proliferation, maturation and differentiation of primary and stem cell-derived CMs (Martinelli, 2013a; Park, 2015; Richards, 2016). The specific physicochemical characteristics and electrical conductivity of these nanomaterials enable promoting specific cellular functionalities. For example, rGONFs are a type of carbon-based nanomaterials featuring high physicochemical reactivity, provided by the abundance of surface functional groups (e.g. hydroxyl and carboxyl) (Dreyer, 2010). This unique physicochemical property was utilized by Park (Park, 2015) to promote cell-ECM interactions in MSC-rGONF microtissues via adsorption of ECM proteins on rGONF's surface. Incorporation of rGONFs led to the formation and maturation of MSC-based microtissues, which were resistant to the deleterious impact of hypoxia and ROS on retention and viability of injected cells. In addition, electrical conductivity of rGONFs (Dreyer, 2010; Gómez-Navarro, 2007) increased the expression of Cx43 gap junctions in MSCs through activation of FAK pathway and upregulation of VEGF expression (Pimentel, 2002), leading to enhanced coupling of injected microtissues with the host myocardium (Sarah Fernandes, 2009; You, 2011).

SiNWs belong to another class of electrically conductive nanomaterials that have been recently employed for engineering scaffold-free microtissues made of iPSC-derived CMs. In a series of studies by Ying Mei's group (Richards, 2016; Y Tan, 2017; Y Tan, 2015), it was shown that SiNWs were able to induce significant cardiogenic maturation of hiPSC-derived CMs. Specifically, upregulated expressions of cardiac-specific markers, including SAC, cTnI, Cx43, and N-cadherin, as well as enhanced assembly and organization of striated sarcomeres were notably evident in the presence of SiNWs. Furthermore, the CM-SiNW microtissues exhibited higher contraction amplitude (i.e. fractional shortening) as well as faster cytoplasmic release of Ca^{2+} ions, indicating the mature phenotype and electrophysiology of microtissues (Pointon, 2015; MC Ribeiro, 2015b). To elucidate the impact of electrical conductivity of SiNWs (doped) on the cardiac phenotype and physiology of iPSC-derived microtissues, non-conductive (undoped) SiNWs were used (Y Tan, 2017). Interestingly, enhanced expressions of SAC and Cx43, and mature handling of cytoplasmic Ca^{2+} transients (i.e. rapid release with high amplitude) of

microtissues were only observed in the presence of electrically conductive (doped) SiNWs. These findings indicated that the electrical conductivity of SiNWs played a key role in maturation of hiPSC-derived CMs.

Despite the significance of previously mentioned studies, the detailed impact of conductive nanomaterials on the electrophysiology of CMs were mostly neglected. Specifically, none one of these studies investigated the influence of electrically conductive nanomaterials on action potential propagation (i.e. conduction velocity) within CM microtissues. Based on our foundational work in the use of GNMs for cardiac tissue engineering (Navaei, 2017; Navaei, 2016a), in this study we aimed to specifically assess the role of conductive nanomaterials on electrophysiology of CMs using microelectrode array. Our further goal was to evaluate cardiac phenotypic and functional maturation in sole presence of GNMs and in absence of scaffolding biomaterials (i.e. scaffold-free microtissues). We synthesized GNWs and conjugated them with RGD peptide to increase the adhesion affinity of nanomaterials to the cells (Choi, 2011). Our working hypothesis was centered on that scaffold-free cardiac microtissues incorporated with biocompatible GNWs, conjugated with RGD, would exhibit enhanced physiological response, including electrical signal propagation and contraction amplitude. We further investigated the influence of conductive GNWs on phenotypic maturation (expression level of SAC, cTnI, and Cx43 proteins) of the cells.

5.2. Experimental Methods

5.2.1. Materials

Carboxymethyl-PEG-thiol (COOH-PEG-SH, MW 3500) was purchased from Laysan Bio (USA). Cyclo (Arg-Gly-Asp-D-Phe-Lys) (cRGD) was purchased from Peptides International (USA). N-hydroxysulfosuccinimide (Sulfo-NHS) was purchased from ThermoFisher. $HAuCl_4$ (>99.9%), $NaBH_4$ (>99%), L-Ascorbic acid (>98%), nitric acid (HNO_3) (70%), N-(3-Dimethylaminopropyl)-N′-ethylcarbodiimide hydrochloride (EDC), and CTAB (>99%) were purchased from Sigma Aldrich (USA). DIW (18 MΩ) was used for all synthesis processes.

5.2.2. Synthesis of CTAB-capped GNWs

GNWs were synthesized based on the seed-mediated growth method (Y-N Wang, 2013). Seed solution containing GNPs is prepared by mixing 2 mL of $HAuCl_4$ (0.5 mM in DIW) and 2 mL of CTAB (0.2 M in DIW) solutions. The GNPs were then synthesized by addition of 180 µL of ice-cold freshly-made $NaBH_4$ (20 mM in DIW) and mixing vigorously for 2-5 min. To allow complete decomposition of NaBH4, the seed solution was kept at 29 ^oC for at least 2 hours before further use. Next, a 30 mL growth solution was prepared by mixing 29.475 µL CTAB (0.1 M in DIW) and 525 µL $HAuCl_4$ (10 mM in DIW).

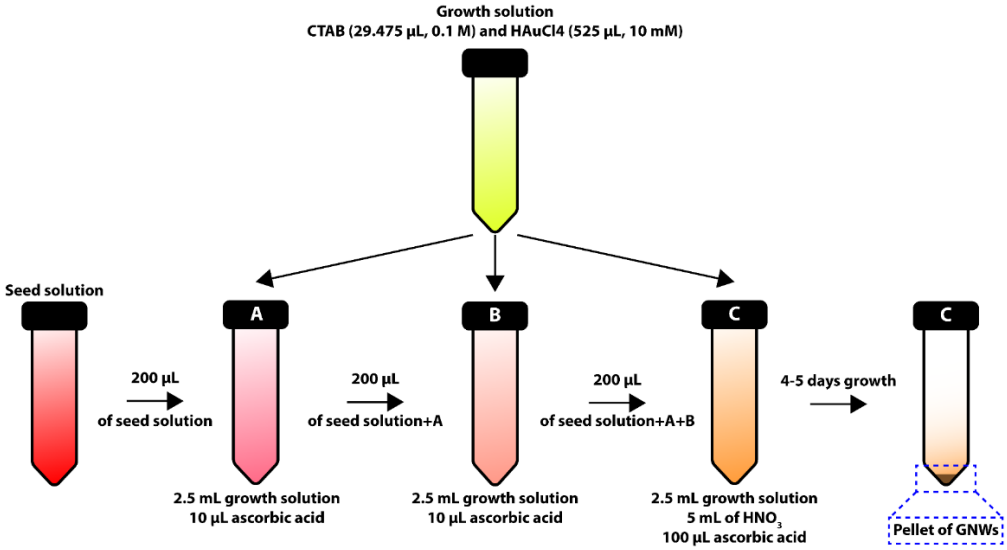

Figure 5.1. Schematic drawing illustrating the seed-mediated growth procedure of GNW-CTAB synthesis. The depicted colors represent actual color change of the solutions during the synthesis.

The growth solution was divided into three separate tubes (A, B, and C) containing 2.5 mL (tube A), 2.5 mL (tube B), and 25 mL (tube C) of the growth solution (Figure 5.1.). 5 mL of HNO_3 (0.5 M in DIW) was introduced to the tube C only and mixed gently. Then, 10, 10, and 100 µL aliquots of ascorbic acid solution (0.1 M in DIW) were added into the tube A, B, and C, respectively. All tubes were gently mixed to which made the solutions colorless. To initiate the sequential growth process, 200 µL of the seed solution was transferred to the tube A and mixed gently for 10 s. Afterwards, 200 µL of the “tube A-seed mixture” was added to the tube B and

gently mixed for 10 s. Finally, 200 µL of the “tube B-tube A mixture” was introduced to tube C and gently swirled for 5 s. The tube C was kept undisturbed at 30 ^{o}C for 4-5 days to allow completion of the growth synthesis. The formed pellet at the bottom of the tube C, which contained mostly GNWs, was harvested by carefully discarding the supernatant and dispersing the pellet in DIW for storage.

5.2.3. PEGylation, RGD conjugation and material characterization of GNWs

PEGylation of CTAB-capped GNWs was performed using a custom-designed 2-step ethanol-assisted exchange process (Kinnear, 2013; Z Zhang, 2014). The exchange procedure is schematically illustrated in Figure 5.2. First, CTAB-capped GNWs (~300 µg) were centrifuged (2000 rpm, 20 min) two times and re-dispersed in a 1 mM CTAB solution to reduce concentration of CTAB to near critical micelle formation concentration (CMC in water for CTAB is ~1 mM) (Moulik, 1996). After second centrifugation step, supernatant was discarded and 400 µL of Tris buffer (50 mM, pH ~3) was added drop-wise to the GNWs pellet. To initiate PEGylation process, 30 µL of COOH-PEG-SH (1 mM in Tris buffer) was added to GNW-Tris mixture while vortexing and kept agitated for 1 min. Final mixture remained undisturbed for 24 hr at room temperature. The mixture was then centrifuged once (4000 rpm, 30-35 min) to remove unreacted COOH-PEG-SH and free CTAB molecules.

To further improve CTAB-PEG exchange, an additional PEGylation step was performed using 20% (v/v) ethanol solution. Then, partially PEGylated GNWs were re-dispersed in 20% ethanol followed by addition of 30 µL of COOH-PEG-SH (1 mM in 20% ethanol) to the mixture under gentle vortexing. Mixture was kept undisturbed at room temperature for 24 hours. Two-step PEGylated GNWs (pGNW-COOH) were harvested by centrifugation at 4500 rpm for 30-35 min, and then dispersion in 300 µL DPBS. In order to conjugate RGD peptides on PEGylated GNWs with free COOH groups (pGNW-COOH), EDC/NHS reaction chemistry was employed (Choi, 2011). Briefly, pGNW-COOH were activated by adding 2.5 mg of EDC and 5.5 mg of Sulfo-NHS consecutively and thoroughly mixed for 5 min at ambient temperature. Afterwards, 200 µL of RGD peptide (1 mg/mL in DPBS) was added to activated pGNW-COOH and the mixture was kept

in 4 °C for 6-8 hours. GNWs with conjugated RGD peptide (pGNW-RGD) were purified by centrifugations in DPBS (4000 rpm, 30-35 min) at 4 °C, and were used immediately for the experiments.

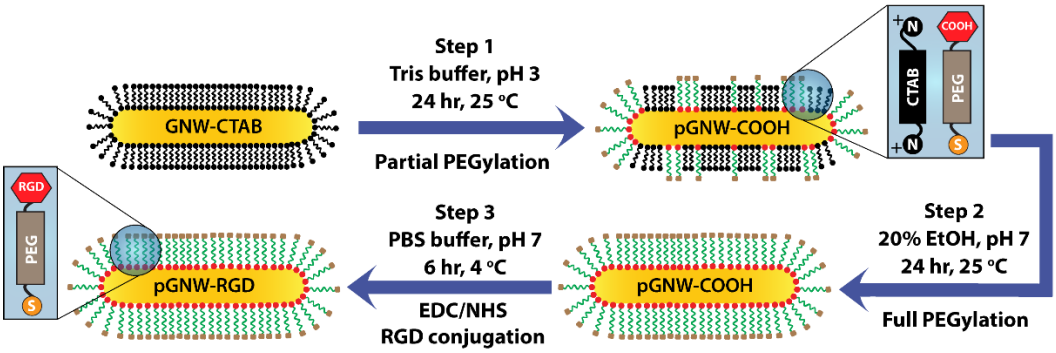

Figure 5.2. Schematic drawing depicting the 2-step ethanol-assisted PEGylation and RGD conjugation of GNWs.

Nano-scale morphology and size measurement of the synthesized GNWs were assessed using TEM (Philips CM200-FEG, USA) operating at an accelerating voltage of 200 kV. In addition, dynamic light scattering (DLS) measurements were carried out using DelsaNano Zetasizer (Beckman Coulter, USA) at 25 °C to evaluate surface charge of nanowires before and after PEGylation process. Furthermore, a Micro-Raman Spectrometer (Goldwater Materials Science Facility, AZ, USA) was utilized to investigate the RGD conjugation on GNWs. The spectroscopy characterization was performed using a 785 nm laser operating at 4-5 mW power 3 times for 10-second-long acquisitions.

5.2.4. Cell isolation and 2D in vitro cytotoxicity assays

CMs from 2-day old rats were isolated and purified using previously established protocol (Navaei, 2017; Navaei, 2016a; Saini, 2015). Cells were cultured in a humidified incubator with 5% CO_2 at 37 °C. The culture medium was composed of DMEM (Gibco, USA), 10% (v/v) FBS (Gibco, USA), L-Glutamine (1%) (Gibco, USA), and 100 units/mL of penicillin-streptomycin. To evaluate the impact of CTAB removal and RGD conjugation on viability and metabolic activity of CMs, Live/Dead and Alamar Blue assays were used. CMs were cultured (45-52 × 10^3 per well) with

GNW-CTAB, pGNW-COOH and pGNW-RGD (1, 10 and 50 µg/mL) for 48 hr. Live/Dead fluorescent images (n=4) were taken using an inverted microscope (Zeiss Observer Z1, Germany) and Alamar Blue (Invitrogen, USA) signals (n=3) were recorded by a plate reader.

5.2.5. Engineering of scaffold-free cardiac microtissues

Scaffold-free cardiac microtissues were developed by culturing CMs and GNWs (pGNW-COOH and pGNW-RGD) within agarose concave microwell arrays (Desroches, 2012). First, high purity agarose (VWR Life Science, USA) was dissolved completely (2% wt/v) in NaCl solution (0.9% wt/v in DIW) using a microwave. Next, 330 µL of agarose solution was injected into a master mold (Microtissue Inc., USA) containing 35 concave recesses (800 µm in diameter and 800 µm depth) and was placed on a cold block until agarose hydrogel was solidified. Fabricated agarose microwell arrays were then detached gently from the master mold and washed twice (10 min intervals) using culture medium prior to cell loading. In the next step, a 75 µL aliquot of CMs (~0.7×10^6 cells/mL) and GNWs (0, 5, and 10 µg/mL) mixture was loaded into the microwells and kept in incubator for 10 min to allow the precipitation of cells. The experimental groups were defined as CM only, CMs with 5 and 10 µg/mL of either pGNW-COOH (CM-COOH5 and CM-COOH10) or pGNW-RGD (CM-RGD5 and CM-RGD10). Afterwards, 600 µL of fresh culture medium was added gently to the surrounding of the microwell array mold and exchanged every other day. The microtissues were cultured for 7 days.

5.2.6. Immunocytochemistry (ICC) and western blot (WB) of the microtissues

The microtissues were harvested after 6 days of culture to evaluate the phenotypic characteristics and expression levels of cardiac-specific markers (SAC, Cx43, and cTnI). ICC technique was utilized to analyze the phenotype of the cardiac markers. Specifically, harvested cardiac microtissues were fixed in PF (4%) for 30 min and then treated with 30% (wt/v) sucrose solution as cryoprotecting agent for 48 hr. Afterwards, microtissues were embedded in optimal cutting temperature compound (OCT) and placed on a pre-cooled aluminum block with liquid nitrogen. Frozen OCT-embedded microtissues were sectioned into 7 µm thick slices using cryotome (Leica). The ICC process of freshly cut microtissue slices started with washes 3 times

of DPBS (5 min intervals) and permeabilization with 0.1% Triton X-100 (5 min). Samples were then blocked in 10% goat serum (Gibco, USA) for 1 hour and exposed to the primary antibodies for SAC (Sigma Aldrich, USA) and Cx43 (Abcam, USA) overnight at 4 ^{o}C. Next, samples were washed 5 times using DPBS (5 min intervals) and stained with secondary antibodies (Life Technologies, USA) for 1-3 hr. Lastly, immunostained microtissue slices were stained for nuclei with DAPI and preserved in antifade solution (VECTASHIELD, USA) prior to imaging. A Zeiss Observer Z1 microscope equipped with Apotome2 (Zeiss, Germany) was used for acquiring fluorescent images.

The WB technique was used for quantification of the expression level of cardiac-specific markers. Cardiac microtissues were collected and digested in lysis buffer (150 mM NaCl, 1% Triton X-100 and 50 mM Tris) for 30-40 min at 4 ^{o}C. The cell lysate was centrifuged at 16,000 × g for 20 min (4 ^{o}C) and the supernatant containing extracted proteins was collected. The extracted proteins ran through a Novex Wedge Well 10-20% Tris-Glycine Gel (Invitrogen, USA) for 2 hr to separate the proteins. After the completion of gel electrophoresis, the proteins were transferred to a cellulose membrane (100 V for 50 min). The transferred blots were then washed two times with PBS, blocked by 5% (v/v) BSA for 2 hr, and incubated with primary antibodies for SAC (Sigma Aldrich, USA) and Cx43 (Abcam, USA) overnight at 4 ^{o}C. Afterwards, the blots were stained with secondary antibodies (Life Technologies, USA) fro 1 hr and then scanned and analyzed using a LI-COR Odyssey Imaging System. GAPDH and β-actin primary antibodies were used as the housekeeping proteins for normalization and calculation of the relative expression results.

5.2.7. External electrical field stimulation and contraction amplitude of the microtissues

Cardiac microtissues were externally stimulated by an electric field using a custom-made chamber (Tandon, 2009). Excitation voltage threshold was defined as minimum required voltage to induce contractions in microtissues in suspension. Electrical pulses with 5 ms durations at 1 and 2 Hz frequencies were generated (BK PRECISION 4052) and the voltage was ramped until the suspended microtissues started contracting (n=3). To measure the contraction amplitude (i.e.

fractional shortening), the suspended microtissues were electrically stimulated (10 V, 1 Hz and 5 ms pulse duration) and simultaneously videos of contractions were recorded. The captured videos were analyzed using NIH ImageJ software and the contraction amplitude (n=3) was extracted based on the edge-detection method (Bazan, 2009). Contraction amplitudes were reported as the percentage of fractional shortening (diameter) of the microtissue in contracted and relaxed states.

5.2.8. Microelectrode array (MEA) electrophysiology of CMs

A 28-microelectrode array system (BMSEED LLC, USA) was utilized to analyze the impact of electrically conductive GNWs on the electrophysiology (Graudejus, 2011; Kang, 2014; Yu, 2009), specifically the conduction velocity (CV) of CMs. MEAs were consisted of 28 microelectrodes (90 μm electrode size) with approximately 200 μm spacing (Figure 5.3A. and 5.3B.), embedded within a PDMS membrane. The MEA was connected to a head-stage board (Plexon, USA) equipped with two amplifiers (Intan Technologies, USA). The whole assembly was connected to a stimulation/reading controller (Intan Technologies USA). The data acquisition was performed using Intan Stimulation/Recording System Software. The recorded data (*.rhs file format) was processed and analyzed using Matlab (MathWork, USA) and OriginPro (OriginLab, USA).

Prior to loading cells, MEAs were washed thoroughly with autoclaved DIW and then sterilized overnight under UV inside a biological safety cabinet. Next, MEAs were treated with oxygen plasma (Harrick Plasma, USA) for 3 min to create a hydrophilic surface and then coated with 0.1% (wt/v) gelatin solution for at least 2 hr. The gelatin coating is vital to promote the tight adhesion and spreading of CMs on the microelectrodes and enhance the signal to noise ratio. After sterilization and gelatin coating of MEAs, a 2 mL CM (0.7×10^6 per mL) suspension containing either pGNW-COOH or pGNW-RGD (5 and 10 μg/mL) was seeded on each MEA, and extracellular voltage potentials were captured (i.e. field potential or FP). The spontaneous FP (Figure 5.3C.) changes are correlated with the action potential triggering and propagation on CMs membrane (Halbach, 2003). The conduction velocity among CMs was measured on days 4 and 6

of culture. Specifically, the activation times for FP signals were extracted for all the working electrodes (impedance less than 1-2 MΩ) and sorted (earliest to latest) using OriginPro software. Afterwards, the direction of FP signal (i.e. propagation directions) was determined based on the order of the activation times.

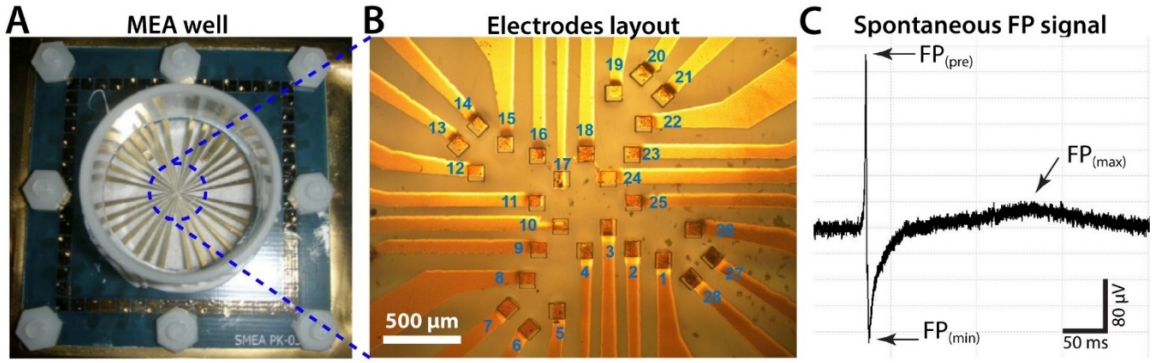

Figure 5.3. A) Photograph of MEA well and B) microelectrodes layout. C) A representative FP signal reading showing the different components of extracellular field potential induced by cardiac action potential.

The conduction velocity (cm/s) among CMs was calculated by dividing the distance between the electrodes to their respective time difference. One minute of electrical activities were processed and analyzed for determining the conduction velocity for each condition. To maintain pH 7 during the experiment, the culture media were exchanged with the one supplemented with HEPES buffer (10 mM) and cells were incubated (37 ^{o}C) for at least 30 min prior to recording FPs. In the gap junction blocking experiment, several concentrations of heptanol including 0.5, 1, 2, and 4 mM were tested. Cells were exposed to heptanol (1 and 2 mM in culture medium + HEPES) and FP signals were immediately recorded for 20 min. Cells were washed 3 times and incubated for at least 1 hr with fresh culture medium plus HEPES to be rescued from heptanol, before measuring FP signals for the second heptanol concentration. The CVs for each concertation of heptanol were measured upon 10 and 20 min exposure. The percentage of reduction in CVs was calculated with respect to the CV of each sample before addition of heptanol. For cleaning and reusing purposes, MEAs were washed with sterile DIW 3-5 times, then incubated (37 ^{o}C) with trypsin (1x) for at least 1 hr. Afterwards, MEAs were washed 3-5

times with sterile DIW and treated with 1mg/mL collagenase (type 1) for at least 1 hr in 37 ^{o}C. MEAs were washed with sterile DIW 3-5 times again and stored in closed containers.

5.2.9. Statistical analysis

All data obtained from the experiments was analyzed based on Student's t-test, one- and two-way ANOVA with Tukey post analysis by GraphPad Prism 6. A p-value less than 0.05 was measured as statistically significant difference within the groups.

5.3. Results and Discussion

5.3.1. Characterization of GNWs PEGylation and RGD conjugation

GNWs were synthesized using serial consecutive anisotropic growths of the seeds (Figure 5.1.) (Y-N Wang, 2013). TEM micrographs (Figure 5.4A.) of freshly synthesized GNWs revealed the wire-like morphology of the synthesized nanomaterials with ultralong aspect ratio of approximately 46. The measured average size of GNWs, based on the TEM images, was 4 ± 1.4 μm in length and 87 ± 32 μm in diameter. CTAB was used as stabilizer-surfactant agent for synthesizing GNWs and preventing agglomeration (Y-N Wang, 2013). However, its cytotoxic effect (Alkilany, 2009) requires elimination before direct exposure to CMs. It has been shown that GNMs biocompatibility can be significantly improved just by removing the free CTAB molecules from the colloid solution through several centrifugations (Alkilany, 2009; Connor, 2005). However, there is still a CTAB coating bilayer on the GNWs that can be toxic to the cells at high concentrations of the nanomaterials (Kinnear, 2013). In this regard, it is critical to exchange CTAB with a biocompatible coating layer, such as thiolated PEG, to complete the removal process of CTAB molecules.

In our work, the concentration of free CTAB in the GNWs colloid solution was reduced by two centrifugations. However, the CTAB concentration was kept at near its CMC (~1 mM in water) to prevent aggregation of GNWs (Moulik, 1996). This step was substantially important to perform a successful PEGylation process with virtually no aggregation of GNWs. In the next step (Figure 5.2.), the CTAB coating bilayer on the GNWs was exchanged with SH-PEG-COOH in Tris

buffer. Typically, one-step (24 hr) PEGylation processes lead to the removal of a significant amount of CTAB coating bilayer (Alkilany, 2009). However, due to the strong interactions between CTAB molecules and Au atoms, as well as the packed bilayer structure of CTAB coating, the PEGylation process is not complete and CTAB residue may remain on the surface of GNWs (Kinnear, 2013). Therefore, a second PEGylation of GNWs was carried out using 20% ethanol (Figure 5.2.) to disrupt the formation of the CTAB bilayer and also facilitate the interaction of SH-PEG-COOH with the surface of GNWs (Kinnear, 2013). As the DLS measurements revealed, zeta potential was +61.5 ± 1.0 mV for GNW-CTAB and -32.9 ± 2.4 mV for pGNW-COOH. The GNW-CTAB was positively charged due to the CTAB coating (Gole, 2004; X Huang, 2009). However, after the exchange of CTAB with SH-PEG-COOH, the zeta potential of pGNW-COOH alternated to a negative value due to the presence of carboxyl groups (-COOH) (Su, 2017).

In addition, Raman spectroscopy (Figure 5.4B.) further confirmed substitution of CTAB with SH-PEG-COOH *via* removal of Au-Br band at 189 cm^{-1} and appearance of Au-S bands at 273 & 295 cm^{-1}. Furthermore, the vibration of C-O-C band at 845 cm^{-1} demonstrated the coating of PEG on GNWs (Liao, 2005; Schulz, 2016; S Sun, 2014; Z Zhang, 2014). Conjugation of RGD peptides on the surface of pGNW-COOH nanomaterials was performed using typical EDC/NHS protocol (Choi, 2011). The Raman spectrum of pGNW-RGD (Figure 5.4B.) demonstrated the appearance of two amide bands, including amide II at 1555 cm^{-1} and amide III at 1275 cm^{-1}, consistent with previously reported studies (Choi, 2011). The amide bands are the result of covalent interactions between carboxyl groups on pGNW-COOH and amine (NH_2) groups in cRGD-Phe-Lys peptide sequence. In addition, the peak near 1015 cm^{-1}, associated with the benzyl ring of the extra Phenylalanine (Phe) in the cRGD peptide sequence, further confirming the successful conjugation of RGD on the surface of GNWs (S Sun, 2014).

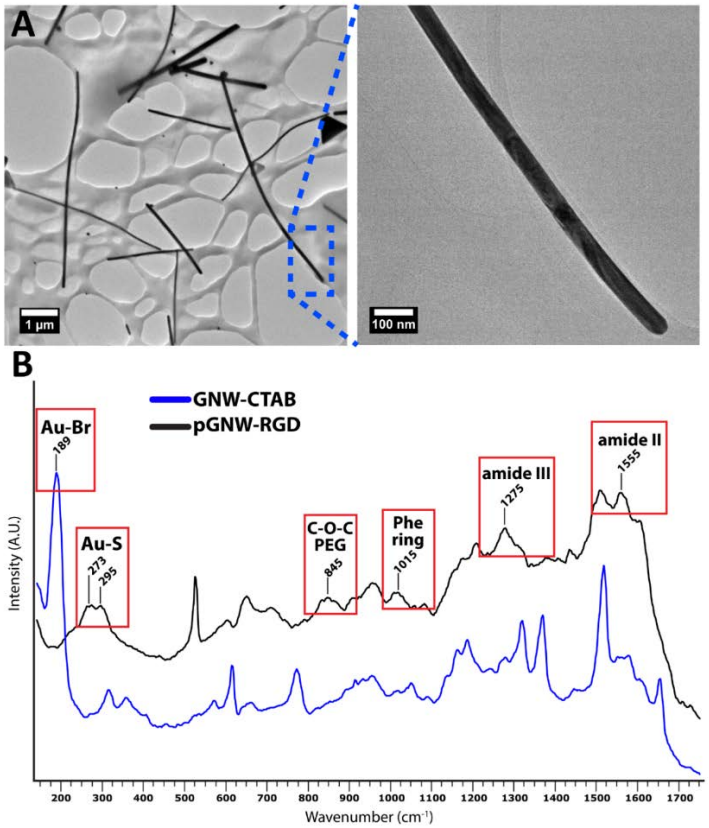

Figure 5.4. A) TEM micro-graph of synthesized GNW-CTAB. B) Raman spectra of GNW-CTAB and pGNW-RGD showing the exchange of CTAB (Au-Br) with PEG (Au-S and C-O-C) along with the conjugation of RGD (amide II, III, and Phe ring) on GNWs.

5.3.2. The impact of CTAB removal and RGD conjugation on cytotoxicity of GNWs

To evaluate the impact of CTAB removal and conjugation of RGD on the cytotoxicity of the GNWs, we performed control experiments, where CMs were cultured with 0, 1, 10, and 50 µg/mL of GNW-CTAB, pGNW-COOH and pGNW-RGD for 48 hr, and viability and metabolic activity of the cells were further assessed. The Live/Dead fluorescent images and quantified viability data (Figure 5.5A. and 5.5B.) confirmed that all three types of GNWs did not induce cytotoxicity at concentration of 1 µg/mL. However, viability of CMs significantly decreased as a function of GNW-CTAB concentration (~60% and ~42% at 10 and 50 µg/mL) in comparison with the pure CMs culture (~89%). In contrast, PEGylated and RGD conjugated GNWs did not induce any cytotoxic effect on CMs at any concentration. Similar trend was observed in terms of metabolic activity of CMs, when cultured with the GNWs. The Alamar Blue signal significantly dropped at 10

and 50 µg/mL concentrations of GNW-CTAB, however, no changes were evident for pGNW-COOH and pGNW-RGD groups compared to the pure CMs culture. These results clearly showed the substantial impact of the CTAB removal on improving the biocompatibility of GNWs. In addition, no major differences in the CMs viability were observed between PEGylated and RGD conjugated GNWs. These findings indicated that CTAB was the major cause of cytotoxicity of the GNW-CTAB, consistent with previous studies (Alkilany, 2009; Khlebtsov, 2011). Conjugation of a cell adhesive peptide, such as RGD (Rask, 2010; Vacharathit, 2011), did not significantly influence the biocompatibility of PEGylated GNWs (pGNW-COOH).

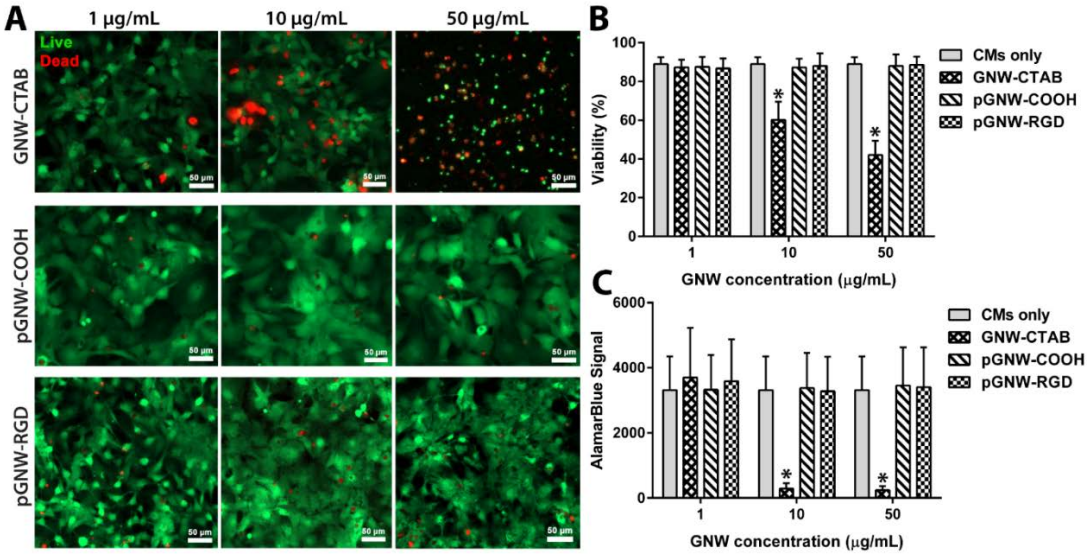

Figure 5.5. A) Live/Dead fluorescent images, B) quantified viability and C) metabolic activity of CMs after 48 hr exposure to GNW-CTAB, pGNW-COOH, pGNW-RGD.

5.3.3. The development and characterization of scaffold-free cardiac microtissues

Scaffold-free cardiac microtissues were formed by culturing CMs on concave microwells with ultra-low cellular adhesion affinity. Without the presence of a scaffolding biomaterials and consequently cell-scaffold interactions, the cell-cell interactions become dominant (Baar, 2005; Desroches, 2012). Enhanced cell-cell interactions result in self-assembly of spherical microtissues, known as cardiac spheroids. In this study, we utilized agarose hydrogel to fabricate concave microwells (Figure 5.6A.) due to the cell repellent nature of agarose hydrogel (Tanaka, 2016). CMs mixed with pGNW-COOH and pGNW-RGD were loaded into the agarose microwell

array (Figure 5.6A.), and their size were monitored for 7 days of culture. The number of CMs per individual microtissues was selected to be ~1300 to achieve microtissues with 150 μm.

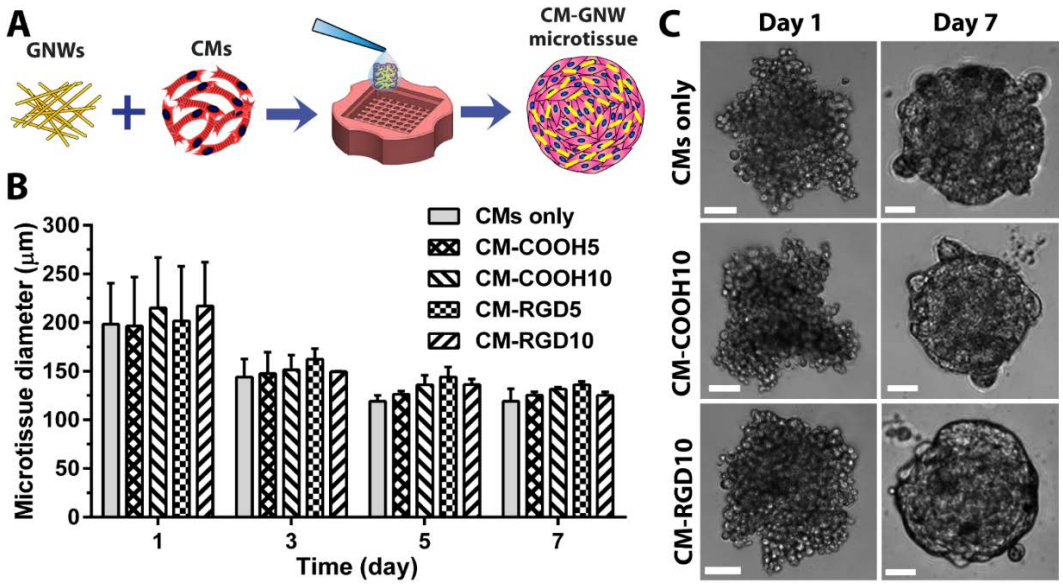

Figure 5.6. A) Schematic illustrating the fabrication procedure of scaffold-free cardiac microtissues embedded with GNWs. B) Size of cardiac microtissues over 7 days of *in vitro* culture. C) Phase-contrast images of cardiac microtissues on day 1 and 7. Scale bars are 20 μm.

Previous studies have demonstrated that cardiac spheroids with similar number of cells can be injected through a standard clinical catheter with minimal damage and higher viability (Emmert, 2013). The size of cardiac microtissues (all conditions) decreased significantly from ~200 μm on day 1 to ~150 μm on day 3 and reached to approximately 120-130 μm on day 7 (Figure 5.6B.). The major size reduction was occurred during the first 3-4 days of culture and the size of microtissues did not significantly decrease afterwards. Furthermore, incorporation of pGNW-COOH and pGNW-RGD did not influence the size of microtissues across culture period. Similar results have been also reported by previously published studies for SiNW-embedded cardiac microtissues (Y Tan, 2017; Y Tan, 2015). Phase-contrast images of microtissues on day 1 and 7 (Figure 5.6C.) demonstrated the transition of CM aggerates with randomly organized on day 1 to spherical cardiac microtissues on day 7.

5.3.4. Effect of GNWs on contractility, electrical excitability, and maturation of scaffold-free microtissues

The contractility and electrical excitability of the cardiac microtissues were assessed by measuring the fractional shortening of beating microtissue and the excitation voltage threshold, respectively. To investigate the impact of GNWs on the electrical excitability of cardiac microtissues, excitation voltage threshold was tested using external electrical field stimulation (Navaei, 2016a; Tandon, 2009). As demonstrated in Figures 5.7A. and 5.7B., no significant differences in the excitation voltage threshold were detected for 1 and 2 Hz frequencies across CMs only, CM-COOH5&10, and CM-RGD5&10 groups on both day 4 and 6 of culture. The excitation thresholds across all microtissues were 7-8 V for 1 and 2 Hz on day 4 and 8-9 V on day 6. This can be attributed to the global propagation of the external electric field stimuli within the microtissues and culture medium in the stimulation chamber. Therefore, investigating the influence of conductive nanomaterials on the electrical excitability and conduction velocity of scaffold-free cardiac microtissues requires other measurement techniques with higher reading precision (i.e. sampling rate) and resolution, such as microelectrode array (Reppel, 2004) or patch clamp (Wilders, 2006).

Contractility of the microtissues was investigated by measuring their fractional shortening (diameter) following the applied electrical stimulation. As it is shown in Figure 5.7C., all groups of microtissues with and without embedded conductive nanomaterials showed 1-1.5% shortening in diameter (both days 4 and 6) after induced contractions compared to their relaxed state. This data indicated that incorporation of GNWs and conjugation of RGD did not improve the contractile functioning of the CMs. The cardiac maturation of microtissues was measured using ICC and WB to investigate the impact of conductive nanomaterials on the expression of contractile proteins (SAC and cTnI) and electrical gap junctions (Cx43). Since, the contractility of microtissues under electrical stimulation (Figure 5.7.) were similar between different concentrations of the GNWs (5 and 10 µg/mL), only the highest concentration (10 µg/mL) was considered for ICC and WB analyses. The immunostained images (Figure 5.8A.) showed well-expression of Cx43 gap

junctions within CMs across all conditions. Additionally, the positive expression of SAC proteins was observed within all types of microtissues. The WB results (Figure 5.8B.) were also in agreement with ICC images, illustrating no statically significant differences in terms of cardiac specific markers across different experimental groups (i.e. pGNW-COOH and pGNW-RGD).

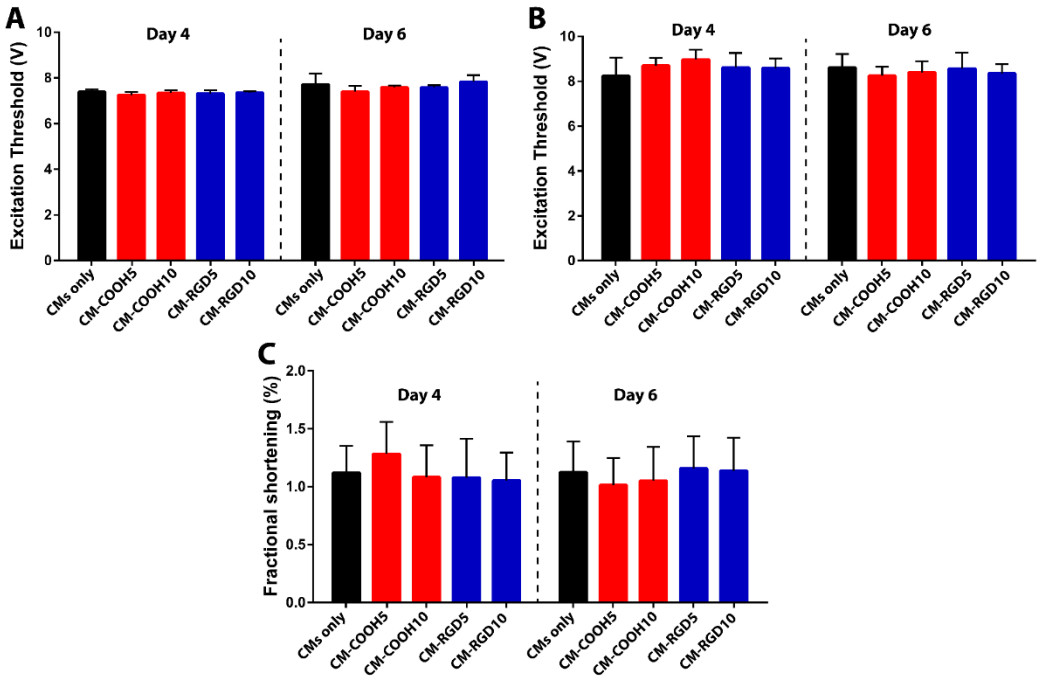

Figure 5.7. A & B) Excitation voltage threshold of the microtissues on day 4 and 6. C) Contraction amplitude measured as fractional shortening of microtissues stimulated by electric field at 1 Hz with 10 V on day 4 and 6.

Similar observations were also reported by Tan (Y Tan, 2017; Y Tan, 2015) for hiPSC-derived cardiac microtissues embedded with electrically conductive SiNWs. They demonstrated that SiNWs did not enhance the contractility of hiPSC-derived cardiac microtissues with similar number of cells (i.e. 1000 per spheroid). Although, it was shown that there was a statistically significant difference between the contraction amplitude of pure (~1.2%) and SiNW-embedded (~1.5%) microtissues, the fold change was also negligible. Notably, the expressions of SAC and Cx43 as well as the formation of sarcomere structures were significantly enhanced with higher number of cells (3000 per spheroid). However, a caveat in generating relatively large-size microtissues (>150 μm) has been demonstrated to be the difficulty in catheter or syringe-based

delivery (Emmert, 2013). Therefore, although electrically conductive nanomaterials have been shown to improve the maturity of hiPSC-derived CMs (Veerman, 2015) through enhancing the expressions of cardiac-specific proteins (SAC, cTnI, and Cx43), however, this scenario was not observed in our work based on the use of primary rat-derived CMs. This highlights the critical influence of cell type along with conductive nanomaterials to establish mature microtissues.

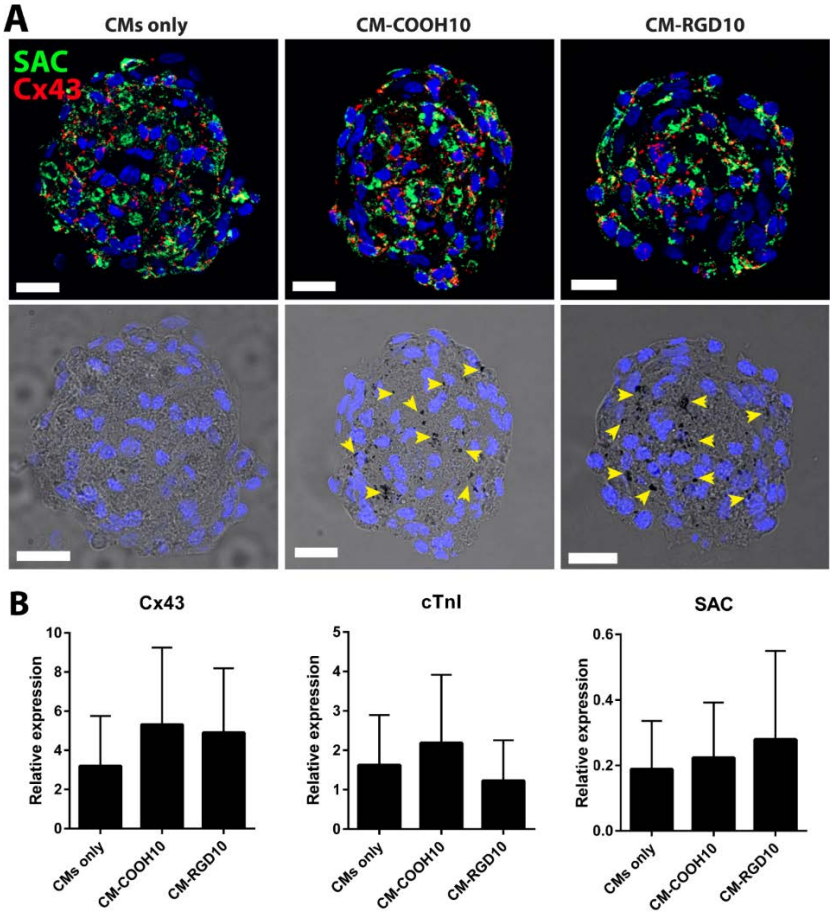

Figure 5.8. A) Immunostaining fluorescent images of SAC (green) and CX43 (red) within CMs only, CM-COOH10 and CM-RGD10 groups on day 7. Yellow arrows locate the embedded GNWs within the microtissue. DAPI represent nuclei. Scale bars are 20 μm. B) Quantified relative protein expression level of SAC, Cx43 and cTnI on day 6.

5.3.5. Electrophysiology of CMs only and GNW-embedded cardiac microtissues

The electrophysiological response of CMs in the presence of electrically conductive GNWs was further assessed using microelectrode array (Graudejus, 2011; Kang, 2014; Yu, 2009), an

aspect that has not been addressed thus far in previous studies. Figure 5.9. demonstrates the representative recorded spontaneous FP signals from 28-electrode sMEA (Figure 5.9A-C.) and measured CV across all conditions (Figure 5.9D. and 5.9E.). The averaged CV (cm/sec) on day 4 was 17.63 for CMs only, 16.92 for CM-COOH5, 17.05 for CM-COOH10, 15.69 for CM-RGD5 and 19.24 for CM-RGD10. There were no significant differences detected across GNW-embedded groups compared to pure CMs culture (i.e. control group). Furthermore, the analyzed results showed statistically similar CV values for both 5 and 10 µg/mL of GNWs. The CV results on day 6 (Figure 5.9E.) were also followed similar trend as day 4. Although the measured CVs for CM-COOH5 (15.91 cm/sec), CM-COOH10 (13.25 cm/sec), CM-RGD5 (16.21 cm/sec) and CM-RGD10 (13.61 cm/sec) were slightly higher than the CMs only (9.14 cm/sec), statistical analysis did not demonstrate any significant differences among them. Our measurements of CVs using the BMSEED platform were consistent with other previously reported values, usually ranging from 18 to 22 cm/sec for rat CMs (N. Bursac, 1999; N. Bursac, 2002; Fast, 1994; Papadaki, 2001; Trantidou, 2015). Although, all the sMEA wells were coated with gelatin prior to cell loading, the robust contractions of CMs led to CMs detachment for longer period of culture beyond 6 days. Electrophysiological assessment of CMs' indicated that, first, incorporation of electrically conductive GNWs (5 and 10 µg/mL) within CMs did not improve cardiac CV neither on day 4 nor 6 of culture. Second, conjugation of RGD, as a cell adhesive peptide, on the PEGylated GNWs (pGNW-RGD) did not also lead to a substantial increase in the CV in comparison with the non-conjugated GNWs (pGNW-COOH).

Cardiac CV is tightly regulated with the expression level and distribution of connexin gap junctions (King, 2013; Rohr, 2004). It has been shown that CMs with non-physiological expressions of connexins demonstrate significantly slow CV (Guerrero, 1997; Kirchhoff, 1998). Therefore, it was possible that the potential impact of the embedded GNWs on enhancing the CV among CMs were neglected due to the well-expression of connexin gap junctions in all experimental conditions (Figure 5.8.). Therefore, we further utilized heptanol to block the connexin gap junctions in CMs (Gizurarson, 2012; Takens-Kwak, 1992; G. Tse, 2016) and further assessed CV across different conditions. Heptanol experiment was performed for CMs only, CM-

COOH10 and CM-RGD10 conditions on day 4 of culture due to similar CV results (Figure 5.9D. and 5.9E.) obtained for the both GNWs concentrations (5 and 10 µg/mL). Since 0.5 mM did not induce any reduction in the CV and 4 mM rapidly ceased the spontaneous contractions of CMs (data not shown). Therefore, 1 and 2 mM heptanol concentrations were selected for the experiment.

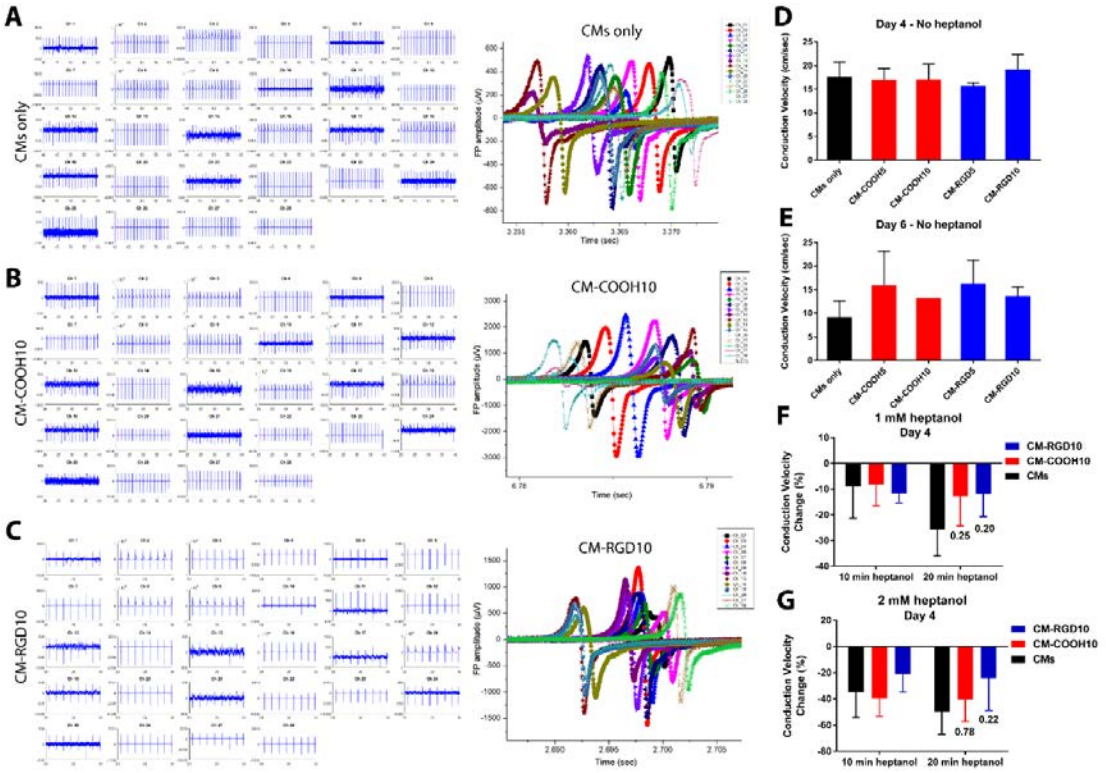

Figure 5.9. The representative FP signals recorded using 28-electrode sMEA for A) CMs only, B) CM-COOH10 and C) CM-RGD10 on day 4 of culture. D & E) Conduction velocity of CMs monolayer cultured with and without pGNW-COOH and pGNW-RGD on day 4 and 6 of culture. F & G) The percentage of conduction velocity reduction due to the addition of gap junction blocker (heptanol) after 10 and 20 min on day 4 of culture. The numbers on the bar graphs are p values for CM-COOH10 and CM-RGD10 with respect to CMs only.

Figures 5.9F. and 5.9G. demonstrate the percent of reduction in CV after addition of 1 and 2 mM heptanol for all groups. CV was decreased as a function of exposure time and concentration of heptanol. Specifically, the average reduction of CV of across all groups was 2-4

fold higher for 2 mM heptanol (~32% after 10 min and ~38% after 20 min) compared to 1 mM concentration (~9% after 10 min and ~16% after 20 min). These observations are consistent with the previously published studies (Gizurarson, 2012; Keevil, 2000; Gary Tse, 2012). In the case of GNW-embedded samples, similar levels of CV reduction were measured for 1 mM (CMs only 9%, CM-COOH10 8% and CM-RGD10 11%) and 2 mM (CMs only 35%, CM-COOH10 40% and CM-RGD10 21%) heptanol after 10 min. Furthermore, CV reductions after 20 min heptanol exposure appeared to be lower for CM-COOH10 (12% for 1 mM and 40% for 2 mM) and CM-RGD10 (12% for 1 mM and 24% for 2 mM) groups compared to CMs only (25% for 1 mM and 50% for 2 mM). However, statistical analysis did not show any significant differences (Figure 5.9F. and 5.9G.).

The electrophysiology investigation in this study was mainly focused on the potential impact of conductive GNWs on enhancing the velocity of action potential propagation (CV) among CMs. It was rationalized that the GNWs can be localized within the intercellular microenvironment to enhance the propagation of electrical signal within CMs. However, our findings did not show any substantial improvement regarding CV in both coupled and uncoupled connexin conditions. On the other hand, it has been theoretically demonstrated that electrical charges induced by the action potentials, generated by a group of CMs, can be transmitted through conductive nanomaterials to remote CMs (physically separated), resulting in the membrane depolarization (Y Wu, 2018). However, the effective signal transmission through conductive nanomaterials between two groups of CMs depends on several factors, including number of cells, surface roughness, nanomaterials conductivity, etc. The attachment strength of CMs' membrane to the conductive nanomaterials (i.e. sealing resistance) has been shown to play a key role in transmission of electrical signal between cells. In this regard, an effective electrical current transmission within CMs only occurs in case of firm cell-nanomaterial attachment conditions (sealing resistance of 10^{14} Ω/sqr) (Y Wu, 2018). Therefore, the location of conductive nanomaterials in respect to the CM's plasma membrane can dictate the ultimate electrical enhancing outcomes (e.g. CV). In our study, it is speculated that the incorporated GNWs were internalized by CMs and did not locate on the cell membrane or extracellular microenvironment, which further led to no significant enhancement of CV in presence of GNWs.

5.4. Conclusion

In this study, electrically conductive cardiac microtissues embedded with functionalized GNWs were developed to address the current limitation of cell-based therapies for treatment of MI. The ultralong CTAB-capped GNWs with aspect ratio of ~46 were synthesized and then the CTAB coating bilayer was exchanged using a 2-step ethanol assisted procedure with SH-PEG-COOH to maximize the biocompatibility of the nanomaterials. PEGylated GNWs were further functionalized with RGD sequence to promote their adhesion affinity to the cells. DLS measurements and Raman spectroscopy results confirmed successful CTAB-PEG exchange as well as the conjugation of RGD on GNWs. Live/Dead fluorescent images and Alamar Blue results demonstrated a significant increase in biocompatibility of GNWs by removing CTAB. The developed GNW-embedded cardiac microtissues were further tested for contraction amplitude, electrical excitability, cardiac-specific protein expression and conduction velocity. Our finding indicated that incorporation of electrically conductive GNWs did not lead to higher fractional shortening and lower excitation voltage threshold of CM microtissues. In addition, ICC and WB characterizations revealed similar expression levels of cardiac markers (SAC, Cx43, and cTnI) for both pure CM and CM-GNW microtissues. Lastly, the electrophysiology of CMs was assessed using microelectrode array. The analyzed data demonstrated that the incorporation of electrically conductive GNWs did not improve the conduction velocity of action potential among CMs. Also, the percentage of conduction velocity reduction in both CM and CM-GNW microtissues were similar in presence of gap junction uncoupler (heptanol), indicating that incorporation of electrically conductive nanomaterials did maintain the conduction velocity. Despite the promising results on cardiac maturation and enhanced contraction amplitude of hiPSC-derived CMs induced by other (rGONFs and SiNWs) conductive nanomaterials (Park, 2015; Y Tan, 2017), we did not observe similar outcomes using GNWs and NRVCMs. It is speculated that the inducing cardiac maturation using conductive nanomaterials can be a cell-dependent process. In addition, it is possible that the GNWs were internalized by NRVCMs and did not locate on the cell membrane or extracellular microenvironment, which further led to no significant enhancement of CV among CMs.

CHAPTER 6

PNIPAAM-BASED BIOHYBRID INJECTABLE HYDROGEL FOR CARDIAC TISSUE ENGINEERING

6.1. Introduction

Bioengineered injectable hydrogels enhance the efficacy of conventional cell-based transplantation for treatment of myocardial infarction (H Wang, 2010). Despite the minimally invasive nature of cell-based therapy, this strategy often suffers from low cell retention and lack of integration with the native myocardium (Leor, 2000; Müller-Ehmsen, 2002; Reinecke, 2002a). Encapsulating exogenous cells within hydrogel-based matrices generates an ideal microenvironment for growth and retention of transplanted cells localized to the infarct region (Karen L. Christman, 2006; Lu, 2008; Zimmermann, 2009). Although there have been significant advances in the development of these technologies, current injectable cell delivery hydrogels do not easily allow accessible tuning of mechanical robustness (Ifkovits, 2010) and cell binding motifs (S. Fernandes, 2012; Giraud, 2012). To date, numerous studies have utilized different natural and synthetic biomaterials for the delivery of cells into the infarct region (Cutts, 2015; Hasan, 2015; H Wang, 2010). Naturally-derived materials provide bioactive sites that enable cell adhesion and migration, as well as eventual degradation of the scaffold (Nicodemus, 2008; Singelyn, 2011; H Tan, 2010). Fibrin, a blood component, has been used in pioneer studies as a matrix to induce angiogenesis, preserve cardiac function, and reduce infarct region expansion (K. L. Christman, 2004a; Karen L. Christman, 2004b; Ryu, 2005). Collagen, an ECM protein that has abundant cell-binding motifs, has also been widely used to support cell delivery and survival, retention, infiltration, and myocardium remodeling (Dai, 2009; Kutschka, 2006; Suuronen, 2006). Matrigel (Kofidis, 2004), chitosan (Lü, 2009; Lu, 2008), gelatin (Annabi, 2013; Kharaziha, 2013; Nakajima, 2015), alginate (Ceccaldi, 2012), and ECM-derived matrices (Seif-Naraghi, 2013; M. Shevach, 2015) are among other alternatives that have been used as suitable scaffolding biomaterial for myocardial regeneration and repair. Although natural based biomaterials promote sufficient cell-matrix interactions, they often suffer from batch-to-batch variability, high

immunogenicity, and low tunability of ligand density and mechanical properties (Little, 2008; Romano, 2011). On the other hand, synthetic biomaterials, such as self-assembling peptides (SAP) (Davis, 2005), poly(lactic acid) and poly(glycolic acid) (C-C Huang, 2012a), PNIPAAm (Cai, 2015; X Li, 2014; T Wang, 2009), and PEG-based copolymers (X-J Jiang, 2009) enable precise control of mechanical and chemical properties with added benefits of industrial-scale production. However, the structure of synthetic biomaterials should be further tailored to incorporate sufficient cell binding motifs. In this regard, a mixture of a synthetic based matrix and a natural hydrogel offers unique beneficial aspects for tissue engineering applications and specifically cardiac regeneration.

We aim to develop a suitable biohybrid injectable hydrogel for cardiac tissue engineering through combining a naturally-derived biopolymer with a tunable synthetic polymer. In particular, the proposed hydrogel matrix (Figure 6.1.) comprised of a thiol-modified gelatin (Gel-S) component to offer a desirable ECM-like bioactive scaffold with adequate cell binding motifs (Heffernan, 2015; Nakajima, 2015). The synthetic component was a PNIPAAm-based copolymer composing of Jeffamine® M-1000 acrylamide (JAAm) and HEMA (Heffernan, 2016). PNIPAAm forms a thermosensitive injectable hydrogel (Schild, 1992), and JAAm increases the gel state equilibrium water content (Overstreet, 2013a; Overstreet, 2013b) to enhance nutrition and gas exchange (Annabi, 2010). After free radical polymerization of PNIPAAm, JAAm, and HEMA, the acrylation of HEMA component (Heffernan, 2016) resulted in the combination of the natural and synthetic components (PNJ-Gelatin), PNIPAAm-JAAm-HEMA (PNJHAc) and Gel-S. Prior to biological studies, the two components were mixed to initiate chemical crosslinking by Michael type reaction (Elbert, 2001). Subsequently, the increase in the temperature induced a physical crosslinking of the hydrogel due to the thermosensitive nature of PNIPAAm (Schild, 1992). The synthesized biohybrid hydrogel ultimately featured dual chemical and thermal crosslinkability, mechanical tunability, and suitable bioactivity.

So far, most of the studies utilizing hydrogel-based matrices for cardiac tissue engineering encompass few in vitro analyses with mono-culture of CMs before in vivo assessments (Cai,

2015; Karen L. Christman, 2004b; Dai, 2009; C-C Huang, 2012a; Ifkovits, 2010; Kutschka, 2006; Lu, 2008; Nakajima, 2015; T Wang, 2009). Although these studies have generated significant *in vivo* findings on the regeneration of infarcted region, we believe that there should be expanded *in vitro* investigations with co-culture of CMs and CFs to comprehensively analyze the performance of the cell-embedded hydrogel matrix prior to *in vivo* studies. Specifically, due to the abundance of resident CFs within the infarct region, it is crucial to find out whether the synthesized hydrogel is capable of accommodating CFs, and what is the subsequent role of infiltrated CFs on the overall functionalities of the formed 3D tissue (Souders, 2009). Therefore, we performed extensive *in vitro* mono- and co-culture studies comprising of cell survival, cytoskeleton and cardiac-specific markers organization, gene expression, as well as tissue-level beating behavior. We hypothesize that the synthesized PNJ-Gelatin biohybrid hydrogel provides a suitable microenvironment to support the functionalities of cardiac cells, ultimately leading to enhanced repair and regeneration of injured myocardium.

6.2. Experimental Methods

6.2.1. Materials

3,3′ Dithiopropionic acid (DTPA), HPLC grade tetrahydrofuran (THF), anhydrous methanol, anhydrous ethanol, acetone, HEMA, 2,2′-Azobisisobutyronitrile (AIBN), acryloyl chloride, hydrazine hydrate (HH), hexane, concentrated sulfuric acid, ethyl ether, 1 N hydrochloric acid (HCl), 1 N sodium hydroxide (NaOH), sodium chloride (NaCl) gelatin type A from porcine skin, EDC, and 5,5′-dithiobis-2-nitrobenzoic acid (Ellman's reagent) were purchased from Sigma Aldrich (St. Louis, MO, USA). Dithiothreitol (DTT) was purchased from Gold Biotechnology (St. Louis, MO, USA). NIPAAm was obtained from Tokyo Chemical Industry Co. (Portland, OR, USA). Jeffamine® M-1000 was gifted by Huntsman Corporation (Salt Lake City, UT, USA).

6.2.2. Polymer synthesis

NIPAAm monomer was recrystallized from hexane, and AIBN initiator was recrystallized from methanol. Jeffamine® M-1000 acrylamide (JAAm) was synthesized in a reaction with Jeffamine® M-1000 and acryloyl chloride (Heffernan, 2016; Overstreet, 2013a). Poly(NIPAAm-co-

JAAm-co-HEMA), or PNJH was synthesized by free radical polymerization. Briefly, NIPAAm (7.5 g), JAAm (2 g), and HEMA (0.5 g) monomers were co-dissolved in THF, heated to 65 °C, and the reaction was initiated with AIBN (83 mg). After 18 h, the PNJH product was re-dissolved in acetone, precipitated in cold ethyl ether, filtered, and vacuum dried. Poly(NIPAAm-co-JAAm-co-HEMA-acrylate), or PNJHAc, was synthesized by converting hydroxyl groups on the HEMA monomer to reactive acrylates, previously reported by Heffernan et al. (Heffernan, 2015; BH Lee, 2006). Briefly, PNJH was dried overnight at 60 °C under vacuum and then dissolved at 10 wt% in THF with TEA (2.11 mL). The reaction was initiated by adding acryloyl chloride (1.21 mL) dropwise to the stirring solution while on ice. The product was precipitated in cold ether, filtered, and vacuum dried. PNJHAc was further purified by dialysis against diH2O (3500 MWCO) for 3 days. The lyophilized polymer was stored at −20 °C. Dithiopropionic dihydrazide (DTPH) was prepared from DTPA using an established procedure (Vercruysse, 1997). Thiolated gelatin (Gel-S) was synthesized from gelatin and DTPH using EDC chemistry based on previously reported studies (Heffernan, 2015; Shu, 2003). To confirm the syntheses, proton nuclear magnetic resonance (^{1}H NMR) spectra were recorded for PNJHAc and Gel-S with D_2O as the solvent (400 MHz Varian liquid state NMR, Agilent Technologies, Santa Clara, CA, USA), while Ellman's reagent test was used to measure the degree of thiolation (Ellman, 1959).

6.2.3. Preparation and physical characterization of the hydrogel matrix

To prepare the hydrogel samples for physical characterization, PNJHAc was dissolved (57.1 mg/mL) in DPBS. Subsequently, 40 mg/mL Gel-S in acidic DPBS (pH 3) was prepared at 37 °C for 5 min. The Gel-S solution was titrated with NaOH to increase the pH to 7, and then the two solutions were mixed to form the final product. SEM (XL30 ESEM-FEG, USA) was utilized to evaluate the macroporous structure of the biohybrid hydrogels. Freshly made and hydrated (24 h at 37 °C in DPBS) samples were frozen in liquid nitrogen followed by lyophilization. Ten SEM images were acquired to analyze the porosity and pore size distribution of the hydrogel constructs using NIH ImageJ software. Briefly, the images were thresholded and the void area was calculated. In addition, pore size was quantified using the line tool. To evaluate swelling behavior

of the PNJ-Gelatin biohybrid, hydrogel constructs were prepared and immediately soaked in vials of 5 mL DPBS and relocated at 37 °C for 48 h. The swollen hydrogels were removed at different time points and weighed. The swelling ratio defined as below (Equation 6.1.):

$$Swelling\ ratio = \frac{M_{wet} - M_{dry}}{M_{wet}} \quad (1)$$

where, M_{wet} is the mass of hydrated hydrogel and M_{dry} is the mass of fresh hydrogel. Three identical samples were selected for each time point. Rheology was completed to quantify the viscoelastic characteristics of the temperature responsive polymer during both chemical (Michael-addition induced) and physical (temperature induced) crosslinking. Rheology solutions were prepared by separately dissolving PNJHAc (57.1 mg/mL) and Gel-S (40 mg/mL) in pH 3 DPBS. The solutions were then combined, titrated to ~pH 7 with 1 N NaOH, vortex mixed for 15 s, and positioned on a parallel plate rheometer (Anton Paar MCR-101). The storage and loss modulus in the solution and gel states were evaluated by a multistep temperature-controlled procedure. In the first step, a time sweep was performed for 4 h at 25 °C to measure the gelation of PNJHAc and Gel-S. Next, the sample was subjected to controlled (0.5 °C/min) and sustained heating (37 °C for 1 h) followed by quick cooling back to room temperature (25 °C for 1 h) to measure the reversible physical crosslinking of the PNJ-Gelatin hydrogel. To simulate the biophysical cues that cultured cardiac cells sense during the preparation and the first 12 h of culture, we performed a separate rheology measurement at 25 °C for 15 min (the sample preparation time) followed by immediate temperature increase to 37 °C for 12 h. In all experiments, an oscillatory 0.5% shear strain deformation was performed a frequency of 1 Hz, and normal force control was utilized to maintain constant contact between the gel and rotating head. The LCST of PNJ-Gelatin following enzymatic digestion with collagenase was evaluated by cloud point measurement. PNJ-Gelatin was dissolved at 0.1 wt% in PBS at pH 7.4 in cuvettes and heated in a water bath from 25 to 37 °C in 1 °C increments and 40-75 °C in 5 °C increments. Samples were maintained at each temperature for at least 120 s before each measurement. Absorbance at 450 nm was recorded with a UV/Vis spectrometer (Pharmacia Biotech Ultrospec 3000). The LCST, which is defined as the temperature at 50% of the maximum absorbance, was then collected. To assess hydrolytic

degradation, hydrogel constructs were prepared and immediately placed in vials of 5 mL DPBS at 37 °C. At different time points, constructs were immersed in liquid nitrogen, followed by lyophilization. Remaining mass percentage was defined as the lyophilized mass to the original one. Three identical samples were selected for each time point.

6.2.4. Cell harvesting and culture

NRVCMs were isolated from 2-day old pups according to the previously established protocol (Saini, 2015) accepted by the Institution of Animal Care at Arizona State University. The isolated cardiac cells were separated into CMs and CFs by pre-plating the cell suspension for 1 h and allowing CFs to attach to the tissue culture flask, due to their higher adhesive nature compared to CMs (Saini, 2015; SR Shin, 2013). After 1 h, the harvested media, mainly containing CMs, was collected and used for further experimentation. We precisely isolated the ventricular tissue to minimize the presence of endothelial or smooth muscle cells, from the aorta region of the heart, within the isolated CMs population. However, the isolated CMs may still contain a few numbers of endothelial cells due to the presence of capillaries within the myocardial tissue. CMs and CFs were cultured in cardiac media containing DMEM (Gibco, USA), 10% FBS (Gibco, USA), L-Glutamine (1%) (Gibco, USA), and 100 units/mL of penicillin-streptomycin. Isolated cardiac cells were cultured under a static condition (no external electrical stimulation) and the cell culture media was changed every other day.

6.2.5. Preparation of the biohybrid cell-laden hydrogel

To prepare the cell-laden injectable PNJ-Gelatin biohybrid hydrogel, CMs (mono-culture condition) or a 2:1 ratio of CMs-CFs (co-culture condition) were dispersed (35×10^6 cells/mL) in a solution of supplemented cardiac media containing 30% FBS and PNJHAc (57.1 mg/mL). Next, a 7.5 µL drop of cardiac cell suspension was placed on top of a sterile 18×18 mm^2 glass slide. Subsequently, a 7.5 µL Gel-S in cardiac media prepared at 40 mg/mL was mixed with the cell suspension with a final cell number of 525,000 CMs in mono-culture and 350,000 CMs and 175,000 CFs in co-culture conditions (Figure 6.1.). The prepared samples were chemically crosslinked in a 24-well plate at room temperature (25 °C) for 10 min followed by the addition of

0.5 mL of warmed cardiac media (37 °C) to initiate the physical crosslinking. The well plates were placed in humidified cell culture incubator (37 °C and 5% CO2) and subsequently cultured for a period of 9 days.

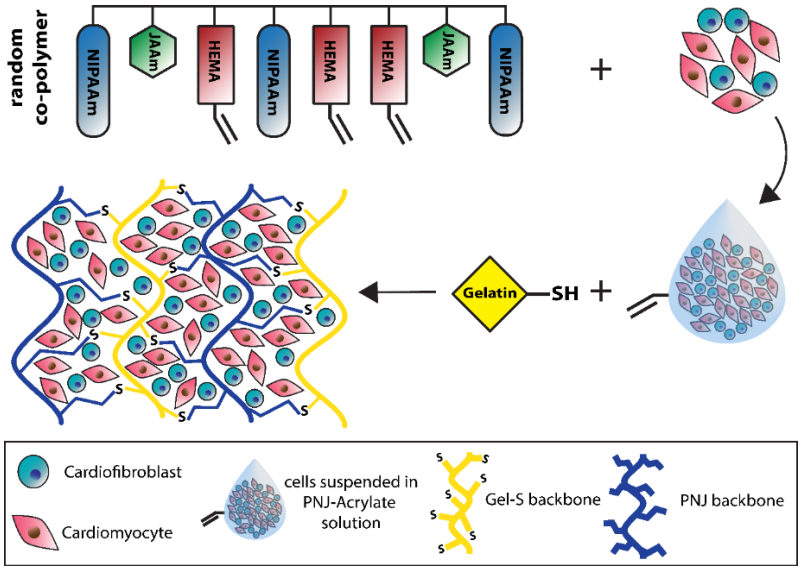

Figure 6.1. The schematic displaying the fabrication procedure of the proposed injectable PNJ-Gelatin hydrogel with encapsulated CMs and CFs.

6.2.6. Cell viability assay

The survival of encapsulated cells within the PNJ-Gelatin hydrogel was evaluated on day 1 and 7 of culture, using a Live/Dead assay kit (Life technologies, USA). Briefly, three individual samples of biohybrid hydrogels were selected for each type of culture (mono- and co-culture) and Z-stack fluorescent images were acquired using an inverted microscope (Observer Z1, Zeiss, Germany) equipped with ApoTome.2 (Zeiss, Germany). The viability percentage was defined as number of viable cultured cardiac cells (green) divided by total number of cells.

6.2.7. F-actin staining and Fast Fourier Transform (FFT) analysis

F-actin fibers were stained to visualize the cytoskeleton organization of cultured cells within the PNJ-Gelatin hydrogel in both mono- and co-culture groups on day 7 of culture. First, the cells were fixed in 4% PF for 30 min. Next, 1% (v/v) Triton x-100 was used to permeabilize the plasma membrane of the cells for 45 min at 25 °C. Afterwards, the fixed cells were blocked in 1% (v/v)

BSA (Sigma Aldrich, USA) for 1 h at 4 °C. Finally, the cells were stained with Alexa Fluor-488 phalloidin (1:40 dilution in 1% BSA, Life technologies, USA) for 1 h and counterstained with DAPI (1:1000 dilution) for 30 min. A fluorescent microscope equipped with ApoTome.2 was utilized to take Z-stack fluorescent images through the samples. FFT images were further obtained and analyzed by means of ImageJ software (NIH) to assess the local organization of the F-actin fibers. To analyze the actin coverage area, the collected regions of interests, (ROIs) (300 × 300 μm^2), were quantified using NIH ImageJ software (n > 10).

6.2.8. Immunostaining of cardiac specific-markers

To investigate the phenotype of cultured cardiac cells (on day 7 of culture), immunostaining method was utilized according to previously developed protocols (Kharaziha, 2013). Briefly, cells were fixed in 4% PF for 40 min followed by treatment with 0.1% Triton x-100 for 45 min at room temperature. Next, the cardiac cells were blocked in 10% goat serum for 2 h at 4 °C. Afterwards, the fixed cells were stained with primary antibodies against SAC, Cx43 (Abcam, USA) and cTnI (Developmental Studies Hybridoma Bank) (1:100 dilution in 10% goat serum) and placed in cold room (4 °C) for 24 h. After the primary staining, samples were washed five time with DPBS (5 min intervals) and stained overnight with secondary antibodies (Life Technologies, USA) comprised of Alexa Fluor-488 for SAC and cTnI, and Alexa Fluor-594 for Cx43 (1:200 dilution in 10% goat serum). Next, cells were stained with DAPI (1:1000 dilution in DPBS) for 30 min to label the nuclei. Finally, the stained samples were mounted and imaged (20× and 40×) using a ZEISS fluorescent microscope equipped with ApoTome.2. The average coverage area (n > 12) for cardiac-specific proteins was assessed similar to F-actin coverage analysis using NIH ImageJ software.

6.2.9. Quantitative polymerase chain reaction (QPCR)

QPCR technique was used to evaluate the expression of certain cardiac specific genes (CTNT, CX43, ACTN1, and MLC2v) for both culture groups. Samples were selected at two considered time points (day 1 and 7 of culture encapsulated within the PNJ-Gelatin hydrogel). For cell-laden matrices, the hydrogels were immersed in collagenase (Worthington Biochemical

Corp., USA) solution (1 mg/mL) for 1 h at 37 °C to collect the encapsulated cardiac cells. After degradation of the hydrogel, the cell suspension was centrifuged at 1000 rpm for 5 min and the resulting supernatant was discarded. In the case of freshly isolated cells, the cell suspension was centrifuged at 1000 rpm for 5 min. RNA was isolated from cells using the NucleoSpin® RNA Kit (Clontech). Reverse transcription was performed with iScript Reverse Transcription Supermix for RT (BioRad). Quantitative PCR was carried out using TaqMan® Assays or SYBR® green dye on a BioRad CFX384 Touch™ Real-Time PCR Detection System. For the QPCR experiments run with TaqMan® Assays, a 10 min gradient to 95 °C followed by 40 cycles at 95 °C for 5 s and 60 °C for 30 s min was used. For QPCR experiments run with SYBR® green dye, a 2 min gradient to 95 °C followed by 40 cycles at 95 °C for 15 s and 60 °C for 1 min was used. Gene expression (Appendix Table B.1.) was normalized to 18S rRNA levels. ΔC_t values were measured as $C_t^{target} - C_t^{18s}$. All experiments were accomplished with two technical replicates and three biological replicates. Relative fold changes in gene expression were quantified using previously established technique (VanGuilder, 2008). Data were presented as the average of the biological replicates ± standard error of the mean (SEM).

6.2.10. Evaluation of spontaneous tissue-level contraction

The spontaneous beating of CMs was monitored and measured every day during the culture period (9 days) using real-time optical microscopy. After detection of synchronous tissue-level (2.5 × 2.5 mm^2) beating, videos (n > 12) were captured by using an inverted microscope equipped with an AxioCam MRm camera (Zeiss, Germany). Furthermore, representative beating signals were acquired using a custom written MATLAB code (SR Shin, 2013). The amplitude and frequency variation indexes were calculated based on an original procedure developed by the authors. In detail, the collected beating signals of subsets (n = 5, 0.5 × 0.5 mm^2) for each sample (n = 4, 2.5 × 2.5 mm^2) were processed using MATLAB software to find the significant peaks. A significant peak was defined as below (Equation 6.2.):

$$Significant\ peaks \geq ((|Amp_{Median} - Amp_{Mean}|) + Amp_{Mean}) \quad (2)$$

where Amp_{Median} and Amp_{Mean} were the median and mean amplitudes respectively. Next, the collected significant peaks (n > 500) were normalized based on their average. The absolute difference between the normalized values and 1 was calculated to obtain the amplitude variation index. In the case of the frequency variation index, the related time for each significant peak was acquired and peak-to-peak time differences were calculated. Subsequently, the time differences were normalized to their average and the absolute difference between the normalized values and 1 was considered as the frequency variation index. Finally, the calculated indexes (n > 20) were compared between mono- and co-culture groups.

6.2.11. External electrical stimulation

The response of the encapsulated cells (CMs and CFs), within the PNJ-Gelatin hydrogels, to external electrical stimulation was evaluated based on previously established protocol (Tandon, 2009). Briefly, a custom-made chamber was assembled using two carbon electrodes (5 mm) with 1 cm spacing attached to a plastic petri dish (6 mm diameter) by silicon adhesive (Appendix Figure B.3A.). Platinum wires were connected to the carbon electrodes (at the opposite ends of each electrode) and all connections were sealed using silicon adhesive. The entire chamber was washed with ethanol (70%) and put under UV light for 1 h for sterilization. To assess cardiac cells' response to the external electrical stimulation, pulsatile electrical signals (BK PRECISION 4052) with 3 ms duration at three different frequencies (1, 2, and 3 Hz) was applied in both mono- and co-culture conditions. The minimum required voltage to obtain contraction of CMs was defined as the excitation threshold.

6.2.12. Statistical analysis

The data was analyzed using t-test and ANOVA statistical methods. The results for viability, cytoskeleton, and cardiac specific markers coverage areas were reported as mean ± standard deviation (SD). To determine a statistically significance difference between the groups, we used Tukey's multiple comparison test, with a p-value < 0.05 considered to be significant. All the statistical analyses were performed by GraphPad Prism software (v.6, GraphPad San Diego).

6.3. Results

6.3.1. Preparation and characterization of PNJ-Gelatin hydrogel

The PNJ-Gelatin hydrogel was obtained by mixing PNJHAc and Gel-S prepolymer solutions at room temperature, which resulted in an orange solution followed by forming a soft gel after 120 s. Figure 6.2A. shows the viscoelastic characteristics of the hydrogel during the chemical crosslinking between PNJHAc and Gel-S. As can be seen in the graph, the storage modulus (G′) increased over time and leveled out at approximately 4 h, indicating completion of chemical crosslinking. There was a sharp increase in G′ (870 Pa) within the first hour of crosslinking, followed by a gradual increase to 1260 Pa up until 4 h. Furthermore, the hydrogel mainly exhibited elastic-behavior due to the negligible loss modulus (G″, 19 Pa after 4 h). To further investigate the impact of the thermosensitivity of the NIPAAm component, the dynamic modulus was measured during a temperature ramp from 25 °C to 37 °C. As shown in Figure 6.2B., the rise in temperature induced an increase in the dynamic modulus of the PNJ-Gelatin hydrogel from 1260 to 2450 Pa, which indicated the occurrence of physical crosslinking. The dual-crosslinking (chemical and physical) nature of the biohybrid hydrogel was confirmed by dropping the temperature to 25 °C (Fig. 2C), which resulted in the same storage modulus (4 h) shown in Figure 6.2A. Furthermore, the simulated rheology measurement (Figure 6.2D.) revealed that the cultured cells initially experienced a slight increase in the modulus up to 90 Pa within the first 15 min. Upon temperature increase occurring from the placement of the hydrogel samples in the incubator, the modulus increased as expected due to the crosslinking of PNIPAAm. To investigate the fate of the LCST after degradation of the gelatin, the PNJ-Gelatin hydrogel was degraded utilizing collagenase and cloud point measurements were taken of the degraded PNJ-Gelatin. The results indicated that LCST was 55 °C (Appendix Figure B.1.) after enzymatic degradation, which is a temperature outside of physiological range. Therefore, it could be possible to utilize this degradation mechanism similar to previously developed degradable PNIPAM-based hydrogels (Zhanwu Cui, 2007).

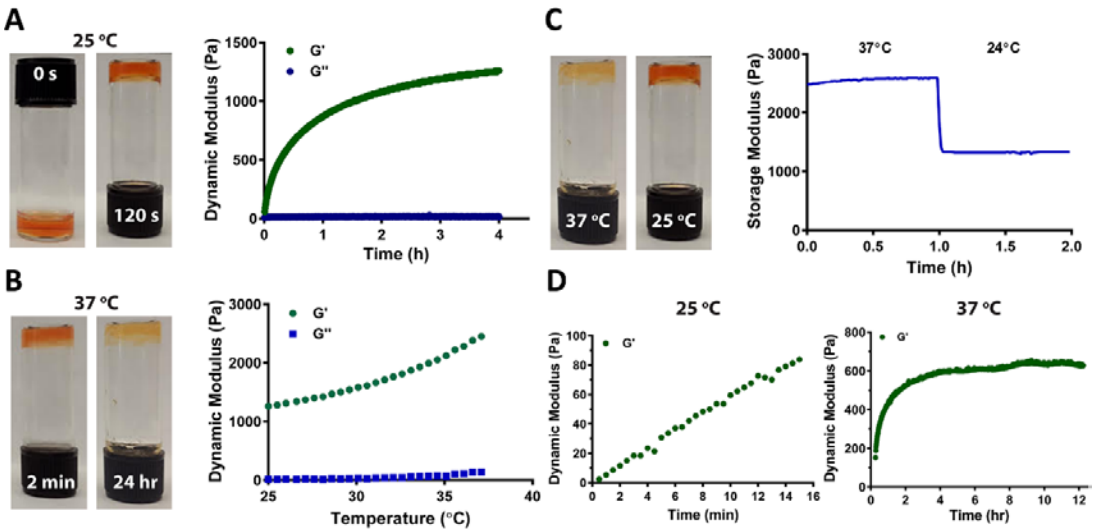

Figure 6.2. The viscoelastic behavior of PNJ-Gelatin hydrogel solutions at (A) room temperature (25 °C for 4 h), followed by measuring during controlled (0.5 °C/min) and (B) sustained heating (37 °C for 1 h), and finally during (C) rapid cooling back to room temperature (25 °C for 1 h). (D) Changes in storage modulus of the PNJ-Gelatin hybrid hydrogel according to the temperature increase from 25 °C (preparation temperature) to 37 °C (incubation temperature). G′: storage modulus, G″: loss modulus.

Figure 6.3A. illustrates the level of water content within the hydrogel constructs. Initially, the hydrogels swelled to 1.2 times their initial mass. After 48 h, hydration decreased to a stable level of 80%. Moreover, to investigate the macroporous architecture of the PNJ-Gelatin constructs, samples were characterized by SEM before and after hydration (24 h). Figure 6.3B. displays the hydrogel porosity percentage as an indicator of void spaces within the constructs. As can be seen, the porosity percentage slightly increased after hydration from 71.1% ± 1.5 to 75.6% ± 2.4. Furthermore, based on the SEM images (Figure 6.3C. and 6.3D.), the macroporous structures appeared to collapse and disorganize before hydration; however, once hydrated, morphology of the pores became more open, intact, and organized. These findings indicated that the absorbed water penetrated throughout the construct and inflated the pores. It was speculated that the average pore diameter would increase due to the higher hydration content, however no differences were observed (data not shown). Instead, the pore size distribution range expanded after hydration while maintaining the same average pore diameter (Figure 6.3E.).

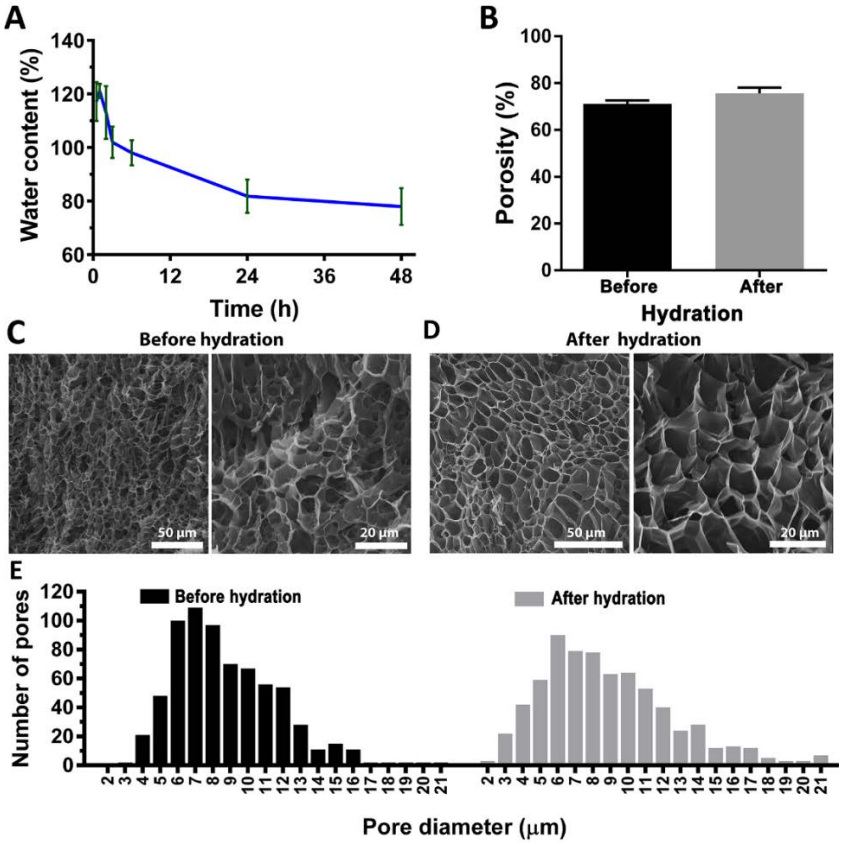

Figure 6.3. (A) The change in water content level (%) of the hydrogel during 48 h of hydration. (B) The percent of porosity, (C) and (D) Low and high magnification SEM micrographs showing macroporous architecture, and (E) pore size distribution of lyophilized hydrogel before and after hydration (24 h).

6.3.2. 3D cell culture and survival

To demonstrate the capability of the PNJ-Gelatin hydrogel as a 3D microenvironment promoting cardiac cell adhesion, spreading, and survival, we encapsulated CMs (mono-culture) and a 2:1 ratio of CMs-CFs (co-culture) within the hydrogel matrix for a period of 9 days. We selected this ratio of CMs to CFs based on our recent study where we found the best viability, cell spreading and tissue-level functionalities (Saini, 2015). Z-stack images (Figure 6.4A.) confirmed successful fabrication of a homogenous 3D (150 µm thick) construct. Figure 6.4B. illustrates the changes in cell morphology as a function of time regardless of culture type. Phase contrast and fluorescent images were used to highlight the cell morphology (Figure 6.4B.) as well as cell

viability (Figure 6.4C.). Both cell types encapsulated within the hydrogel matrix adopted a round morphology on day 1 of culture (Figure 6.4B.).

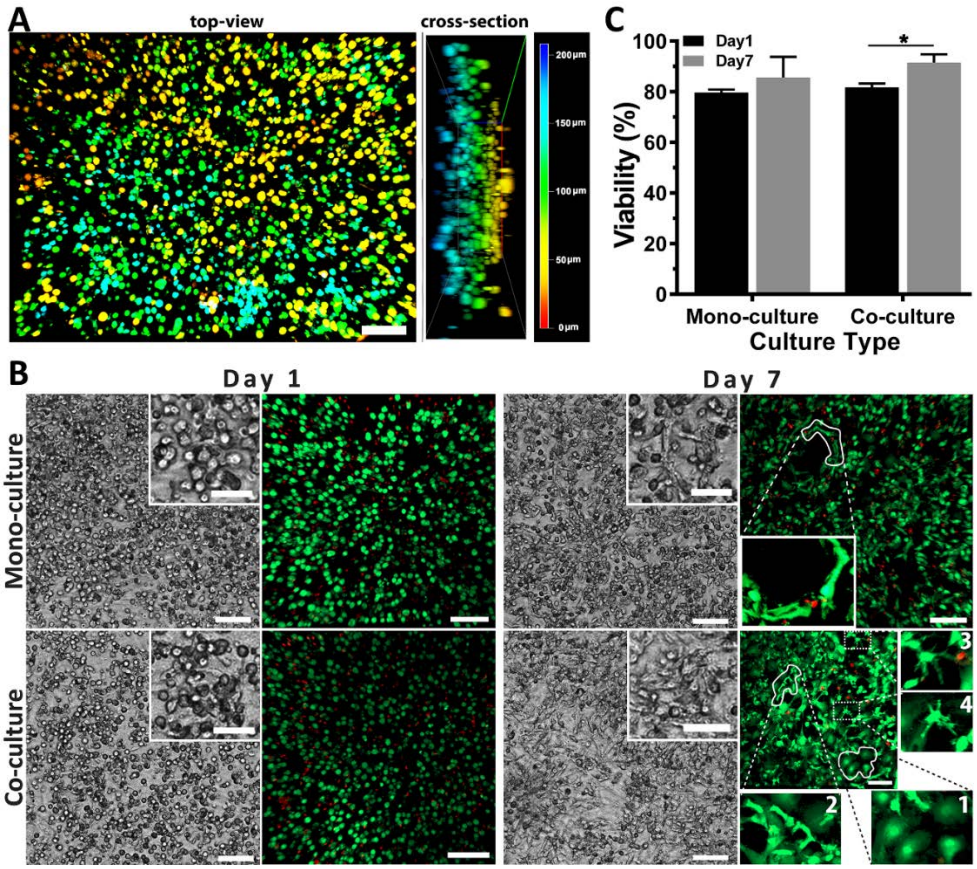

Figure 6.4. (A) The depth coding image (scale bar is 100 µm) of encapsulated cardiac cells within PNJ-Gelatin hydrogel (top-view & cross-section) (day 1). (B) The phase-contrast (scale bars are 100 µm) and fluorescent images (green (live) and red (dead)) of mono- and co-culture groups illustrating cell morphology at days 1 and 7 of culture. Insets on phase-contrast (scale bars are 50 µm) and stained images show the magnified images (inset #1 and 2 show CFs and CMs respectively; inset #3 and 4 display small protrusions in CMs). (C) Quantified viability (%) of both mono- and co-cultured groups at days 1 and 7. (n = 3; *p < 0.05).

The synthesized matrix supported the gradual spreading of both cells in the two culture conditions as a function of time. However, on day 4, the co-culture group demonstrated a higher number of elongated cardiac cells, whereas mono-culture mostly exhibited cells with round morphology (Appendix Figure B.2.). In addition, round and elongated cardiac cells formed

clusters in the co-culture group in comparison to separated arrangements of the cells in the mono-culture. By day 7, the CMs and CFs in the both culture groups exhibited higher numbers of elongated and spread cells in comparison to the first day (Figure 6.4B.). In particular, CFs demonstrated a larger cell area (Figure 6.4B., co-culture inset #1) compared to CMs (Figure 6.4B., mono-culture inset & co-culture inset #2). Interestingly, CMs in the co-culture exhibited small protrusions, which were rarely seen in mono-culture (Figure 6.4B., co-culture inset #3 & 4). Overall, the cells exhibited well-connected structures in co-culture condition as compared to the mono-culture. Figure 6.4C. represents the quantitative results of the cell viability where both culture groups exhibited high levels of cell survival. Particularly, mono- and co-culture groups resulted in approximately 80% overall cell viability on day 1, while the average overall cell viability increased to 85% for mono-culture and 90% for co-culture by day 7. There were no statistically significant differences among the culture days for mono-culture. In contrast, due to the proliferative nature of CFs (Saini, 2015; Sigel, 1996), co-culture group exhibited an increase in overall cell viability (t-test (two tailed); $p < 0.05$).

6.3.3. Assessment of cytoskeleton organization

F-actin fibers were stained on day 7 of culture to determine the cytoskeleton organization and morphology of the cells in mono- and co-culture groups. Co-culture of the cells produced an intact and dense organization of cytoskeleton (F-actin) compared to mono-culture, which exhibited a discrete and loosely packed arrangement of F-actin fibers (Figure 6.5A.). These observations were consistent with phase contrast images demonstrating pronounced network of connected cells in the co-culture condition. Furthermore, FFT analysis was performed on 20x and 40x images to assess alignment of F-actin fibers (Figure 6.5A., FFT insets). There was no overall tissue-level alignment, however, numerous local alignments were detected across both culture conditions. FFT images (dashed rectangles, subsets of 40x images in Figure 6.5A.) of small cell clusters illustrated the local cellular alignment. Additionally, the actin area coverage was analyzed within both culture conditions. As can be seen in Figure 6.5B., a significant difference ($p < 0.05$)

in terms of actin coverage was observed between the culture groups pointing to the contributions of CFs in assembling a dense cell organization in co-culture condition (Saini, 2015).

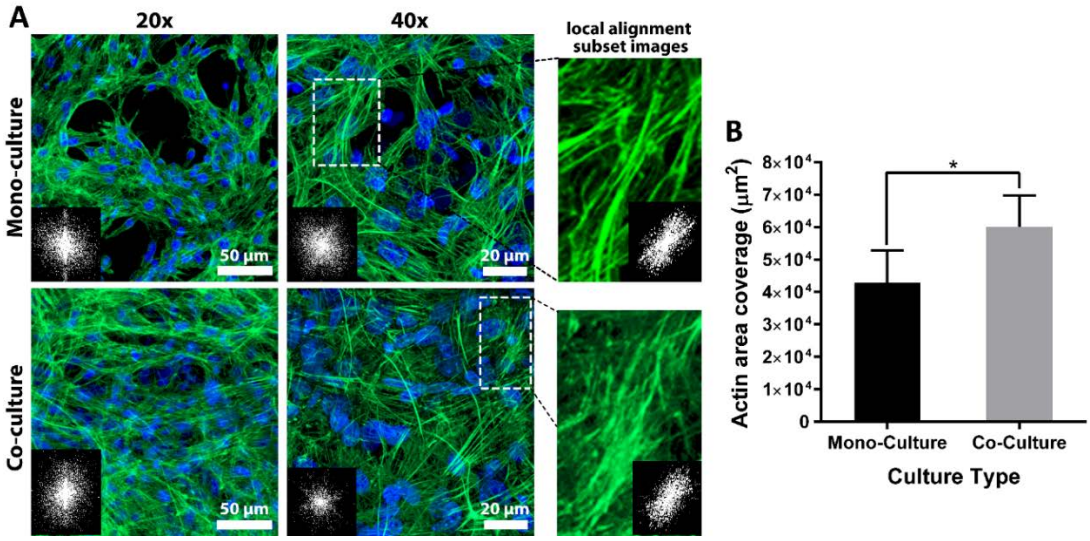

Figure 6.5. (A) F-actin fibers (green) stained images in both culture groups representing the cytoskeleton organization at 20x and 40x magnifications; FFT images (inset) indicate fiber alignment within the formed 3D cardiac tissue. The magnified spots and related inset FFT images illustrate the local alignment of F-actin fibers. (B) The average coverage area (μm^2) of the F-actin fibers at day 7 of culture ($n > 10$; $*p < 0.05$).

6.3.4. Analyses of cardiac-specific markers

SAC, cTnI, and Cx43 were stained to assess cardiac cells phenotype within the PNJ-Gelatin biohybrid hydrogel. Figure 6.6A. represents the immunostained images of both mono- and co-culture groups at day 7. As can be seen in the co-culture images, the sarcomeric structures demonstrated defined, uniaxial, and extended arrangements. Moreover, a homogenous distribution pattern of Cx43 was observed for co-culture in comparison to the disarrayed expression of these gap junctions in mono-culture condition. In addition, the fluorescence coverage area (Figure 6.6B.), correlating to the architecture and distribution of expressed cardiac proteins, was quantified based on 20x immunostained images. SAC and Cx43 displayed statistically (t-test (two tailed); $p < 0.05$) higher coverage area in co-culture condition.

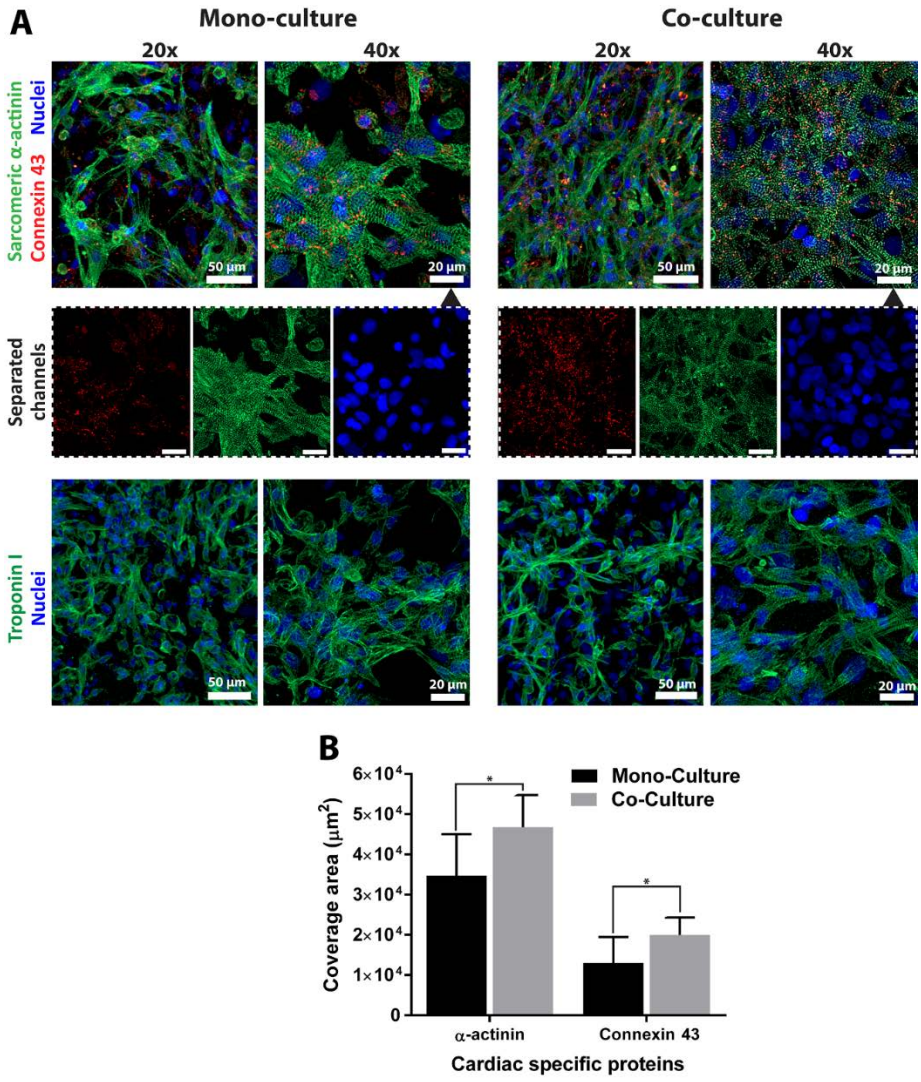

Figure 6.6. (A) The immunostained images (day 7) of mono- and co-culture groups illustrating the structure and distribution of SAC, cTnI, and Cx43 at two different magnifications (20x, 40x). (B) The average coverage area (μm^2) of SAC and Cx43 proteins at day 7 ($n > 12$; $^*p < 0.05$).

The cells exhibited a well distribution of cTnI in both culture conditions. Overall, the presence of CFs assisted CMs to connect and form cell-cell junctions (as indicated by Cx43), producing well-distributed and connected clusters of cells. To demonstrate that encapsulation and subsequent culture of cardiac cells within the PNJ-Gelatin hydrogel did not alter their gene expression profile, we performed QPCR analysis on day 1 and 7. This analysis revealed that there were no statistically significant (t-test (two tailed); $p > 0.05$) changes in expression of CMs

specific genes including cTNT, MLC2v, ACTN1, and Cx43 in both the mono- and co-culture condition over the course of 7 days of culture (Figure 6.7.).

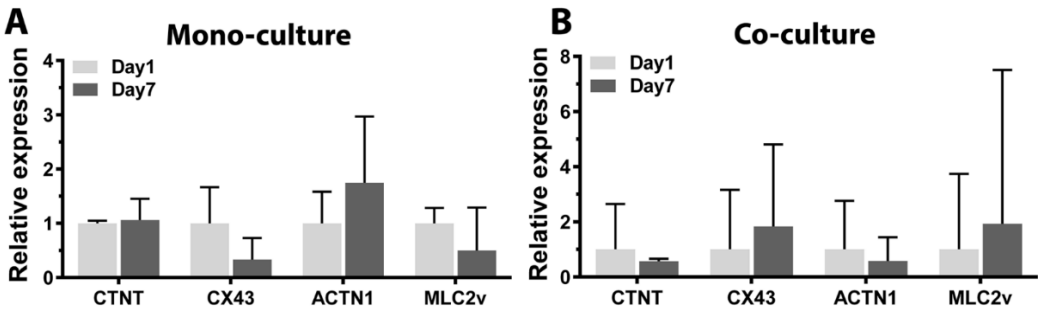

Figure 6.7. Evaluation of the cardiac specific gene expression within PNJ-Gelatin hydrogel. The expression level of CTNT, CX43, ACTN1, and MLC2v genes at two different time points (day 1 and 7) for (A) mono-culture and (B) co-culture.

6.3.5. Beating behavior of the encapsulated cardiac cells

Beating behavior of cardiac cells was examined by analyzing the number of tissue-level (2.5 × 2.5 mm^2 field of view) synchronous contraction in a daily manner. The results in Figure 6.8A. and 6.8B. show the average number of beats per minute (BPM) within both mono- and co-culture groups. In mono-culture, the encapsulated cardiac cells started beating individually on day 3 (Appendix C.15.). As the cells came into contact with each other, they demonstrated a synchronized beating behavior starting at day 6 of culture (57 ± 19 BPM) (Figure 6.8A.; Appendix C.16.). These observations were consistent with network formation of the cells based on the phase contrast and fluorescence images (Figure 6.4B.). The BPM reached the highest value (92 ± 42 BPM, $p < 0.05$) on day 7 followed by a significant decline to 36 ± 28 BPM by day 9. Additionally, the beating behavior was not maintained uniformly over the culture period (unstable trend represented by the blue line). On the other hand, the co-culture group (Figure 6.8B.) exhibited synchronous beating as early as day 3 of culture (39 ± 20 BPM) (Appendix C.17. and C.18.) and maintained a stable trend (represented by the blue line) in terms of BPM up to day 9 (30 ± 8 BPM) (Appendix C.19.). To further investigate contraction signal synchrony in terms of amplitude and frequency, the tissue-level field of view (2.5 × 2.5 mm^2) was subdivided in to 0.5 × 0.5 mm^2 subsets. Figure 6.8C. and 6.8D. show beating signals of subsets within a single

representative field of view. As can be seen, the mono-culture signals displayed high fluctuations in peak to peak amplitude and period whereas co-culture condition exhibited uniform signals.

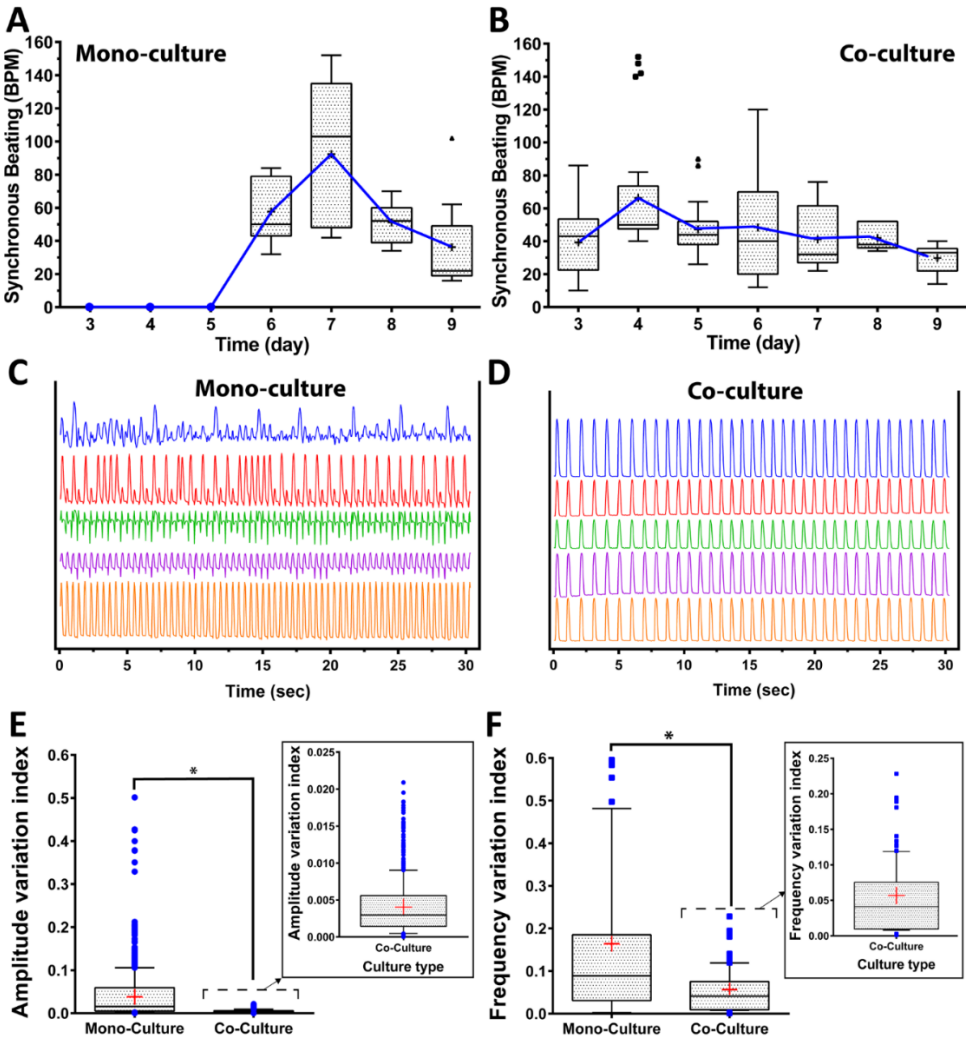

Figure 6.8. The average number of beats per minute (BPM) for (A) mono- and (B) co-culture groups from day 3 to 9 of culture. (C) and (D) represent beating signals of five different subsets (0.5 × 0.5 mm^2) within hydrogel sample (2.5 × 2.5 mm^2) at day 7. The quantified (E) amplitude and (F) frequency variations represented as indexes comparing the synchrony of beating for mono- and co-culture groups.

Furthermore, similar frequencies between subset signals were observed for co-culture, whereas such behavior was not seen in mono-culture of the CMs. These findings indicated that the different subset areas within one field of view for the co-culture group were in synchrony

compared to the mono-culture condition. Moreover, amplitude and frequency variation indexes were developed to further quantitatively analyze the tissue-level synchrony. Amplitude and frequency variations were found to be significantly lower in co-culture compared to mono-culture, indicating higher tissue-level synchrony in the co-culture condition (Figure 6.8E. and 6.8F.).

6.3.6. External electrical stimulation

To investigate the response of encapsulated CMs and CFs within the PNJ-Gelatin hydrogel to external electrical stimulation, samples were treated by pulsatile electrical signals at day 7. Appendix Figure B.3. shows the assembled chamber and the excitation threshold for both mono- and co-culture groups. Despite lower excitation threshold for the co-culture of the cells, no significant differences were detected between the two culture groups for the applied frequencies (1, 2, and 3 Hz). In addition, only individual areas within the hydrogel samples responded to the external electrical field and started to contract.

6.4. Discussion

Although current hydrogels provide a desirable matrix for the delivery of exogenous cells to the infarct region, the majority of developed biomaterials suffer from well-tuned properties, such as lack of cell-adhesion motifs (Heffernan, 2016; Hunt, 2014; Jongpaiboonkit, 2008) or robust mechanical properties (Little, 2008; Romano, 2011). Particularly, a large body of the previous work on injectable hydrogels has been concentrated on animal studies without extensive *in vitro* analyses on functionalities of cardiac cells to define an optimal culture condition (Fujimoto, 2009; X Li, 2014; Wall, 2010). Moreover, most of the earlier studies focused on the use of only CMs rather than co-culture conditions with CFs, being the most abundant cell within the myocardium after CMs (Souders, 2009). For instance, Li et al. (X Li, 2014) utilized CNTs modified PNIPAAm for cardiac regeneration applications. They performed minimal *in vitro* studies prior to *in vivo* work, demonstrating that the presence of CNTs significantly promoted cellular adhesion and spreading. In another study by Wall et al. (Wall, 2010), semi-interpenetrating hydrogels of p(NIPAAm)-co-Polyacrylic acid (pAAc) hydrogels with matrix metalloproteinase labile crosslinkers were developed for transplantation of bone marrow-derived MSCs and treatment of cardiac

injuries. Cellular proliferation was investigated within the proposed matrices, as a function of mechanical stiffness and RGD concentration, to select a suitable matrix prior to *in vivo* work. Cui et al. (H Cui, 2014) presented an injectable matrix using PolyNIPAM-based copolymers and electroactive tetraaniline (TA) for transplantation of rat cardiac myoblast within the infarct region. They performed material characterization and viability testing before animal studies. Wagner's group (Fujimoto, 2009) also developed a copolymer made of N-isopropylacrylamide (NIPAAm), acrylic acid (AAc) and hydroxyethyl methacrylate-poly(trimethylene carbonate) (HEMAPTMC) (poly(NIPAAm-co-AAc-co-HEMAPTMC)) for cardiac regeneration upon myocardial infarction. They performed extensive characterizations to define the optimal monomer ratios with respect to gelation, solubility and degradation of the material. *In vitro* viability studies (rat vascular smooth muscle cells) was performed prior to *in vivo* testing. Therefore, it is crucial to perform extensive *in vitro* analyses on cardiac function before continuing to *in vivo* experimentation. Likewise, there is a critical need to discover whether the synthesized injectable hydrogel will accommodate the resident CFs within the infarct region as well as determining the subsequent influences of CFs on tissue-level functionalities.

In this work, a biohybrid injectable hydrogel was developed from gelatin and PNIPAAm-based copolymers to address these limitations. Gelatin, a naturally-derived biomaterial, was chosen to provide a suitable microenvironment with high bioactivity for cell growth and spreading (Nakajima, 2015; Nicodemus, 2008; Singelyn, 2011; H Tan, 2010), while PNIPAAm was selected to induce physical crosslinking and obtain sufficient mechanical robustness for the accommodation of dynamic tissue-level beating (Cai, 2015; X Li, 2014; T Wang, 2009). The synthesized hydrogel provided a dual-crosslinkable matrix, where the thiols and acrylates initiated a chemical gelation along with a secondary physical crosslinking to induce mechanical enhancement. The rheology results (Figure 6.2.) supported the chemical and physical crosslinking nature of the PNJ-Gelatin injectable hydrogel. Because the standard rheology approach may not represent the exact biophysical cues that the cells feel during the sample preparation, we devised a simple test to simulate the viscoelastic behavior of the biohybrid hydrogel with cells during the initial 12 h of culture. As seen in Figure 6.2D., the cells experienced

the chemical crosslinking first, followed by the hydrogel physical crosslinking once the samples were placed inside the incubator. However, these results still may not fully represent the actual biophysical cues, due to many other factors that influence the final modulus, such as hydrogel swelling, degradation, and ECM deposition (Banerjee, 2006).

The ECM-like macroporous structures, provided by PNJ-Gelatin hydrogels, make these types of biomaterials a desirable candidate for cell growth. Typically, PNIPAAm-based hydrogels exhibit low water content equilibrium, which can limit nutrient and gas exchange within the hydrogel structure (Heffernan, 2016). To that regard, gelatin and JAAm were included as the key components within the PNJ-Gelatin hydrogel, which consequently resulted in enhanced water retention (Overstreet, 2013a). After hydration, the porous structures of the hydrogel increased slightly, indicating the retention of water (Figure 6.3B.). The difference in the water content can be equated to the hydrogel porous structures becoming more uniform and open (Figure 6.3D.) along with the increase in the range of pore diameters (Figure 6.3E.). Therefore, the material characterizations ensured suitable and tunable properties for cellular delivery based on the natural/synthetic nature of the proposed hydrogel matrix.

An ideal cell delivery hydrogel needs to provide a suitable microenvironment to enhance cardiac cell biological functions and promote cell survival, spreading, cytoskeletal organization, and specific markers expression (Hasan, 2015; Paul, 2014). The PNJ-Gelatin was used to encapsulate two different cell culture systems (CMs and 2:1 CMs-CFs) to assess the performance of the synthesized hydrogel for cardiac tissue engineering. We used 2:1 culture ratio based on our earlier optimization studies (Saini, 2015). In this work, both culture groups demonstrated high cell viability and spreading within the 3D PNJ-Gelatin hydrogel (Figure 6.4.). These findings can be attributed to the high bioactivity of gelatin (Heffernan, 2015; Nakajima, 2015), adequate pore size distribution, and water content (Annabi, 2010), which are required for sufficient cell infiltration and nutrition, waste, and gas exchange within the 3D ($10 \times 10 \times 0.2$ mm^3) matrix. The co-culture group exhibited a significant increase in viability by day 7 which can be associated to the highly proliferative nature of CFs (Souders, 2009). This is also reflected in the

day 7 images (Figure 6.4B.) of co-culture, where there appeared to be a network of elongated cells located between the round cells. The findings from the viability and cell spreading analyses could be attributed to the incorporation of a highly bioactive component (gelatin) within the synthetic, PNIPAAm-based hydrogel. Gelatin not only provided sufficient cell adhesion motifs, but it also offered a high level of bioactivity as well as inducing high water retention that was overall missing in PNIPAAm. In addition, we performed hydrolytic degradation of the hydrogel. Our data indicated a sharp decrease in the molecular mass after 1 day, but the trend stabilized for the next few weeks (Appendix Figure B.4.). We concluded that this decrease was not degradation, but uncrosslinked products being released from the material. Nonetheless, gelatin was able to be degraded enzymatically (Nakajima, 2015), but the PNIPAAm-based components did not contain any degradable monomers. After enzymatic degradation, it was expected that LCST would have increased due to gelatin chains breaking down and separating the NIPAAm components resulting in NIPAAm units with short hydrophilic gelatin tails. In addition, the increase in LCST beyond physiological temperatures means that the polymer may become soluble within the body and cleared. However, the molecular weight of the byproducts was not investigated and may result in toxicity if too high. For future work, our group has a plan to improve the degradability of the PNJ-Gelatin hydrogel by incorporation of biodegradable components from our previous studies (Overstreet, 2013a).

The resulting cell specific characteristics (Figures 6.5., 6.6. and 6.7.) and functionalities (Figure 6.8.) within the PNJ-Gelatin highlighted the potential of the proposed hydrogel as an efficient and bioactive cardiac cell delivery system and further revealed the dissimilarities between the two investigated cell culture conditions (CM and 2:1 CM-CF). First, phenotypic differences in the distribution and structures of cytoskeleton and cardiac specific proteins were observed across both cultured cell systems (Figures 6.5. and 6.6.). The presence of CFs can be accredited to these differences by providing structural support as well as mechanical, electrical, and biochemical cues (Banerjee, 2006; Souders, 2009). Primarily, distributions of F-actin, SAC, and Cx43 proteins in co-culture were more uniformly organized contrary to the discrete arrangement in mono-culture. In this regard, CFs may have enhanced cell-cell and cell-ECM

mechanical interactions by amplifying the availability of cadherin- and integrin-based anchoring points as demonstrated in our and other previous works (Banerjee, 2006; Baxter, 2008; Kohl, 2003; Saini, 2015). This resulted in enhanced spreading of cardiac cells, which increased the coverage area of F-actin (Figure 6.5B.) and SAC (Figure 6.6B.). Furthermore, CFs facilitate cell-cell electrical coupling by contributing Cx43 gap junctions (Camelliti, 2005; Camelliti, 2004; Chilton, 2007), which is reflected by the homogenous distribution (Figure 6.6A., 40x) and higher coverage area in co-culture condition (Figure 6.6B.). Secondly, QPCR analysis revealed that encapsulation and subsequent culture of CMs, either alone or with CFs, in the PNJ-Gelatin hydrogel had no effect on their gene expression profile. Third, incorporation of CFs with CMs gave rise to a dramatic difference in beating behavior, which correlates to cardiac cell and tissue functions (Kaneko, 2011; Souders, 2009). We have observed that as CMs reached to each other and formed clusters of cells as they began to contract. However, such behavior was more pronounced in the presence of CFs, as helper cells. To that regard, the mechanical and electrical signaling provided by the CFs was speculated to induce higher cell-cell coupling (Banerjee, 2006; Camelliti, 2004; Chilton, 2007; Kohl, 2003), which resulted in earlier tissue-level contractions, as well as relatively stable average BPM in co-culture condition (Figure 6.8A. and 6.8B.). In addition, the CFs engaged in signal propagation within the formed cardiac tissue, as demonstrated by the synchronous contraction signals (Figure 6.8C. and 6.8D.) taken from the different areas (0.5 × 0.5 mm^2) of a single hydrogel sample (2.5 × 2.5 mm^2). Such behavior was also quantitatively represented as amplitude and frequency variation indexes, which determined tissue-level (2.5 × 2.5 mm^2) synchrony (Figure 6.8E. and 6.8F.). The mono-culture group mostly demonstrated asynchronous beating fashion, which can cause low action potential signal propagation upon injection within the host myocardium. These observations are indeed consistent with our previous work on the development of microtissues embedded with the co-cultures of the CMs and CFs (with optimized ratio of 2:1) within a gelatin methacrylate (GelMA) hydrogel (Saini, 2015). However, CMs in mono-culture did not spread or exhibit any spontaneous contraction in GelMA hydrogel. Such differences further indicated that the proposed hydrogel exhibits superior properties and can be used as a suitable matrix to supports cardiac cells functionalities in both

mono-culture and co-culture conditions. The influence of paracrine signaling between CMs and CFs is subject of our future studies. Furthermore, we intend to test the *in vivo* functionalities of the cell-embedded hydrogel matrix in our future work.

External electrical stimulation setup (Appendix Figure B.3.) was employed to assess the response of cardiac cells to the electrical stimulation. Both mono- and co-culture groups reacted to the applied stimulation similarly and no significant differences were observed. Furthermore, the inclusion of CFs in co-culture, which resulted to a significant synchronous contraction compared to the mono-culture condition, did not facilitate the propagation of external electrical pulses throughout the hydrogel constructs.

6.5. Conclusion

In this study, we synthesized PNJ-Gelatin hydrogel as an injectable matrix for cardiac cells delivery and tissue engineering applications. The proposed material featured chemical crosslinking to combine gelatin to the thermo-responsive PNIPAAm in a time dependent manner to induce a mechanically robust injectable hydrogel. Furthermore, incorporation of gelatin and JAAm into the hydrogel offered bioactivity and higher water content leading to excellent cell survival, adhesion, spreading, cytoskeletal and cardiac specific markers organization. The two cultured groups within the PNJ-Gelatin hydrogel demonstrated desirable phenotypic and functional outcomes, which illustrated the potential of the injectable matrix for cardiac tissue engineering and cell delivery applications. In addition, the synthesized matrix was able to home CFs (often found within the infarct region) to enhance the overall functionalities of the cell-embedded hydrogel. Particularly, the co-culture group exhibited higher synchronous tissue-level contractions, which could be attributed to the structural and distribution differences of cardiac specific markers (SAC and Cx43) as well as cytoskeleton organization (F-actin fibers).

CHAPTER 7

SUMMARY AND FUTURE PERSPECTIVE

7.1. Summary of Findings

7.1.1. Specific aim1: Development of gelatin-GNM cardiac patches with enhanced contractile and electrical functionalities

Under specific aim1, we designed and fabricated electrically conductive GelMA-GNR hydrogels for engineering scaffold-based cardiac tissues. We performed material characterization to determine the impact of embedded GNRs on electrical, mechanical and topographical properties of GelMA-GNR hydrogels. We also conducted extensive in vitro cellular assessments to investigate the influence of incorporated GNRs on maturation, contractility and excitability of the conductive cardiac tissues. Lastly, we performed a mechanistic study to dissect the impact of enhanced mechanical stiffness and nano-scale topographies of GelMA-GNR hydrogels on maturation and excitability of engineered cardiac tissues from the role of hydrogel electrical conductivity.

Initially (in chapter 2), we determined that the incorporation of GNRs within GelMA matrix enhanced electrical conductivity and mechanical stiffness (Young's modulus) of the hydrogel. In addition, we demonstrated that the embedded GNRs were localized on the surface of GelMA matrix, which led to generation of nano-scale topographies. Cardiomyocytes seeded on GelMA-GNR hydrogels exhibited excellent cell retention and viability. The increased cell adhesion resulted in the formation of an integrated tissue layer on GelMA-GNR hydrogels. Immunostained images of integrin β-1 confirmed the improved cell-matrix interaction on GNR-embedded hydrogels. In addition, formation of uniaxially aligned sarcomeres and homogenous distribution of Cx43 gap junctions were observed on GelMA-GNR hydrogels. GelMA-GNR hydrogels supported synchronous tissue-level beating of cardiomyocytes, demonstrated by fluorescent detecting of calcium transients among CMs. Lastly, conductive GelMA-GNR cardiac tissues demonstrated significantly higher electrical excitability (i.e. lower excitation threshold) as compared to pure GelMA hydrogels.

Next (in chapter 3), we introduced anisotropic surface micropatterns (50 μm wide microgrooves) on GelMA-GNR hydrogels to develop engineered cardiac tissues with native-like cytoarchitecture. F-Actin stained images and fluorescent area coverage data revealed formation of uniform and uniaxially aligned cardiac microtissues on GelMA-GNR hydrogels. Immunostaining images of cardiac markers, including SAC and Cx43, also showed higher sarcomere alignment and enhanced cellular connectivity on GelMA-GNR hydrogels. Microtissues formed on both GelMA and GelMA-GNR constructs demonstrated spontaneous contractility from day 4 to 7 of culture. However, only conductive GelMA-GNR microtissues showed a consistent response with low excitation thresholds in changing beat rate because of electrical stimulation.

Lastly (in chapter 4), we developed conductive and non-conductive engineered cardiac tissues to investigate, side-by-side, the impact of matrix electrical, mechanical and topographical characteristics on CMs retention, maturation and excitation threshold. We fabricated four different hydrogel groups including 5% GelMA (control group), 20% GelMA (mechanically stiff), GelMA-SNP (non-conductive with nano-topographies) and GelMA-GNR (conductive with nano-topographies). Our results demonstrated that GelMA-SNP and GelMA-GNR hydrogels significantly improved CMs adhesion affinity as compared to pure GelMA (5% and 20%), highlighting the influence of nano-scale topography on cellular adhesion and retention. The expressions of cardiac specific proteins demonstrated that both stiffness (20% GelMA) and nano-scale topographies (GelMA-SNP and GelMA-GNR) promoted the cardiac maturation. The impact of increased stiffness and nano-scale topography, induced by incorporation of SNPs and GNRs, significantly decreased the excitation threshold. In addition, GelMA-SNP and GelMA-GNR cardiac tissues were accommodated external electrical stimuli at higher frequencies in both coupled and uncoupled gap junction conditions. Most importantly, no significant differences regarding cell retention, cardiac maturation and electrical excitability were observed between conductive GelMA-GNR and non-conductive GelMA-SNP tissues. Our findings indicated the prominent impact of hydrogel matrix stiffness and nano-scale surface topography on the overall tissue function, regardless of electrical conductivity.

7.1.2. Specific aim2: Engineering and characterization of electrically conductive scaffold-free cardiac microtissues

Under specific aim2, we engineered scaffold-free cardiac microtissues incorporated with GNWs functionalized with RGD to study the impact of conductive nanomaterials on maturation and electrophysiology of CMs. We performed western blotting and immunocytochemistry to evaluate the role of GNWs on CMs maturation. In addition, we conducted extensive electrophysiology experiments to study the influence of embedded functionalized GNWs on conduction velocity of CMs in both coupled and uncoupled (heptanol treated) gap junctions.

We synthesized ultralong GNWs with aspect ratio of ~46, then their cytotoxic CTAB coating were exchanged with biocompatible PEG using a customized 2-step ethanol-assisted procedure. PEGylated GNWs were functionalized with RGD peptide to promote their adhesion affinity to the cells. Live/Dead fluorescent images and Alamar Blue results demonstrated a significant increase in biocompatibility of GNWs by removing CTAB. In terms of contractility and excitability properties, our finding indicated that incorporation of electrically conductive GNWs did not lead to higher fractional shortening and lower excitation threshold of CM microtissues. In addition, similar levels of maturation, via analysis of the cardiac specific markers (SAC, Cx43, and cTnI), were observed for both CM and CM-GNW microtissues. Lastly, our electrophysiology data demonstrated that the incorporation of electrically conductive GNWs did not improve the conduction velocity of CMs. Furthermore, the percentage of conduction velocity reduction in both CM and CM-GNW were similar in presence of gap junction uncoupler (heptanol), indicating that incorporation of electrically conductive nanomaterials did not maintain the CM conduction velocity.

Despite the enhanced cardiac maturation and contraction amplitude of hiPSC-derived CMs induced by other conductive nanomaterials (rGONFs and SiNWs), reported in the literature, we did not observe similar outcomes using GNWs and NRVCMs. We speculate that enhancing the maturation of CMs using conductive nanomaterials can be a cell-dependent process. In addition,

it is possible that the GNWs were internalized and did not locate on the cell membrane or extracellular microenvironment, which further led to no significant enhancement of CV.

7.1.3. Specific Aim3: Fabrication and characterization of biohybrid injectable PNIPAAm-gelatin hydrogel tissues for cardiac regeneration

Under specific aim3, we conducted a comprehensive in vitro biological assessment to evaluate the suitability of an injectable biohybrid PNIPAAm-Gelatin hydrogel for cardiac tissue engineering applications. Specifically, the functionalities of CMs alone and in co-culture with CFs were evaluated within the hydrogel matrix. The encapsulated cells demonstrated a high level of cell survival and spreading throughout the hydrogel matrix in both culture conditions. A dense network of stained F-actin fibers illustrated the formation of an intact and 3D cell-embedded matrix. Furthermore, immunostaining and gene expression analyses revealed mature phenotypic characteristics of cardiac cells. Notably, the co-culture group exhibited superior structural organization, spontaneous contractility and cell–cell synchronicity. The outcome of this study is envisioned to open a new avenue for extensive in vitro characterization of injectable matrices embedded with 3D mono- and co-culture of cardiac cells prior to in vivo experiments.

7.2. Significance and Contributions

In this dissertation, the overarching objective was to develop electrically conductive cardiac tissues to study the role of GNMs on maturation and electrophysiology of CMs. In this regard, we utilized integrated micro- and nanoscale technologies to engineer two classes of conductive cardiac tissues, scaffold-based and scaffold-free, to conduct our study. The significance of our work is mainly categorized to 1) dissecting the role of matrix conductivity on maturation and electrical excitability of scaffold-based cardiac tissues from matrix mechanical and topographical properties, and 2) identifying the impact of sole presence of conductive GNWs on conduction velocity of CMs.

Scaffold-based GelMA-GNR cardiac tissues: Incorporation of conductive nanomaterials within scaffold leads to a combinatorial enhancement of all electrical, mechanical, and

topographical characteristics. However, to date, none of the studies focusing on the development of conductive cardiac tissues have aimed to answer the critical question that, could non-conductive nanomaterials induce synchronized electrical and contractile functionalities among CMs by only enhancing the cardiac maturation rather than inducing the exogenous electrical conductivity?

In this dissertation, for the first time, we developed conductive and non-conductive engineered cardiac tissues to comprehensively investigate, side-by-side, the impact of matrix electrical, mechanical, and topographical characteristics on retention, maturation and excitation threshold of CMs. Our findings demonstrated the prominent impact of hydrogel matrix stiffness and nano-scale surface topography on maturation and excitability of engineered cardiac tissues, regardless of matrix electrical conductivity.

Scaffold-free CM-GNW cardiac microtissues: Despite the promising outcomes demonstrating the potential of conductive nanomaterials to enhance the maturation of CMs, the impact of nanomaterials' electrical conductivity on signal propagation and electrophysiology of cells/tissues has not been investigated. Therefore, we developed electrically conductive cardiac microtissues embedded with functionalized GNWs with RGD peptide to study CM contraction amplitude, maturation and electrophysiology.

In this dissertation, for the first time, we comprehensively investigated the direct influence of electrically conductive GNWs on conduction velocity of CMs using microelectrode array. Our finding indicated that embedded GNWs did not improve conduction velocity of CMs. Also, the percentage of conduction velocity reduction were similar in presence of a gap junction uncoupler (heptanol), indicating that incorporation of GNWs did maintain the conduction velocity.

The outcomes of our work have been presented as peer-reviewed journal articles, book chapter, patent and oral/poster presentations in national and international conferences. Summary of our contributions are listed in below.

Journal articles:

1- **Ali Navaei** et al., PNIPAAm-based biohybrid injectable hydrogel for cardiac tissue engineering, Acta Biomaterialia (2016).
2- **Ali Navaei** et al., Gold nanorod-incorporated gelatin-based conductive hydrogels for engineering cardiac tissue constructs, Acta biomaterialia (2016).
3- **Ali Navaei** et al., Electrically conductive hydrogel-based micro-topographies for the development of organized cardiac tissues, RSC Advances (2017).
4- S. Liu, **Ali Navaei**, X. Meng, M. Nikkhah, J. Chae, Wireless Passive Stimulation of Engineered Cardiac Tissues, ACS Sensors (2017).

Book chapter:

1- L. Karperien, **Ali Navaei**, B. Godau, A. Dolatshahi-Pirouz, M. Akbari, M. Nikkhah, Chapter 5: Nanoengineered biomaterials for cardiac regeneration, *Nanoengineered Biomaterials for Regenerative Medicine,* Elsevier (2018).

Talk/poster conferences:

1- **Ali Navaei** et al., Gold nanorod incorporated gelatin-based hybrid hydrogels for myocardial tissue engineering, BMES Annual Meeting, Tampa, FL (2015), Platform presentation.
2- **Ali Navaei** et al., Nanoengineered hybrid hydrogels for cardiac tissue engineering, NHLBI Symposium on Cardiovascular Regenerative Medicine, Bethesda MD, (2015), Poster presentation.
3- **Ali Navaei** et al., Nanoengineered hybrid hydrogels for cardiac tissue engineering, 4th Nano Today Conference, Dubai, UAE, (2015), Platform presentation.
4- **Ali Navaei** et al., PNIPAAm-based biohybrid injectable hydrogel for cardiac tissue engineering, World Biomaterials Congress, Montreal, Canada, (2016), Platform presentation.
5- **Ali Navaei** et al., Nanoengineered hydrogel topographies for the development of organized cardiac tissues, BMES Annual Meeting, Minneapolis, MN (2016), Poster presentation.

6- **Ali Navaei** et al., Nanoscale decoration of cardiac microtissues using functionalized gold nanowires for cell-based therapies, BMES Annual Meeting, Phoenix, AZ (2017), Poster presentation.

7- **Ali Navaei** et al., Electrically conductive hybrid hydrogels with anisotropic topographical features for engineering functional cardiac tissues, TERMIS, Kyoto, Japan (2018). Platform presentation.

Patent:

1- M. Nikkhah and **Ali Navaei**, Gold nanorod incorporated gelatin-based hybrid hydrogels for cardiac tissue engineering and related methods, US20170143871A.

7.3. Project Challenges

We have encountered several challenges during this work that may have delayed our progress, however, enriched our knowledge and expertise significantly. For example, we had challenges regarding PEGylation and RGD conjugation of GNWs, since there was not any reported protocol specifically for ultralong GNWs, elsewhere. The difficulties were including extensive aggregation of GNWs during CTAB-PEG exchange process. A minimum concentration of free CTAB in the GNMs colloidal solutions is required for effective PEGylation. However, as the concentration of free CTAB decreases, the probability of GNMs aggregation increases. Based on these facts, we designed a 2-step PEGylation process. In the first step, the concentration of free CTAB was kept at its CMC (1 mM at room temperature in DIW) to provide just enough CTAB molecules to protect GNWs from aggregation during PEGylation. Afterwards, we performed a second PEGylation step with 20% ethanol to complete the CTAB removal by preventing the bilayer coating formation of CTAB on GNWs. Our biocompatibility results demonstrated substantial improvement of viability and metabolic activity of CMs when cultured with PEGylated GNWs as compared to GNW-CTAB.

Another challenge that we have faced was related to the electrophysiology assessment of scaffold-free cardiac microtissues. Our initial attempt was based on the use of external electric field stimulation technique by a custom-designed chamber consisting of two carbon electrodes

connected to a function generator. However, due to the global propagation of the electric field stimuli within microtissues and culture medium in the stimulation chamber, we were not able to assess the influence of GNWs on the electrical excitability and conduction velocity of scaffold-free cardiac microtissues. To address this challenge, we utilized a microelectrode array (MEA) platform developed by BMSEED LLC, as the measurement technique with high reading precision and resolution. We had spent extensive effort on optimizing the surface coating of MEA chamber to achieve a stable and tight attachment of CMs on the microelectrodes to obtain field potential signals with high signal to noise ratio. In addition, due to the lack of universal data acquisition/analysis software for BMSEED MEA, we had allocated significant efforts on the large-scale data processing and analysis using other available software including OriginPro, MATLAB and Microsoft Excel.

Analyzing the spontaneous contractility of pure GelMA and GelMA-GNR cardiac tissues was among other challenges that we have encountered. Initially, we had considered spontaneous beats per minute (i.e. BPM) as a quantifiable parameter to evaluate the contractile maturation of engineered cardiac tissues. However, we later had observed high levels of randomness regarding beating frequency among similar samples (i.e. technical replicates) in the same experimental condition (0, 0.5, 1 or 1.5 mg/mL GNRs). In some cases, there were samples that did not exhibit any spontaneous beating at the time of measurement, while other samples in the same group were beating robustly. Therefore, we rationalized that the spontaneous beating frequency (i.e. BPM) can be used as a qualitative parameter to evaluate the overall suitability of scaffolding biomaterials (e.g. hydrogels) for engineering cardiac constructs, however, it may not be an appropriate metric for solid conclusions regarding tissue maturation and contractile functioning.

We have utilized electric field stimulation to assess the excitability of engineered GelMA-GNR tissues by measuring excitation voltage threshold. The use of field stimulation enabled us to measure tissue-level excitability of cardiac constructs. Despite the significance of our work, there are still important electrophysiological parameters, including membrane depolarization threshold and action potential propagation velocity, which cannot be investigated using the electric field

stimulation chamber. Therefore, utilization of other procedures, such as voltage sensitive fluorescent dyes along with point stimulation using bipolar microelectrodes, can provide more comprehensive understanding about the impact of scaffold conductivity on electrophysiology of engineered cardiac tissues.

7.4. Future Perspective

In the context of developing conductive cardiac tissues to enhance the maturation and electrical coupling (i.e. synchronicity) of CMs, several promising in vitro studies have been reported. However, there is still a significant knowledge gap regarding the extent of electrical integration of conductive tissues with the native myocardium in MI-induced animal models (i.e. in vivo studies) in comparison with non-conductive tissues. In this regard, the use of characterization methods, such as electrocardiography (ECG) or optical mapping of Langendorff-perfused whole heart, could provide valuable information on the organ-level electrical activity of the native myocardium upon implantation of conductive cardiac tissues. The fate of utilized conductive nanomaterials, after in vivo implantation of engineered tissues, is another very important factor that needs to be investigated. After degradation of scaffolding biomaterial, the released nanomaterials could be distributed within the heart itself or other tissues/organs (e.g. blood vessels or lung), which could potentially lead to unwanted side effects. In this regard, biodistribution as well as long-term cytotoxicity and immunogenicity assessments, using in vivo animal models (e.g. rats and pigs), are necessary to shed more light on the biosafety of conductive nanomaterials. In our opinion, we believe that such in vivo experiments are vital for the future clinical translation of electrically conductive cardiac patches and cell-based therapies for treatment of MI.

In our opinion, it is critically necessary for future studies to thoroughly investigate the localization and fate of conductive nanomaterials. Additionally, since we focused our studies on RNVCM, the impact of nanomaterials on electrophysiology and electrical integration of stem cells derived CMs in vitro, needs to further be investigated. Below, we have briefly described our

insights for design of experiments, specifically for scaffold-free conductive microtissues, to investigate the interactions between nanomaterials and cells.

Localization and fate of nanomaterials: Transmission electron microscopy (TEM) can be used for probing nanomaterials within the microtissues. TEM enables us to measure the endocytosed nanomaterials as well as nano-scale localization of nanomaterials within extracellular environment. However, this technique is relatively expensive, especially if multiple time point measurements are required, and it cannot be performed on live cells. Another method for tracking nanomaterials is fluorescent labeling and microscopy. Nanomaterials, such GNMs, can be tagged with fluorescent dyes using EDC/NHS or Streptavidin/Biotin chemistries, which enables the fluorescent tracking at both live and fixed cells/microtissues. Despite the advantage of live imaging and relatively facile technical procedure of fluorescence tracking, there are still challenges associated with this technique. Specifically, 3D probing of intact microtissues can be challenging due to the large size of cellular cluster (e.g. 150 μm diameter). In addition, precise localization of labeled nanomaterials requires secondary fluorescent staining of other cellular compartments, such as plasma membrane, early/late endosomes and lysosomes, to probe intra- or extracellular location of nanomaterials.

In vitro electrophysiology: To assess the impact of conductive nanomaterials on electrophysiology of stem-cell derived CMs, different approaches and measurement techniques can be utilized. First, the direct influence of nanomaterials on cell membrane resting potential and excitation threshold can be measured using patch clamp or voltage sensitive fluorescent dyes. These techniques provide direct measurement of cell membrane electrical activity and can be used to determine conduction velocity within cells. Despite the significance, technical difficulties, include use of high speed cameras, micro-manipulator handling system and risk of extensive phototoxicity. Second approach to investigate the electrophysiology of cardiac cells can be focused on in vitro assessment of electrical integration between nanomaterial-embedded and pure cardiac cells/microtissues. For example, a monolayer of quiescence CMs (i.e. minimal spontaneous contractile and electrical activity) can be prepared as the model for the host tissue.

Afterwards, nanomaterial-embedded microtissues, the cardiac graft, are seeded on the host monolayer and electrical integration of the graft with the host can be assessed using voltage sensitive dye or microelectrode array.

REFERENCES

Aaronson, P. I., Ward, J. P. T., & Connolly, M. J. (2013). *The cardiovascular system at a glance* (4th ed.). Chichester, West Sussex ; Malden, MA: Wiley-Blackwell.

Ahadian, S., Ramón-Azcón, J., Estili, M., Liang, X., Ostrovidov, S., Shiku, H., et al. (2014). Hybrid hydrogels containing vertically aligned carbon nanotubes with anisotropic electrical conductivity for muscle myofiber fabrication. *Scientific Reports, 4*, 4271. doi:10.1038/srep04271

Ahadian, S., Yamada, S., Ramón-Azcón, J., Estili, M., Liang, X., Nakajima, K., et al. (2016). Hybrid hydrogel-aligned carbon nanotube scaffolds to enhance cardiac differentiation of embryoid bodies. *Acta Biomaterialia, 31*, 134-143. doi: 10.1016/j.actbio.2015.11.047

Aikawa, Y., Rohde, L., Plehn, J., Greaves, S. C., Menapace, F., Arnold, J. M. O., et al. (2001). Regional wall stress predicts ventricular remodeling after anteroseptal myocardial infarction in the healing and early afterload reducing trial (heart): An echocardiography-based structural analysis. *American Heart Journal, 141*(2), 234-242. doi: 10.1067/mhj.2001.112237

Alkilany, A. M., Nagaria, P. K., Hexel, C. R., Shaw, T. J., Murphy, C. J., & Wyatt, M. D. (2009). Cellular uptake and cytotoxicity of gold nanorods: Molecular origin of cytotoxicity and surface effects. *Small, 5*(6), 701-708. doi:doi:10.1002/smll.200801546

Amado, L. C., Saliaris, A. P., Schuleri, K. H., St. John, M., Xie, J.-S., Cattaneo, S., et al. (2005). Cardiac repair with intramyocardial injection of allogeneic mesenchymal stem cells after myocardial infarction. *Proceedings of the National Academy of Sciences of the United States of America, 102*(32), 11474-11479. doi:10.1073/pnas.0504388102

Anderson, S. H. C., Elliott, H., Wallis, D. J., Canham, L. T., & Powell, J. J. (2003). Dissolution of different forms of partially porous silicon wafers under simulated physiological conditions. *Physica Status Solidi (A) Applied Research, 197*(2), 331-335. doi:10.1002/pssa.200306519

Angelos, M. G., Kutala, V. K., Torres, C. A., He, G., Stoner, J. D., Mohammad, M., et al. (2006). Hypoxic reperfusion of the ischemic heart and oxygen radical generation. *American Journal of Physiology-Heart and Circulatory Physiology, 290*(1), H341-H347. doi:10.1152/ajpheart.00223.2005

Annabi, N., Nichol, J. W., Zhong, X., Ji, C., Koshy, S., Khademhosseini, A., et al. (2010). Controlling the porosity and microarchitecture of hydrogels for tissue engineering. *Tissue Engineering Part B: Reviews, 16*(4), 371-383. doi:10.1089/ten.teb.2009.0639

Annabi, N., Tsang, K., Mithieux, S. M., Nikkhah, M., Ameri, A., Khademhosseini, A., et al. (2013). Highly elastic micropatterned hydrogel for engineering functional cardiac tissue. *Advanced Functional Materials, 23*(39), 4950-4959. doi:10.1002/adfm.201300570

Atmanli, A., & Domian, I. J. (2016). Recreating the cardiac microenvironment in pluripotent stem cell models of human physiology and disease. *Trends in Cell Biology, 27*(5), 352-364. doi:10.1016/j.tcb.2016.11.010

Aubin, H., Nichol, J. W., Hutson, C. B., Bae, H., Sieminski, A. L., Cropek, D. M., et al. (2010). Directed 3d cell alignment and elongation in microengineered hydrogels. *Biomaterials, 31*(27), 6941-6951. doi: 10.1016/j.biomaterials.2010.05.056

Avolio, E., Meloni, M., Spencer, H. L., Riu, F., Katare, R., Mangialardi, G., et al. (2015). Combined intramyocardial delivery of human pericytes and cardiac stem cells additively improves the healing of mouse infarcted hearts through stimulation of vascular and muscular repair. *Circulation Research, 116*(10), e81. Retrieved from http://circres.ahajournals.org/content/116/10/e81.abstract

Baar, K., Birla, R., Boluyt, M. O., Borschel, G. H., Arruda, E. M., & Dennis, R. G. (2005). Self-organization of rat cardiac cells into contractile 3-d cardiac tissue. *The FASEB Journal, 19*(2), 275-277. doi:10.1096/fj.04-2034fje

Baei, P., Jalili-Firoozinezhad, S., Rajabi-Zeleti, S., Tafazzoli-Shadpour, M., Baharvand, H., & Aghdami, N. (2016). Electrically conductive gold nanoparticle-chitosan thermosensitive hydrogels for cardiac tissue engineering. *Materials Science and Engineering: C, 63*, 131-141. doi: 10.1016/j.msec.2016.02.056

Banerjee, I., Yekkala, K., Borg, T. K., & Baudino, T. A. (2006). Dynamic interactions between myocytes, fibroblasts, and extracellular matrix. *Annals of the New York Academy of Sciences, 1080*(1), 76-84. doi:10.1196/annals.1380.007

Baranes, K., Shevach, M., Shefi, O., & Dvir, T. (2016). Gold nanoparticle-decorated scaffolds promote neuronal differentiation and maturation. *Nano Letters, 16*(5), 2916-2920. doi:10.1021/acs.nanolett.5b04033

Bartolucci, J., Verdugo, F. J., González, P. L., Larrea, R. E., Abarzua, E., Goset, C., et al. (2017). Safety and efficacy of the intravenous infusion of umbilical cord mesenchymal stem cells in patients with heart failure. *Circulation Research, 121*(10), 1192. Retrieved from http://circres.ahajournals.org/content/121/10/1192.abstract

Baxter, S. C., Morales, M. O., & Goldsmith, E. C. (2008). Adaptive changes in cardiac fibroblast morphology and collagen organization as a result of mechanical environment. *Cell Biochemistry and Biophysics, 51*(1), 33-44. doi:10.1007/s12013-008-9013-8

Bazan, C., Barba, D. T., Blomgren, P., & Paolini, P. (2009). Image processing techniques for assessing contractility in isolated adult cardiac myocytes. *International Journal of Biomedical Imaging, 2009*, 11. doi:10.1155/2009/352954

Bellamy, V., Vanneaux, V., Bel, A., Nemetalla, H., Emmanuelle Boitard, S., Farouz, Y., et al. (2015). Long-term functional benefits of human embryonic stem cell-derived cardiac progenitors embedded into a fibrin scaffold. *The Journal of Heart and Lung Transplantation, 34*(9), 1198-1207. doi: 10.1016/j.healun.2014.10.008

Belostotskaya, G., & Golovanova, T. (2014). Characterization of contracting cardiomyocyte colonies in the primary culture of neonatal rat myocardial cells: A model of in vitro cardiomyogenesis. *Cell Cycle, 13*(6), 910-918. doi:10.4161/cc.27768

Beltrami, A. P., Barlucchi, L., Torella, D., Baker, M., Limana, F., Chimenti, S., et al. (2003). Adult cardiac stem cells are multipotent and support myocardial regeneration. *Cell, 114*(6), 763-776. doi: 10.1016/S0092-8674(03)00687-1

Benjamin, E. J., Blaha, M. J., Chiuve, S. E., Cushman, M., Das, S. R., Deo, R., et al. (2017). Heart disease and stroke statistics-2017 update: A report from the american heart association. *Circulation, 135*(10), e146-e603. doi:10.1161/CIR.0000000000000485

Bergmann, O., Bhardwaj, R. D., Bernard, S., Zdunek, S., Barnabé-Heider, F., Walsh, S., et al. (2009). Evidence for cardiomyocyte renewal in humans. *Science, 324*(5923), 98-102. doi:10.1126/science.1164680

Bertassoni, L. E., Cecconi, M., Manoharan, V., Nikkhah, M., Hjortnaes, J., Cristino, A. L., et al. (2014). Hydrogel bioprinted microchannel networks for vascularization of tissue engineering constructs. *Lab on a Chip, 14*(13), 2202-2211. doi:10.1039/C4LC00030G

Betancourt, T., & Brannon-Peppas, L. (2006). Micro- and nanofabrication methods in nanotechnological medical and pharmaceutical devices. *International Journals of Nanomedicine, 1*(4), 483-495. Retrieved from https://www.ncbi.nlm.nih.gov/pubmed/17722281

Bhana, B., Iyer, R. K., Chen, W. L. K., Zhao, R., Sider, K. L., Likhitpanichkul, M., et al. (2010). Influence of substrate stiffness on the phenotype of heart cells. *Biotechnology and Bioengineering, 105*(6), 1148-1160. doi:10.1002/bit.22647

Bhang, S. H., Cho, S.-W., La, W.-G., Lee, T.-J., Yang, H. S., Sun, A.-Y., et al. (2011). Angiogenesis in ischemic tissue produced by spheroid grafting of human adipose-derived stromal cells. *Biomaterials, 32*(11), 2734-2747. doi: 10.1016/j.biomaterials.2010.12.035

Bonios, M., Terrovitis, J., Chang, C. Y., Engles, J. M., Higuchi, T., Lautamäki, R., et al. (2011). Myocardial substrate and route of administration determine acute cardiac retention and lung bio-distribution of cardiosphere-derived cells. *Journal of Nuclear Cardiology, 18*(3), 443. doi:10.1007/s12350-011-9369-9

Boothe, S. D., Myers, J. D., Pok, S., Sun, J., Xi, Y., Nieto, R. M., et al. (2016). The effect of substrate stiffness on cardiomyocyte action potentials. *Cell Biochemistry and Biophysics, 74*(4), 527-535. doi:10.1007/s12013-016-0758-1

Buckberg, G., Mahajan, A., Saleh, S., Hoffman, J. I. E., & Coghlan, C. (2008). Structure and function relationships of the helical ventricular myocardial band. *The Journal of Thoracic and Cardiovascular Surgery, 136*(3), 578-589.e511. doi: 10.1016/j.jtcvs.2007.10.088

Bursac, N., Loo, Y., Leong, K., & Tung, L. (2007). Novel anisotropic engineered cardiac tissues: Studies of electrical propagation. *Biochemical and Biophysical Research Communications, 361*(4), 847-853. doi: 10.1016/j.bbrc.2007.07.138

Bursac, N., Papadaki, M., Cohen, R. J., Schoen, F. J., Eisenberg, S. R., Carrier, R., et al. (1999). Cardiac muscle tissue engineering: Toward an in vitro model for electrophysiological studies. *American Journal of Physiology-Heart and Circulatory Physiology, 277*(2), H433-H444. doi:10.1152/ajpheart.1999.277.2.H433

Bursac, N., Parker, K. K., Iravanian, S., & Tung, L. (2002). Cardiomyocyte cultures with controlled macroscopic anisotropy: A model for functional electrophysiological studies of cardiac muscle. *Circulation Research, 91*(12), e45-e54. doi:10.1161/01.res.0000047530.88338.eb

Cai, L., Dewi, R. E., & Heilshorn, S. C. (2015). Injectable hydrogels with in situ double network formation enhance retention of transplanted stem cells. *Advanced Functional Materials, 25*(9), 1344-1351. doi:10.1002/adfm.201403631

Camci-Unal, G., Annabi, N., Dokmeci, M. R., Liao, R., & Khademhosseini, A. (2014). Hydrogels for cardiac tissue engineering. *Npg Asia Materials, 6*, e99. doi:10.1038/am.2014.19

Camelliti, P., Borg, T. K., & Kohl, P. (2005). Structural and functional characterisation of cardiac fibroblasts. *Cardiovascular Research, 65*(1), 40-51. doi:10.1016/j.cardiores.2004.08.020

Camelliti, P., Devlin, G. P., Matthews, K. G., Kohl, P., & Green, C. R. (2004). Spatially and temporally distinct expression of fibroblast connexins after sheep ventricular infarction. *Cardiovascular Research, 62*(2), 415-425. doi:10.1016/j.cardiores.2004.01.027

Camelliti, P., Gallagher, J. O., Kohl, P., & McCulloch, A. D. (2006). Micropatterned cell cultures on elastic membranes as an in vitro model of myocardium. *Nature Protocols, 1*, 1379. doi:10.1038/nprot.2006.203

Campbell, N. G., & Suzuki, K. (2012). Cell delivery routes for stem cell therapy to the heart: Current and future approaches. *Journal of Cardiovascular Translational Research, 5*(5), 713-726. doi:10.1007/s12265-012-9378-3

Carbone, F., Nencioni, A., Mach, F., Vuilleumier, N., & Montecucco, F. (2013). Pathophysiological role of neutrophils in acute myocardial infarction. *Thromb Haemost, 110*(3), 501-514. doi:10.1160/TH13-03-0211

Carson, D., Hnilova, M., Yang, X., Nemeth, C. L., Tsui, J. H., Smith, A. S. T., et al. (2016). Nanotopography-induced structural anisotropy and sarcomere development in human cardiomyocytes derived from induced pluripotent stem cells. *ACS Applied Materials & Interfaces, 8*(34), 21923-21932. doi:10.1021/acsami.5b11671

Ceccaldi, C., Fullana, S. G., Alfarano, C., Lairez, O., Calise, D., Cussac, D., et al. (2012). Alginate scaffolds for mesenchymal stem cell cardiac therapy: Influence of alginate composition. *Cell Transplantation, 21*(9), 1969-1984. doi:10.3727/096368912x647252

Cellot, G., Cilia, E., Cipollone, S., Rancic, V., Sucapane, A., Giordani, S., et al. (2008). Carbon nanotubes might improve neuronal performance by favouring electrical shortcuts. *Nature Nanotechnology, 4*, 126. doi:10.1038/nnano.2008.374

Cha, C., Soman, P., Zhu, W., Nikkhah, M., Camci-Unal, G., Chen, S., et al. (2014). Structural reinforcement of cell-laden hydrogels with microfabricated three dimensional scaffolds. *Biomaterials Science, 2*(5), 703-709. doi:10.1039/C3BM60210A

Chan, J., Hanekom, L., Wong, C., Leano, R., Cho, G.-Y., & Marwick, T. H. (2006). Differentiation of subendocardial and transmural infarction using two-dimensional strain rate imaging to assess short-axis and long-axis myocardial function. *Journal of the American College of Cardiology, 48*(10), 2026-2033. doi: 10.1016/j.jacc.2006.07.050

Chang, J.-C., Hsu, S.-h., & Su, H.-L. (2009). The regulation of the gap junction of human mesenchymal stem cells through the internalization of quantum dots. *Biomaterials, 30*(10), 1937-1946. doi: 10.1016/j.biomaterials.2008.12.039

Chen, X., You, B., Zhou, S., & Wu, L. (2003). Surface and interface characterization of polyester-based polyurethane/nano-silica composites. *Surface and Interface Analysis, 35*(4), 369-374. doi:10.1002/sia.1544

Chilton, L., Giles, W. R., & Smith, G. L. (2007). Evidence of intercellular coupling between co-cultured adult rabbit ventricular myocytes and myofibroblasts. *The Journal of Physiology, 583*(1), 225-236. doi:10.1113/jphysiol.2007.135038

Chiu, L. L. Y., Janic, K., & Radisic, M. (2012). Engineering of oriented myocardium on three-dimensional micropatterned collagen-chitosan hydrogel. *The International Journal of Artificial Organs, 35*(4), 237-250. doi:10.5301/ijao.5000084

Choi, J., Yang, J., Park, J., Kim, E., Suh, J. S., Huh, Y. M., et al. (2011). Specific near-ir absorption imaging of glioblastomas using integrin-targeting gold nanorods. *Advanced Functional Materials, 21*(6), 1082-1088. doi:doi:10.1002/adfm.201002253

Chong, J. J. H., Yang, X., Don, C. W., Minami, E., Liu, Y.-W., Weyers, J. J., et al. (2014). Human embryonic-stem-cell-derived cardiomyocytes regenerate non-human primate hearts. *Nature, 510*, 273. doi:10.1038/nature13233

Christia, P., Bujak, M., Gonzalez-Quesada, C., Chen, W., Dobaczewski, M., Reddy, A., et al. (2013). Systematic characterization of myocardial inflammation, repair, and remodeling in a mouse model of reperfused myocardial infarction. *Journal of Histochemistry & Cytochemistry, 61*(8), 555-570. doi:10.1369/0022155413493912

Christman, K. L., Fok, H. H., Sievers, R. E., Fang, Q., & Lee, R. J. (2004a). Fibrin glue alone and skeletal myoblasts in a fibrin scaffold preserve cardiac function after myocardial infarction. *Tissue Eng, 10*(3-4), 403-409. doi:10.1089/107632704323061762

Christman, K. L., & Lee, R. J. (2006). Biomaterials for the treatment of myocardial infarction. *Journal of the American College of Cardiology, 48*(5), 907-913. doi: 10.1016/j.jacc.2006.06.005

Christman, K. L., Vardanian, A. J., Fang, Q., Sievers, R. E., Fok, H. H., & Lee, R. J. (2004b). Injectable fibrin scaffold improves cell transplant survival, reduces infarct expansion, and induces neovasculature formation in ischemic myocardium. *Journal of the American College of Cardiology, 44*(3), 654-660. doi: 10.1016/j.jacc.2004.04.040

Chugh, A. R., Beache, G. M., Loughran, J. H., Mewton, N., Elmore, J. B., Kajstura, J., et al. (2012). Administration of cardiac stem cells in patients with ischemic cardiomyopathy: The scipio trial. *Circulation, 126*(11 suppl 1), S54-S64.doi:10.1161/circulationaha.112.092627

Chung, E. S., Miller, L., Patel, A. N., Anderson, R. D., Mendelsohn, F. O., Traverse, J., et al. (2015). Changes in ventricular remodelling and clinical status during the year following a single administration of stromal cell-derived factor-1 non-viral gene therapy in chronic ischaemic heart failure patients: The stop-hf randomized phase ii trial. *European Heart Journal, 36*(33), 2228-2238. doi:10.1093/eurheartj/ehv254

Cleutjens, J. P. M., Kandala, J. C., Guarda, E., Guntaka, R. V., & Weber, K. T. (1995). Regulation of collagen degradation in the rat myocardium after infarction. *Journal of Molecular and Cellular Cardiology, 27*(6), 1281-1292. doi: 10.1016/S0022-2828(05)82390-9

Cobley, C. M., Chen, J., Cho, E. C., Wang, L. V., & Xia, Y. (2011). Gold nanostructures: A class of multifunctional materials for biomedical applications. *Chemical Society Reviews, 40*(1), 44-56. doi:10.1039/B821763G

Coghlan, H. C., Coghlan, A. R., Buckberg, G. D., Gharib, M., & Cox, J. L. (2001). The structure and function of the helical heart and its buttress wrapping. Iii. The electric spiral of the heart: The hypothesis of the anisotropic conducting matrix. *Seminars in Thoracic and Cardiovascular Surgery, 13*(4), 333-341. doi: 10.1053/stcs.2001.29955

Connor, E. E., Mwamuka, J., Gole, A., Murphy, C. J., & Wyatt, M. D. (2005). Gold nanoparticles are taken up by human cells but do not cause acute cytotoxicity. *Small, 1*(3), 325-327. doi:10.1002/smll.200400093

Cui, H.-F., Vashist, S. K., Al-Rubeaan, K., Luong, J. H. T., & Sheu, F.-S. (2010). Interfacing carbon nanotubes with living mammalian cells and cytotoxicity issues. *Chemical Research in Toxicology, 23*(7), 1131-1147. doi:10.1021/tx100050h

Cui, H., Liu, Y., Cheng, Y., Zhang, Z., Zhang, P., Chen, X., et al. (2014). In vitro study of electroactive tetraaniline-containing thermosensitive hydrogels for cardiac tissue engineering. *Biomacromolecules, 15*(4), 1115-1123. doi:10.1021/bm4018963

Cui, Z., Lee, B. H., & Vernon, B. L. (2007). New hydrolysis-dependent thermosensitive polymer for an injectable degradable system. *Biomacromolecules, 8*(4), 1280-1286. doi:10.1021/bm061045g

Cui, Z., Yang, B., & Li, R.-K. (2016). Application of biomaterials in cardiac repair and regeneration. *Engineering, 2*(1), 141-148. doi: 10.1016/J.ENG.2016.01.028

Cutts, J., Nikkhah, M., & Brafman, D. A. (2015). Biomaterial approaches for stem cell-based myocardial tissue engineering:Supplementary issue: Stem cell biology. *Biomarker Insights, 10s1*, BMI.S20313. doi:10.4137/bmi.s20313

Czyz, J., Guan, K., Zeng, Q., & Wobus, A. M. (2005). Loss of beta 1 integrin function results in upregulation of connexin expression in embryonic stem cell-derived cardiomyocytes. *Int J Dev Biol, 49*(1), 33-41. doi:10.1387/ijdb.041835jc

Dai, W., Hale, S. L., Kay, G. L., Jyrala, A. J., & Kloner, R. A. (2009). Delivering stem cells to the heart in a collagen matrix reduces relocation of cells to other organs as assessed by nanoparticle technology. *Regenerative Medicine, 4*(3), 387-395. doi:10.2217/rme.09.2

Dalby, M. J., Gadegaard, N., Tare, R., Andar, A., Riehle, M. O., Herzyk, P., et al. (2007). The control of human mesenchymal cell differentiation using nanoscale symmetry and disorder. *Nature Materials, 6*, 997. doi:10.1038/nmat2013

Davis, M. E., Motion, J. P., Narmoneva, D. A., Takahashi, T., Hakuno, D., Kamm, R. D., et al. (2005). Injectable self-assembling peptide nanofibers create intramyocardial microenvironments for endothelial cells. *Circulation, 111*(4), 442-450. doi:10.1161/01.CIR.0000153847.47301.80

Deok-Ho, K., Pilnam, K., Suh, K. Y., Seung Kyu, C., Sang Ho, L., & Byungkyu, K. (2005, 17-18 Jan. 2006). *Modulation of adhesion and growth of cardiac myocytes by surface nanotopography.* Paper presented at the 2005 IEEE Engineering in Medicine and Biology 27th Annual Conference.

Desroches, B. R., Zhang, P., Choi, B.-R., King, M. E., Maldonado, A. E., Li, W., et al. (2012). Functional scaffold-free 3-d cardiac microtissues: A novel model for the investigation of heart cells. *American Journal of Physiology-Heart and Circulatory Physiology, 302*(10), H2031-H2042. doi:10.1152/ajpheart.00743.2011

Dolatshahi-Pirouz, A., Nikkhah, M., Gaharwar, A. K., Hashmi, B., Guermani, E., Aliabadi, H., et al. (2014). A combinatorial cell-laden gel microarray for inducing osteogenic differentiation of human mesenchymal stem cells. *Scientific Reports, 4*, 3896. doi:10.1038/srep03896

Dreyer, D. R., Park, S., Bielawski, C. W., & Ruoff, R. S. (2010). The chemistry of graphene oxide. *Chemical Society Reviews, 39*(1), 228-240. doi:10.1039/B917103G

Dumortier, H. (2013). When carbon nanotubes encounter the immune system: Desirable and undesirable effects. *Advanced Drug Delivery Reviews, 65*(15), 2120-2126. doi: 10.1016/j.addr.2013.09.005

Dvir, T., Kedem, A., Ruvinov, E., Levy, O., Freeman, I., Landa, N., et al. (2009). Prevascularization of cardiac patch on the omentum improves its therapeutic outcome. *Proceedings of the National Academy of Sciences, 106*(35), 14990-14995. doi:10.1073/pnas.0812242106

Dvir, T., Timko, B. P., Brigham, M. D., Naik, S. R., Karajanagi, S. S., Levy, O., et al. (2011). Nanowired three-dimensional cardiac patches. *Nature Nanotechnology, 6*, 720. doi:10.1038/nnano.2011.160

Dykman, L., & Khlebtsov, N. (2012). Gold nanoparticles in biomedical applications: Recent advances and perspectives. *Chemical Society Reviews, 41*(6), 2256-2282. doi:10.1039/C1CS15166E

Eatemadi, A., Daraee, H., Karimkhanloo, H., Kouhi, M., Zarghami, N., Akbarzadeh, A., et al. (2014). Carbon nanotubes: Properties, synthesis, purification, and medical applications. *Nanoscale Research Letters, 9*(1), 393. doi:10.1186/1556-276x-9-393

Elbert, D. L., & Hubbell, J. A. (2001). Conjugate addition reactions combined with free-radical cross-linking for the design of materials for tissue engineering. *Biomacromolecules, 2*(2), 430-441. Retrieved from https://www.ncbi.nlm.nih.gov/pubmed/11749203

Ellman, G. L. (1959). Tissue sulfhydryl groups. *Archives of Biochemistry and Biophysics, 82*(1), 70-77. doi: 10.1016/0003-9861(59)90090-6

Emmert, M. Y., Wolint, P., Winklhofer, S., Stolzmann, P., Cesarovic, N., Fleischmann, T., et al. (2013). Transcatheter based electromechanical mapping guided intramyocardial transplantation and in vivo tracking of human stem cell based three dimensional microtissues in the porcine heart. *Biomaterials, 34*(10), 2428-2441. doi: 10.1016/j.biomaterials.2012.12.021

Eng, G., Lee, B. W., Protas, L., Gagliardi, M., Brown, K., Kass, R. S., et al. (2016). Autonomous beating rate adaptation in human stem cell-derived cardiomyocytes. *Nature Communications, 7*, 10312. doi:10.1038/ncomms10312

Engelmayr Jr, G. C., Cheng, M., Bettinger, C. J., Borenstein, J. T., Langer, R., & Freed, L. E. (2008). Accordion-like honeycombs for tissue engineering of cardiac anisotropy. *Nature Materials, 7*, 1003. doi:10.1038/nmat2316

Eschenhagen, T., Eder, A., Vollert, I., & Hansen, A. (2012). Physiological aspects of cardiac tissue engineering. *American Journal of Physiology-Heart and Circulatory Physiology, 303*(2), H133-H143. doi:10.1152/ajpheart.00007.2012

Fan, C., & Wang, D.-A. (2017). Macroporous hydrogel scaffolds for three-dimensional cell culture and tissue engineering. *Tissue Engineering Part B: Reviews, 23*(5), 451-461. doi:10.1089/ten.teb.2016.0465

Farahmand, P., Lai, T. Y. Y., Weisel, R. D., Fazel, S., Yau, T., Menasche, P., et al. (2008). Skeletal myoblasts preserve remote matrix architecture and global function when implanted early or late after coronary ligation into infarcted or remote myocardium. *Circulation, 118*(14 suppl 1), S130-S137. doi:10.1161/circulationaha.107.757617

Fast, V. G., & Kléber, A. G. (1994). Anisotropic conduction in monolayers of neonatal rat heart cells cultured on collagen substrate. *Circulation Research, 75*(3), 591-595. doi:10.1161/01.res.75.3.591

Fernandes, S., Kuklok, S., McGonigle, J., Reinecke, H., & Murry, C. E. (2012). Synthetic matrices to serve as niches for muscle cell transplantation. *Cells Tissues Organs, 195*(1-2), 48-59. Retrieved from https://www.karger.com/DOI/10.1159/000331414

Fernandes, S., Rijen, H. V. M. v., Forest, V., Evain, S., Leblond, A.-L., Mérot, J., et al. (2009). Cardiac cell therapy: Overexpression of connexin43 in skeletal myoblasts and prevention of ventricular arrhythmias. *Journal of Cellular and Molecular Medicine, 13*(9b), 3703-3712. doi:10.1111/j.1582-4934.2009.00740.x

Firme, C. P., & Bandaru, P. R. (2010). Toxicity issues in the application of carbon nanotubes to biological systems. *Nanomedicine: Nanotechnology, Biology and Medicine, 6*(2), 245-256. doi: 10.1016/j.nano.2009.07.003

Fisher, S. A., Zhang, H., Doree, C., Mathur, A., & Martin-Rendon, E. (2015). Stem cell treatment for acute myocardial infarction. *Cochrane Database of Systematic Reviews*(9). doi:10.1002/14651858.CD006536.pub4

Fitzpatrick, S. D., Jafar Mazumder, M. A., Lasowski, F., Fitzpatrick, L. E., & Sheardown, H. (2010). Pnipaam-grafted-collagen as an injectable, in situ gelling, bioactive cell delivery scaffold. *Biomacromolecules, 11*(9), 2261-2267. doi:10.1021/bm100299j

Fleischer, S., Shapira, A., Feiner, R., & Dvir, T. (2017). Modular assembly of thick multifunctional cardiac patches. *Proceedings of the National Academy of Sciences, 114*(8), 1898-1903. doi:10.1073/pnas.1615728114

Fleischer, S., Shevach, M., Feiner, R., & Dvir, T. (2014). Coiled fiber scaffolds embedded with gold nanoparticles improve the performance of engineered cardiac tissues. *Nanoscale, 6*(16), 9410-9414. doi:10.1039/C4NR00300D

Forte, G., Pagliari, S., Ebara, M., Uto, K., Tam, J. K. V., Romanazzo, S., et al. (2012). Substrate stiffness modulates gene expression and phenotype in neonatal cardiomyocytes in vitro. *Tissue Engineering Part A, 18*(17-18), 1837-1848. doi:10.1089/ten.tea.2011.0707

Frangogiannis, N. G. (2015). Pathophysiology of myocardial infarction. *Comprehensive Physiology, 5*(4), 1841-1875. doi:10.1002/cphy.c150006

Frens, G. (1973). Controlled nucleation for the regulation of the particle size in monodisperse gold suspensions. *Nature Physical Science, 241*, 20. doi:10.1038/physci241020a0

Fuhrmann, A., Staunton, J. R., Nandakumar, V., Banyai, N., Davies, P. C., & Ros, R. (2011). Afm stiffness nanotomography of normal, metaplastic and dysplastic human esophageal cells. *Phys Biol, 8*(1), 015007. doi:10.1088/1478-3975/8/1/015007

Fujimoto, K. L., Ma, Z., Nelson, D. M., Hashizume, R., Guan, J., Tobita, K., et al. (2009). Synthesis, characterization and therapeutic efficacy of a biodegradable, thermoresponsive hydrogel designed for application in chronic infarcted myocardium. *Biomaterials, 30*(26), 4357-4368. doi: 10.1016/j.biomaterials.2009.04.055

Furuta, A., Miyoshi, S., Itabashi, Y., Shimizu, T., Kira, S., Hayakawa, K., et al. (2006). Pulsatile cardiac tissue grafts using a novel three-dimensional cell sheet manipulation technique functionally integrates with the host heart, in vivo. *Circulation Research, 98*(5), 705-712. doi:10.1161/01.res.0000209515.59115.70

Gaharwar, A. K., Peppas, N. A., & Khademhosseini, A. (2014). Nanocomposite hydrogels for biomedical applications. *Biotechnology and Bioengineering, 111*(3), 441-453. doi:10.1002/bit.25160

Gaharwar, A. K., Rivera, C., Wu, C.-J., Chan, B. K., & Schmidt, G. (2013). Photocrosslinked nanocomposite hydrogels from peg and silica nanospheres: Structural, mechanical and cell adhesion characteristics. *Materials Science and Engineering: C, 33*(3), 1800-1807. doi: 10.1016/j.msec.2012.12.099

Gaharwar Akhilesh, K., Kishore, V., Rivera, C., Bullock, W., Wu, C. J., Akkus, O., et al. (2012). Physically crosslinked nanocomposites from silicate-crosslinked peo: Mechanical properties and osteogenic differentiation of human mesenchymal stem cells. *Macromolecular Bioscience, 12*(6), 779-793. doi:10.1002/mabi.201100508

Gailit, J., Colflesh, D., Rabiner, I., Simone, J., & Goligorsky, M. S. (1993). Redistribution and dysfunction of integrins in cultured renal epithelial cells exposed to oxidative stress. *American Journal of Physiology-Renal Physiology, 264*(1), F149-F157. doi:10.1152/ajprenal.1993.264.1.F149

GEANDR-Co. (2018). General engineering and research company. Retrieved from https://geandr.com/collections/silica-products/products/silicananoparticles?variant=1190959415302

Giraud, M.-N., Guex, A. G., & Tevaearai, H. T. (2012). Cell therapies for heart function recovery: Focus on myocardial tissue engineering and nanotechnologies. *Cardiology Research and Practice, 2012*, 10. doi:10.1155/2012/971614

Gizurarson, S., Shao, Y., Miljanovic, A., Råmunddal, T., Borén, J., Bergfeldt, L., et al. (2012). Electrophysiological effects of lysophosphatidylcholine on hl-1 cardiomyocytes assessed with a microelectrode array system. *Cellular Physiology and Biochemistry, 30*(2), 477-488. Retrieved from https://www.karger.com/DOI/10.1159/000339029

Gole, A., & Murphy, C. J. (2004). Seed-mediated synthesis of gold nanorods: Role of the size and nature of the seed. *Chemistry of Materials, 16*(19), 3633-3640. doi:10.1021/cm0492336

Gómez-Navarro, C., Weitz, R. T., Bittner, A. M., Scolari, M., Mews, A., Burghard, M., et al. (2007). Electronic transport properties of individual chemically reduced graphene oxide sheets. *Nano Letters, 7*(11), 3499-3503. doi:10.1021/nl072090c

Graudejus, O., Morrison, B., Goletiani, C., Yu, Z., & Wagner, S. (2011). Encapsulating elastically stretchable neural interfaces: Yield, resolution, and recording/stimulation of neural activity. *Advanced Functional Materials, 22*(3), 640-651. doi:10.1002/adfm.201102290

Grover, C. N., Gwynne, J. H., Pugh, N., Hamaia, S., Farndale, R. W., Best, S. M., et al. (2012). Crosslinking and composition influence the surface properties, mechanical stiffness and cell reactivity of collagen-based films. *Acta Biomaterialia, 8*(8), 3080-3090. doi: 10.1016/j.actbio.2012.05.006

Guerrero, P. A., Schuessler, R. B., Davis, L. M., Beyer, E. C., Johnson, C. M., Yamada, K. A., et al. (1997). Slow ventricular conduction in mice heterozygous for a connexin43 null mutation. *The Journal of Clinical Investigation, 99*(8), 1991-1998. doi:10.1172/JCI119367

Gyöngyösi, M., Wojakowski, W., Lemarchand, P., Lunde, K., Tendera, M., Bartunek, J., et al. (2015). Meta-analysis of cell-based cardiac studies (accrue) in patients with acute myocardial infarction based on individual patient data. *Circulation Research, 116*(8), 1346. Retrieved from http://circres.ahajournals.org/content/116/8/1346.abstract

Habib, M., Shapira-Schweitzer, K., Caspi, O., Gepstein, A., Arbel, G., Aronson, D., et al. (2011). A combined cell therapy and in-situ tissue-engineering approach for myocardial repair. *Biomaterials, 32*(30), 7514-7523. doi:10.1016/j.biomaterials.2011.06.049

Halbach, M. D., Egert, U., Hescheler, J., & Banach, K. (2003). Estimation of action potential changes from field potential recordings in multicellular mouse cardiac myocyte cultures.

Cellular Physiology and Biochemistry, 13(5), 271-284. Retrieved from https://www.karger.com/DOI/10.1159/000074542

Han, J., Kim, B., Shin, J. Y., Ryu, S., Noh, M., Woo, J., et al. (2015). Iron oxide nanoparticle-mediated development of cellular gap junction crosstalk to improve mesenchymal stem cells' therapeutic efficacy for myocardial infarction. *ACS Nano, 9*(3), 2805-2819. doi:10.1021/nn506732n

Hansson, E. M., & Lendahl, U. (2013). Regenerative medicine for the treatment of heart disease. *Journal of Internal Medicine, 273*(3), 235-245. doi:10.1111/joim.12033

Hasan, A., Khattab, A., Islam, M. A., Hweij, K. A., Zeitouny, J., Waters, R., et al. (2015). Injectable hydrogels for cardiac tissue repair after myocardial infarction. *Advanced Science, 2*(11), 1500122-n/a. doi:10.1002/advs.201500122

Hass, R., Kasper, C., Böhm, S., & Jacobs, R. (2011). Different populations and sources of human mesenchymal stem cells (msc): A comparison of adult and neonatal tissue-derived msc. *Cell Communication and Signaling, 9*(1), 12. doi:10.1186/1478-811x-9-12

Hassaballah, A. I., Hassan, M. A., Mardi, A. N., & Hamdi, M. (2013). An inverse finite element method for determining the tissue compressibility of human left ventricular wall during the cardiac cycle. *PLOS ONE, 8*(12), e82703. doi:10.1371/journal.pone.0082703

He, J. Q., Ma, Y., Lee, Y., Thomson, J. A., & Kamp, T. J. (2003). Human embryonic stem cells develop into multiple types of cardiac myocytes - action potential characterization. *Circulation Research, 93*(1), 32-39. doi:10.1161/01.Res.0000080317.92718.99

Heffernan, J. M., Overstreet, D. J., Le, L. D., Vernon, B. L., & Sirianni, R. W. (2015). Bioengineered scaffolds for 3d analysis of glioblastoma proliferation and invasion. *Annals of Biomedical Engineering, 43*(8), 1965-1977. doi:10.1007/s10439-014-1223-1

Heffernan, J. M., Overstreet, D. J., Srinivasan, S., Le, L. D., Vernon, B. L., & Sirianni, R. W. (2016). Temperature responsive hydrogels enable transient three-dimensional tumor cultures via rapid cell recovery. *Journal of Biomedical Materials Research Part A, 104*(1), 17-25. doi:10.1002/jbm.a.35534

Hong, K. U., Guo, Y., Li, Q.-H., Cao, P., Al-Maqtari, T., Vajravelu, B. N., et al. (2014). C-kit+ cardiac stem cells alleviate post-myocardial infarction left ventricular dysfunction despite poor engraftment and negligible retention in the recipient heart. *PLOS ONE, 9*(5), e96725. doi:10.1371/journal.pone.0096725

Horckmans, M., Ring, L., Duchene, J., Santovito, D., Schloss, M. J., Drechsler, M., et al. (2017). Neutrophils orchestrate post-myocardial infarction healing by polarizing macrophages towards a reparative phenotype. *Eur Heart J, 38*(3), 187-197. doi:10.1093/eurheartj/ehw002

Hou, D., Youssef, E. A.-S., Brinton, T. J., Zhang, P., Rogers, P., Price, E. T., et al. (2005). Radiolabeled cell distribution after intramyocardial, intracoronary, and interstitial retrograde coronary venous delivery. *Implications for Current Clinical Trials, 112*(9 suppl), I-150-I-156. doi:10.1161/circulationaha.104.526749

Hsiao, C.-W., Bai, M.-Y., Chang, Y., Chung, M.-F., Lee, T.-Y., Wu, C.-T., et al. (2013). Electrical coupling of isolated cardiomyocyte clusters grown on aligned conductive nanofibrous meshes for their synchronized beating. *Biomaterials, 34*(4), 1063-1072. doi: 10.1016/j.biomaterials.2012.10.065

Hu, M., Chen, J., Li, Z.-Y., Au, L., Hartland, G. V., Li, X., et al. (2006). Gold nanostructures: Engineering their plasmonic properties for biomedical applications. *Chemical Society Reviews, 35*(11), 1084-1094. doi:10.1039/B517615H

Huang, C.-C., Wei, H.-J., Yeh, Y.-C., Wang, J.-J., Lin, W.-W., Lee, T.-Y., et al. (2012a). Injectable plga porous beads cellularized by hafscs for cellular cardiomyoplasty. *Biomaterials, 33*(16), 4069-4077. doi: 10.1016/j.biomaterials.2012.02.024

Huang, X., Neretina, S., & El-Sayed, M. A. (2009). Gold nanorods: From synthesis and properties to biological and biomedical applications. *Advanced Materials, 21*(48), 4880-4910. doi:10.1002/adma.200802789

Huang, Y. Y., & Terentjev, E. M. (2012b). Dispersion of carbon nanotubes: Mixing, sonication, stabilization, and composite properties. *Polymers, 4*(1), 275. Retrieved from http://www.mdpi.com/2073-4360/4/1/275

Huff, T. B., Hansen, M. N., Zhao, Y., Cheng, J.-X., & Wei, A. (2007). Controlling the cellular uptake of gold nanorods. *Langmuir, 23*(4), 1596-1599. doi:10.1021/la062642r

Hunt, J. A., Chen, R., van Veen, T., & Bryan, N. (2014). Hydrogels for tissue engineering and regenerative medicine. *Journal of Materials Chemistry B, 2*(33), 5319-5338. doi:10.1039/C4TB00775A

Ifkovits, J. L., Tous, E., Minakawa, M., Morita, M., Robb, J. D., Koomalsingh, K. J., et al. (2010). Injectable hydrogel properties influence infarct expansion and extent of postinfarction left ventricular remodeling in an ovine model. *Proceedings of the National Academy of Sciences, 107*(25), 11507-11512. doi:10.1073/pnas.1004097107

Ince, H., Petzsch, M., Rehders, T. C., Chatterjee, T., & Nienaber, C. A. (2004). Transcatheter transplantation of autologous skeletal myoblasts in postinfarction patients with severe left ventricular dysfunction. *Journal of Endovascular Therapy, 11*(6), 695-704. doi:10.1583/04-1386r.1

Israeli-Rosenberg, S., Manso, A. M., Okada, H., & Ross, R. S. (2014). Integrins and integrin-associated proteins in the cardiac myocyte. *Circulation Research, 114*(3), 572-586. doi:10.1161/circresaha.114.301275

Jacot, J. G., McCulloch, A. D., & Omens, J. H. (2008). Substrate stiffness affects the functional maturation of neonatal rat ventricular myocytes. *Biophysical Journal, 95*(7), 3479-3487. doi:10.1529/biophysj.107.124545

Jadczyk, T., Faulkner, A., & Madeddu, P. (2013). Stem cell therapy for cardiovascular disease: The demise of alchemy and rise of pharmacology. *British Journal of Pharmacology, 169*(2), 247-268. doi:doi:10.1111/j.1476-5381.2012.01965.x

Jain, S., & Kapur, R. (2012). Comparative evaluation of accuracy of two electronic apex locators in the presence of various irrigants: An in vitro study. *Contemporary Clinical Dentistry, 3*(6), 140-145. doi:10.4103/0976-237x.101068

Jiang, X.-J., Wang, T., Li, X.-Y., Wu, D.-Q., Zheng, Z.-B., Zhang, J.-F., et al. (2009). Injection of a novel synthetic hydrogel preserves left ventricle function after myocardial infarction. *Journal of Biomedical Materials Research Part A, 90A*(2), 472-477. doi:10.1002/jbm.a.32118

Jiang, X.-M., Wang, L.-M., Wang, J., & Chen, C.-Y. (2012). Gold nanomaterials: Preparation, chemical modification, biomedical applications and potential risk assessment. *Applied Biochemistry and Biotechnology, 166*(6), 1533-1551. doi:10.1007/s12010-012-9548-4

Jing, D., Parikh, A., Canty, J. M., & Tzanakakis, E. S. (2008). Stem cells for heart cell therapies. *Tissue Engineering Part B: Reviews, 14*(4), 393-406. doi:10.1089/ten.teb.2008.0262

Johnson, T. D., & Christman, K. L. (2013). Injectable hydrogel therapies and their delivery strategies for treating myocardial infarction. *Expert Opinion on Drug Delivery, 10*(1), 59-72. doi:10.1517/17425247.2013.739156

Jongpaiboonkit, L., King, W. J., Lyons, G. E., Paguirigan, A. L., Warrick, J. W., Beebe, D. J., et al. (2008). An adaptable hydrogel array format for 3-dimensional cell culture and analysis. *Biomaterials, 29*(23), 3346-3356. doi: 10.1016/j.biomaterials.2008.04.040

Jung, D., Minami, I., Patel, S., Lee, J., Jiang, B., Yuan, Q., et al. (2012). Incorporation of functionalized gold nanoparticles into nanofibers for enhanced attachment and differentiation of mammalian cells. *Journal of Nanobiotechnology, 10*(1), 23. doi:10.1186/1477-3155-10-23

Kaneko, T., Nomura, F., & Yasuda, K. (2011). On-chip constructive cell-network study (i): Contribution of cardiac fibroblasts to cardiomyocyte beating synchronization and community effect. *Journal of Nanobiotechnology, 9*(1), 21. doi:10.1186/1477-3155-9-21

Kanelidis, A. J., Premer, C., Lopez, J., Balkan, W., & Hare, J. M. (2017). Route of delivery modulates the efficacy of mesenchymal stem cell therapy for myocardial infarction. *Circulation Research, 120*(7), 1139-1150. doi:10.1161/circresaha.116.309819

Kang, W. H., Cao, W., Graudejus, O., Patel, T. P., Wagner, S., Meaney, D. F., et al. (2014). Alterations in hippocampal network activity after in vitro traumatic brain injury. *Journal of Neurotrauma, 32*(13), 1011-1019. doi:10.1089/neu.2014.3667

Keevil, V. L., Huang, C. L. H., Chau, P. L., Sayeed, R. A., & Vandenberg, J. I. (2000). The effect of heptanol on the electrical and contractile function of the isolated, perfused rabbit heart. *Pflügers Archiv, 440*(2), 275-282. doi:10.1007/s004240000264

Khalil, S., & Sun, W. (2009). Bioprinting endothelial cells with alginate for 3d tissue constructs. *Journal of Biomechanical Engineering, 131*(11), 111002-111002-111008. doi:10.1115/1.3128729

Kharaziha, M., Memic, A., Akbari, M., Brafman, D. A., & Nikkhah, M. (2016). Nano-enabled approaches for stem cell-based cardiac tissue engineering. *Advanced Healthcare Materials, 5*(13), 1533-1553. doi:10.1002/adhm.201600088

Kharaziha, M., Nikkhah, M., Shin, S.-R., Annabi, N., Masoumi, N., Gaharwar, A. K., et al. (2013). Pgs:Gelatin nanofibrous scaffolds with tunable mechanical and structural properties for engineering cardiac tissues. *Biomaterials, 34*(27), 6355-6366. doi: 10.1016/j.biomaterials.2013.04.045

Kharaziha, M., Shin, S. R., Nikkhah, M., Topkaya, S. N., Masoumi, N., Annabi, N., et al. (2014). Tough and flexible cnt–polymeric hybrid scaffolds for engineering cardiac constructs. *Biomaterials, 35*(26), 7346-7354. doi: 10.1016/j.biomaterials.2014.05.014

Khelifa, F., Druart, M.-E., Habibi, Y., Rioboo, R., Olivier, M., De Coninck, J., et al. (2013). Effect of photo-crosslinking on the performance of silica nanoparticle-filled epoxidized acrylic copolymer coatings. *Journal of Materials Chemistry A, 1*(35), 10334-10344. doi:10.1039/C3TA11668A

Khera, S., Kolte, D., & Bhatt, D. L. (2016). Chapter 16 - percutaneous coronary intervention a2 - aronow, wilbert s. In J. A. McClung (Ed.), *Translational research in coronary artery disease* (pp. 179-194). Boston: Academic Press.

Khlebtsov, N., & Dykman, L. (2011). Biodistribution and toxicity of engineered gold nanoparticles: A review of in vitro and in vivo studies. *Chemical Society Reviews, 40*(3), 1647-1671. doi:10.1039/C0CS00018C

Kikuchi, K., & Poss, K. D. (2012). Cardiac regenerative capacity and mechanisms. *Annual Review of Cell and Developmental Biology, 28*(1), 719-741. doi:10.1146/annurev-cellbio-101011-155739

Kim, D.-H., Lipke, E. A., Kim, P., Cheong, R., Thompson, S., Delannoy, M., et al. (2010). Nanoscale cues regulate the structure and function of macroscopic cardiac tissue constructs. *Proceedings of the National Academy of Sciences, 107*(2), 565-570. doi:10.1073/pnas.0906504107

Kim, S.-W., Houge, M., Brown, M., Davis, M. E., & Yoon, Y.-s. (2014). Cultured human bone marrow–derived cd31+ cells are effective for cardiac and vascular repair through enhanced angiogenic, adhesion, and anti-inflammatory effects. *Journal of the American College of Cardiology, 64*(16), 1681-1694. doi: 10.1016/j.jacc.2014.06.1204

Kim, S. B., Bae, H., Cha, J. M., Moon, S. J., Dokmeci, M. R., Cropek, D. M., et al. (2011). A cell-based biosensor for real-time detection of cardiotoxicity using lensfree imaging. *Lab on a Chip, 11*(10), 1801-1807. doi:10.1039/C1LC20098D

King, J., Huang, C., & Fraser, J. (2013). Determinants of myocardial conduction velocity: Implications for arrhythmogenesis. *Frontiers in Physiology, 4*(154). doi:10.3389/fphys.2013.00154

Kinnear, C., Dietsch, H., Clift Martin, J. D., Endes, C., Rothen-Rutishauser, B., & Petri-Fink, A. (2013). Gold nanorods: Controlling their surface chemistry and complete detoxification by a two-step place exchange. *Angewandte Chemie International Edition, 52*(7), 1934-1938. doi:10.1002/anie.201208568

Kirchhoff, S., Nelles, E., Hagendorff, A., Krüger, O., Traub, O., & Willecke, K. (1998). Reduced cardiac conduction velocity and predisposition to arrhythmias in connexin40-deficient mice. *Current Biology, 8*(5), 299-302. doi: 10.1016/S0960-9822(98)70114-9

Klotz, B. J., Gawlitta, D., Rosenberg, A. J. W. P., Malda, J., & Melchels, F. P. W. (2016). Gelatin-methacryloyl hydrogels: Towards biofabrication-based tissue repair. *Trends in Biotechnology, 34*(5), 394-407. doi: 10.1016/j.tibtech.2016.01.002

Kofidis, T., de Bruin, J. L., Hoyt, G., Lebl, D. R., Tanaka, M., Yamane, T., et al. (2004). Injectable bioartificial myocardial tissue for large-scale intramural cell transfer and functional recovery of injured heart muscle. *The Journal of Thoracic and Cardiovascular Surgery, 128*(4), 571-578. doi: 10.1016/j.jtcvs.2004.05.021

Kofron Celinda, M., & Mende, U. (2017). In vitro models of the cardiac microenvironment to study myocyte and non-myocyte crosstalk: Bioinspired approaches beyond the polystyrene dish. *The Journal of Physiology, 595*(12), 3891-3905. doi:10.1113/JP273100

Kohl, P. (2003). Heterogeneous cell coupling in the heart: An electrophysiological role for fibroblasts. *Circulation Research, 93*(5), 381-383. doi:10.1161/01.res.0000091364.90121.0c

Kolanowski, T. J., Antos, C. L., & Guan, K. (2017). Making human cardiomyocytes up to date: Derivation, maturation state and perspectives. *International Journal of Cardiology, 241*, 379-386. doi: 10.1016/j.ijcard.2017.03.099

Konstam, M. A., Kramer, D. G., Patel, A. R., Maron, M. S., & Udelson, J. E. (2011). Left ventricular remodeling in heart failure: Current concepts in clinical significance and assessment. *JACC: Cardiovascular Imaging, 4*(1), 98-108. doi: 10.1016/j.jcmg.2010.10.008

Kraehenbuehl, T. P., Zammaretti, P., Van der Vlies, A. J., Schoenmakers, R. G., Lutolf, M. P., Jaconi, M. E., et al. (2008). Three-dimensional extracellular matrix-directed cardioprogenitor differentiation: Systematic modulation of a synthetic cell-responsive peg-hydrogel. *Biomaterials, 29*(18), 2757-2766. doi: 10.1016/j.biomaterials.2008.03.016

Kubasiak, L. A., Hernandez, O. M., Bishopric, N. H., & Webster, K. A. (2002). Hypoxia and acidosis activate cardiac myocyte death through the bcl-2 family protein bnip3. *Proceedings of the National Academy of Sciences, 99*(20), 12825-12830. doi:10.1073/pnas.202474099

Kumar, V., Abbas, A. K., Aster, J. C., & Perkins, J. A. (2017). *Robbins basic pathology* (Tenth edition. ed.). Philadelphia, Pennsylvania: Elsevier.

Kutschka, I., Chen, I. Y., Kofidis, T., Arai, T., von Degenfeld, G., Sheikh, A. Y., et al. (2006). Collagen matrices enhance survival of transplanted cardiomyoblasts and contribute to functional improvement of ischemic rat hearts. *Circulation, 114*(1 suppl), I-167-I-173. doi:10.1161/circulationaha.105.001297

Lambert, J. M., Lopez, E. F., & Lindsey, M. L. (2008). Macrophage roles following myocardial infarction. *International Journal of Cardiology, 130*(2), 147-158. doi: 10.1016/j.ijcard.2008.04.059

Lavine, L., & Upcott, H. (1937). Myocardial ischaemia treated by graft of skeletal muscle to the heart. *Proc R Soc Med, 30*(6), 772. Retrieved from https://www.ncbi.nlm.nih.gov/pubmed/19991105

Le, T. Y. L., & Chong, J. J. H. (2016). Cardiac progenitor cells for heart repair. *Cell Death Discovery, 2*, 16052. doi:10.1038/cddiscovery.2016.52

Lee, B. H., West, B., McLemore, R., Pauken, C., & Vernon, B. L. (2006). In-situ injectable physically and chemically gelling nipaam-based copolymer system for embolization. *Biomacromolecules, 7*(6), 2059-2064. doi:10.1021/bm060211h

Lee, E. J., Park, S. J., Kang, S. K., Kim, G.-H., Kang, H.-J., Lee, S.-W., et al. (2012). Spherical bullet formation via e-cadherin promotes therapeutic potency of mesenchymal stem cells derived from human umbilical cord blood for myocardial infarction. *Molecular Therapy, 20*(7), 1424-1433. doi: 10.1038/mt.2012.58

Lee, T.-J., Kang, S., Jeong, G.-J., Yoon, J.-K., Bhang, S. H., Oh, J., et al. (2014). Incorporation of gold-coated microspheres into embryoid body of human embryonic stem cells for cardiomyogenic differentiation. *Tissue Engineering Part A, 21*(1-2), 374-381. doi:10.1089/ten.tea.2014.0015

Lee, W.-Y., Wei, H.-J., Lin, W.-W., Yeh, Y.-C., Hwang, S.-M., Wang, J.-J., et al. (2011). Enhancement of cell retention and functional benefits in myocardial infarction using human amniotic-fluid stem-cell bodies enriched with endogenous ecm. *Biomaterials, 32*(24), 5558-5567. doi: 10.1016/j.biomaterials.2011.04.031

Lee, Y. H., Lee, J. H., An, I.-G., Kim, C., Lee, D. S., Lee, Y. K., et al. (2005). Electrospun dual-porosity structure and biodegradation morphology of montmorillonite reinforced plla nanocomposite scaffolds. *Biomaterials, 26*(16), 3165-3172. doi: 10.1016/j.biomaterials.2004.08.018

Leor, J., Aboulafia-Etzion, S., Dar, A., Shapiro, L., Barbash, I. M., Battler, A., et al. (2000). Bioengineered cardiac grafts: A new approach to repair the infarcted myocardium? *Circulation, 102*(suppl 3), Iii-56-Iii-61. doi:10.1161/01.CIR.102.suppl_3.III-56

Li, K., Chi, Y., Gao, K., Yan, Q., Matsue, H., Takeda, M., et al. (2013). Connexin43 hemichannel-mediated regulation of connexin43. *PLoS ONE, 8*(2), e58057-e58057. doi:10.1371/journal.pone.0058057

Li, L., Chen, X., Wang, W. E., & Zeng, C. (2016a). How to improve the survival of transplanted mesenchymal stem cell in ischemic heart? *Stem Cells International, 2016*, 14. doi:10.1155/2016/9682757

Li, Q., Barrett, D. G., Messersmith, P. B., & Holten-Andersen, N. (2016b). Controlling hydrogel mechanics via bio-inspired polymer–nanoparticle bond dynamics. *ACS Nano, 10*(1), 1317-1324. doi:10.1021/acsnano.5b06692

Li, R.-K., Jia, Z.-Q., Weisel, R. D., Mickle, D. A. G., Choi, A., & Yau, T. M. (1999). Survival and function of bioengineered cardiac grafts. *Circulation, 100*(suppl 2), II-63-Ii-69. doi:10.1161/01.CIR.100.suppl_2.II-63

Li, X., Zhou, J., Liu, Z., Chen, J., Lü, S., Sun, H., et al. (2014). A pnipaam-based thermosensitive hydrogel containing swcnts for stem cell transplantation in myocardial repair. *Biomaterials, 35*(22), 5679-5688. doi: 10.1016/j.biomaterials.2014.03.067

Li, X. Y., Wang, T., Jiang, X. J., Lin, T., Wu, D. Q., Zhang, X. Z., et al. (2010). Injectable hydrogel helps bone marrow-derived mononuclear cells restore infarcted myocardium. *Cardiology, 115*(3), 194-199. Retrieved from https://www.karger.com/DOI/10.1159/000281840

Li, Z., & Guan, J. (2011). Hydrogels for cardiac tissue engineering. *Polymers, 3*(2), 740. Retrieved from http://www.mdpi.com/2073-4360/3/2/740

Liao, H., & Hafner, J. H. (2005). Gold nanorod bioconjugates. *Chemistry of Materials, 17*(18), 4636-4641. doi:10.1021/cm050935k

Liau, B., Zhang, D., & Bursac, N. (2012). Functional cardiac tissue engineering. *Regenerative Medicine, 7*(2), 187-206. doi:10.2217/rme.11.122

Linares, J., Matesanz, M. C., Vila, M., Feito, M. J., Gonçalves, G., Vallet-Regí, M., et al. (2014). Endocytic mechanisms of graphene oxide nanosheets in osteoblasts, hepatocytes and macrophages. *ACS Applied Materials & Interfaces, 6*(16), 13697-13706. doi:10.1021/am5031598

Ling, Z., Juan, S., & Yuemei, H. (2011). Engineering heart tissue grafts improve electrical characteristics. *Heart, 97*(Suppl 3), A67-A67. doi:10.1136/heartjnl-2011-300867.193

Linkermann, A., Konstantinidis, K., & Kitsis, R. N. (2015). Catch me if you can: Targeting the mitochondrial permeability transition pore in myocardial infarction. *Cell Death And Differentiation, 23*, 1. doi:10.1038/cdd.2015.151

Little, L., Healy, K. E., & Schaffer, D. (2008). Engineering biomaterials for synthetic neural stem cell microenvironments. *Chem Rev, 108*(5), 1787-1796. doi:10.1021/cr078228t

Liu, K., Sun, Y., Lin, X., Zhou, R., Wang, J., Fan, S., et al. (2010). Scratch-resistant, highly conductive, and high-strength carbon nanotube-based composite yarns. *ACS Nano, 4*(10), 5827-5834. doi:10.1021/nn1017318

Lloret, P., Longinotti, G., Ybarra, G., Socolovsky, L., & Moina, C. (2013). Synthesis, characterization and biofunctionalization of magnetic gold nanostructured particles. *Materials Research Bulletin, 48*(10), 3671-3676. doi:10.1016/j.materresbull.2013.05.066

Locke Davenport, H., Miles, M., Yimu, Z., Yun, X., Genevieve, C., Anastasia, K., et al. (2015). Biomaterial based cardiac tissue engineering and its applications. *Biomedical Materials, 10*(3), 034004. Retrieved from http://stacks.iop.org/1748-605X/10/i=3/a=034004

Loffredo, Francesco S., Steinhauser, Matthew L., Gannon, J., & Lee, Richard T. (2011). Bone marrow-derived cell therapy stimulates endogenous cardiomyocyte progenitors and promotes cardiac repair. *Cell Stem Cell, 8*(4), 389-398. doi:10.1016/j.stem.2011.02.002

Loh, Q. L., & Choong, C. (2013). Three-dimensional scaffolds for tissue engineering applications: Role of porosity and pore size. *Tissue Engineering Part B: Reviews, 19*(6), 485-502. doi:10.1089/ten.teb.2012.0437

Lovat, V., Pantarotto, D., Lagostena, L., Cacciari, B., Grandolfo, M., Righi, M., et al. (2005). Carbon nanotube substrates boost neuronal electrical signaling. *Nano Letters, 5*(6), 1107-1110. doi:10.1021/nl050637m

Lü, S., Wang, H., Lu, W., Liu, S., Lin, Q., Li, D., et al. (2009). Both the transplantation of somatic cell nuclear transfer- and fertilization-derived mouse embryonic stem cells with temperature-responsive chitosan hydrogel improve myocardial performance in infarcted rat hearts. *Tissue Engineering Part A, 16*(4), 1303-1315. doi:10.1089/ten.tea.2009.0434

Lu, W.-N., Lü, S.-H., Wang, H.-B., Li, D.-X., Duan, C.-M., Liu, Z.-Q., et al. (2008). Functional improvement of infarcted heart by co-injection of embryonic stem cells with temperature-responsive chitosan hydrogel. *Tissue Engineering Part A, 15*(6), 1437-1447. doi:10.1089/ten.tea.2008.0143

Ma, Z., Nelson, D. M., Hong, Y., & Wagner, W. R. (2010). Thermally responsive injectable hydrogel incorporating methacrylate-polylactide for hydrolytic lability. *Biomacromolecules, 11*(7), 1873-1881. doi:10.1021/bm1004299

Ma, Z., Wang, J., Loskill, P., Huebsch, N., Koo, S., Svedlund, F. L., et al. (2015). Self-organizing human cardiac microchambers mediated by geometric confinement. *Nature Communications, 6*, 7413. doi:10.1038/ncomms8413

Malliaras, K., Makkar, R. R., Smith, R. R., Cheng, K., Wu, E., Bonow, R. O., et al. (2014). Intracoronary cardiosphere-derived cells after myocardial infarction: Evidence of therapeutic regeneration in the final 1-year results of the caduceus trial (cardiosphere-derived autologous stem cells to reverse ventricular dysfunction). *Journal of the American College of Cardiology, 63*(2), 110-122. doi: 10.1016/j.jacc.2013.08.724

Marder, V. J. (2013). Thrombolytic therapy a2 - kitchens, craig s. In C. M. Kessler & B. A. Konkle (Eds.), *Consultative hemostasis and thrombosis (third edition)* (pp. 526-537). Philadelphia: W.B. Saunders.

Martinelli, V., Cellot, G., Fabbro, A., Bosi, S., Mestroni, L., & Ballerini, L. (2013a). Improving cardiac myocytes performance by carbon nanotubes platforms. *Frontiers in Physiology, 4*(239). doi:10.3389/fphys.2013.00239

Martinelli, V., Cellot, G., Toma, F. M., Long, C. S., Caldwell, J. H., Zentilin, L., et al. (2012). Carbon nanotubes promote growth and spontaneous electrical activity in cultured cardiac myocytes. *Nano Letters, 12*(4), 1831-1838. doi:10.1021/nl204064s

Martinelli, V., Cellot, G., Toma, F. M., Long, C. S., Caldwell, J. H., Zentilin, L., et al. (2013b). Carbon nanotubes instruct physiological growth and functionally mature syncytia: Nongenetic engineering of cardiac myocytes. *ACS Nano, 7*(7), 5746-5756. doi:10.1021/nn4002193

Maseri, A., Chierchia, S., & Davies, G. (1986). Pathophysiology of coronary occlusion in acute infarction. *Circulation, 73*(2), 233-239. doi:10.1161/01.cir.73.2.233

Masoudpour, H., & Laflamme, M. A. (2017). Cardiac repair with pluripotent stem cell–derived cardiomyocytes: Proof of concept but new challenges. *The Journal of Thoracic and Cardiovascular Surgery, 154*(3), 945-948. doi: 10.1016/j.jtcvs.2017.05.088

Masuda, S., Shimizu, T., Yamato, M., & Okano, T. (2008). Cell sheet engineering for heart tissue repair. *Advanced Drug Delivery Reviews, 60*(2), 277-285. doi: 10.1016/j.addr.2007.08.031

Masumoto, H., Ikuno, T., Takeda, M., Fukushima, H., Marui, A., Katayama, S., et al. (2014). Human ips cell-engineered cardiac tissue sheets with cardiomyocytes and vascular cells for cardiac regeneration. *Scientific Reports, 4*, 6716. doi:10.1038/srep06716

Matsuura, K., Masuda, S., Haraguchi, Y., Yasuda, N., Shimizu, T., Hagiwara, N., et al. (2011). Creation of mouse embryonic stem cell-derived cardiac cell sheets. *Biomaterials, 32*(30), 7355-7362. doi: 10.1016/j.biomaterials.2011.05.042

Mawad, D., Mansfield, C., Lauto, A., Perbellini, F., Nelson, G. W., Tonkin, J., et al. (2016). A conducting polymer with enhanced electronic stability applied in cardiac models. *Science Advances, 2*(11). doi:10.1126/sciadv.1601007

Mazzatenta, A., Giugliano, M., Campidelli, S., Gambazzi, L., Businaro, L., Markram, H., et al. (2007). Interfacing neurons with carbon nanotubes: Electrical signal transfer and synaptic stimulation in cultured brain circuits. *The Journal of Neuroscience, 27*(26), 6931-6936. doi:10.1523/jneurosci.1051-07.2007

McCain, M. L., Agarwal, A., Nesmith, H. W., Nesmith, A. P., & Parker, K. K. (2014). Micromolded gelatin hydrogels for extended culture of engineered cardiac tissues. *Biomaterials, 35*(21), 5462-5471. doi: 10.1016/j.biomaterials.2014.03.052

Mercado, M. G., Smith, D. K., & McConnon, M. L. (2013). Myocardial infarction: Management of the subacute period. *Am Fam Physician, 88*(9), 581-588. Retrieved from https://www.ncbi.nlm.nih.gov/pubmed/24364634

Mihic, A., Cui, Z., Wu, J., Vlacic, G., Miyagi, Y., Li, S.-H., et al. (2015). A conductive polymer hydrogel supports cell electrical signaling and improves cardiac function after implantation into myocardial infarct. *Circulation, 132*(8), 772-784. doi:10.1161/circulationaha.114.014937

Mitchell, G. F., Lamas, G. A., Vaughan, D. E., & Pfeffer, M. A. (1992). Left ventricular remodeling in the year after first anterior myocardial infarction: A quantitative analysis of contractile segment lengths and ventricular shape. *Journal of the American College of Cardiology, 19*(6), 1136-1144. doi: 10.1016/0735-1097(92)90314-D

Miura, M., Nishio, T., Hattori, T., Murai, N., Stuyvers, B. D., Shindoh, C., et al. (2010). Effect of nonuniform muscle contraction on sustainability and frequency of triggered arrhythmias in rat cardiac muscle. *Circulation, 121*(25), 2711-2717. doi:10.1161/circulationaha.109.907717

Monteiro, L. M., Vasques-Nóvoa, F., Ferreira, L., Pinto-do-Ó, P., & Nascimento, D. S. (2017). Restoring heart function and electrical integrity: Closing the circuit. *npj Regenerative Medicine, 2*(1), 9. doi:10.1038/s41536-017-0015-2

Montgomery, M., Ahadian, S., Davenport Huyer, L., Lo Rito, M., Civitarese, R. A., Vanderlaan, R. D., et al. (2017). Flexible shape-memory scaffold for minimally invasive delivery of functional tissues. *Nature Materials, 16*, 1038. doi:10.1038/nmat4956

Mosher, D. F., & Furcht, L. T. (1981). Fibronectin: Review of its structure and possible functions. *Journal of Investigative Dermatology, 77*(2), 175-180. doi: 10.1111/1523-1747.ep12479791

Moulik, S. P., Haque, M. E., Jana, P. K., & Das, A. R. (1996). Micellar properties of cationic surfactants in pure and mixed states. *The Journal of Physical Chemistry, 100*(2), 701-708. doi:10.1021/jp9506494

Mozaffarian, D., Benjamin, E. J., Go, A. S., Arnett, D. K., Blaha, M. J., Cushman, M., et al. (2015). Heart disease and stroke statistics—2015 update: : A report from the american heart association. *Circulation, 131*(4), e29-e322. doi:10.1161/cir.0000000000000152

Müller-Ehmsen, J., Whittaker, P., Kloner, R. A., Dow, J. S., Sakoda, T., Long, T. I., et al. (2002). Survival and development of neonatal rat cardiomyocytes transplanted into adult myocardium. *Journal of Molecular and Cellular Cardiology, 34*(2), 107-116. doi: 10.1006/jmcc.2001.1491

Nadal-Ginard, B., Ellison, G. M., & Torella, D. (2014). The cardiac stem cell compartment is indispensable for myocardial cell homeostasis, repair and regeneration in the adult. *Stem Cell Research, 13*(3, Part B), 615-630. doi: 10.1016/j.scr.2014.04.008

Nakajima, K., Fujita, J., Matsui, M., Tohyama, S., Tamura, N., Kanazawa, H., et al. (2015). Gelatin hydrogel enhances the engraftment of transplanted cardiomyocytes and angiogenesis to ameliorate cardiac function after myocardial infarction. *PLOS ONE, 10*(7), e0133308. doi:10.1371/journal.pone.0133308

Navaei, A., Moore, N., Sullivan, R. T., Truong, D., Migrino, R. Q., & Nikkhah, M. (2017). Electrically conductive hydrogel-based micro-topographies for the development of organized cardiac tissues. *RSC Advances, 7*(6), 3302-3312. doi:10.1039/C6RA26279A

Navaei, A., Saini, H., Christenson, W., Sullivan, R. T., Ros, R., & Nikkhah, M. (2016a). Gold nanorod-incorporated gelatin-based conductive hydrogels for engineering cardiac tissue constructs. *Acta Biomaterialia, 41*, 133-146. doi: 10.1016/j.actbio.2016.05.027

Navaei, A., Truong, D., Heffernan, J., Cutts, J., Brafman, D., Sirianni, R. W., et al. (2016b). Pnipaam-based biohybrid injectable hydrogel for cardiac tissue engineering. *Acta Biomaterialia, 32*, 10-23. doi: 10.1016/j.actbio.2015.12.019

Neely, J. R. (1986, 1986//). *The role of atp depletion and accumulated metabolic products during myocardial ischemia.* Paper presented at the Facts and Hopes in Thrombolysis in Acute Myocardial Infarction, Heidelberg.

Nguyen, Doan C., Hookway, Tracy A., Wu, Q., Jha, R., Preininger, Marcela K., Chen, X., et al. (2014). Microscale generation of cardiospheres promotes robust enrichment of cardiomyocytes derived from human pluripotent stem cells. *Stem Cell Reports, 3*(2), 260-268. doi:10.1016/j.stemcr.2014.06.002

Nguyen, P. K., Rhee, J., & Wu, J. C. (2016). Adult stem cell therapy and heart failure, 2000 to 2016: A systematic review. *JAMA Cardiology, 1*(7), 831-841. doi:10.1001/jamacardio.2016.2225

Nguyen, P. K., & Wu, J. C. (2015). Large animal models of ischemic cardiomyopathy: Are they enough to bridge the translational gap? *Journal of Nuclear Cardiology, 22*(4), 666-672. doi:10.1007/s12350-015-0078-7

Nichol, J. W., Koshy, S. T., Bae, H., Hwang, C. M., Yamanlar, S., & Khademhosseini, A. (2010). Cell-laden microengineered gelatin methacrylate hydrogels. *Biomaterials, 31*(21), 5536-5544. doi: 10.1016/j.biomaterials.2010.03.064

Nicodemus, G. D., & Bryant, S. J. (2008). Cell encapsulation in biodegradable hydrogels for tissue engineering applications. *Tissue Engineering Part B: Reviews, 14*(2), 149-165. doi:10.1089/ten.teb.2007.0332

Nikkhah, M., Eshak, N., Zorlutuna, P., Annabi, N., Castello, M., Kim, K., et al. (2012). Directed endothelial cell morphogenesis in micropatterned gelatin methacrylate hydrogels. *Biomaterials, 33*(35), 9009-9018. doi: 10.1016/j.biomaterials.2012.08.068

Nikoobakht, B., & El-Sayed, M. A. (2003). Preparation and growth mechanism of gold nanorods (nrs) using seed-mediated growth method. *Chemistry of Materials, 15*(10), 1957-1962. doi:10.1021/cm020732l

Orlic, D., Kajstura, J., Chimenti, S., Jakoniuk, I., Anderson, S. M., Li, B., et al. (2001). Bone marrow cells regenerate infarcted myocardium. *Nature, 410*, 701. doi:10.1038/35070587

Overstreet, D. J., Huynh, R., Jarbo, K., McLemore, R. Y., & Vernon, B. L. (2013a). In situ forming, resorbable graft copolymer hydrogels providing controlled drug release. *Journal of Biomedical Materials Research Part A, 101A*(5), 1437-1446. doi:10.1002/jbm.a.34443

Overstreet, D. J., McLemore, R. Y., Doan, B. D., Farag, A., & Vernon, B. L. (2013b). Temperature-responsive graft copolymer hydrogels for controlled swelling and drug delivery. *Soft Materials, 11*(3), 294-304. doi:10.1080/1539445X.2011.640731

Oyamada, M., Kimura, H., Oyamada, Y., Miyamoto, A., Ohshika, H., & Mori, M. (1994). The expression, phosphorylation, and localization of connexin 43 and gap-junctional intercellular communication during the establishment of a synchronized contraction of cultured neonatal rat cardiac myocytes. *Experimental Cell Research, 212*(2), 351-358. doi: 10.1006/excr.1994.1154

Papadaki, M., Bursac, N., Langer, R., Merok, J., Vunjak-Novakovic, G., & Freed, L. E. (2001). Tissue engineering of functional cardiac muscle: Molecular, structural, and electrophysiological studies. *American Journal of Physiology-Heart and Circulatory Physiology, 280*(1), H168-H178. doi:10.1152/ajpheart.2001.280.1.H168

Park, J., Kim, Y. S., Ryu, S., Kang, W. S., Park, S., Han, J., et al. (2015). Graphene potentiates the myocardial repair efficacy of mesenchymal stem cells by stimulating the expression of angiogenic growth factors and gap junction protein. *Advanced Functional Materials, 25*(17), 2590-2600. doi:10.1002/adfm.201500365

Passier, R., van Laake, L. W., & Mummery, C. L. (2008). Stem-cell-based therapy and lessons from the heart. *Nature, 453*, 322. doi:10.1038/nature07040

Paul, A., Hasan, A., Kindi, H. A., Gaharwar, A. K., Rao, V. T. S., Nikkhah, M., et al. (2014). Injectable graphene oxide/hydrogel-based angiogenic gene delivery system for vasculogenesis and cardiac repair. *ACS Nano, 8*(8), 8050-8062. doi:10.1021/nn5020787

Pedron, S., van Lierop, S., Horstman, P., Penterman, R., Broer, D. J., & Peeters, E. (2011). Stimuli responsive delivery vehicles for cardiac microtissue transplantation. *Advanced Functional Materials, 21*(9), 1624-1630. doi:10.1002/adfm.201002708

Peela, N., Sam, F. S., Christenson, W., Truong, D., Watson, A. W., Mouneimne, G., et al. (2016). A three dimensional micropatterned tumor model for breast cancer cell migration studies. *Biomaterials, 81*, 72-83. doi: 10.1016/j.biomaterials.2015.11.039

Peña, B., Martinelli, V., Jeong, M., Bosi, S., Lapasin, R., Taylor, M. R. G., et al. (2016). Biomimetic polymers for cardiac tissue engineering. *Biomacromolecules, 17*(5), 1593-1601. doi:10.1021/acs.biomac.5b01734

Pfeffer, M. A., & Braunwald, E. (1990). Ventricular remodeling after myocardial infarction. Experimental observations and clinical implications. *Circulation, 81*(4), 1161-1172. doi:10.1161/01.cir.81.4.1161

Pfuntner, A., Wier, L. M., & Steiner, C. (2006). Costs for hospital stays in the united states, 2011: Statistical brief #168 *Healthcare cost and utilization project (hcup) statistical briefs*. Rockville (MD).

Pijnappels, D. A., Gregoire, S., & Wu, S. M. (2010). The integrative aspects of cardiac physiology and their implications for cell-based therapy. *Annals of the New York Academy of Sciences, 1188*(1), 7-14. doi:10.1111/j.1749-6632.2009.05077.x

Pimentel, R. C., Yamada, K. A., Kléber, A. G., & Saffitz, J. E. (2002). Autocrine regulation of myocyte cx43 expression by vegf. *Circulation Research, 90*(6), 671. Retrieved from http://circres.ahajournals.org/content/90/6/671.abstract

Pointon, A., Harmer, A. R., Dale, I. L., Abi-Gerges, N., Bowes, J., Pollard, C., et al. (2015). Assessment of cardiomyocyte contraction in human-induced pluripotent stem cell-derived cardiomyocytes. *Toxicological Sciences, 144*(2), 227-237. doi:10.1093/toxsci/kfu312

Pok, S., Myers, J. D., Madihally, S. V., & Jacot, J. G. (2013). A multilayered scaffold of a chitosan and gelatin hydrogel supported by a pcl core for cardiac tissue engineering. *Acta Biomaterialia, 9*(3), 5630-5642. doi: 10.1016/j.actbio.2012.10.032

Pok, S., Vitale, F., Eichmann, S. L., Benavides, O. M., Pasquali, M., & Jacot, J. G. (2014). Biocompatible carbon nanotube–chitosan scaffold matching the electrical conductivity of the heart. *ACS Nano, 8*(10), 9822-9832. doi:10.1021/nn503693h

Prabhu, S. D., & Frangogiannis, N. G. (2016). The biological basis for cardiac repair after myocardial infarction. *From Inflammation to Fibrosis, 119*(1), 91-112. doi:10.1161/circresaha.116.303577

Qin, D., Xia, Y., & Whitesides, G. M. (2010). Soft lithography for micro- and nanoscale patterning. *Nature Protocols, 5*, 491. doi:10.1038/nprot.2009.234

Radisic, M., Park, H., Shing, H., Consi, T., Schoen, F. J., Langer, R., et al. (2004). Functional assembly of engineered myocardium by electrical stimulation of cardiac myocytes cultured on scaffolds. *Proceedings of the National Academy of Sciences, 101*(52), 18129-18134. doi:10.1073/pnas.0407817101

Rask, F., Mihic, A., Reis, L., Dallabrida, S. M., Ismail, N. S., Sider, K., et al. (2010). Hydrogels modified with qhredgs peptide support cardiomyocyte survival in vitro and after sub-cutaneous implantation. *Soft Matter, 6*(20), 5089-5099. doi:10.1039/C0SM00362J

Ravichandran, R., Sridhar, R., Venugopal, J. R., Sundarrajan, S., Mukherjee, S., & Ramakrishna, S. (2014). Gold nanoparticle loaded hybrid nanofibers for cardiogenic differentiation of stem cells for infarcted myocardium regeneration. *Macromolecular Bioscience, 14*(4), 515-525. doi:10.1002/mabi.201300407

Reinecke, H., MacDonald, G. H., Hauschka, S. D., & Murry, C. E. (2000). Electromechanical coupling between skeletal and cardiac muscle. *Journal of Cell Biology, 149*(3), 731-740. doi:10.1083/jcb.149.3.731

Reinecke, H., & Murry, C. E. (2002a). Taking the death toll after cardiomyocyte grafting: A reminder of the importance of quantitative biology. *Journal of Molecular and Cellular Cardiology, 34*(3), 251-253. doi: 10.1006/jmcc.2001.1494

Reinecke, H., Poppa, V., & Murry, C. E. (2002b). Skeletal muscle stem cells do not transdifferentiate into cardiomyocytes after cardiac grafting. *Journal of Molecular and Cellular Cardiology, 34*(2), 241-249. doi: 10.1006/jmcc.2001.1507

Ren, F., Yesildag, C., Zhang, Z., & Lensen, M. C. (2017). Functional peg-hydrogels convey gold nanoparticles from silicon and aid cell adhesion onto the nanocomposites. *Chemistry of Materials, 29*(5), 2008-2015. doi:10.1021/acs.chemmater.6b03548

Reppel, M., Pillekamp, F., Lu, Z. J., Halbach, M., Brockmeier, K., Fleischmann, B. K., et al. (2004). Microelectrode arrays: A new tool to measure embryonic heart activity. *Journal of Electrocardiology, 37*, 104-109. doi:10.1016/j.jelectrocard.2004.08.033

Ribeiro, A. J. S., Ang, Y.-S., Fu, J.-D., Rivas, R. N., Mohamed, T. M. A., Higgs, G. C., et al. (2015a). Contractility of single cardiomyocytes differentiated from pluripotent stem cells depends on physiological shape and substrate stiffness. *Proceedings of the National Academy of Sciences, 112*(41), 12705-12710. doi:10.1073/pnas.1508073112

Ribeiro, M. C., Tertoolen, L. G., Guadix, J. A., Bellin, M., Kosmidis, G., D'Aniello, C., et al. (2015b). Functional maturation of human pluripotent stem cell derived cardiomyocytes in vitro – correlation between contraction force and electrophysiology. *Biomaterials, 51*, 138-150. doi: 10.1016/j.biomaterials.2015.01.067

Richards, D. J., Tan, Y., Coyle, R., Li, Y., Xu, R., Yeung, N., et al. (2016). Nanowires and electrical stimulation synergistically improve functions of hipsc cardiac spheroids. *Nano Letters, 16*(7), 4670-4678. doi:10.1021/acs.nanolett.6b02093

Ridolfi, R. L., & Hutchins, G. M. (1977). The relationship between coronary artery lesions and myocardial infarcts: Ulceration of atherosclerotic plaques precipitating coronary

thrombosis. *American Heart Journal, 93*(4), 468-486. doi: 10.1016/S0002-8703(77)80410-9

Robertson, C., Tran, D. D., & George, S. C. (2013). Concise review: Maturation phases of human pluripotent stem cell-derived cardiomyocytes. *STEM CELLS, 31*(5), 829-837. doi:10.1002/stem.1331

Robertson, J. A. (1987). Supply and distribution of hearts for transplantation: Legal, ethical, and policy issues. *Circulation, 75*(1), 77-87. Retrieved from https://www.ncbi.nlm.nih.gov/pubmed/3539399

Robey, T. E., Saiget, M. K., Reinecke, H., & Murry, C. E. (2008). Systems approaches to preventing transplanted cell death in cardiac repair. *Journal of Molecular and Cellular Cardiology, 45*(4), 567-581. doi: 10.1016/j.yjmcc.2008.03.009

Rodell, C. B., Lee, M. E., Wang, H., Takebayashi, S., Takayama, T., Kawamura, T., et al. (2016). Injectable shear-thinning hydrogels for minimally invasive delivery to infarcted myocardium to limit left ventricular remodeling. *Circulation: Cardiovascular Interventions, 9*(10). doi:10.1161/circinterventions.116.004058

Rodriguez, Anthony G., Han, Sangyoon J., Regnier, M., & Sniadecki, Nathan J. (2011). Substrate stiffness increases twitch power of neonatal cardiomyocytes in correlation with changes in myofibril structure and intracellular calcium. *Biophysical Journal, 101*(10), 2455-2464. doi: 10.1016/j.bpj.2011.09.057

Rohr, S. (2004). Role of gap junctions in the propagation of the cardiac action potential. *Cardiovascular Research, 62*(2), 309-322. doi:10.1016/j.cardiores.2003.11.035

Romano, N. H., Sengupta, D., Chung, C., & Heilshorn, S. C. (2011). Protein-engineered biomaterials: Nanoscale mimics of the extracellular matrix. *Biochimica et Biophysica Acta (BBA) - General Subjects, 1810*(3), 339-349. doi: 10.1016/j.bbagen.2010.07.005

Rubart, M., Pasumarthi, K. B. S., Nakajima, H., Soonpaa, M. H., Nakajima, H. O., & Field, L. J. (2003). Physiological coupling of donor and host cardiomyocytes after cellular transplantation. *Circulation Research, 92*(11), 1217-1224. doi:10.1161/01.res.0000075089.39335.8c

Ryu, J. H., Kim, I.-K., Cho, S.-W., Cho, M.-C., Hwang, K.-K., Piao, H., et al. (2005). Implantation of bone marrow mononuclear cells using injectable fibrin matrix enhances neovascularization in infarcted myocardium. *Biomaterials, 26*(3), 319-326. doi: 10.1016/j.biomaterials.2004.02.058

Saini, H., Navaei, A., Van Putten, A., & Nikkhah, M. (2015). 3d cardiac microtissues encapsulated with the co-culture of cardiomyocytes and cardiac fibroblasts. *Advanced Healthcare Materials, 4*(13), 1961-1971. doi:10.1002/adhm.201500331

Samarel, A. M. (2005). Costameres, focal adhesions, and cardiomyocyte mechanotransduction. *American Journal of Physiology-Heart and Circulatory Physiology, 289*(6), H2291-H2301. doi:10.1152/ajpheart.00749.2005

Sanganalmath, S. K., & Bolli, R. (2013). Cell therapy for heart failure. *Circulation Research, 113*(6), 810-834. doi:10.1161/circresaha.113.300219

Scaringi, R., Piccoli, M., Papini, N., Cirillo, F., Conforti, E., Bergante, S., et al. (2013). Neu3 sialidase is activated under hypoxia and protects skeletal muscle cells from apoptosis through the activation of the epidermal growth factor receptor signaling pathway and the hypoxia-inducible factor (hif)-1α. *Journal of Biological Chemistry, 288*(5), 3153-3162. doi:10.1074/jbc.M112.404327

Schild, H. G. (1992). Poly(n-isopropylacrylamide): Experiment, theory and application. *Progress in Polymer Science, 17*(2), 163-249. doi: 10.1016/0079-6700(92)90023-R

Schulz, F., Friedrich, W., Hoppe, K., Vossmeyer, T., Weller, H., & Lange, H. (2016). Effective pegylation of gold nanorods. *Nanoscale, 8*(13), 7296-7308. doi:10.1039/C6NR00607H

Seif-Naraghi, S. B., Singelyn, J. M., Salvatore, M. A., Osborn, K. G., Wang, J. J., Sampat, U., et al. (2013). Safety and efficacy of an injectable extracellular matrix hydrogel for treating myocardial infarction. *Science Translational Medicine, 5*(173), 173ra125-173ra125. doi:10.1126/scitranslmed.3005503

Shachar, M., Tsur-Gang, O., Dvir, T., Leor, J., & Cohen, S. (2011). The effect of immobilized rgd peptide in alginate scaffolds on cardiac tissue engineering. *Acta Biomaterialia, 7*(1), 152-162. doi: 10.1016/j.actbio.2010.07.034

Shapira, A., Feiner, R., & Dvir, T. (2016). Composite biomaterial scaffolds for cardiac tissue engineering. *International Materials Reviews, 61*(1), 1-19. doi:10.1179/1743280415Y.0000000012

Sharma, V., Kaur, R., Bhatnagar, A., & Kaur, J. (2015). Low-ph-induced apoptosis: Role of endoplasmic reticulum stress-induced calcium permeability and mitochondria-dependent signaling. *Cell Stress and Chaperones, 20*(3), 431-440. doi:10.1007/s12192-014-0568-6

Shevach, M., Fleischer, S., Shapira, A., & Dvir, T. (2014). Gold nanoparticle-decellularized matrix hybrids for cardiac tissue engineering. *Nano Letters, 14*(10), 5792-5796. doi:10.1021/nl502673m

Shevach, M., Maoz, B. M., Feiner, R., Shapira, A., & Dvir, T. (2013). Nanoengineering gold particle composite fibers for cardiac tissue engineering. *Journal of Materials Chemistry B, 1*(39), 5210-5217. doi:10.1039/C3TB20584C

Shevach, M., Zax, R., Abrahamov, A., Fleischer, S., Shapira, A., & Dvir, T. (2015). Omentum ecm-based hydrogel as a platform for cardiac cell delivery. *Biomedical Materials, 10*(3). doi:10.1088/1748-6041/10/3/034106

Shiba, Y., Gomibuchi, T., Seto, T., Wada, Y., Ichimura, H., Tanaka, Y., et al. (2016). Allogeneic transplantation of ips cell-derived cardiomyocytes regenerates primate hearts. *Nature, 538*, 388. doi:10.1038/nature19815

Shin, M., Ishii, O., Sueda, T., & Vacanti, J. P. (2004). Contractile cardiac grafts using a novel nanofibrous mesh. *Biomaterials, 25*(17), 3717-3723. doi: 10.1016/j.biomaterials.2003.10.055

Shin, S. R., Bae, H., Cha, J. M., Mun, J. Y., Chen, Y.-C., Tekin, H., et al. (2012). Carbon nanotube reinforced hybrid microgels as scaffold materials for cell encapsulation. *ACS Nano, 6*(1), 362-372. doi:10.1021/nn203711s

Shin, S. R., Jung, S. M., Zalabany, M., Kim, K., Zorlutuna, P., Kim, S. b., et al. (2013). Carbon-nanotube-embedded hydrogel sheets for engineering cardiac constructs and bioactuators. *ACS Nano, 7*(3), 2369-2380. doi:10.1021/nn305559j

Shin, S. R., Zihlmann, C., Akbari, M., Assawes, P., Cheung, L., Zhang, K., et al. (2016). Reduced graphene oxide-gelma hybrid hydrogels as scaffolds for cardiac tissue engineering. *Small, 12*(27), 3677-3689. doi:10.1002/smll.201600178

Shintani, Y., Fukushima, S., Varela-Carver, A., Lee, J., Coppen, S. R., Takahashi, K., et al. (2009). Donor cell-type specific paracrine effects of cell transplantation for post-infarction heart failure. *Journal of Molecular and Cellular Cardiology, 47*(2), 288-295. doi: 10.1016/j.yjmcc.2009.05.009

Shu, X. Z., Liu, Y., Palumbo, F., & Prestwich, G. D. (2003). Disulfide-crosslinked hyaluronan-gelatin hydrogel films: A covalent mimic of the extracellular matrix for in vitro cell growth. *Biomaterials, 24*(21), 3825-3834. doi: 10.1016/S0142-9612(03)00267-9

Shukla, R., Bansal, V., Chaudhary, M., Basu, A., Bhonde, R. R., & Sastry, M. (2005). Biocompatibility of gold nanoparticles and their endocytotic fate inside the cellular compartment: A microscopic overview. *Langmuir, 21*(23), 10644-10654. doi:10.1021/la0513712

Sigel, A. V., Centrella, M., & Eghbali-Webb, M. (1996). Regulation of proliferative response of cardiac fibroblasts by transforming growth factor-β1. *Journal of Molecular and Cellular Cardiology, 28*(9), 1921-1929. doi: 10.1006/jmcc.1996.0185

Silva, G. V., Litovsky, S., Assad, J. A. R., Sousa, A. L. S., Martin, B. J., Vela, D., et al. (2005). Mesenchymal stem cells differentiate into an endothelial phenotype, enhance vascular density, and improve heart function in a canine chronic ischemia model. *Circulation, 111*(2), 150-156. doi:10.1161/01.cir.0000151812.86142.45

Simon, A., Maletz, S. X., Hollert, H., Schäffer, A., & Maes, H. M. (2014). Effects of multiwalled carbon nanotubes and triclocarban on several eukaryotic cell lines: Elucidating cytotoxicity, endocrine disruption, and reactive oxygen species generation. *Nanoscale Research Letters, 9*(1), 396. doi:10.1186/1556-276x-9-396

Singelyn, J. M., & Christman, K. L. (2011). Modulation of material properties of a decellularized myocardial matrix scaffold. *Macromolecular Bioscience, 11*(6), 731-738. doi:10.1002/mabi.201000423

Singh, A., Singh, A., & Sen, D. (2016). Mesenchymal stem cells in cardiac regeneration: A detailed progress report of the last 6 years (2010–2015). *Stem Cell Research & Therapy, 7*(1), 82. doi:10.1186/s13287-016-0341-0

Sneddon, I. N. (1965). The relation between load and penetration in the axisymmetric boussinesq problem for a punch of arbitrary profile. *International Journal of Engineering Science, 3*(1), 47-57. doi: 10.1016/0020-7225(65)90019-4

Song, H., Cha, M.-J., Song, B.-W., Kim, I.-K., Chang, W., Lim, S., et al. (2010). Reactive oxygen species inhibit adhesion of mesenchymal stem cells implanted into ischemic myocardium via interference of focal adhesion complex. *STEM CELLS, 28*(3), 555-563. doi:10.1002/stem.302

Souders, C. A., Bowers, S. L. K., & Baudino, T. A. (2009). Cardiac fibroblast: The renaissance cell. *Circulation Research, 105*(12), 1164-1176. doi:10.1161/circresaha.109.209809

Sousa, A. M., Liu, T., Guevara, O., Stevens, J., Fanburg, B. L., Gaestel, M., et al. (2007). Smooth muscle α-actin expression and myofibroblast differentiation by tgfβ are dependent upon mk2. *Journal of Cellular Biochemistry, 100*(6), 1581-1592. doi:10.1002/jcb.21154

Sridhar, S., Venugopal, J. R., Sridhar, R., & Ramakrishna, S. (2015). Cardiogenic differentiation of mesenchymal stem cells with gold nanoparticle loaded functionalized nanofibers. *Colloids and Surfaces B: Biointerfaces, 134*, 346-354. doi: 10.1016/j.colsurfb.2015.07.019

Stefanadis, C., Antoniou, C. K., Tsiachris, D., & Pietri, P. (2017). Coronary atherosclerotic vulnerable plaque: Current perspectives. *Journal of the American Heart Association, 6*(3). doi:10.1161/jaha.117.005543

Stout, D. A., Raimondo, E., Marostica, G., & Webster, T. J. (2014). Growth characteristics of different heart cells on novel nanopatch substrate during electrical stimulation. *Biomed Mater Eng, 24*(6), 2101-2107. doi:10.3233/BME-141020

Su, L., Hu, S., Zhang, L., Wang, Z., Gao, W., Yuan, J., et al. (2017). A fast and efficient replacement of ctab with mua on the surface of gold nanorods assisted by a water-immiscible ionic liquid. *Small, 13*(11), 1602809. doi:doi:10.1002/smll.201602809

Sun, H., Lü, S., Jiang, X.-X., Li, X., Li, H., Lin, Q., et al. (2015). Carbon nanotubes enhance intercalated disc assembly in cardiac myocytes via the β1-integrin-mediated signaling pathway. *Biomaterials, 55*, 84-95. doi: 10.1016/j.biomaterials.2015.03.030

Sun, H., Tang, J., Mou, Y., Zhou, J., Qu, L., Duval, K., et al. (2017). Carbon nanotube-composite hydrogels promote intercalated disc assembly in engineered cardiac tissues through β1-integrin mediated fak and rhoa pathway. *Acta Biomaterialia, 48*, 88-99. doi: 10.1016/j.actbio.2016.10.025

Sun, S., Zhou, C., Chen, S., Liu, J., Yu, J., Chilek, J., et al. (2014). Surface-chemistry effect on cellular response of luminescent plasmonic silver nanoparticles. *Bioconjugate Chemistry, 25*(3), 453-459. doi:10.1021/bc500008a

Sutton, M. G. S. J., & Sharpe, N. (2000). Left ventricular remodeling after myocardial infarction. *Pathophysiology and Therapy, 101*(25), 2981-2988. doi:10.1161/01.cir.101.25.2981

Suuronen, E. J., Veinot, J. P., Wong, S., Kapila, V., Price, J., Griffith, M., et al. (2006). Tissue-engineered injectable collagen-based matrices for improved cell delivery and vascularization of ischemic tissue using cd133⁺ progenitors expanded from the peripheral blood. *Circulation, 114*(1 suppl), I-138-I-144. doi:10.1161/circulationaha.105.001081

Suzuki, K. (2014). 5 - cell delivery routes for cardiac stem cell therapy *Cardiac regeneration and repair* (pp. 99-117): Woodhead Publishing.

Takens-Kwak, B. R., Jongsma, H. J., Rook, M. B., & Van Ginneken, A. C. (1992). Mechanism of heptanol-induced uncoupling of cardiac gap junctions: A perforated patch-clamp study. *American Journal of Physiology-Cell Physiology, 262*(6), C1531-C1538. doi:10.1152/ajpcell.1992.262.6.C1531

Talman, V., & Ruskoaho, H. (2016). Cardiac fibrosis in myocardial infarction—from repair and remodeling to regeneration. *Cell and Tissue Research, 365*(3), 563-581. doi:10.1007/s00441-016-2431-9

Tan, H., & Marra, K. G. (2010). Injectable, biodegradable hydrogels for tissue engineering applications. *Materials, 3*(3), 1746. Retrieved from http://www.mdpi.com/1996-1944/3/3/1746

Tan, Y., Richards, D., Coyle, R. C., Yao, J., Xu, R., Gou, W., et al. (2017). Cell number per spheroid and electrical conductivity of nanowires influence the function of silicon nanowired human cardiac spheroids. *Acta Biomaterialia, 51*, 495-504. doi: 10.1016/j.actbio.2017.01.029

Tan, Y., Richards, D., Xu, R., Stewart-Clark, S., Mani, S. K., Borg, T. K., et al. (2015). Silicon nanowire-induced maturation of cardiomyocytes derived from human induced pluripotent stem cells. *Nano Letters, 15*(5), 2765-2772. doi:10.1021/nl502227a

Tanaka, N., Moriguchi, H., Sato, A., Kawai, T., Shimba, K., Jimbo, Y., et al. (2016). Microcasting with agarose gel via degassed polydimethylsiloxane molds for repellency-guided cell patterning. *RSC Advances, 6*(60), 54754-54762. doi:10.1039/C6RA11563B

Tandon, N., Cannizzaro, C., Chao, P.-H. G., Maidhof, R., Marsano, A., Au, H. T. H., et al. (2009). Electrical stimulation systems for cardiac tissue engineering. *Nature Protocols, 4*, 155. doi:10.1038/nprot.2008.183

Tang, J., Cui, X., Caranasos, T. G., Hensley, M. T., Vandergriff, A. C., Hartanto, Y., et al. (2017). Heart repair using nanogel-encapsulated human cardiac stem cells in mice and pigs with myocardial infarction. *ACS Nano, 11*(10), 9738-9749. doi:10.1021/acsnano.7b01008

Tarus, B., Fadel, N., Al-Oufy, A., & El-Messiry, M. (2016). Effect of polymer concentration on the morphology and mechanical characteristics of electrospun cellulose acetate and poly (vinyl chloride) nanofiber mats. *Alexandria Engineering Journal, 55*(3), 2975-2984. doi: 10.1016/j.aej.2016.04.025

Taylor, D. A., Atkins, B. Z., Hungspreugs, P., Jones, T. R., Reedy, M. C., Hutchinson, K. A., et al. (1998). Regenerating functional myocardium: Improved performance after skeletal myoblast transplantation. *Nature Medicine, 4*, 1200. doi:10.1038/2701

Teplenin, A., Krasheninnikova, A., Agladze, N., Sidoruk, K., Agapova, O., Agapov, I., et al. (2015). Functional analysis of the engineered cardiac tissue grown on recombinant spidroin fiber meshes. *PLOS ONE, 10*(3), e0121155. doi:10.1371/journal.pone.0121155

Ter Keurs, H. E. D. J. (2011). Electromechanical coupling in the cardiac myocyte; stretch-arrhythmia feedback. *Pflügers Archive - European Journal of Physiology, 462*(1), 165-175. doi:10.1007/s00424-011-0944-3

Tian, B., Liu, J., Dvir, T., Jin, L., Tsui, J. H., Qing, Q., et al. (2012). Macroporous nanowire nanoelectronic scaffolds for synthetic tissues. *Nature Materials, 11*, 986. doi:10.1038/nmat3404

Timko, B. P., Cohen-Karni, T., Qing, Q., Tian, B., & Lieber, C. M. (2010). Design and implementation of functional nanoelectronic interfaces with biomolecules, cells, and tissue using nanowire device arrays. *IEEE Transactions on Nanotechnology, 9*(3), 269-280. doi:10.1109/TNANO.2009.2031807

Tjong, S. C. (2006). Structural and mechanical properties of polymer nanocomposites. *Materials Science and Engineering: R: Reports, 53*(3), 73-197. doi: 10.1016/j.mser.2006.06.001

Toma, C., Pittenger, M. F., Cahill, K. S., Byrne, B. J., & Kessler, P. D. (2002). Human mesenchymal stem cells differentiate to a cardiomyocyte phenotype in the adult murine heart. *Circulation, 105*(1), 93-98. Retrieved from https://www.ncbi.nlm.nih.gov/pubmed/11772882

Tonsho, M., Michel, S., Ahmed, Z., Alessandrini, A., & Madsen, J. C. (2014). Heart transplantation: Challenges facing the field. *Cold Spring Harb Perspect Med, 4*(5). doi:10.1101/cshperspect.a015636

Trantidou, T., Terracciano, C. M., Kontziampasis, D., Humphrey, E. J., & Prodromakis, T. (2015). Biorealistic cardiac cell culture platforms with integrated monitoring of extracellular action potentials. *Scientific Reports, 5*, 11067. doi:10.1038/srep11067

Traverse, J. H. (2012). Using biomaterials to improve the efficacy of cell therapy following acute myocardial infarction. *Journal of Cardiovascular Translational Research, 5*(1), 67-72. doi:10.1007/s12265-011-9330-y

Truong, D., Puleo, J., Llave, A., Mouneimne, G., Kamm, R. D., & Nikkhah, M. (2016). Breast cancer cell invasion into a three dimensional tumor-stroma microenvironment. *Scientific Reports, 6*, 34094. doi:10.1038/srep34094

Tse, G., Hothi, S. S., Grace, A. A., & Huang, C. L. H. (2012). Ventricular arrhythmogenesis following slowed conduction in heptanol-treated, langendorff-perfused mouse hearts. *The Journal of Physiological Sciences, 62*(2), 79-92. doi:10.1007/s12576-011-0187-2

Tse, G., Yeo, J. M., Tse, V., Kwan, J., & Sun, B. (2016). Gap junction inhibition by heptanol increases ventricular arrhythmogenicity by reducing conduction velocity without affecting repolarization properties or myocardial refractoriness in langendorff-perfused mouse hearts. *Molecular Medicine Reports, 14*(5), 4069-4074. doi:10.3892/mmr.2016.5738

Vacharathit, V., Silva, E. A., & Mooney, D. J. (2011). Viability and functionality of cells delivered from peptide conjugated scaffolds. *Biomaterials, 32*(15), 3721-3728. doi: 10.1016/j.biomaterials.2010.12.048

Van Den Borne, S. W. M., Diez, J., Blankesteijn, W. M., Verjans, J., Hofstra, L., & Narula, J. (2009). Myocardial remodeling after infarction: The role of myofibroblasts. *Nature Reviews Cardiology, 7*, 30. doi:10.1038/nrcardio.2009.199

Van Den Bulcke, A. I., Bogdanov, B., De Rooze, N., Schacht, E. H., Cornelissen, M., & Berghmans, H. (2000). Structural and rheological properties of methacrylamide modified gelatin hydrogels. *Biomacromolecules, 1*(1), 31-38. doi:10.1021/bm990017d

VanGuilder, H. D., Vrana, K. E., & Freeman, W. M. (2008). Twenty-five years of quantitative pcr for gene expression analysis. *Biotechniques, 44*(5), 619-626. doi:10.2144/000112776

Vardharajula, S., Ali, S. Z., Tiwari, P. M., Eroglu, E., Vig, K., Dennis, V. A., et al. (2012). Functionalized carbon nanotubes: Biomedical applications. *International Journal of Nanomedicine, 7*, 5361-5374. doi:10.2147/IJN.S35832

Veerman, C. C., Kosmidis, G., Mummery, C. L., Casini, S., Verkerk, A. O., & Bellin, M. (2015). Immaturity of human stem-cell-derived cardiomyocytes in culture: Fatal flaw or soluble problem? *Stem Cells and Development, 24*(9), 1035-1052. doi:10.1089/scd.2014.0533

Veleirinho, B., Rei, M. F., & Lopes-Da-Silva, J. A. (2008). Solvent and concentration effects on the properties of electrospun poly(ethylene terephthalate) nanofiber mats. *Journal of Polymer Science Part B: Polymer Physics, 46*(5), 460-471. doi:10.1002/polb.21380

Vercruysse, K. P., Marecak, D. M., Marecek, J. F., & Prestwich, G. D. (1997). Synthesis and in vitro degradation of new polyvalent hydrazide cross-linked hydrogels of hyaluronic acid. *Bioconjug Chem, 8*(5), 686-694. doi:10.1021/bc9701095

Vogt, A. M., Ackermann, C., Yildiz, M., Schoels, W., & Kübler, W. (2002). Lactate accumulation rather than atp depletion predicts ischemic myocardial necrosis: Implications for the development of lethal myocardial injury. *Biochimica et Biophysica Acta (BBA) - Molecular Basis of Disease, 1586*(2), 219-226. doi: 10.1016/S0925-4439(01)00100-4

Wall, S. T., Yeh, C.-C., Tu, R. Y. K., Mann, M. J., & Healy, K. E. (2010). Biomimetic matrices for myocardial stabilization and stem cell transplantation. *Journal of Biomedical Materials Research Part A, 95A*(4), 1055-1066. doi:10.1002/jbm.a.32904

Wang, H.-B., Dembo, M., & Wang, Y.-L. (2000a). Substrate flexibility regulates growth and apoptosis of normal but not transformed cells. *American Journal of Physiology-Cell Physiology, 279*(5), C1345-C1350. doi:10.1152/ajpcell.2000.279.5.C1345

Wang, H., Zhou, J., Liu, Z., & Wang, C. (2010). Injectable cardiac tissue engineering for the treatment of myocardial infarction. *Journal of Cellular and Molecular Medicine, 14*(5), 1044-1055. doi:10.1111/j.1582-4934.2010.01046.x

Wang, T., Wu, D.-Q., Jiang, X.-J., Zhang, X.-Z., Li, X.-Y., Zhang, J.-F., et al. (2009). Novel thermosensitive hydrogel injection inhibits post-infarct ventricle remodelling. *European Journal of Heart Failure, 11*(1), 14-19. doi:10.1093/eurjhf/hfn009

Wang, Y.-N., Wei, W.-T., Yang, C.-W., & Huang, M. H. (2013). Seed-mediated growth of ultralong gold nanorods and nanowires with a wide range of length tunability. *Langmuir, 29*(33), 10491-10497. doi:10.1021/la400985n

Wang, Y. G., Samarel, A. M., & Lipsius, S. L. (2000b). Laminin acts via β1 integrin signalling to alter cholinergic regulation of l-type ca2+ current in cat atrial myocytes. *The Journal of Physiology, 526*(1), 57-68. doi:10.1111/j.1469-7793.2000.t01-1-00057.x

Weber, K. T., Sun, Y., & Katwa, L. C. (1996). Wound healing following myocardial infarction. *Clinical Cardiology, 19*(6), 447-455. doi:10.1002/clc.4960190602

Webster, K. A. (2012). Mitochondrial membrane permeabilization and cell death during myocardial infarction: Roles of calcium and reactive oxygen species. *Future Cardiology, 8*(6), 863-884. doi:10.2217/fca.12.58

Weinberger, F., Breckwoldt, K., Pecha, S., Kelly, A., Geertz, B., Starbatty, J., et al. (2016). Cardiac repair in guinea pigs with human engineered heart tissue from induced pluripotent stem cells. *Science Translational Medicine, 8*(363), 363ra148-363ra148. doi:10.1126/scitranslmed.aaf8781

Weining, B., Christopher, P. J., & Nenad, B. (2014). Controlling the structural and functional anisotropy of engineered cardiac tissues. *Biofabrication, 6*(2), 024109. Retrieved from http://stacks.iop.org/1758-5090/6/i=2/a=024109

Wilders, R. (2006). Dynamic clamp: A powerful tool in cardiac electrophysiology. *The Journal of Physiology, 576*(2), 349-359. doi:doi:10.1113/jphysiol.2006.115840

Williams, A. R., Hatzistergos, K. E., Addicott, B., McCall, F., Carvalho, D., Suncion, V., et al. (2013). Enhanced effect of combining human cardiac stem cells and bone marrow mesenchymal stem cells to reduce infarct size and to restore cardiac function after myocardial infarction. *Circulation, 127*(2), 213-223. doi:10.1161/circulationaha.112.131110

Wu, X., Sun, Z., Foskett, A., Trzeciakowski, J. P., Meininger, G. A., & Muthuchamy, M. (2010). Cardiomyocyte contractile status is associated with differences in fibronectin and integrin interactions. *American Journal of Physiology-Heart and Circulatory Physiology, 298*(6), H2071-H2081. doi:10.1152/ajpheart.01156.2009

Wu, Y., & Guo, L. (2018). Enhancement of intercellular electrical synchronization by conductive materials in cardiac tissue engineering. *IEEE Transactions on Biomedical Engineering, 65*(2), 264-272. doi:10.1109/TBME.2017.2764000

Xavier, J. R., Thakur, T., Desai, P., Jaiswal, M. K., Sears, N., Cosgriff-Hernandez, E., et al. (2015). Bioactive nanoengineered hydrogels for bone tissue engineering: A growth-factor-free approach. *ACS Nano, 9*(3), 3109-3118. doi:10.1021/nn507488s

Xiong, Q., Hill, K. L., Li, Q., Suntharalingam, P., Mansoor, A., Wang, X., et al. (2011). A fibrin patch-based enhanced delivery of human embryonic stem cell-derived vascular cell transplantation in a porcine model of postinfarction left ventricular remodeling. *STEM CELLS, 29*(2), 367-375. doi:10.1002/stem.580

Yang, X., Pabon, L., & Murry, C. E. (2014). Engineering adolescence. *Circulation Research, 114*(3), 511. Retrieved from http://circres.ahajournals.org/content/114/3/511.abstract

Ye, L., Chang, Y.-H., Xiong, Q., Zhang, P., Zhang, L., Somasundaram, P., et al. (2014). Cardiac repair in a porcine model of acute myocardial infarction with human induced pluripotent stem cell-derived cardiovascular cells. *Cell Stem Cell, 15*(6), 750-761. doi: 10.1016/j.stem.2014.11.009

Yeo, Y., Geng, W., Ito, T., Kohane, D. S., Burdick, J. A., & Radisic, M. (2007). Photocrosslinkable hydrogel for myocyte cell culture and injection. *Journal of Biomedical Materials Research Part B: Applied Biomaterials, 81B*(2), 312-322. doi:10.1002/jbm.b.30667

You, J.-O., Rafat, M., Ye, G. J. C., & Auguste, D. T. (2011). Nanoengineering the heart: Conductive scaffolds enhance connexin 43 expression. *Nano Letters, 11*(9), 3643-3648. doi:10.1021/nl201514a

Young, J. L., Kretchmer, K., Ondeck, M. G., Zambon, A. C., & Engler, A. J. (2014). Mechanosensitive kinases regulate stiffness-induced cardiomyocyte maturation. *Scientific Reports, 4*, 6425. doi:10.1038/srep06425

Yu, Z., Graudejus, O., Tsay, C., Lacour, S. P., Wagner, S., & Morrison, B. (2009). Monitoring hippocampus electrical activity in vitro on an elastically deformable microelectrode array. *Journal of Neurotrauma, 26*(7), 1135-1145. doi:10.1089/neu.2008.0810

Zhang, J. (2015a). Engineered tissue patch for cardiac cell therapy. *Current Treatment Options in Cardiovascular Medicine, 17*(8), 37. doi:10.1007/s11936-015-0399-5

Zhang, S., Liu, P., Chen, L., Wang, Y., Wang, Z., & Zhang, B. (2015b). The effects of spheroid formation of adipose-derived stem cells in a microgravity bioreactor on stemness properties and therapeutic potential. *Biomaterials, 41*, 15-25. doi: 10.1016/j.biomaterials.2014.11.019

Zhang, Y., Wang, D., Chen, M., Yang, B., Zhang, F., & Cao, K. (2011). Intramyocardial transplantation of undifferentiated rat induced pluripotent stem cells causes tumorigenesis in the heart. *PLOS ONE, 6*(4), e19012. doi:10.1371/journal.pone.0019012

Zhang, Z., & Lin, M. (2014). Fast loading of peg-sh on ctab-protected gold nanorods. *RSC Advances, 4*(34), 17760-17767. doi:10.1039/C3RA48061E

Zhou, J., Chen, J., Sun, H., Qiu, X., Mou, Y., Liu, Z., et al. (2014). Engineering the heart: Evaluation of conductive nanomaterials for improving implant integration and cardiac function. *Scientific Reports, 4*, 3733. doi:10.1038/srep03733

Zhu, Y., & Li, W. (2008). Cytotoxicity of carbon nanotubes. *Science in China Series B: Chemistry, 51*(11), 1021-1029. doi:10.1007/s11426-008-0120-6

Zimmermann, W.-H., & Cesnjevar, R. (2009). Cardiac tissue engineering: Implications for pediatric heart surgery. *Pediatric Cardiology, 30*(5), 716-723. doi:10.1007/s00246-009-9405-6

Zimmermann, W.-H., Melnychenko, I., Wasmeier, G., Didié, M., Naito, H., Nixdorff, U., et al. (2006). Engineered heart tissue grafts improve systolic and diastolic function in infarcted rat hearts. *Nature Medicine, 12*, 452. doi:10.1038/nm1394

APPENDIX A

SUPPLEMENTARY FIGURES FOR CHAPTER 2

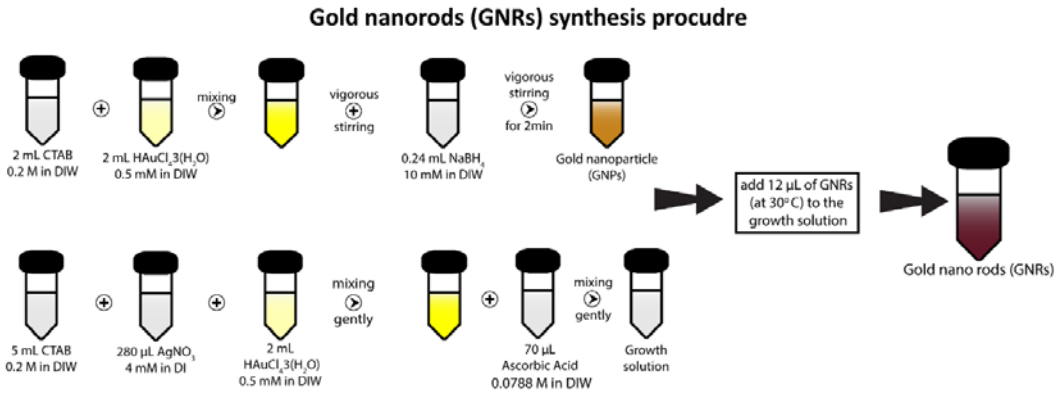

Figure A.1. Schematic illustration showing the GNRs synthesis steps by using a seed-mediated method.

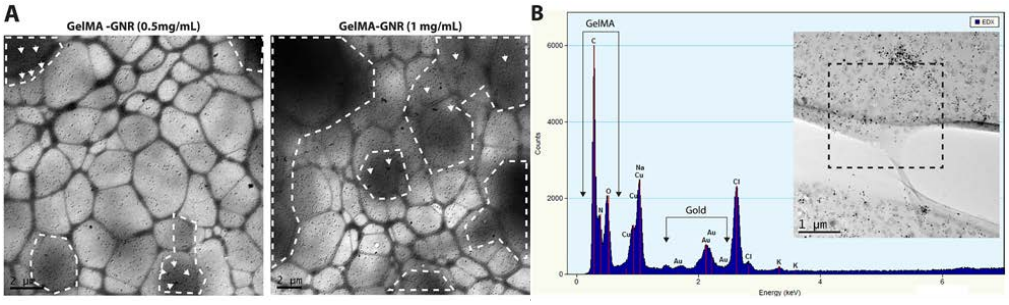

Figure A.2. A) TEM micrographs of a thin layer (dashed area) of GelMA-GNR hybrid hydrogels (0.5 and 1 mg/mL) demonstrating that GNRs (white arrows) were successfully embedded within the hydrogel matrix (dashed areas). B) EDX spectrum of GelMA-GNR hybrid hydrogel (1.5 mg/mL) further confirming the presence of gold (Au) and GelMA elements.

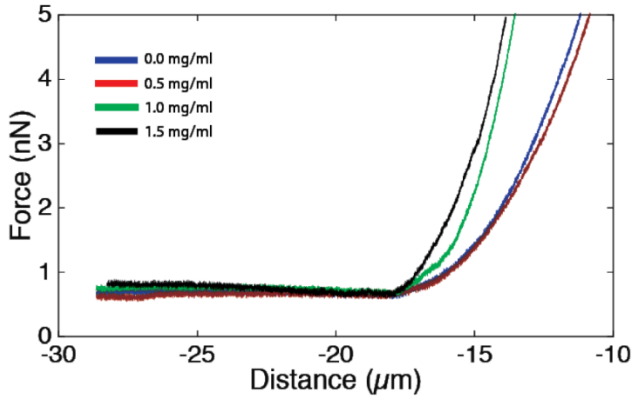

Figure A.3. Representative force-indentation distance curves of pure GelMA and GelMA-GNR hybrid hydrogels.

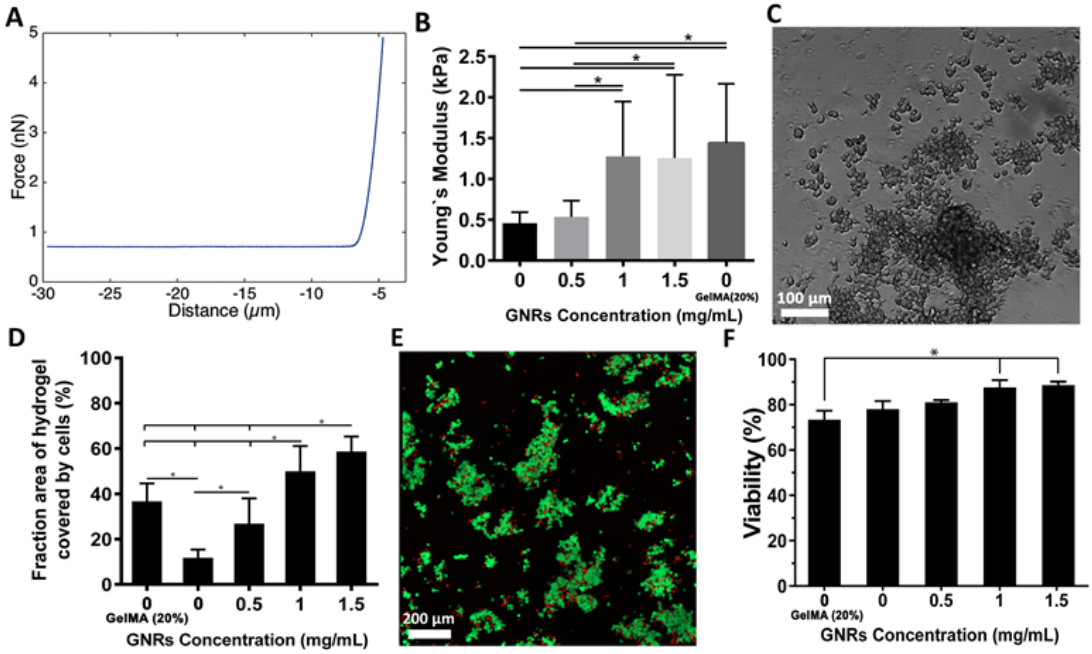

Figure A.4. A) Representative Force-Indentation Distance curves of pure 20% GelMA (wt/v) hydrogel illustrating B) similar mechanical stiffness compared to GelMA-GNR hybrid hydrogels (1 and 1.5 mg/mL of GNRs) and significantly higher stiffness than pure 5% GelMA (wt/v). C) Phase-contrast image of CMs seeded on 20% GelMA (wt/v) hydrogel on day 1 of culture. D) Quantified cell retention on day 1. E) A representative fluorescent image demonstrating the dead (red) and live (green) cardiomyocytes on 20 % GelMA (wt/v) control hydrogel at day 1along with F) quantified cell survival data.

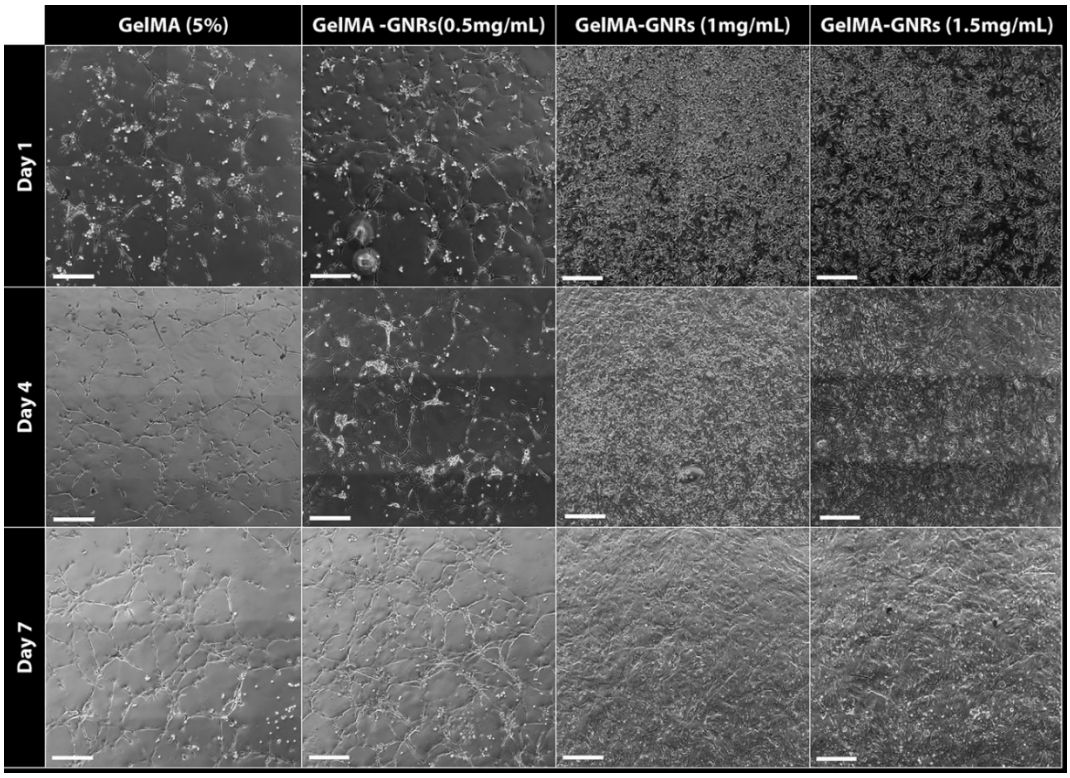

Figure A.5. Phase-contrast optical microscopy images of cultured cardiomyocytes on top of hybrid GelMA-GNR and pure GelMA hydrogels at day 1, 4, and 7 illustrating cell retention and spreading over the culture period. Scale bars represent 250 µm.

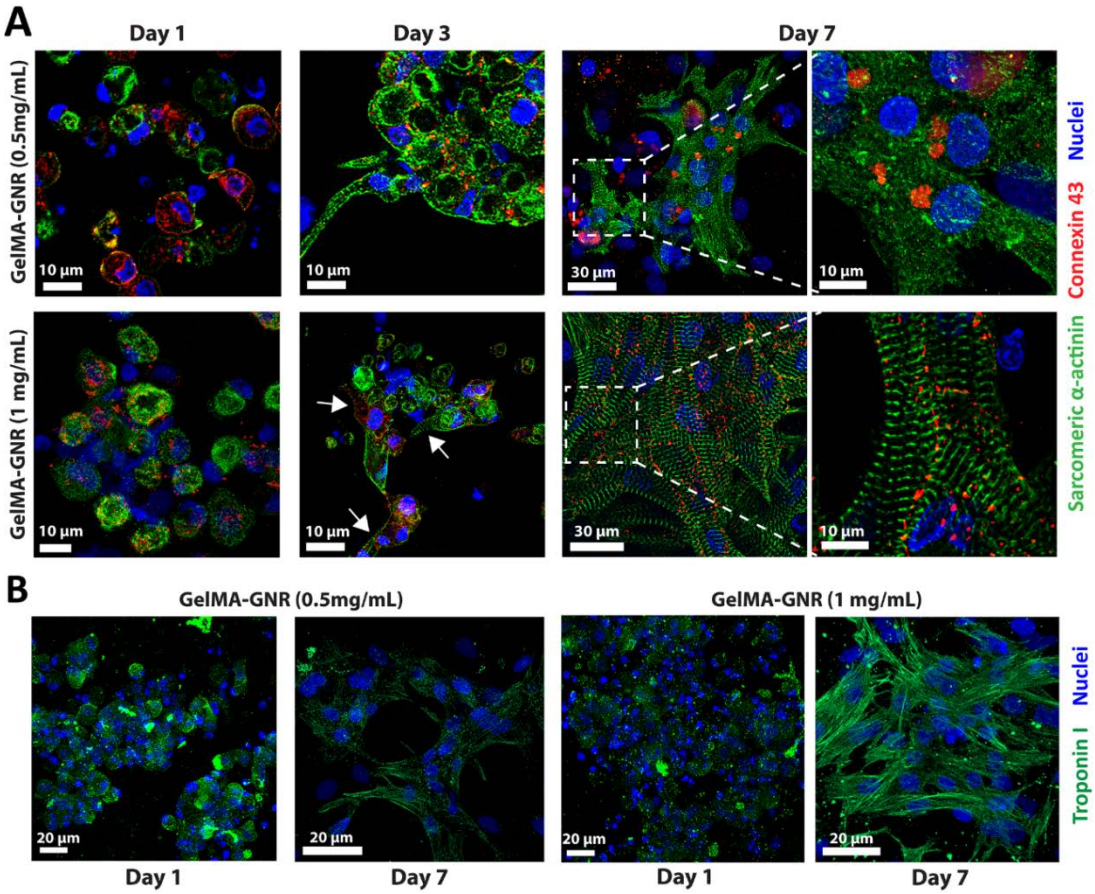

Figure A.6. A) Z-stack immunostained images of cardiac-specific markers within GelMA-GNR hybrid hydrogel with 0.5 and 1 mg/ml of GNRs. Representative immunostained images showing the expression of SAC (green) and Cx43 (red) on day 1, 3 (arrows showing sarcomeres formation) and 7; B) Immunostained images of cTnI (green) on day 1 and 7 of culture for GelMA-GNR (0.5 and 1 mg/mL) hybrid hydrogel constructs.

APPENDIX B

SUPPLEMENTARY FIGURES FOR CHAPTER 6

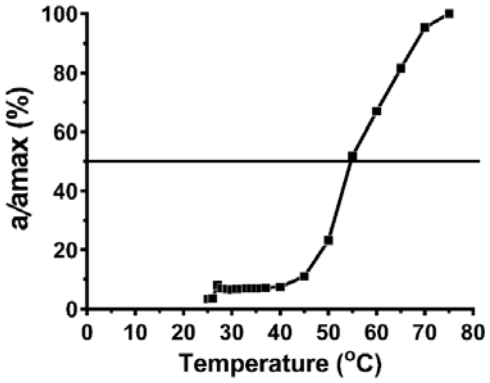

Figure B.1. The relative cloud point (a/amax(%)) for enzymatically degraded PNJ-Gel hydrogel.

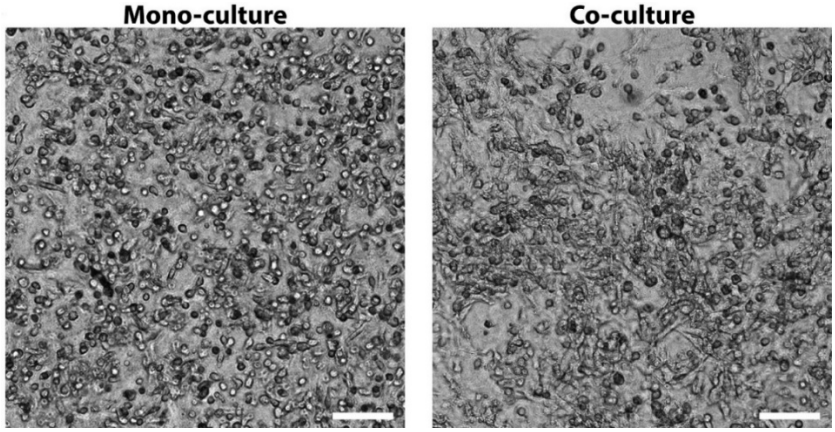

Figure B.2. Phase-contrast (scale bars represent 100 µm) mono- and co-culture groups illustrating cell morphology at day 4of culture.

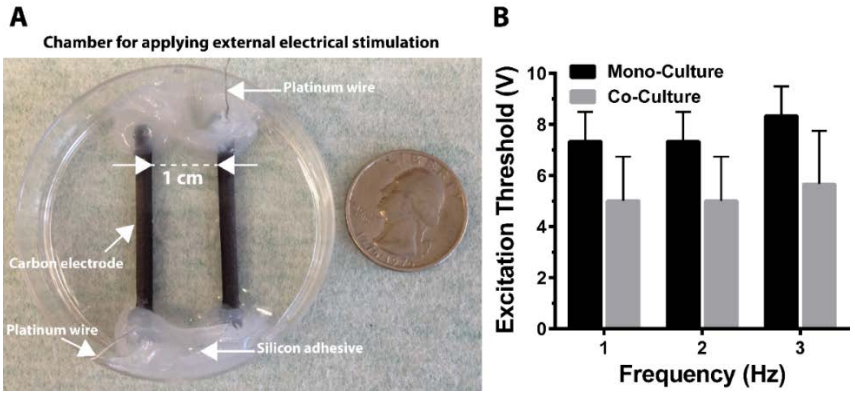

Figure B.3. External electrical stimulation setup. A) Photograph of the fabricated chamber and B) the excitation threshold (V) for different applied frequencies (1, 2, and 3 Hz) for mono- and co-culture groups (day 7).

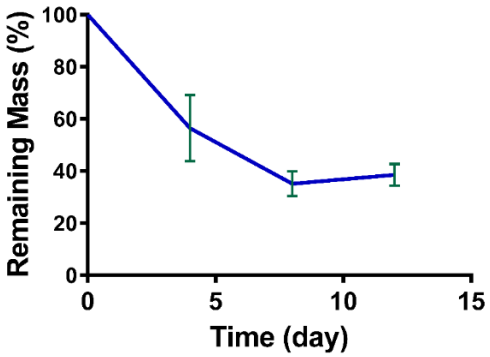

Figure B.4. Hydrolytic degradation profile of the synthesized hydrogel.

Table B.1.

The TaqMan primers which were used for qPCR analysis

TaqMan Primers	
Target Name	Cat No
cTNT	Rn01483694_m1
Cx43	Rn01433957_m1
MLC2v	Rn02769676_s1
GAPDH	Rn01775763_g1

Table B.2.

The SYBR primers which were used for qPCR analysis

SYBR Primers		
Target Name	FWD Sequence	RVS Sequence
18S	GCAATTATTCCCCATGAACG	GGCCTCACTAAACCATCCAA
ACTN1	CACCACCGCTGAACGTGAAA	AGTCTCAGGACAGCGGAAAC

APPENDIX C

LIST OF SUPPLEMENTARY VIDEOS

Supplementary videos are readable using media players in Windows operating system.

Chapter 2:

C.1. Representative video of synchronous beating of CMs cultured on pure GelMA hydrogel at day 7.

C.2. Representative video of synchronous beating of CMs cultured on 0.5 mg/mL GelMA-GNR hybrid hydrogel at day 7.

C.3. Representative video of synchronous beating of CMs cultured on 1 mg/mL GelMA-GNR hybrid hydrogel at day 7.

C.4. Representative video of synchronous beating of CMs cultured on 1.5 mg/mL GelMA-GNR hybrid hydrogel at day 7.

C.5. Representative video of synchronous contraction of the centimeter scale 1 mg/mL GelMA-GNR hybrid tissue at day 7.

C.6. Representative video of synchronous contraction of the centimeter scale 1.5 mg/mL GelMA-GNR hybrid tissue at day 7.

C.7. Representative video illustrating spontaneous Ca2+ puffs of cells on GelMA (5%) and GelMA-GNR hybrid hydrogels.

C.8. Representative video of CMs beating on GelMA (5%) at three different frequencies (1, 2, and 3 Hz) applied by an external pulse generator.

C.9. Representative video of CMs beating on GelMA-GNR (0.5 mg/mL) at three different frequencies (1, 2, and 3 Hz) applied by an external pulse generator.

C.10. Representative video of CMs beating on GelMA-GNR (1 mg/mL) at three different frequencies (1, 2, and 3 Hz) applied by an external pulse generator.

C.11. Representative video of CMs beating on GelMA-GNR (1.5 mg/mL) at three different frequencies (1, 2, and 3 Hz) applied by an external pulse generator.

Chapter 3:

C.12. Representative video of synchronous beating of CMs cultured on GelMA hydrogels at day 7.

C.13. Representative video of synchronous beating of CMs cultured on GelMA-GNR hydrogels at day 7.

C.14. Representative video of CMs beating on GelMA and GelMA-GNR at three different frequencies (0.5, 1, and 2 Hz) applied by an external pulse generator.

Chapter 6:

C.15. Representative video of synchronous beating of CMs (mono-culture) cultured within PNJ-Gelatin hydrogel at day 3.

C.16. Representative video of synchronous beating of CMs (mono-culture) cultured within PNJ-Gelatin hydrogel at day 6.

C.17. Representative video of synchronous beating of co-culture of the cells (CMs and CFs) within PNJ-Gelatin hydrogel at day 3.

C.18. Representative video (low magnification) of synchronous beating of co-culture of the cells (CMs and CFs) within PNJ-Gelatin hydrogel at day 3.

C.19. Representative video (low magnification) of synchronous beating of co-culture of the cells (CMs and CFs) within PNJ-Gelatin hydrogel at day 9.

APPENDIX D

COPYRIGHT PERMISSIONS

Copyright permissions for Figure 1.2.

Ali Navaei <anavaei@asu.edu>

Thank you for your order with RightsLink / Springer Nature

no-reply@copyright.com <no-reply@copyright.com> Fri, Jul 6, 2018 at 3:36 PM
To: anavaei@asu.edu

SPRINGER NATURE

Thank you for your order!

Dear Mr. Ali Navaei,

Thank you for placing your order through Copyright Clearance Center's RightsLink® service.

Order Summary

Licensee:	Arizona State University
Order Date:	Jul 6, 2018
Order Number:	4383300031858
Publication:	Nature Nanotechnology
Title:	Nanowired three-dimensional cardiac patches
Type of Use:	Thesis/Dissertation
Order Total:	0.00 USD

View or print complete details of your order and the publisher's terms and conditions.

Sincerely,

Copyright Clearance Center

Tel: +1-855-239-3415 / +1-978-646-2777
customercare@copyright.com
https://myaccount.copyright.com

Copyright Clearance Center RightsLink®

Home | Account Info | Help

Title:	Carbon-Nanotube-Embedded Hydrogel Sheets for Engineering Cardiac Constructs and Bioactuators
Author:	Su Ryon Shin, Sung Mi Jung, Momen Zalabany, et al
Publication:	ACS Nano
Publisher:	American Chemical Society
Date:	Mar 1, 2013

Logged in as:
Ali Navaei
Arizona State University
Account #:
3001166390

LOGOUT

PERMISSION/LICENSE IS GRANTED FOR YOUR ORDER AT NO CHARGE

This type of permission/license, instead of the standard Terms & Conditions, is sent to you because no fee is being charged for your order. Please note the following:

- Permission is granted for your request in both print and electronic formats, and translations.
- If figures and/or tables were requested, they may be adapted or used in part.
- Please print this page for your records and send a copy of it to your publisher/graduate school.
- Appropriate credit for the requested material should be given as follows: "Reprinted (adapted) with permission from (COMPLETE REFERENCE CITATION). Copyright (YEAR) American Chemical Society." Insert appropriate information in place of the capitalized words.
- One-time permission is granted only for the use specified in your request. No additional uses are granted (such as derivative works or other editions). For any other uses, please submit a new request.

If credit is given to another source for the material you requested, permission must be obtained from that source.

BACK | CLOSE WINDOW